

Roll-to-Roll Advanced Materials Manufacturing DOE Laboratory Collaboration - Early Stage R&D Phase 2 and FY 2021 Final Report

ORNL/SPR-2022/2412

March 2022

Funding provided by:

U.S. Department of Energy

Office of Energy Efficiency and Renewable Energy

Advanced Manufacturing Office

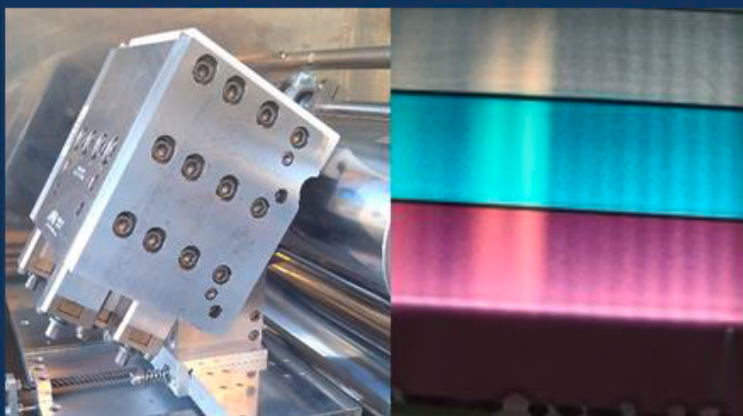
ORNL R2R Slot Die Coating of PEMFC Bilayers



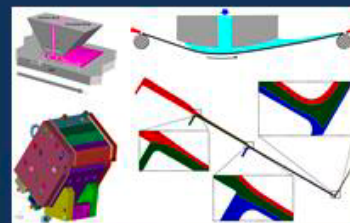
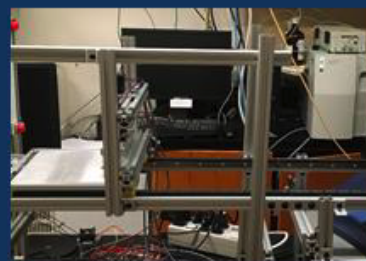
ANL R2R Electrospinning System



NREL R2R Slide Die & Bilayer Coating



LBLN Modular Automated
Coating/Drying
Observation System with
Confocal Microscope



SNL R2R Slot & Slide
Die Coating Models



Disclaimer

This report was prepared as an account of work sponsored by an agency of the United States government. Neither the United States government nor any agency thereof, nor any of their employees, makes any warranty, express or implied, or assumes any legal liability or responsibility for the accuracy, completeness, or usefulness of any information, apparatus, product, or process disclosed or represents that its use would not infringe privately owned rights. Reference herein to any specific commercial product, process, or service by trade name, trademark, manufacturer, or otherwise does not necessarily constitute or imply its endorsement, recommendation, or favoring by the United States government or any agency thereof. The views and opinions of authors expressed herein do not necessarily state or reflect those of the United States government or any agency thereof.

DOCUMENT AVAILABILITY

Reports produced after January 1, 1996, are generally available free via US Department of Energy (DOE) SciTech Connect.

Website <http://www.osti.gov/scitech/>

Reports Produced before January 1, 1996, may be purchased by members of the public from the following source:

National Technical Information Service
5285 Port Royal Road
Springfield, VA 22161
Telephone 703-605-6000 (1-800-553-6847)
TDD 703-487-4639
Fax 703-605-6900
E-mail info@ntis.gov
Website <http://www.ntis.gov/help/ordermethods.aspx>

Reports are available to DOE employees, DOE contractors, Energy Technology Data Exchange representatives, and International Nuclear Information System representatives from the following source:

Office of Science and Technical Information
PO Box 62
Oak Ridge, TN 37831
Telephone 865-576-8401
Fax 865-576-5728
Email reports2osti.gov
Website <http://www.osti.gov/contact.html>

Foreword

Oak Ridge National Laboratory (ORNL), ANL National Laboratory (ANL), Lawrence Berkeley National Laboratory (LBNL), and the National Renewable Energy Laboratory (NREL) performed as a collaborative Roll-to-Roll Advanced Materials Manufacturing (R2R AMM) Department of Energy (DOE) Laboratory Consortium during Fiscal Year (FY) 2016 through FY 2018. This was considered Phase 1 of a multi-year program approach to respond to near- to mid-term AMO requirements and future AMO program strategies. In June 2018, the Consortium responded to a FY 2019 Advanced Manufacturing Office (AMO) Lab Call, DE-LC-000L059, for Topic 3 titled “Roll-to-Roll Processing” with a proposal “Early-stage advanced national multi-laboratory roll-to-roll research and development (R&D) collaboration with industrial Cooperative Research and Development Agreement (CRADA) collaboration”. ORNL solicited research concepts from other National Laboratories, including the four Phase 1 Consortium laboratories, and received over 50 white papers. Five were selected for inclusion in the proposal to the Lab Call. One paper from Sandia National Laboratories (SNL), Albuquerque, NM and the University of New Mexico (UNM) for process modelling was also selected, so SNL was added to the multi-laboratory collaboration. The R2R Consortium was rebranded to be the R2R AMM DOE Laboratory Collaboration (i.e., R2R Collaboration) for consistency with the AMO Lab Call title. The proposal was accepted for funding in FY 2019 through FY 2021, contingent on annual budget authorizations, and this was a three-year Phase 2 project. This report discusses tasks, results, and findings during the third and final year of Phase 2 for each performing laboratory.

This R2R Collaboration’s goal is to advance the understanding of R2R processing for high-throughput advanced manufacturing through an early-stage research approach to enable new devices and lower the cost of existing processing routes for competitive U.S. manufacturing. The projects directly address the AMO’s Multi-Year Program Plan (MYPP) challenges for the use of multilayer coating technologies applicable to flexible and integrated electronics, separation membranes, photovoltaics (PV), and selective barrier materials [1]. Collaborative research addresses the AMO identified targets of (1) processing technologies with up to a 10x production capacity increase and (2) in-line instrumentation tools to evaluate the material performance and functionality. Working with industry partners through CRADA projects, the R2R Collaboration is addressing challenges and barriers for continuous R2R processing, registration and alignment, scalability, materials compatibility and defects, macroscopic and continuum drying process model development, stoichiometry control, and the availability of materials data for R2R processing. Program goals target the development of technologies that reduce the cost per manufactured product throughput of continuous R2R manufacturing processes, and the development of in-line instrumentation tools that will evaluate the quality of single and multilayer materials on process weblines.

The FY 2021 core program continued efforts from the second year of Phase 2 and consisted of a broad range of research task areas focused on colloidal chemistry and slurry formulation, novel R2R deposition systems based on electrospinning (ES) technology, in-line real-time non-destructive evaluation (NDE) and advanced in-situ testing capabilities, physics and methodologies for multilayer coatings, ink formulations and rheology, modeling and simulation of drying and mixing processes, and continuum-scale process models for the capillary hydrodynamics of coating deposition. One CRADA project continued into FY 2021 with the primary applications of the research to develop a R2R process for direct coating of anode catalyst layer to a perfluoro sulfonic acid (PFSA) membrane.

The Collaboration laboratories have unique assets that complement each other for the research, development, testing and evaluation of these clean energy technologies. These include the following infrastructure, testing, operations, characterization, and analysis capabilities:

- Precision coating equipment
- Laboratory and pilot-scale R2R operations

- Device fabrication and assembly
- Electrochemical and cell performance evaluation
- State-of-the-art microscopy and tomography
- Surface characterization
- X-ray and neutron characterization facilities
- Computational science
- Process modeling and characterization
- World-class data analysis
- In-line quality control (QC)

DOE cost targets for advanced energy storage and conversion applications will not be commercialized without significant and timely advancements in R2R manufacturing. Required R2R advances include adaptation of existing processing methods (gravure, slot die, slide die) and development of novel approaches (simultaneous multilayer coatings and ES) that have the potential to significantly impact U.S. manufacturing sector recovery, environmental applications in clean water, energy security, decarbonization and sustainable transportation. Economies of scale through increased manufacturing volumes based on traditional assembly and processing methods will not suffice. For example, the current goal for the DOE Vehicle Technologies Office (VTO) is to reduce the cost of electric vehicle batteries to less than \$100/kWh and ultimately to \$80/kWh while increasing the range of electric vehicles to 300 miles and decreasing the charge time to 15 minutes or less[2] [3]. Commercial lithium (Li) ion technology is largely limited to cells with gravimetric energy densities of <250 Wh/kg and volumetric energy densities of <650 Wh/L. Volumetric energy densities are often more important for portable electronics and electric vehicles. There is immense need to push the energy densities to as high as ~500 Wh/kg and 1,000 Wh/L [4]. Novel R2R processing technologies will be required to manufacture Li-ion technologies with these energy densities in high volume.

Current polymer electrolyte membrane (PEM) electrolyzers require 65-75% cost reduction from \$1100/kW to \$400/kW. The DOE Hydrogen and Fuel Cells Technology Office (HFTO) target that guides fuel cell R&D is to reduce the cost for a fuel cell electric vehicle system from \$180/kW at a low-volume production rate to an ultimate target of \$30/KW [5]. Water consumption for renewable energy technologies can be as high as a medium value 4,500 gallons/megawatt-hours and more than 44,000 gallons/megawatt-hours for non-renewable energy applications [6]. New technologies are needed to increase the capacity of these systems to meet future needs. Other examples of the Energy Efficiency and Renewable Energy (EERE) Office funded technologies that have a similar cost-target issue are chemical-process industry membranes, window films, PV films, and flexible electronic films. The EERE AMO is poised to assist in reaching the low dollars per unit costs of these various critical energy related applications through addressing R2R manufacturing problems common to each application.

Preface

This report provides a description of the program structure for FY 2021 and the progress made during Phase 2 of the R2R Collaboration to overcome technical challenges and manufacturing barriers for expanding use of R2R technologies and processes for clean energy applications. The R&D documented in the report was performed by five DOE National Laboratories as a collaborative group with participation from industry through formal and informal partnerships. The approach of the collaboration involves advancing methods for the preparation of materials for coating, novel and improved methods and techniques for multilayer coatings, and improved post-processing material methods that can be used for R2R processes that are applicable to enhancing the performance of renewable energy technologies and systems. Specific areas of interest investigated include colloidal chemistry, surfactant research, slurry processing, and drying and curing; novel R2R deposition using ES; methodologies for ink formulations, multilayer coatings, rheology, and deposition of battery and fuel cell materials; fabrication and in-situ characterization of prototype components and devices; and in-line real-time NDE. The particle-scale and continuum-scale modeling and simulations for these layered materials, energy storage technologies, and continuous manufacturing processes that are being developed will allow for improvements and advances in R2R manufacturing applications, particularly for design and scale-up.

This effort supports building the foundation of technologies, processes and a U.S. manufacturing base that will enable an order of magnitude reduction in process development cycles with the pathway for initial commercialization within months instead of years.

Acknowledgements

First and foremost, the following scientists, investigators and technical support who are working diligently to realize their innovative ideas and technological developments in R2R processing and their desire to deploy them broadly for energy storage applications are acknowledged for their contributions:

ANL: Gregory Krumdick, Yuepeng Zhang, Donna Brunner, Deborah Myers, Devon Powers, Jae Hyung Park, Albert Lipson, Erik Dahl, Mones Omari, Ashley Simmons, Li Cao, Mark Koziel

ORNL: Georgios Polyzos, Jaswinder Sharma, Jianlin Li, Erin Creel, Kelsey (Grady) Livingston, Ritu Sahore, Charl Jafta, Alexander Kukay, Emily Bott

NREL: Michael Ulsh, Peter Rupnowski, Brian Green, Scott Mauger, KC Neyerlin, Sunil Khandavalli, Jason Pfeilsticker, Janghoon Park, Reilly Seban, Maikel van Hest, Bertrand Tremolet deVillers, Carlos Baez-Cotto, Sanghun Lee

LBNL: Vince Battaglia, Kenny Higa, Zhi Huang, Bei Fan, Buyi Zhang, Ravi Prasher

SNL/UNM: P. Randall Schunk, Kristianto Tjiptowidjojo, Nelson Bell, Chris Wall, Ben Wall, Marvin Larsen, Robert Malakhov, Chance Parrish

DOE EERE AMO: Brian Valentine (Technical Project Management)

DOE EERE HFTO: Nancy Garland and Michael Hahn (Technical Project Management)

We would also like to acknowledge the principal investigators and project managers at Nel Hydrogen, Giner, Plug Power, Eastman Kodak, and Saint-Gobain for their coordination and collaboration on the R2R projects.

Finally, we would also like to acknowledge the contributions of Fred Crowson, Energetics, for his project management assistance and involvement in preparing and publishing this report.

The research at

- Oak Ridge National Laboratory, managed by University of Tennessee Battelle, LLC for the U.S. Department of Energy, under contract DE-AC05-00OR22725
- ANL National Laboratory, managed by University of Chicago ANL, LLC for the U.S. Department of Energy, under contract DE-AC02-06CH11357
- Lawrence Berkeley National Laboratory, managed by University of California for the U.S. Department of Energy, under contract DE-AC02-05CH11231
- National Renewable Energy Laboratory, managed by Alliance for Sustainable Energy, LLC for the U.S. Department of Energy, under contract DE-AC36-08GO28308
- Sandia National Laboratories managed and operated by National Technology and Engineering Solutions of Sandia, LLC., a wholly owned subsidiary of Honeywell International, Inc., for the U.S. Department of Energy's National Nuclear Security Administration under contract DE-NA-0003525.

was sponsored by EERE AMO, Valri Lightner and Brian Valentine.

Acronyms and Abbreviations

μA	microamp
μm or μ	micrometers or microns
μs	microsecond
Ω	ohm
2D	two dimensional
3D	three dimensional
Ag	silver
AI	artificial intelligence
Al	aluminum
Al-LLZO	aluminum-doped LLZO
AMM	Advanced Materials Manufacturing
AMO	Advanced Manufacturing Office
ANL	ANL National Laboratory
APS	Advanced Photon Source
ATR-FTIR	Attenuated Total Reflectance - Fourier Transform Infrared
$^{\circ}\text{C}$	degrees Centigrade
C	chemical symbol for carbon (when referring to the chemical element)
C	capacitance (when referring to electrical property)
CA	California
CB	carbon black
CCM	catalyst coated membrane
CEI	cathode-electrolyte-interface
c-LLZO	cubic phase lithium lanthanum zirconium oxide
cm	centimeter
cm^2	centimeter squared
CMC	carboxymethyl cellulose
CO	Colorado
CO	carbon monoxide
CO_2	carbon dioxide
COVID	COronaVIRus Disease
cP	centipoise
CRADA	Cooperative Research and Development Agreement
Cu	copper
DAKOTA	software for advanced parametric analyses that enables design exploration, model calibration, risk analysis, and quantification of margins and uncertainty with computational models
DC	District of Columbia
DC	direct current
DI	deionized water
DOE	U.S. Department of Energy
DT	digital twin
EB	electron beam
EDS or EDX	energy dispersive X-ray spectroscopy
EERE	Energy Efficiency and Renewable Energy
e.g.	abbreviation meaning “for example”; a Latin phrase, “ <i>exempli gratia</i> ” meaning “for the sake of example”
ES	electrospinning

etc.	abbreviation for the Latin phrase “et cetera” which means “and so forth”
EtOH	ethanol
F	fluorine
fpm or ft/min	feet per minute
FTIR	Fourier-transform infrared (spectroscopy)
FY	fiscal year
g	gram or grams
GDE	gas diffusion electrode
GDL	gas diffusion layer
GOMA 6.0	an open-source, parallel, and scalable multiphysics software package for modeling and simulation of physical processes
h or hr	hour
H ₂ O	water
HFIR	High Flux Isotope Reactor
HFTO	Hydrogen and Fuel Cell Technologies Office
HSC	high surface carbon
Hz	hertz
I/C, I:C, I/C _{at}	ionomer-to-catalyst ratio
IL	Illinois
IPA	isopropyl alcohol
IR	infrared
IrO ₂	iridium oxide
J/cm ²	joules per square centimeter
kDA	kilodalton
kg	kilogram
kV	kilovolt
kW	kilowatt
kWh	kilowatt hour
L	inductance
La	lanthanum
LBNL	Lawrence Berkeley National Laboratory
Li	lithium
LiCoO ₂	lithium cobalt oxide
LiTFSI	lithium bis(trifluoromethanesulfonyl) imide
LLC	limited liability company
LLZO	lithium lanthanum zirconium oxide, Li ₇ La ₃ Zr ₂ O ₁₂
LSCF	lanthanum strontium cobalt ferrite, (La _{0.6} Sr _{0.4}) _{0.95} Co _{0.2} Fe _{0.8} O _{3-x}
M	meter(s) (when referring to length)
M	million (when referring to a numerical value)
M	molar (when referring to chemical concentration)
mA	milliamp
MATLAB	<u>MAT</u> rix <u>LAB</u> oratory, a multi-paradigm numerical computing environment and programming language
MEA	membrane electrode assembly
MERF	Materials Engineering and Research Facility
mg/cm ²	milligram per square centimeter
mg _{Pt} /cm ²	milligrams of platinum per square centimeter
min(s)	minute(s)
ml or mL	milliliter

ML	machine learning
mL/hr	milliliters per hour
mL/min	milliliters per minute
mm	millimeters
mm ² /min	square millimeter per minute
m/min	meters per minute
mS/cm	milli-Siemens per centimeter
MYPP	multi-year program plan
NACENT	National Science Foundation Engineering Research Center
NaCl	sodium chloride
NDE	non-destructive evaluation
NEA	Nordland Electrical Adhesive
nm	nanometer
NM	New Mexico
NMC	nickel-manganese-cobalt
NMP	N-methyl-2-pyrrolidone
nPA	normal propyl alcohol (or normal propanol)
NREL	National Renewable Energy Laboratory
O	monatomic oxygen
ORNL	Oak Ridge National Laboratory
P3H7	poly(3-hexylthiophene)
Pa.s	Pascal seconds
PAA	polyacrylic acid
PAN	polyacrylonitrile
PEM	polymer electrolyte membrane
PEMFC	polymer electrolyte membrane fuel cell
PEO	poly(ethylene oxide)
PFSA	perfluoro sulfonic acid
PMA	poly(methyl acrylate)
PMOS	p-channel metal-oxide semiconductor
PSA	particle size analyzer
Pt	chemical symbol for platinum
Pt/C	platinum to carbon ratio
PTFE	polytetrafluoroethylene
PV	photovoltaic
PVDF	polyvinylidene fluoride
PVP	polyvinylpyrrolidone
QC	quality control
R	resistance
R&D	research and development
R2R	roll-to-roll
RL	reinforcement learning
rpm	revolutions per minute
s	second(s)
S	sulfur
S/cm	Siemens per centimeter
SANS	small angle neutron scattering
SAXS	small-angle X-ray scattering
SEM	scanning electron microscope (or microscopy)

SiO ₂	silicon dioxide
SNL	Sandia National Laboratories
SNS	Spallation Neutron Source
SOFC	solid-oxide fuel cell
SSB	solid state battery
SWT	SolarWindow Technologies, Inc.
SWNT	single-walled nanotube
TEM	transmission electron microscopy (or microscope)
TN	Tennessee
UNM	University of New Mexico
U.S.	United States
USAXS	ultra-small angle X-ray scattering
UV	ultraviolet
VDD	supply drain DC voltage
VGG	a model having a series of convolutional layers followed by one or a few dense (or fully connected) layers
vs.	versus
VTO	Vehicle Technologies Office
Vu	Vulcan
WAXS	wide-angle X-ray scattering
Wh/kg	watt-hour per kilogram
Wh/L	watt-hour per liter
wt. %	percent by weight
XPS	X-ray photoelectron spectroscopy
XRD	X-ray diffraction
XRF	X-ray fluorescence spectroscopy
YSZ	yttria-stabilized zirconia
Zr	chemical symbol for zirconium

Table of Contents

Disclaimer	i
Foreword	ii
Preface	iv
Acknowledgements	v
Acronyms and Abbreviations	vi
Table of Contents	x
List of Figures	xiii
List of Tables	xix
Executive Summary	1
Accomplishments	3
Technology Assessment	12
Roll-to-Roll Advanced Materials Manufacturing DOE Laboratory Collaboration Project Overview	13
Collaboration Contacts	13
Annual Operating Plan Title and Corporate Planning System (CPS) Agreement Numbers	14
Project Introduction	15
Objectives	15
Approach	16
Core Program	16
Potential New Efforts for Phase 3	16
Technology Transfer Paths	16
Results	17
Novel R2R Deposition System Based on ES Technology and Advanced/In-Situ Characterization and Testing (ANL Lead Laboratory)	17
Task 3. Electrospinning scale-up using SSBs and SOFCs as example technologies	17
R2R spinning of LLZO fiber for densified solid-state battery electrolytes	18
Energy conversion material nanofiber ES studies including fiber characterization and device fabrication/testing	19
Spinning scale-up for fibers containing surface electrocatalyst particles	23
Cationic and anionic fiber spinning scale-up for deionization membranes	24
SOFC fiber spinning scale-up	27
Fiber ink rheological property measurements	28

Task 7: Printed Electronics - flexible electronics with micro- and nano- structuring.....	28
Conductive and dielectric ink study for R2R printed electronics.....	29
Design of a logical device circuit.....	32
Exploratory study of ML for slot-die coating process optimization.....	33
Education, information dissemination, publications, and technology transfer	37
Colloidal Chemistry, Surfactant Research, Slurry Processing, Deposition and Drying/Curing Methods (ORNL Lead Laboratory).....	37
Task 1. Multilayer coatings for PEMFC and LIB.....	37
Validation of coating window model with low solids-loading ink.....	37
Accurate modeling of the coating window for high-solids inks.....	38
Multilayer coating of PEMFCs.....	40
Task 2. Formulation chemistry including mixing, deposition, and drying/curing	41
Effect of mixing method, time, and speed on PEMFC cathode morphology.....	41
Planetary mixing	44
Drying physics studies	47
Task 3. R2R ES recipe and platform development support	48
Synthesis and characterization of composite cathodes for SSBs based on the fiber electrolytes	48
Education, information dissemination, publications, and technology transfer	51
Physics and Methodologies for Multilayer Coatings/Deposition; Fabrication and In-Situ Testing of Prototype Components and Devices; and Novel Non-Destructive Evaluation, Quality Control and Metrology (NREL Lead Laboratory)	52
Task 1. Multilayer coatings for PEMFC and LIBs (including device fabrication and testing, in-line NDE, metrology and defect detection development).....	52
Slide die development.....	52
In-line spectroscopic method development.....	59
Task 2. Formulation chemistry for multilayer architectures.....	62
Mixing studies.....	62
Task 3. Electrospinning scale-up	67
Task 4. Drying physics studies	73
Education, information dissemination, publications, and technology transfer	74
Macroscopic Mathematical Model of the Drying of a Single Layer Generic Slurry Containing Monodispersed Colloidal Particles, Binder and Solvent (LBNL Lead Laboratory).....	74
Task 6. Modeling	74

Slurry mixing experiments and drying model	78
Ink crack dynamics	80
Education, information dissemination, publications, and technology transfer	82
Validated Continuum-Scale Models to Accelerate Design and Scale-up of Simultaneous Die Coating Process Technology (SNL Lead Laboratory).....	82
Task 6. Model development and validation for multilayer R2R applications	82
Deposition model	82
Continuum drying model	86
Tensioned web model	89
Education, information dissemination, publications, and technology transfer	92
Collaboration/Coordination/Outreach/CRADA Projects.....	93
Core Program.....	93
CRADA project.....	93
Nel Hydrogen collaboration.....	93
IrO ₂ inks	94
Catalyst layer coating.....	95
QC technique	98
Workforce Development/Educational Outreach.....	100
Challenges/Contingencies.....	101
Risks and Risk Handling.....	101
Project Ratings	102
Conclusions.....	102
Key Publications	104
References.....	105

List of Figures

Figure 1. The R2R AMM DOE Laboratory Collaboration team and members of the R2R Industry Engagement Panel.....	1
Figure 2. The ES setup at the ANL MERF. Source: ANL	18
Figure 3. Plan-view SEM images of LLZO polymer precursor nanofibers produced by R2R ES at (a) a low fabrication rate (10 wt.% solid in precursor solution and 1 mL/h injection rate) and (b) at a high fabrication rate (17.5 wt.% solid in precursor solution and 10 mL/h injection rate). Source: ANL	18
Figure 4. θ -2 θ XRD profile of LLZO nanofibers formed at 750°C. Source: ANL	19
Figure 5. Photographs of (a) PEO-LiTFSI acetonitrile solution without LLZO fibers, (b) PEO-LiTFSI-LLZO slurry, and (c) a cast PEO-LiTFSI-LLZO membrane. Source: ANL.....	19
Figure 6. Cross-sectional images of the PEO and PEO-LLZO-LiTFSI samples. Source: ANL	20
Figure 7. Nyquist plots of a Li/PEO-LiTFSI-LLZO/Li cell measured at 60 °C (red) and 100 °C (blue). Source: ANL	20
Figure 8. SEM cross-sectional images of a drop cast PEO-LiTFSI-LLZO membrane cut by FIB. The left image was taken from the top section of the membrane while the right image was taken from the bottom of the membrane (e.g., opposite side). These images indicated a higher fiber density at the bottom, which is likely related to gravity effect. In addition, voids were observed as indicated by the yellow arrow. Source: ANL	21
Figure 9. (a) Photograph of a 25mm wide by 100 mm long PEO-LiTFSI-LLZO membrane prepared by slot-die coating with a PEO:LLZO mass ratio of 1:1, and (b) a cross-sectional SEM images of the PEO-LiTFSI-LLZO membrane showing a smooth surface and relatively uniform LLZO fiber distribution within the membrane. Source: ANL	22
Figure 10. (a) Charging and discharging voltage profiles of a symmetric Li PEO-LiTFSI-LLZO Li cell under a variety of current densities up to 4.2 mA/cm ² and 3 mAh/cm ² , and (b) voltage profile of the sample where only the 4.2 mA/cm ² current density data were included to show the steady voltage region where the polarization voltage was less than 0.4 V. Source: ANL	22
Figure 11. SEM images for (a) LLZO+PEO+LiTFSI and (b) PEO+LiTFSI. Source: ANL	23
Figure 12. SEM-EDS elemental maps for a slot-die coated PEO-LiTFSI-LLZO sample after cycling. Source: ANL	23
Figure 13. SEM images of CuAg nanoparticles embedded in polymer fibers where nanoparticles in (a) and (b) agglomerated and in (c) were dispersed more uniformly and showed less clusters. Source: ANL.....	24
Figure 14. (a) Low and (b) high magnification SEM images of co-spun Nafion and Sustainion fibers. Source: ANL	25
Figure 15. (a) The old ES unit that has one-sided spinning and (b) the new multi-nozzle co-ES unit with needle racks mounted on the opposite sides of a drum collector. Source: ANL.....	25
Figure 16. Plan-view SEM images of Nafion-Sustainion mixed-fiber mat using (a) the previous co-ES setup and (b) the new co-ES setup. Source: ANL	26
Figure 17. SEM images of LSCF:PVP nanofibers from the R2R electrospinner of (a) fibers spun from a working distance of 10 cm and voltage of 22 kV and (b) a working distance of 17.5 cm and 28-30 kV. Source: ANL	27

Figure 18. Viscosity versus shear rate for pure PEO polymer ink and the LLZO-PEO fiber-polymer composite inks with different solid contents and fiber loading ratios. Source: ANL	28
Figure 19. Viscosity as a function of temperature plots for three conductive inks. Source: ANL	29
Figure 20. Shear rate plot for a neat UV-curable dielectric ink and for various dilutions. Source: ANL	30
Figure 21. SEM plan-view images of the photonic curing samples processed with different power level and pulse numbers and thermally annealed sample. Source: ANL	31
Figure 22. (a) The PMOS inverter layout design and (b) the printed device. Source: ANL	32
Figure 23. The dynamic switching of the logic gates showing (a) the input and (b) output voltages. Source: ANL	33
Figure 24. Viscosity measurement for alumina inks of different solute concentrations (e.g., dilution rate). Source: ANL	35
Figure 25. Photographs of alumina coatings prepared using 126 cp ink and three different flow rates: (a) 10 ml/min; (b) 14 ml/min, and (c) 18 ml/min and coating gaps between 200-500 μm . Source: ANL.....	35
Figure 26. Simulated and experimental observed stable and unstable conditions. Source: ANL	36
Figure 27. SEM images of (a) a regular sample and (b) a sample that has bubble defects. Source: ANL	36
Figure 28. (a) An illustration of five-fold cross-validation approach; (b) training results of four models based on transfer learning and five-fold cross-validation. Model M1, M2, and M3 showed good consistency between the training and validation accuracy. Model M4 showed overfitting where the training accuracy is higher than validation accuracy. Source: ANL	37
Figure 29. Results from the GOMA and Visco modeling studies for coatings applied at different vacuum and line speeds. Source: ORNL	38
Figure 30. Comparison of the measured shear viscosity (dots) and Carreau rheology model fits (lines) for the dilute and concentrated inks. The viscosity of the concentrated ink depends on the measurement conditions (Viscosity 1, Viscosity 2). Source: ORNL.....	39
Figure 31. Predicted and experimental defect-free slot die coating windows for catalyst inks. GOMA predictions are solid lines and viscocapillary predictions are dashed lines. Closed circles are for an experimentally defect-free coating and open circles are for an experimentally defected coating. (a) Coating window for dilute ink, (b) coating window for concentrated ink, Viscosity 1, and (c) coating window for concentrated ink, Viscosity 2. Source: ORNL	39
Figure 32. Simultaneous bilayer R2R slot die coating of Pt/Vu ink on top of Pt/HSC ink. (a) At web speeds of 1 m/min, the Pt/Vu layer spreads out wider than the width defined by the shim inside the slot die. The Pt/HSC layer that does not spread out is visible underneath (darker area in the middle of the coating width). (b) At web speeds of 3 m/min, both Pt/Vu and Pt/HSC layers are coated in the width defined by the slot die shim. Source: ORNL.....	40
Figure 33. TEM images showing the simultaneously slot-die-deposited bilayer of Pt/Vu on top of Pt/HSC. The Pt/Vu layer has larger primary particle sizes than the Pt/HSC layer. Source: ORNL	41
Figure 34. Agglomerate particles (black) in optical microscope images at various durations of mixing with an 18G mixer at 10,000 rpm. Source: ORNL	42
Figure 35. Number of agglomerates with equivalent diameter larger than 15 μm in the dry cathode catalyst layer made from inks mixed with an 18G mixer for various times and rotational speeds. Source: ORNL	42

Figure 36. Number of agglomerates with equivalent diameter larger than 15 μm in the dry cathode catalyst layer made from inks mixed at various mixing times and mixing speeds with two different rotor-stator mixers, 18G and 25F. Source: ORNL.....	43
Figure 37. Number of agglomerates with equivalent diameter larger than 15 μm in the dry cathode catalyst layer made from inks mixed at various mixing times with a planetary or ball mill mixer. Source: ORNL.....	44
Figure 38. Number of agglomerates with equivalent diameter larger than 15 μm in the dry cathode catalyst layer made from inks mixed at various mixing times with a tube drive mixer shown as an overlay on the plot. Source: ORNL	44
Figure 39. Planetary mixer used in the ORNL and NREL mixing studies. Source: ORNL.....	45
Figure 40. Exponential decrease in large agglomerates for various mixing times. Source: ORNL	45
Figure 41. Decrease in equivalent diameter for various mixing times. Source: ORNL	46
Figure 42. Shear viscosity measurements showing increasing viscosity after an hour and stabilizing after 18 hours. Source: ORNL.....	46
Figure 43. Summary of data obtained from three mixing methods. Source: ORNL	46
Figure 44. (a) The cross-sectional EDX area of the electrode with minimal void space and topological differences, (b) the sodium signal, and (c) the fluorine signal acquired from cross-sectional EDX map. Source: ORNL.....	47
Figure 45. Horizontal line scans acquired from cross-sectional EDX maps. Source: ORNL	48
Figure 46. Five point smooth of both sodium and fluorine signal text files acquired from cross-sectional EDX analysis. Each signal has been normalized to highlight the difference in distribution rather than total content. Data from the horizontal line scans were also plotted to confirm the distribution across the total thickness of the electrode. Source: ORNL.....	48
Figure 47. (a) Post-mortem XPS survey spectra of the composite cathodes with and without (control) Al-LLZO scaffold additives. (b) Element atomic percent. Source: ORNL.....	48
Figure 48. SEM images of solid-state electrolyte based on PEO/LiTFSI and Al-LLZO fibers. (a) The formation of spherulites and (b) Al-LLZO fibers indicated by the arrow. Source: ORNL	49
Figure 49. Post-cycling high resolution XPS spectra and peak fit analysis of the composite cathodes (a) control cathode, (b) cathode with ligament scaffold additives and (c) cathode with fiber scaffold additives. (d) summarized plot of the CEI chemical functionalities. Source: ORNL.....	50
Figure 50. Arrhenius plot for the conductivity of the PEO based electrolytes. Source: ORNL	50
Figure 51. SEM images of the electrospun PEO fiber at different magnifications. Source: ORNL	51
Figure 52. SEM images of the electrospun YSZ nanofibers. Source: ORNL	51
Figure 53. (a) Machined base and mounting plates with gap and yaw control, and (b) the slide die mounted on new hardware. Source: NREL	52
Figure 54. (a) Single layer slide die flow using red-dyed 1 wt.% solids PEO ink and (b) two-layer slide die flow with red layer on bottom and blue layer on top. Source: NREL	53
Figure 55. Flow stability imaging of two-layer slide flows of 1% PEO dispersions. Source: NREL	55
Figure 56. Flow stability imaging of two-layer slide flows of 2% PEO dispersions. Source: NREL	55
Figure 57. Flow stability imaging with higher viscosity dispersion in the bottom layer. Source: NREL	55

Figure 58. Two-layer slide die electrode coating showing poor quality due to high viscosity of bottom layer ink. Source: NREL	56
Figure 59. Single-layer slide die electrode coating using lower viscosity Pt/Vu ink showing good quality. Source: NREL	56
Figure 60. Rheology and formulations of Pt/HSC and HSC-only inks. Source: NREL	57
Figure 61. Yield stress assessment of the Pt/HSC inks. Source: NREL	57
Figure 62. Slide flow at 7.5 mL/min as a function of catalyst solids. Source: NREL	58
Figure 63. Slide flow for 3.2 wt.% ink at four flowrates. Source: NREL Comparison of the fiber diameter for the full electrode ink process window. Source: NREL	58
Figure 64. Slide flow for 4 wt.% ink at three flowrates. Source: NREL	58
Figure 65. IR transmission spectra for 25- μ m and 125- μ m thick membrane samples with two having a thin active layer. Source: NREL	59
Figure 66. IR transmission spectra for uncoated membrane samples of different thickness. Source: NREL	60
Figure 67. IR transmission spectra for 25- μ m thick membrane samples with no active layer and with three different active layer thicknesses. Source: NREL	60
Figure 68. IR transmission spectra showing sensitivity to membrane thickness and active layer at 17 μ m. Source: NREL	60
Figure 69. Agreement between algorithm and actual half-CCM electrode loadings by FTIR method. Source: NREL	61
Figure 70. Agreement between algorithm and actual half-CCM membrane thickness by FTIR method. Source: NREL	61
Figure 71. Overview of mixing study. Source: NREL	62
Figure 72. Rheology comparison of inks mixed with a Turrax 18G head over a range of mixing speeds at (a) 5 and (b) 30 minutes of mixing time. Source: NREL	63
Figure 73. Optical microscopy of coated catalyst ink mixed for 30 minutes at different RPMs with Turrax mixer/18G head. Source: NREL	64
Figure 74. Comparison of ball milled and Turrax mixed coatings after 1 (top) and 5 (bottom) hours of mixing. Source: NREL	65
Figure 75. Comparison of Turrax Tube Drive and standard Turrax mixed coatings, both at 6k RPM, after 15 minutes of mixing. Source: NREL	65
Figure 76. Order of mixing analysis with standard Turrax 18G head showing the NREL standard mixing order (top), the NREL comparative case to match ORNL mixing order (middle), and the ORNL mixing order (bottom). Source: NREL	66
Figure 77. Rheology comparison of Turrax mixed inks, at several mixing times, using the two different mixing orders. Source: NREL	66
Figure 78. Shear viscosity at 1 /s for four mixing cases. Source: NREL	67
Figure 79. PAA fiber formation as a function of excitation voltage and slurry flowrate. Source: NREL	68
Figure 80. PAA fiber formation as a function of PAA concentration and IPA content. Source: NREL	68

Figure 81. (a) Fiber diameter distribution and (b) rheology as a function of PAA concentration and IPA content. Source: NREL	69
Figure 82. Filament relaxation time for PAA slurries as a function of IPA fraction. Source: NREL	70
Figure 83. SEM images of anionic ionomer fiber formation under different conditions. Source: NREL.....	71
Figure 84. SEM image of a 5 wt.% composition in methanol with some fiber formation. Source: NREL	72
Figure 85. (a) Anionic ionomer fiber formation and (b) fiber diameter distribution (right). Source: NREL.....	72
Figure 86. Schematic of drying physics chamber. Source: NREL	73
Figure 87. Steady-state particle size distributions of CB and CB/Nafion in different mixtures of IPA and DI water at a mixing speed of 2000 rpm. Source: LBNL	74
Figure 88. Initial results of mixing experiments for (a) 5 wt.% Nafion in water and in IPA without mixing and (b) 5 wt.% Nafion in water at three mixing speeds. Source: LBNL	75
Figure 89. Open flow cell used to observe particle dynamics. Source: LBNL.....	75
Figure 90. Complete experimental setup. Source: LBNL.....	76
Figure 91. (a) 10X laser-illuminated thick and thin graphite and thick Li-ion electrodes, (b) 150X white light and laser-illuminated thin Li-ion electrodes, and (c) 150X white light and laser-illuminated thick Li-ion electrodes. Source: LBNL.....	77
Figure 92. Drying process of graphite slurry for 25 wt.% graphite in 1 wt.% CMC in water. Source: LBNL ...	77
Figure 93. An optical section of an ink sample and the processed image. Source: LBNL	78
Figure 94. Histogram of particle sizes generated from an image (radii are measured in μm). Source: LBNL ...	79
Figure 95. The modular automated coating/drying observation system for use with the confocal microscope. Source: LBNL	79
Figure 96. Crack formation starting at aggregates at different wetting thicknesses of 100 μm , 150 μm , and 200 μm , more for I:C of 0.5 than for I:C of 0.2. Source: LBNL	80
Figure 97. Confocal microscope images for the drying process of a Li-ion battery cathode wetted and dried slurries showing NMC particles. Source: LBNL	80
Figure 98. Crack generation and development at I:C or 1.2. Source: LBNL	81
Figure 99. Close view of crack generation process. Source: LBNL.....	81
Figure 100. Crack patterns at different I:C ratios. Source: LBNL.....	82
Figure 101. Computed free surface and interfacial shapes of three-layer slide coating flow. Source: SNL	83
Figure 102. Initial results for the three-layer slide die flow. Source: SNL.....	84
Figure 103. Experimental validation of process window predictions for 3.5 wt.% Pt/HSC with a wet thickness of 60 μm and a die gap of 150 μm . Source: SNL	85
Figure 104. Comparison of predicted operability windows in applied vacuum pressure and web speed. Source: SNL	85
Figure 105. (a) Sample chamber design with a lid to control initial drying transient, and (b) the configuration for the rheolaser and radiative heating elements. Source: SNL	86

Figure 106. Sartorius M35 moisture balance and Formulation rheolaser COATING Optical Film Formation Analyzer. Source: Sartorius and Formulation	86
Figure 107. Rheolaser measurements showing the particle fluidity during drying for a toluene+SiO ₂ +poly(vinyl acetate) sample. Source: SNL	87
Figure 108. Parameters for a toluene-polyvinyl acetate system. Source: SNL.....	88
Figure 109. Results for the predicted residual solvent and the measured residual solvent. Source: SNL.....	88
Figure 110. Model results and sensitivity of the transient solvent mass fraction for the inside and outside of the polymer-solvent layer. Source: SNL.....	89
Figure 111. Schematic of the tensioned web over the slot-die coating. Source: SNL.....	90
Figure 112. (a) Basic coating configuration and (b) finite element model of tensioned web slot coating of a surface treatment ink. Source: SNL	90
Figure 113. The modeling approach for tensioned web slot-die coating. Source: SNL	91
Figure 114. Computational steady-state solution from equations for tensioned web slot-die coating. Source: SNL	91
Figure 115. Coating window used for the fixed gap slot-die coating. Source: UNM	92
Figure 116. Simulation for a curved-lip slot-die configuration. Source: UNM.....	92
Figure 117. Change in the contact angle and droplets for varying concentrations of water and 1-propanol. Source: NREL	94
Figure 118. (a) Zeta potential measurements of dispersions of IrO ₂ particles without ionomer (0 I/C) and with ionomer (0.1 I/C and 0.3 I/C). (b) Z-average hydrodynamic diameter of the same dispersions. Source: NREL.95	
Figure 119. (a) Membrane from the gravure coating station with wrinkling caused by swelling and (b) the smooth, normal membrane after drying. Source: NREL	96
Figure 120. Steady-shear rheology of two IrO ₂ catalyst inks. Source: NREL	96
Figure 121. Electrolyzer testing of a three-cell stack at 1.8 A/cm ² for anodes prepared by NREL and assembled into full MEAs and tested at Nel Hydrogen. Source Nel Hydrogen	97
Figure 122. Comparison of gravure coating and gravure printing. Source: NREL	97
Figure 123. Correlation of XRF-measured catalyst loading and optical transmission for Nel Hydrogen and NREL CCMs. Source: NREL	98
Figure 124. (a) Optical transmission image of half CCM. (b) Comparison of transmission and XRF-measured loading along line 1 in (a). (c) High resolution spatial map of loading based on transmission-to-loading correlation generated from line scans. Source: NREL.....	98
Figure 125. (a) Comparison of the optical transmission image with the loading from the optical image after calibration, (b) transmission results from NREL and Nel Hydrogen CCMs, and (c) XRF measured loading compared to the optically measured loading including apparent defects. Source: NREL and Nel Hydrogen	99
Figure 126. Transmission-mode optical scanning images of anode decal materials, with increasing catalyst coating wet thickness. In the cross-web direction, samples with numbers ending in 2 and 3 show a trend of decreased signal in the central region of the coating, likely corresponding to the slight increase in loading in the same region seen in XRF measurements. Source: ORNL	100

List of Tables

Table I. Table I Composition, Thickness, and Bulk Conductivity of PEO-LiTFSI-LLZO Membranes	21
Table II. Optimized Recipe for Fiber Deposition	24
Table III. Ionic Conductivity of Nafion/Sustainion Dual Fiber Mat in 0.085 M NaCl	26
Table IV. Summary of R2R ES Conditions and Measured Fiber Diameters	28
Table V. Resistance of Printed Dog Bone Structures That Were Annealed at Different Conditions.....	31
Table VI. Parameters for the Coating Experiments	34
Table VII. Comparison of Rotor-Stator High Shear Mixing Elements	43
Table VIII. Critical Dispersion Properties for Two-layer Slide Die Flow Testing.....	54
Table IX. Spinning Conditions and Results for Carrier-Polymer-Free Slurries	71
Table X. Protonic Ionomer Slurry Formulations and Results.....	72
Table XI. Slurry Compositions with the NREL Novel Ionic Polymer	73
Table XII. Educational Development at the R2R Collaboration Laboratories in Phase 2	100

Executive Summary

R2R processing is used to manufacture a wide range of products for various applications which span many industrial business sectors. The overall R2R methodology has been in use for decades and this continuous technique traditionally involves deposition of material(s) onto substrates or membranes that are on moving webs, carriers or other continuous belt-fed or conveyor-based processes that enable successive steps to build a final product. Established methods that typify R2R processing include tape casting, silk-screen printing, reel-to-reel vacuum deposition/coating, and R2R lithography. Products supported by R2R manufacturing include micro-electronics, electro-chromic window films, PVs, fuel cells for energy conversion, battery electrodes and electrolytes for energy storage, and barrier and membrane materials for decarbonization and air and water filtration. Due to innovation in materials and process equipment, high-quality yet very low-cost multilayer technologies have the potential to be manufactured on a very cost-competitive basis. To move energy-related products from high-cost niche applications to the commercial sector, the means must be available to enable manufacture of these products in a cost-competitive manner. Fortunately, products such as fuel cells, thin- and mid-film PVs, batteries, electrochromic and piezoelectric films, water separation membranes, and other energy saving technologies readily lend themselves to manufacture using R2R approaches. However, more early-stage research is needed to solve the challenge of linking the materials (particles, polymers, solvents, additives) used in ink and slurry formulations and the coating and heated drying processes to the ultimate performance of the final R2R product, especially for a process that uses multiple layers of deposition to achieve the end product.

To solve the problems associated with these challenges, the R2R Collaboration is executing a research program with outcomes that will ultimately link modeling, processing, metrology and defect detection tools, thereby directly relating the properties of constituent particles and processing conditions to the performance of final devices. The Collaboration team and their research efforts with industry involvement are illustrated schematically in Figure 1. In FY 2021, the R2R Industry Engagement Panel was convened as a means of collaborating with strategic industry partners on pre-competitive R2R manufacturing research that focuses on “particles to performance” and is mutually beneficial in developing critical processing understanding and next-generation device commercialization. This collaborative approach was designed to foster identification and development of materials and processes related to R2R manufacturing for clean-energy materials development. Using computational and experimental capabilities by acknowledged subject matter experts within the supported National Laboratory system and recommendations from the industry partners, this project leverages the capabilities and expertise at each of five National Laboratories to further the development of multilayer technologies that will enable high-volume, cost-competitive platforms.

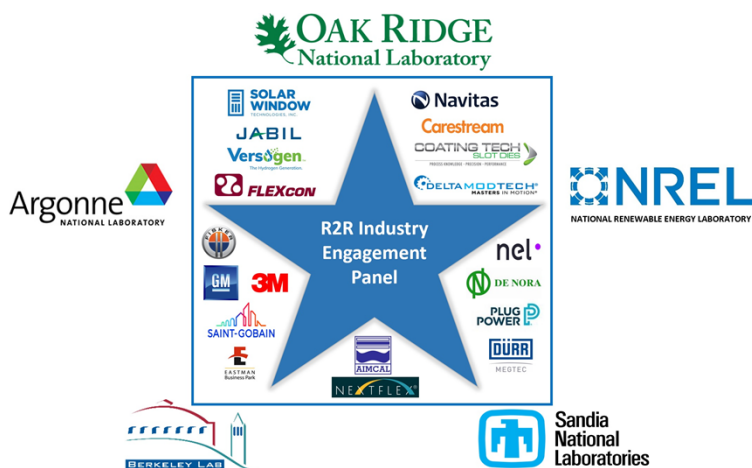


Figure 1. The R2R AMM DOE Laboratory Collaboration team and members of the R2R Industry Engagement Panel. Source: ORNL

A typical R2R process has three basic steps: (1) mixing of particles and various constituents in a slurry, (2) coating of the ink/slurry mixture on a substrate, and (3) drying/curing and processing of the coated substrate. The final performance of devices made via R2R processes is dependent on the active materials (e.g., electrochemical particles in battery or fuel cell electrodes) and the device structure that stems from the governing component interactions within the various steps. However, a fundamental understanding of the underlying mechanisms and phenomena is still lacking, which is why industrial-scale R2R process development and manufacturing is still largely empirical in nature.

The Phase 2 of the R2R Collaboration addresses aspects of the following two targets from the AMO Multi-Year Program Plan:

- Target 8.1 Develop technologies to reduce the cost per manufactured throughput of continuous R2R manufacturing processes.
 - Increasing throughput of R2R processes by 5 times for batteries (to 50 square feet per minute) and capacitors and 10 times for printed electronics and the manufacture of other substrates and membranes used in support of these products.
 - Developing resolution capabilities to enable registration and alignment that will detect, align, and co-deposit multiple layers of coatings and print < 1 micron (1 μm) features using continuous process scalable for commercial production.
 - Developing scalable and reliable R2R processes for solution deposition of ultra-thin (<10 nm) films for active and passive materials.
 - Develop in-line multilayer (<1 μm) coating technology on thin films (5 – 10 μm) with yields greater than 95%.
- Target 8.2 Develop in-line instrumentation tools that will evaluate the quality of single and multilayer materials in-process.
 - Developing in-line quality control technologies and methodologies for real-time identification of defects and expected product properties “in-use/application” during continuous processing at all size-scales with a focus on the “micro” and “nano” scale traces, lines, and devices, i.e., <1 μm at 300 ft./min for R2R processing in air and <10 nm at 20 ft./min for vacuum processing.
 - Developing technologies to increase the measurement frequency of surface rheology without significant cost increases with a goal of a 10-nanometer in-line profilometry at a production rate of 100,000 square millimeters per minute (100,000 mm^2/min).

The category of electrochemical conversion devices that apply to fuel cells was selected in FY 2019 and continued through FY 2020; however, research was kept general enough that other applications could include solid-state batteries (SSBs), solid oxide fuel cells (SOFCs), low-temperature water electrolysis, carbon dioxide (CO_2) separation/reduction and water filtration/purification. ES was a specific technology of interest to integrate and adopt as a R2R processing method across a wide range of applications and industrial domains because of its ability to fabricate advanced nanofiber-based materials. This process offers a high surface-to-volume ratio which makes nanofibers the ideal candidate for various applications where high porosity and high surface areas are desirable. Development of a R2R synthesis of nanofiber non-woven structures and membranes was a focus area in FY 2021 for a variety of value-added energy generation, conversion, and storage components and devices.

The R2R Collaboration laboratories successfully completed all tasks toward development of materials, QC techniques, and an ES method for R2R manufacturing processes. Additionally, efforts continued for macro-scale and continuum-scale modeling, simulation, processing, manufacturing techniques, and metrology that

demonstrated the feasibility and potential for scale-up. The primary tasks for Phase 2 continued through FY 2021 to develop materials, methods and processes that will enable the transition of DOE-supported innovative technologies and practices into U.S. manufacturing capabilities.

Accomplishments

COVID-19 Statement

In March 2020, all National Laboratories were closed, and no in-house laboratory work was allowed because of COVID-19 restrictions imposed by guidance at the State level. The impact from the COVID-19 restrictions caused most of the FY 2020 tasks to be reprogrammed in FY 2021. This significantly impacted the research tasks and milestone schedules; however, the majority of tasks continued to produce results and accomplishments that allowed the Laboratories to meet the rescheduled milestones in FY 2021.

High-impact accomplishments from Phase 2 that were considered to advance the science and understanding of the R2R processes from an industrial perspective are as follows:

Core Program Projects

Note: Late receipt of funding and initiation of several new start tasks resulted in minimal progress in FY 2019.

ANL - Novel R2R Deposition System Based on ES Technology and Advanced/In-Situ Characterization and Testing Capabilities

Slot-Die Coating and Advanced/In-Situ Synchrotron Characterization

FY 2019

- Established roll-to-roll (R2R) electrospinning capability, which demonstrated scalable electrospinning processes on PVDF membranes using a continuously moved web of 0.55 m x 30 m surface area and 56 nozzles with specially designed nozzle shape and multiple spinning events for each individual nozzle. With this system, a maximum homogeneous deposition speed of 3 m/min can be achieved. The system also has flexibility to apply four separately controlled voltages to enable deposition of more than one nanofiber materials.
- Demonstrated the synthesis of nanofibers for three applications: (1) a lithium lanthanum zirconium oxide, $\text{Li}_7\text{La}_3\text{Zr}_2\text{O}_{12}$ (LLZO), solid electrolyte; (2) a lanthanum strontium cobalt ferrite, $\text{La}_{0.6}\text{Sr}_{0.4}\text{Co}_{0.2}\text{Fe}_{0.8}\text{O}_3$ (LSCF), oxide fuel cell electrode; and (3) a polyvinylidene fluoride (PVDF) water filtration membrane.
- Achieved optimum electrospinning recipes for LLZO precursor fiber fabrication using in-situ small angle x-ray scattering (SAXS), which accelerated the development speed of LLZO. Fabricated nanocrystalline high-ionic-conductivity c-LLZO fibers out of the polymer precursor fibers at 700°C.

FY 2020

- Developed scalable nanofiber membrane synthesis recipes and processes for a number of high-profile material systems and applications enabling R2R production, including solid-state battery electrolytes, fuel cell electrodes, ion-exchange membranes, and N95 filter media, which demonstrated ~150x increase in production rate as compared to lab-scale electrospinning (ES).

- Established a low temperature fabrication pathway to synthesize large-quantity, high-purity, undoped cubic phase LLZO nanofibers at a temperature that is 500 °C lower than sintered LLZO. This development demonstrated the benefit of continuous R2R membrane synthesis in solid-state Lithium battery electrolyte applications.
- Designed and built a scaled co-electrospinning tool that enabled continuous, scalable synthesis of composite and hybrid nano- and micro-fiber membranes with significantly increased material and structure versatility. Demonstrated dual-fiber ion-exchange membranes using co-electrospinning technology, which showed more uniform distribution of functionalities. The application of the continuous synthesis process made it possible to scale-up the membrane for water purification, biofuel treatment, and carbon dioxide capture applications.
- Converted the R2R ES platform to fabricate reusable N95 facepiece respirator filter media development during the COVID pandemic, in support of the DOE BES office National Virtual Biotechnology Laboratory (NVBL) program. ANL's electrospun filter media showed >95% filtration efficiency and no efficiency degradation after autoclaving disinfection. Our filter media also incorporated antiviral function and showed acute virus kill effects with 15 minutes of exposure time, which enabled extended facemask use time and reduced bio waste. This R2R synthesis of reusable N95 filters attracted commercial interest, leading to initiation of a technology transfer process.
- Applied in-situ SAXS study of the ES process and simultaneous SAXS, wide angle x-ray scattering (WAXS), and CO₂ detection of in-situ electrospun fiber annealing at ANL's Advanced Photon Source (APS), which revealed material-process-property relationships during ES and phase transformation kinetics during polymer-ceramic fiber conversion. This knowledge enabled further advancement of continuous R2R processing of nanofiber and membrane products.
- Provided advanced materials analysis and characterization to support R2R process development at partner laboratories, such as SAXS/USAXS analysis of nanofiber inks for R2R coating of fuel cell membranes and confocal Raman for spatially resolved spectroscopy of R2R laser scribing in organic photovoltaic devices.
- Generated four publications expanding the knowledge of R2R materials processing.

FY 2021

- Developed new synthesis pathways for making LLZO nanofiber-polymer composite solid-state lithium battery electrolytes using R2R electrospinning and slot-die coating technologies. The nanocomposite solid electrolyte membranes showed much improved mechanical and chemical stability than the conventional polymer electrolytes, which enabled high current density cycling up to 8 mA/cm² at 1 mAh/cm² for several hundred hours with a small polarization voltage.
- Achieved 10x higher production rate of the LLZO nanofibers by improving R2R electrospinning processing conditions, which demonstrated scale-up potential for the nanofiber-based solid electrolytes.
- Developed a methodology to integrate nanoparticulate catalysts into nanofibers to form catalyst-on-fiber membranes based on R2R electrospinning, which can enable more efficient electrocatalysis process for a number of electrochemical applications, such as water splitting, bio treatment, and CO₂ conversion. The benefits of catalyst-on-fiber structure include reaction and/or conversion efficiency enhancement and catalysts operation life improvement.

- Increased the production rate of the dual-fiber deionization membranes for more than 3x by simultaneously optimizing electrospinning conditions for cationic and anionic fiber deposition during the continuous co-electrospinning process.
- Performed ink material exploration study for printed electronics, an emerging electronic device fabrication method that has niche applications in flexible and wearable devices.
- Demonstrated feasibility of applying printed electronic technology to active microelectronic device fabrication by developing a fully printed PMOS inverter. Since inverters are the most basic building blocks within all digital logic gates used in active components of electronic devices, this work showed promise for making logic devices via additive manufacturing, which is more compatible to R2R manufacturing and is less costly than traditional silicon wafer manufacturing processes.
- Generated three publications expanding the knowledge of R2R materials processing.

ORNL - Colloidal Chemistry, Surfactant Research, Slurry Processing, Deposition and Drying and Curing and Curing Methods

FY 2019

- Produced uniform PEMFC cathode gas diffusion electrode (GDE) coatings with a composition of 12.16% Solids, 8 wt% platinum (Pt) to carbon(C) (Pt/C) on the ORNL pilot slot-die coating line with a uniform coating thickness $\approx 20 \mu\text{m}$ and micron-size cracks.
- Assembled a membrane electrode assembly without an overlayer on a cathode GDE ($0.38 \text{ mg-Pt}/\text{cm}^2$).
- Fabricated cubic-phase LLZO nanofibers, which is several orders of magnitude more conductive than the tetragonal phase, after annealing at 700°C for two hours.

FY 2020

- Simultaneously coated a catalyst ink and an ionomer overlayer onto the gas diffusion layer (GDL) using a dual slot die. This may be the first dual slot-die coating of this kind.
- Conducted annealing studies on LLZO fiber morphology with results that LLZO fibers must be annealed in argon to remove the carbonates and to increase their conductivity.
- Determined that larger variabilities occurred for the thickness and platinum (Pt) loading of a coating prepared from a concentrated slurry for a slot-die coating. Data was provided for SNL modeling to identify improvements to the coating process parameters by adjusting the catalyst slurry formulation. Changes to the operability window achieved a catalyst layer loading of the targeted $0.1 \text{ mg}_{\text{Pt}}/\text{cm}^2$ across multiple GDEs with 8 wt.% Pt/C slurries processed with a R2R slot-die.
- Performed coating trials with coating gaps smaller and larger than the wet coating thickness resulting in larger gaps having smaller Pt loading variations (4-7%) than the smaller gaps (Pt loading variation 10-40%). The larger coating gaps produced a very high mean areal Pt loading of $0.351 \text{ mgPt}/\text{cm}^2$.
- Wetting experiments showed that a lower alcohol content (higher water content) results in higher contact angles because of the hydrophobic microporous layer surface. This knowledge allowed improvements that optimized the solvent selection and process conditions for slot-die coating.

- Achieved deposition of an ionomer overlayer on a polymer electrolyte membrane fuel cell (PEMFC) cathode simultaneously with the cathode electrocatalyst layer and completed experiments that eliminated the need for an overlayer altogether.
- Synthesized composite aluminum-doped LLZO (Al-LLZO) and polyacrylonitrile (PAN) nanofibers with diameters from approximately 800 nm to 1.4 μm that produced uniformly distributed Al-LLZO on carbon fiber structures. Assembled and tested coin cells based on composite cathodes that exhibited more noticeable power law contributions, in the low frequency regime, which is indicative of a more pronounced ion diffusion mechanism. At higher charge rates, a marked improvement in the specific capacity was evident for the coin cells and especially for the cathode filled with Al-LLZO fibers.
- Scaled LLZO and Al-LLZO nanofibers that can be manufactured using ES with aqueous and non-aqueous precursors. The nanofibers were crystallized in the cubic phase. The fabrication conditions were optimized to tailor the diameter of the nanofibers.
- Fabricated dual functionality Al-LLZO/PAN fibers using a core-sheath configuration that can be scaled using coaxial ES to obtain uniform fibers. The fibers were carbonized to obtain ionically and electronically conductive nanofibers, and spectroscopic analyses showed that the Al-LLZO was uniformly distributed on the carbon fiber structures

FY 2021

- Validated the SNL 2D GOMA model by coating a 3.5 wt.% Pt/C slurry on Al foil using the predicted defect-free coating window. Characterization of composite cathodes based on Al-LLZO fibers was completed and superior cycling performance at high rates of the Al-LLZO based cathodes was obtained. Solid state composite electrolytes based on PEO/LiTFSI (3:1 weight ratio) and Al-LLZO fibers were synthesized.
- Investigate the effects of mixing time and speed on five different mechanical mixers. Higher mixing speeds showed a considerably lower number of large agglomerate particles, indicating that a significant number of agglomerates have been broken up after brief shear mixing.
- Established a stable, defect-free catalyst layer coating at multiple line speeds (with constant wet thickness) and vacuum pressures on Al foil. The experimental coating window on the foil closely matched the modeled coating window produced by SNL.
- Employed nanostructured Al-LLZO fiber scaffolds to tailor the chemical functionalities of a cathode-electrolyte-interface layer resulting in significant improvements in the macroscopic electrochemical properties of assembled coin cells.
- Fabricated composite polymer electrolytes based on PEO using the Al-LLZO ligament scaffolds resulting in a threefold increase in electrical conductivity attributed to the ionically conductive Al-LLZO cubic phase.
- Synthesized electrospun yttria-stabilized zirconia (YSZ) nanofibers using the same processing conditions that were used for the synthesis of the LLZO nanofibers to demonstrate the flexibility of ES.
- Demonstrated electron beam (e-beam) radiation for curing in a nitrogen atmosphere a two-layer coating that used aqueous dispersions of acrylated polyurethane and carboxymethyl cellulose as binders. The required radiation was 180 kGy at a line speed of 4 feet per minute.

NREL - Physics and Methodologies for Multilayer Coatings/Deposition; Fabrication and In-Situ Testing of Prototype Components and Devices; and Novel NDE, Quality Control and Metrology

FY 2019

- In support of the development of simultaneous multilayer coating for fuel cell membrane electrode assemblies (MEAs), developed full-quadratic models for catalyst ink surface tension, density and viscosity using the Box-Behnken experimental design methodology and provided the models to SNL for the development of their multi-layer slide die continuum models.
- In support of the development of highly porous and high performing electrodes for fuel cell MEAs, completed a study showing a multi-region electrospinning process window characterized by droplet spraying, spinning of fibers and beads, spinning of fibers only (desired case), and an unstable flow region with viscous instability in the Taylor cone.

FY 2020

- Commissioned a multilayer slide die to explore the potential benefits of multilayer R2R coating for reduction of manufacturing energy consumption, footprint, and capital expenditures as well as the potential for new device structures with improved performance and lifetime across several DOE-relevant applications.
- Performed studies that confirmed the relationship between heterogeneous ink mixing conditions and the macro-scale morphology of a coated layer, which will assist in the optimization of ink and coating processing across a broad range of industrial applications.
- Developed novel fast spectroscopy techniques capable of in-line implementation that will enable not-currently-available in-line NDE measurements for multilayer structures like filtration membranes and fuel cell MEAs.

FY 2021

- Developed and demonstrated a novel IR-spectroscopy-based quality-inspection method to simultaneously measure membrane and electrode thickness in a catalyst-coated membrane (CCM). A record of invention was filed.
- Using analog particle-polymer inks with similar rheological behavior as PEMFC catalyst inks, demonstrated stable slide flow and good coating quality of simultaneous two-layer slide die coatings under a wide range of ink properties and coating conditions. This effort establishes the basis for lower-cost, lower-energy-consuming processing of multilayer structures across a range of applications.
- Provided constituent- and ink-level property measurement data for 62 different PEM fuel cell and electrolyzer catalyst inks to LBNL in support of novel heterogeneous non-Newtonian ink model development.

LBNL - Macroscopic Mathematical Model of the Drying of a Single Layer Generic Slurry Containing Monodisperse Colloidal Particles, Binder, and Solvent

FY 2019

- Developed generic particle network settling model with intuitively reasonable results; however, limited available information on dense, multicomponent suspensions, along with assumptions made to build model, suggested that greater understanding of component-level interactions during drying is needed.
- Devised experiments to obtain information needed for model development using a wide array of analytical tools, including those at the Advanced Light Source (ALS).

FY 2020

- Designed a coating and drying observation table to simulate the R2R fabrication conditions of materials used by the other laboratories but at a scale that is small enough to be easily combined with analytical tools such as those at the LBNL ALS beamlines. The observation table will be used to observe solidification of coatings at a microscopic level to collect data for the development and refinement of macroscopic drying models.
- Constructed an automated mixing experimental setup comprised of custom electronics and computer-controlled components, and a flow-through particle size analyzer that can operate at up to a 5 Hz sampling rate. This setup is to quantitatively characterize agglomerate evolution in dilute inks and slurries during mixing. The information collected will be used to develop mixing/agglomeration models to improve control over ink and slurry properties and ultimately coating characteristics. The chiller for this setup was upgraded with a serial communication port and additional code was added to the equipment control library to control and query the chiller to improve compatibility with the dispersion preparation techniques used by the other R2R teams. Performed preliminary experiments with carbon black dispersed in mixtures of 70% alcohol in water and 10% alcohol in water. Results showed significant effects of solvent composition on particle size distribution.
- Built a custom cart with adjustable platforms to isolate the motorized components of the mixing experiment setup (mixer, stage, pump, and chiller) from vibration-sensitive instruments (particle size analyzer and soon, confocal microscope) and to position the mixer and pump in a consistently reproducible position relative to different instruments, Transforming the automated mixing experimental setup into a portable mixing station allowing reliable recreation of samples in the vicinities of instruments in different locations with minimum variation in samples to improve consistency of experimental results.
- Released an update to PyGDH, LBNL's highly flexible open-source simulation package that will be used to implement future models. The open source software is available for download from <https://bitbucket.org/berkeleylab/esdr-pygdh>.

FY 2021

- Implemented equations from the literature to describe drying a coating with a moving surface. A progression of particle volume fraction profiles in a simulated coating undergoing drying were generated.
- Installed an optical table and confocal microscope and constructed an open flow cell for use with the automated mixing setup to observe particles in dilute aqueous dispersions under the confocal microscope.
- Developed novel optical sectioning capability for the confocal microscope (advertised as a microscope for surface analysis), then collected optical section images and developed an image analysis program to obtain histograms of optical size for agglomerates.

- Constructed a modular automated miniature coating observation platform (jointly with VTO and FCTO funding) to observe drying coating samples with the confocal microscope and ALS 8.3.2. hard X-ray microtomography beamline. This miniature coating line includes a custom computer-controlled doctor blade which can vary coating height during a coating process. The system was demonstrated using a doctor blade coating of an N-methyl-2-pyrrolidone (NMP)-based slurry (used in battery applications) followed immediately by confocal imaging.

SNL - Validated Continuum-Scale Models to Accelerate Design and Scale-Up of Simultaneous Die Coating Process Technology

FY 2019

- Completed two-layer slide-die and slot-die coating models using the 2014 R&D Magazine top 100 technology products, Goma 6.0, Goma 6.0 is a finite element software expressly developed for free and moving boundary problems, with target applications mainly in the liquid coating film industries and related capillary hydrodynamics applications.
- Designed parameterized models for slot- and slide-deposition systems with accommodation for three or more simultaneous miscible layers (multiple layers of varying rheology). Model parameters were chosen to parallel typical operator actions taken to establish high-quality films during start-up.

FY 2020

- Established models and workflows for single-layer slot-die and slide-die capillary hydrodynamic coating models that can be used to simulate ink deposition from die to substrate and determine the boundaries (in parameter space of web speed, coating die geometry and configuration relative to the web, vacuum pressure, and film thickness) for the R2R process operability window.
- Completed three-layer slide-coating model demonstration. The simulation of simultaneous three-layer slide coating flow is the first of its kind to be published in the literature
- Incorporated complex ink rheology in all coating deposition models using power-law, Carreau, and Carreau-Ysuda constitutive equations for shear-rate-dependent viscosity.
- Validated the single-layer slot-die coating model against coating trials at ORNL with PEM inks and a platinum catalyst on a carbon support and an ionomer in a water-alcohol solvent. The model is predictive of the coating operability windows for lower concentrations of particles.
- Developed a user-interface for a slot-die coating simulator that enables wider usage.
- Validated a drying and solidification model with published polymer-solvent drying data, specifically for poly(methyl acrylate) (PMA) polymer and toluene solvent
- Developed an experimental drying capability that enables measurement of solvent loss with time and visualization of particle motion during drying. Constructed a companion drying model by extending existing, validated polymer-solvent model to account for the presence of consolidating particles.
- Fitted rheological data for a representative single- and two-layer-slot coating stack with standard constitutive equations and implemented the new equations in the models.

- Validated process models that predicted the coating window (vacuum of 11-in H₂O for 60-μm gap and 14-in H₂O for 60-μm at 3 ft/min coating speed) for ORNL single-layer slot-die coating trials with a complex 8 wt.% Pt/C catalyst inks. Successful validation enabled the guidance of subsequent experiments aimed at increasing the coating gap (slot-to-web) from 60 μm to 90 μm for better coating quality at a 30-μm coating wet thickness. Significant material and time savings for these studies was realized.
- Developed a new mesh/solid-model design for the slot-die model to better enable gap-based parameter studies. An experimentally-unverified significant finding was that the models predict that the low-vacuum limit disappears at all web speeds for smaller gaps and concentrated Pt/C inks. A stability analysis on the slide-only multilayer models revealed a potential for interlayer defects.
- Advanced a machine-learning (ML) model to connect coating defects of particulate conductive films (pinholes, striations) to process parameters for gravure coating/printing.

FY 2021

- Completed a special slide-only model to aid redesign of a slide die lip geometry.
- Achieved a fully-converged steady-state model of three-layer slide coating flow with the actual ink rheology of a PEMFC construction for the first time. Calculations of coating windows are a first for multilayer slide die coating, and very little data exist other than NREL results.
- Successfully demonstrated a single-layer solvent-polymer drying model that was regressed with ML software using experimental data in the literature. Completed an experimental setup to obtain drying weight time histories, complementary to the setup at LBNL, for model validation and tuning.
- Updated deposition models of single- and two-layer slot-die coating flow and validated the updated single-layer slot-die coating model against coating trial observations at ORNL and improved the process window for inks at various concentrations of catalyst and carbon support. The coating process window predictions for operating vacuum were used to achieve a smooth coating without streaks on subsequent trials.
- Successfully, ran the polymer/solvent/particle drying model and showed expected results with “fast” drying, indicating a particle skinning effect. A test fixture to better control for start-up of the drying coat-weight measurements was designed to aid in model validation.
- Refined tensioned web (without a backing roll) models as well for a surface-treatment ink used in precision coatings were developed.
- Designed a test fixture that will be used to measure heat and mass transfer coefficients for the drying model and demonstrated the utility of the rheolaser detection of particle motion during drying.

CRADA Projects

Several CRADAs were initiated with U.S. businesses on R2R coating technology in Phases 1 and 2. Accomplishments for each CRADA project are summarized below:

- CRADA with Fisker, Inc. (LBNL and ORNL collaboration): A scaffold of cathode and solid electrolyte was developed using freeze cast to enable a solid-state battery. All-solid-state batteries

were demonstrated based on LLZO separators and cathode scaffolds and scaled a freeze casting coating process to the pilot level at ORNL.

- CRADA with Navitas Systems (ORNL and NREL collaboration): A R2R process was developed for fabricating a ceramic-coated separator, replacing the conventional discrete operations, and enabled superior safety, high throughput, and low manufacturing cost. The technology sped up the cell assembly throughput and improved the alignment of jelly-roll stack, which could enable up to a 2% cost savings on the cell product for Navitas.
- CRADA with SolarWindow Technologies, Inc. (NREL and ANL collaboration): Diffractive multiplexing for high-throughput R2R laser patterning of flexible organic PV modules was demonstrated. The objective of the CRADA project was to greatly facilitate the processing steps needed to make a thin-film photovoltaic module.
- CRADA with Nel Hydrogen (previously Proton OnSite) (NREL, ORNL, and ANL collaboration): The objective was to develop R2R manufacturing of advanced (low loading and directly coated onto the membrane) electrolysis electrodes for low-cost hydrogen production. Ink characterization and optimization, R2R coating, advanced electrode characterization, and metrology development capabilities at the National Laboratories were used to support the overall goals of reducing the manufacturing labor for the MEA by a factor of 15-20 and the overall cost of the MEA by over 60%. Work began for this project in January 2020.

The Nel Hydrogen CRADA began in FY 2020 and continued into FY 2021. Accomplishments during Phase 2 for this CRADA include the following:

FY 2020

- NREL performed experiments to study the absorption rate of water/alcohol mixtures by PFSA membranes to elucidate and optimize ink formulations for direct coating onto membranes. Measurements showed that PFSA membranes with different side chain length had similar absorption characteristics and had high absorption for near 1-to-1 mixtures (by weight) and lower absorption rates for pure water or alcohol.
- NREL successfully coated two different IrO₂ catalysts directly onto a PFSA membrane and achieved the target loading. This was the first demonstration of direct membrane coating of IrO₂ electrolysis anodes in the literature. Samples were provided to Nel Hydrogen for in-situ electrochemical testing. The catalyst layers were tested in a three-cell electrolyzer stack at Nel Hydrogen (in FY21) and the results showed that all cells had stable performance, even after unplanned interruptions to operation at 122 hours and 357 hours.

FY 2021

- NREL measured the steady-shear rheology of the catalyst inks with IrO₂ from different suppliers. It was determined that one catalyst material resulted in higher viscosity and lower fluid transfer from the gravure cylinder to the membrane substrate, which was attributed to higher catalyst surface area. Catalyst ink formulations from these measurements and R2R-coating trials in FY20 were used as the basis for Nel's pilot-scale R2R coating at Kodak.
- NREL evaluated optical QC inspection techniques for measuring IrO₂ loading and defect detection using IrO₂ catalyst layers coated on membranes created at Nel Hydrogen, NREL and Nel's pilot R2R run at Kodak. The average loading of the whole catalyst layer area (measured with x-ray fluorescence) showed a strong correlation to optical transmission. Good correlation was also observed between the local IrO₂ loading and local transmission values. And visually apparent defects in the coating were

detected in the transmission imaging. This method has a potential to become a valuable loading characterization technique for in-line monitoring of fabrication processes of PEM water electrolysis anodes.

Collaboration and Outreach

The R2R Collaboration team participated in monthly review meetings with DOE AMO, HFTO, and VTO Technology Managers to ensure information for each project was available on a continuous and regular basis. Team members also presented (virtually) at the Association of International Metallizers, Coaters and Laminators R2R Conference; the fall meeting of the Electrochemical Society; the Center for Compact and Efficient Fluid Power Summit; the Beyond Lithium Ion XIII Symposium; the 2021 TMS Annual Meeting and Exhibition; the Battery Congress 2021; the 2021 DOE Hydrogen and Fuel Cells Program Annual Merit Review, and the 2021 Vehicle Technologies Office Annual Merit Review. Principal investigators collaborated with the principal investigators of the industry partner during the CRADA project described above. Additionally, a R2R Industry Engagement Panel was formed, and a kickoff meeting was held that included the five Collaboration Laboratories and 17 industry panel members (see Figure 1 above). Educational outreach by the R2R Collaboration has supported a total of 43 post docs, graduate and undergraduate students, and interns from 36 separate universities since FY 2018.

Technology Assessment

Because of the nature of the early-stage research tasks, the technologies under development were not matured sufficiently for direct transfer to industry; however, technology transfer for these and other technologies applicable to R2R manufacturing was initiated through information exchange with industry partners and in public forums, technical journal articles, and patent applications. Additionally, the CRADA projects and other associated program areas leveraged the benefits of the R2R Collaboration for the technologies under consideration by the CRADA partners. Since Phase 2 was a three-year research effort (FY 2019 through FY 2021), technologies and models under development continued to mature towards commercialization throughout FY 2021.

Roll-to-Roll Advanced Materials Manufacturing DOE Laboratory Collaboration Project Overview

Collaboration Contacts

Yarom Polsky, Collaboration Team Lead

Oak Ridge National Laboratory (ORNL)
National Transportation Research Center
2360 Cherahala Blvd.
Knoxville, TN 37932
Phone: 865-576-0593
Email: polskyy@ornl.gov

Georgios Polyzos, ORNL Project Team Lead

Oak Ridge National Laboratory (ORNL)
National Transportation Research Center
2360 Cherahala Blvd.
Knoxville, TN 37932
Phone: 865-576-2348
Email: polyzosg@ornl.gov

Gregory K. Krumdick, ANL Project Team Lead

Argonne National Laboratory (ANL)
9700 S. Cass Avenue
Building 362
Lemont, IL 60439-4844
Phone: 630-252-3952
Email: gkrumdick@anl.gov

Michael Ulsh, NREL Project Team Lead

National Renewable Energy Laboratory (NREL)
15013 Denver West Parkway
Golden, CO 80401
Phone: 303-275-3842
Email: Michael.Ulsh@nrel.gov

Vince Battaglia, LBNL Project Team Lead

Lawrence Berkeley National Laboratory (LBNL)
1 Cyclotron Road
MS 70R 0108B
Berkeley, CA 94720
Phone: 510-495-2679
Email: vsbattaglia@lbl.gov

P. Randall (Randy) Schunk, SNL Project Team Lead

Sandia National Laboratories (SNL)
Advanced Materials Laboratory
1001 University Blvd., SE
Albuquerque, NM 87106

Phone: 505-844-5992
Email: prschun@sandia.gov

Brian Valentine, DOE Roll-to-Roll Technical Project Officer

Department of Energy (DOE)
Energy Efficiency and Renewable Energy (EERE), EE-5A
Advanced Manufacturing Office (AMO)
1000 Independence Ave., S.W., Suite 5F-063
Washington, DC 20585-0121
Phone: 202-586-9741
E-mail: brian.valentine@ee.doe.gov

Technical Contacts:

ORNL: Jianlin, Li, Jaswinder Sharma, Erin Creel, Alexander Kukay
ANL: Yuepeng Zhang, Deborah Myers, Devon Powers
NREL: Scott Mauger, Peter Rupnowski, Bertrand Tremolet deVillers, Kenneth C. Neyerlin
LBNL: Kenny Higa, Buyi Zhang
SNL: P. Randall Schunk, Nelson Bell
UNM: Kristianto Tjiptowidjojo, Marvin Larsen, Chris Wall, Ben Wall, Robert Malakhov, Chance Parrish

Industry Engagement Panel Partners:

3M
AIMCAL
Carestream
Coating Tech Slot Dies
Delta ModTech
De Nora
Dürr USA
Eastman Kodak Business Park
FLEXcon
General Motors
Jabil
Navitas Systems
Nel Hydrogen US
NextFlex
Plug Power
Saint-Gobain
Versogen

Annual Operating Plan Title and Corporate Planning System (CPS) Agreement Numbers

Roll-to-Roll Manufacturing Science and Applications: From Ideal Materials to Real-World Devices

ORNL CPS# 97995
ANL CPS #s 29915, 32553 and 32681
NREL CPS #97995
LBNL CPS #31112
SNL CPS #35102

Project Introduction

Modern variants of proven, classical R2R coating technologies, as well as new coating methods, are needed for enabling widespread commercialization of renewable energy storage and conversion technologies. Established coating methods, such as multilayer slot-die, gravure, reverse comma, tape casting, etc. with homogeneity and uniformity superior to spraying methods need to be further adapted for improving performance of various technologies. The shape, size, and morphology of the materials, the chemistry of the formulation, the nature of slurries, their coating rate, the rate of drying etc. all play a role in determining the final coating architecture, quality, and performance. In addition, NDE of the produced coatings for improving in-line QC and identification of defects, prior to down-stream value added steps being performed, is of paramount importance.

More early-stage research is required to solve the challenge of linking particles used in material formulations to the performance of the final R2R product, especially for a process that uses multiple layers of deposition to achieve the end product. The R2R Collaboration brought together expertise from five National Laboratories to understand the complex nature of the R2R processes and develop methods to improve existing production capabilities.

Objectives

The overall objective of the R2R Collaboration is to advance technologies applicable to continuous manufacturing to reduce cost, increase precision, and enable in-line QC and defect detection that will result in expanded use of R2R processing to produce clean energy technologies. Modeling and simulation of the materials and processes being developed will be used to understand the fundamental physics and particle interactions of those materials as they relate to the manufacturing process on both a macroscopic scale and a continuum scale.

Specific research objectives and areas include, but are not limited to the following:

1. Fundamental understanding of colloidal chemistry (particle-particle and particle-solvent interactions)
2. Tailoring formulations of slurries and inks for optimized coating structures
3. Novel coating deposition methods for multilayer architectures
4. Novel non-woven structure and membrane deposition
5. Advanced characterization and testing (neutron scattering, high energy X-ray scattering, HR-TEM, tomography, in-situ methods, etc.)
6. Physics understanding and methods optimization of coating and drying
7. Novel non-destructive-evaluation (NDE) and QC metrology techniques
8. Macroscopic mathematical modeling of slurries and inks
9. Printing and coating technology exploration for microelectronic component fabrication
10. Continuum-scale models to accelerate the design and scale-up of coating and drying processes for continuous R2R manufacturing

NREL, ORNL, and ANL pilot lines combined with the subject matter experts at the National Laboratories provide unique resources when combined with testing, characterization, modeling and simulation, metrology, and data analytics facilities.

Approach

Core Projects

The core program tasks that were initiated in FY 2019 as part of the three-year Phase 2 effort continued through FY 2021 and is scheduled to complete by December 2021. If approved and funded, Phase 3 which is planned for FY 2022 through FY 2024 will continue some of the technology developments from Phase 2 and will expand to include technologies for decarbonization, CO₂ reduction, and other separation technologies

Potential New Efforts for Phase 3

Future efforts will continue to address key barriers in the areas of (1) materials and substrates, (2) novel processing of flexible electronics, (3) multicomponent slurry formulation and processing, (4) drying and curing technologies, (5) material deposition and R2R coating techniques, (6) quality control, in-situ evaluation, process control and optimization, (7) predictive modeling and simulation to guide experimental efforts, (8) data science and ML development to more quickly achieve the above developments, and (9) quantify and optimize favorable energy for new process development through LCA and TEA analysis. Some potential new efforts for all the R2R Collaboration laboratories to address these barriers and technology challenges and to enable technology transfer to the commercial sector are as follows:

- Decarbonization
 - Hydrogen production and use
 - Electrochemical and electrocatalysis systems for manufacturing, e.g., CO₂ reduction
 - Membranes and structures for water applications and critical materials and bio-separations
 - Flexible electronics
- Technology Development Informed by the IEP
 - Multilayer structures, e.g., electrodes, separators, membranes
 - Highly loaded inks and slurries
 - Quality inspection methods to address uniformity (defects/properties) and dimensional attributes
 - Drying physics and methods to reduce energy consumption
 - Support model development and validation
 - Integration of metrology, ML, and process control
- New CRADAs to Engage Industry and Accelerate Impact of R2R Processing
 - Support small business entry into R2R for new idea process development
 - Translate novel consortium approaches to practice using prototyping facilities and equipment

Technology Transfer Paths

For the core program tasks, technology is transferred through collaboration with industry (e.g., the R2R IEP) and companies with CRADA contracts. The National Laboratory team will work closely with any companies to ensure technologies are accepted for commercialization. General results for the research efforts of the R2R Collaboration program are presented at conferences, symposia, peer reviews and during direct contact with industry and the commercial sector. Specific research is reported in technical journals and in patents.

The models and simulations can be extended to encompass not only materials discovery, but also to accelerate materials synthesis and fabrication applicable to industry. This effort leverages the R2R processes and technologies at ORNL; the electrochemical and membrane synthesis expertise and research facilities such as the Materials Engineering and Research Facility (MERF) and Advanced Photon Source (APS) at ANL; and the metrology, R2R processing, and device fabrication and testing capabilities at NREL, in conjunction with the materials design computational efforts of SNL and LBNL. SNL and LBNL will continue to provide open

access to the upgrades for the modeling and simulation tools to industry, all National Laboratories, and academic partners.

Results

Phase 2 was comprised of seven major tasks with collaboration between individual Labs:

- Task 1: Multilayer coatings with PEMFC and Li battery electrodes as example technologies (ORNL/NREL/SNL)
- Task 2: Formulation chemistry for multilayer architectures with support from the Advanced Photon Source (APS), the Spallation Neutron Source (SNS), and the High Flux Isotope Reactor (HFIR) (ORNL/NREL/LBNL)
- Task 3: Electrospinning scale-up with SSBs and SOFCs as example technologies (ANL/ORNL/NREL)
- Task 4: Drying physics studies (SNL/ORNL/LBNL)
- Task 5: UV and electron beam (EB) curing and energetic post-processing (ORNL)
- Task 6: Modeling (LBNL/SNL with data from ANL/ORNL/NREL)
- Task 7: Flexible electronics with micro- and nano- structuring (ANL/SNL)

The following sections provide details of the R&D conducted by the Labs for the tasks and their collaborative involvement for the last year of Phase 2 (FY 2021). Details for the first and second years of Phase 2 (FY 2019 and FY 2020) can be found in the final reports for those years. [7][8]

Novel R2R Deposition System Based on ES Technology and Advanced/In-Situ Characterization and Testing Capabilities (ANL Lead Laboratory)

The goal is to improve the scientific understanding of the R2R ES process and demonstrate its application in a variety of clean energy technologies, such as lithium battery electrolytes and electrodes, ion transport media for water filtration and purification, air purification media, and fuel cell membranes. Advanced ES ink characterization at the ANL APS using SAXS and USAXS, as well as exploratory studies of ink formulations for printed electronics, were also performed within the context of new ink materials development for R2R manufacturing.

Task 3. Electrospinning scale-up using SSBs and SOFCs as example technologies

There are currently a few barriers to commercialization of ES: (1) ES is mostly limited to filtration applications produced in single-step, batch processes; (2) advanced materials used in electronics, fuel cells and batteries that require continuous, post-ES processing; (3) complex multi-step physiochemical processes that create challenges transferring technology from the bench to commercial production; and (4) time-consuming material transfer process steps. Capabilities that can address these technical barriers need to be developed. The objective was to develop a R2R ES platform that is capable of synthesizing multilayer composite membranes. This highly versatile deposition process will enable significantly improved device quality as compared to conventional batch deposition methods, and increased productivity and processing rate for a wide range of

renewable energy applications. Figure 2 shows the ANL ES setup at the MERF with an insert showing microjets during the ES process.

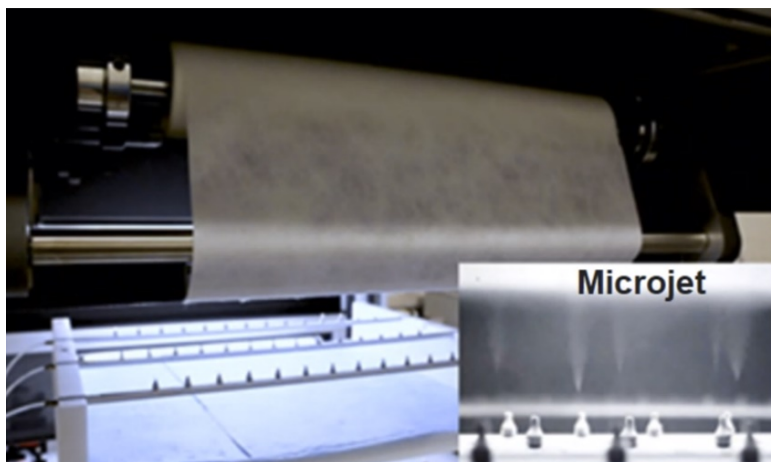


Figure 2. The ES setup at the ANL MERF. Source: ANL

R2R spinning of LLZO fiber for densified solid-state battery electrolytes

The goal was to develop conditions that can rapidly fabricate electrospun precursor fibers of Al-doped LLZO using R2R ES. The ES recipes and process conditions were developed during FY 2020. FY 2021 efforts focused on increasing the fiber production rate to improve process scalability, and to accumulate materials for battery cell assembly and testing. Figure 3(a) shows the scanning electron microscope (SEM) image of polymer precursor fibers prepared using the previously developed recipes. By adjusting the spinning precursor solution concentration and injection rate as well as electric field strength, the production rate was increased 10 times without breaking the well-formed fiber morphology shown in Figure 3(b). After thermal annealing in air at 750 °C for 2h, the precursor fibers converted into cubic phase LLZO fibers (c-LLZO) as determined by the powder X-ray diffraction (XRD) profile shown in Figure 4. No impurity phase was observed.

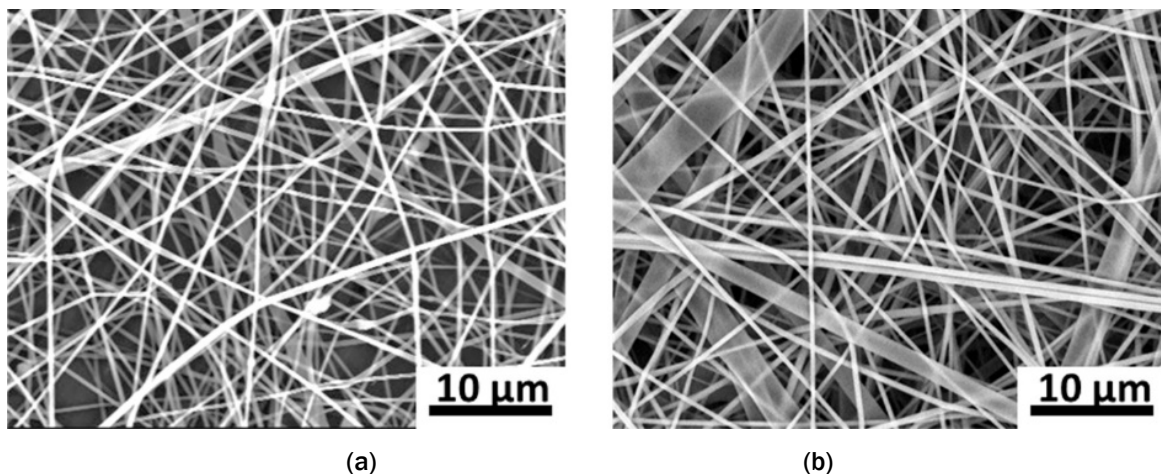


Figure 3. Plan-view SEM images of LLZO polymer precursor nanofibers produced by R2R ES at (a) a low fabrication rate (10 wt.% solid in precursor solution and 1 mL/h injection rate) and (b) at a high fabrication rate (17.5 wt.% solid in precursor solution and 10 mL/h injection rate). Source: ANL

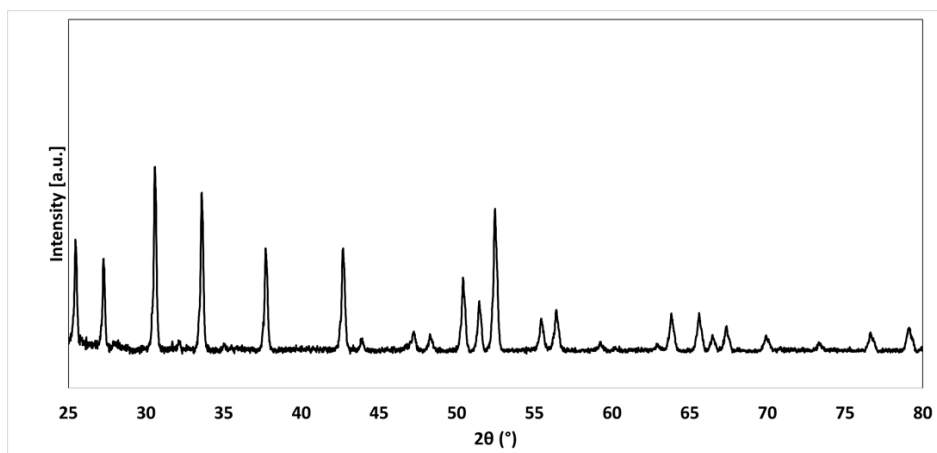


Figure 4. θ -2 θ XRD profile of LLZO nanofibers formed at 750°C. Source: ANL

Energy conversion material nanofiber ES studies including fiber characterization and device fabrication/testing

Composite LLZO fiber-polymer electrolyte membranes were developed, and their ionic conductivity behavior was studied. The composite was prepared by first dissolving PEO and lithium bis(trifluoromethanesulfonyl) imide (LiTFSI) in acetonitrile as shown in Figure 5(a). LLZO fibers were then introduced and sonicated in the solution to achieve a good dispersion shown in Figure 5(b). The fiber containing slurry was drop cast in a mold to form the thin membrane shown in Figure 5(c) after the acetonitrile evaporated. Finally, a 5/8" diameter disk was punched out of the membrane for Li|PEO-LiTFSI-LLZO|Li cell assembly.

To achieve mechanically robust membranes, different PEO molecular weights (20 kDa, 100 kDa, 600 kDa, and 1,000 kDa) and LLZO loading ratios (LLZO/PEO = 0.66 and 1.80) were examined. The results indicated that the sample made from 600 kDa PEO with a LLZO/PEO fiber loading ratio of 1.8 led to a dense yet flexible membrane. A low PEO molecular weight caused brittleness and porosity of the membrane, whereas a very high PEO molecular weight resulted in high slurry viscosity and LLZO fiber agglomeration. In addition, two different LiTFSI concentrations, EO:Li⁺ molar ratio of 15 or 20, were studied to compare ionic conductivity of the PEO-LiTFSI matrices. Cross-sectional SEM image of a PEO-LiTFSI-LLZO membrane sample is shown in Figure 6(b). Surface roughness and a non-uniform distribution of the fibers was observed. In comparison, a pure PEO membrane prepared in the same process was examined, which showed a slightly more uniform structure than the PEO-LLZO sample. However, the surface roughness is still high.



Figure 5: Photographs of (a) PEO-LiTFSI acetonitrile solution without LLZO fibers, (b) PEO-LiTFSI-LLZO slurry, and (c) a cast PEO-LiTFSI-LLZO membrane. Source: ANL

SEM imaging for cross sections of samples cut with a razor blade showed fibers with large a loading ratio and a dense distribution of fibers in the polymer as seen in Figure 6. Defects (voids and a gap at the surface) and a non-uniform distribution of the fibers were observed which create a resistance and reduce conductivity. It was suspected that some of the defects may have occurred during sample preparation, so more samples were prepared using a focused ion-beam to produce a smooth cross section. The SEM images for the top and bottom of these samples showed different densities. Again, voids were observed which can create a large impedance in the samples.

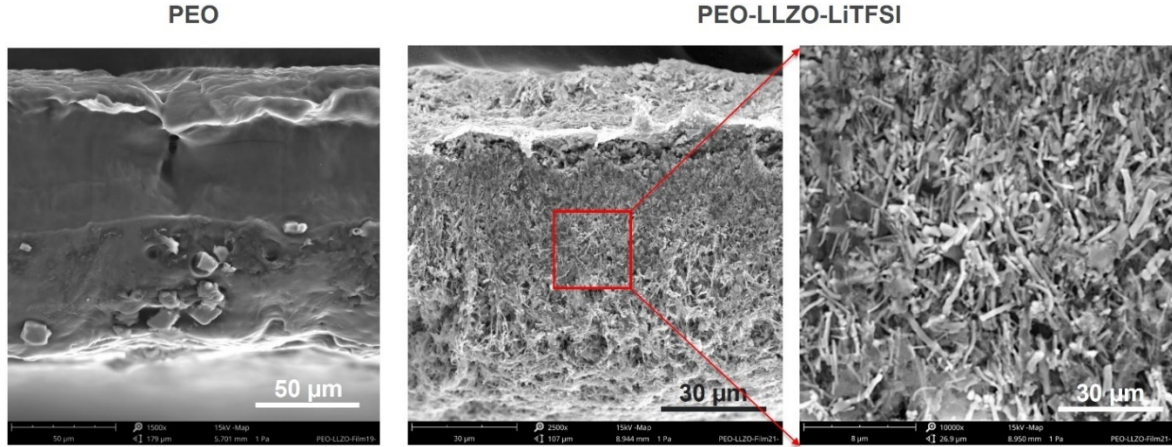


Figure 6. Cross-sectional images of the PEO and PEO-LLZO-LiTFSI samples. Source: ANL

The ionic conductivity of the PEO-LiTFSI-LLZO membranes with an EO:Li⁺ ratio of 20 and LLZO:PEO ratio of 1.8 were characterized by AC impedance spectroscopy of Li/membrane/Li symmetric cells in the frequency range of 1 kHz ~ 1 MHz. Figure 7 shows the impedance data measured at 60 °C and 100 °C. The 60 °C measured Nyquist plot showed a distinctive double-semicircle feature, which indicated a relatively large interface resistance of the sample. The semicircle at high frequencies are often ascribed to bulk, while the semicircle at low frequencies (the second semicircle) is often linked to the double-layer capacitance of the interface between the electrolyte and electrodes [9][10]. In this study, the double semicircle feature is not obvious for the 100 °C measurement (shows as a non-symmetrical semicircle) suggesting that the interface resistance was significantly reduced at high temperatures. The bulk conductivity of the Li|PEO-LiTFSI-LLZO|Li cells was estimated as 1.6×10^{-4} S/cm and 3.9×10^{-4} S/cm at 60 °C and 100 °C, respectively. Table I summarized the sample composition, thickness and bulk conductivity.

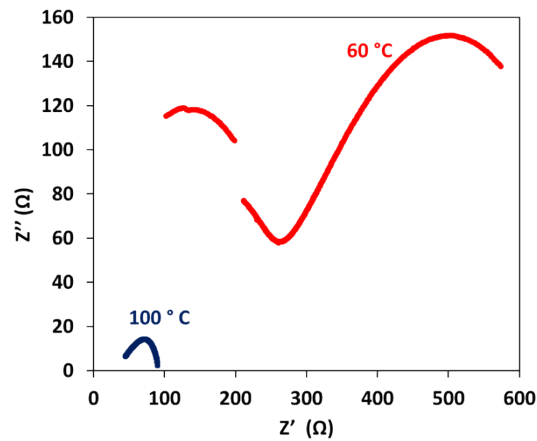


Figure 7. Nyquist plots of Li/PEO-LiTFSI-LLZO/Li cell measured at 60 °C (red) and 100 °C (blue). Source: ANL

Table I. Composition, Thickness, and Bulk Conductivity of PEO-LiTFSI-LLZO Membranes

Sample	Conductivity (S/cm) at 60 °C	Conductivity (S/cm) at 100 °C	LLZO:PEO ratio (wt.%)	EO:Li ⁺ ratio (mol)	Thickness (μm)
PEO-LiTFSI-LLZO	1.6E-04	3.9E-04	1.8	20	151

The drop cast PEO-LiTFSI-LLZO membrane had a rough surface, which can result in a large interfacial resistance between PEO-LiTFSI-LLZO and Li. To characterize the LLZO fiber distribution within the PEO-LiTFSI-LLZO membranes, SEM imaging of FIB cut samples was carried out, which showed different LLZO fiber densities at the top and bottom sections of the membrane, as well as voids in the sample that are marked by the yellow arrows in Figure 8. The structural non-uniformity and defects can increase the resistance of the membrane. A better method to control the membrane microstructure was needed. Therefore, ANL developed a slot-die coating process, where both ink composition and coating parameters were optimized. Figure 9 shows the photograph of a 25mm x 100 mm (width by length) PEO-LiTFSI-LLZO slot-die coating membrane, which has a PEO:LLZO=1 mass ratio. Cross-sectional SEM images of this membrane showed a smooth surface and a relatively uniform LLZO fiber distribution within the membrane was observed. The thickness of the film is around 50 μm. This sample showed a similar ionic conductivity of 1.7×10^{-4} S/cm at 60 °C but a more robust charge and discharge cycling performance. Figure 10 shows the voltage profile of the coated membrane during cycling. After initial voltage fluctuation under 1 mA/cm² current density, the sample showed a steady voltage profile up to 55 hours up to 4.2 mA/cm² and 3 mAh/cm². Polarization voltage of less than 0.4 V was observed.

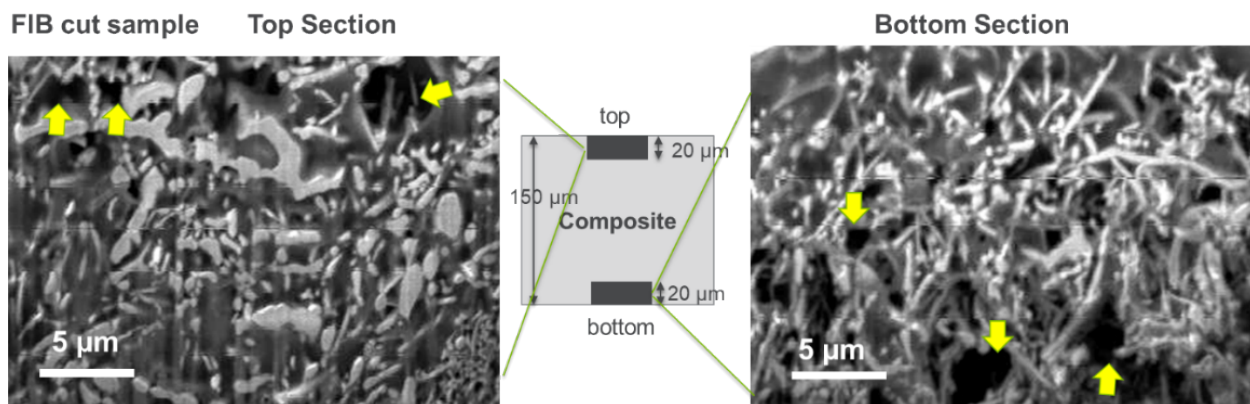


Figure 8. SEM cross-sectional images of a drop cast PEO-LiTFSI-LLZO membrane cut by FIB. The left image was taken from the top section of the membrane while the right image was taken from the bottom of the membrane (e.g., opposite side). These images indicated a higher fiber density at the bottom, which is likely related to gravity effect. In addition, voids were observed as indicated by the yellow arrow. Source: ANL

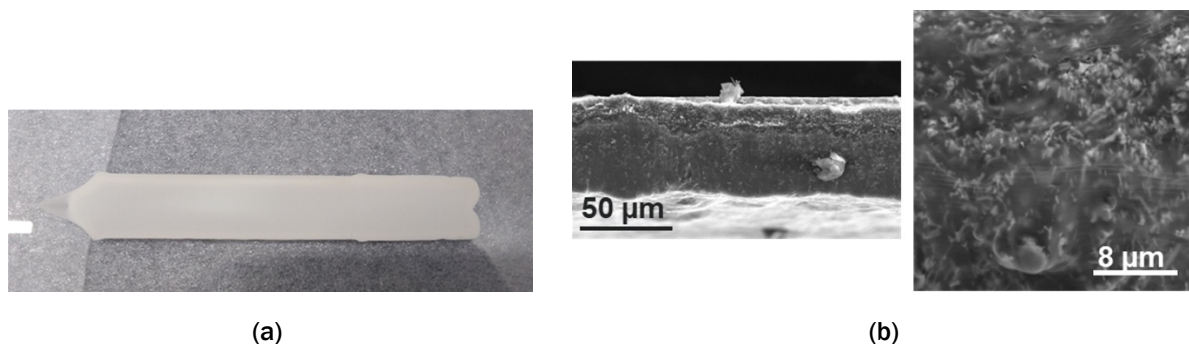


Figure 9. (a) Photograph of a 25mm wide by 100 mm long PEO-LiTFSI-LLZO membrane prepared by slot-die coating with a PEO:LLZO mass ratio of 1:1, and (b) a cross-sectional SEM images of the PEO-LiTFSI-LLZO membrane showing a smooth surface and relatively uniform LLZO fiber distribution within the membrane.

Source: ANL

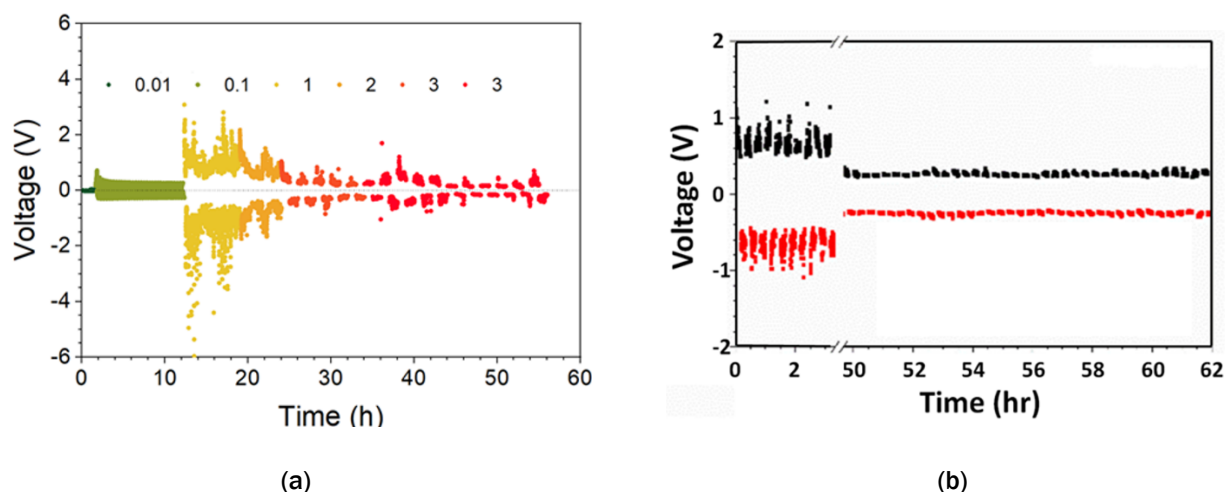


Figure 10. (a) Charging and discharging voltage profiles of a symmetric Li|PEO-LiTFSI-LLZO|Li cell under a variety of current densities up to 4.2 mA/cm² and 3 mAh/cm², and (b) voltage profile of the sample where only the 4.2 mA/cm² current density data were included to show the steady voltage region where the polarization voltage was less than 0.4 V. Source: ANL

After the cycling tests, the microstructures were examined. Figure 11(a) shows the SEM images of the cross sections of the sample with fibers. The middle part is the electrolyte layer with a thickness of 150 μm , and the top and bottom parts are the Li electrode layers which could not be separated from the electrolyte layer. Examination of a different area of the LLZO fiber-containing membrane showed no change in thickness or morphology. This indicated that the LLZO nanofiber reinforced the mechanical strength and structure robustness of the composite membrane. On the other hand, the PEO membranes without fibers showed varied thicknesses at different sample locations after cycling, indicating that this sample could not maintain structural stability during cycling as shown in Figure 11(b). The EDS elemental maps shown in Figure 12 were obtained for the LLZO fiber containing membrane, where La and Zr were from LLZO; F, and S were from the LiTFSI salt; C was mainly from PEO and LiTFSI; and O was mainly from both PEO and LLZO. The fact that all the elements were distributed relatively uniformly indicates that this sample had good chemical stability in addition to mechanical stability, which suggests that slot-die process has indeed improved the microstructure of the PEO-LiTFSI-LLZO membrane. The charge and discharge experiments of this membrane showed more than 250 hours cycling life.

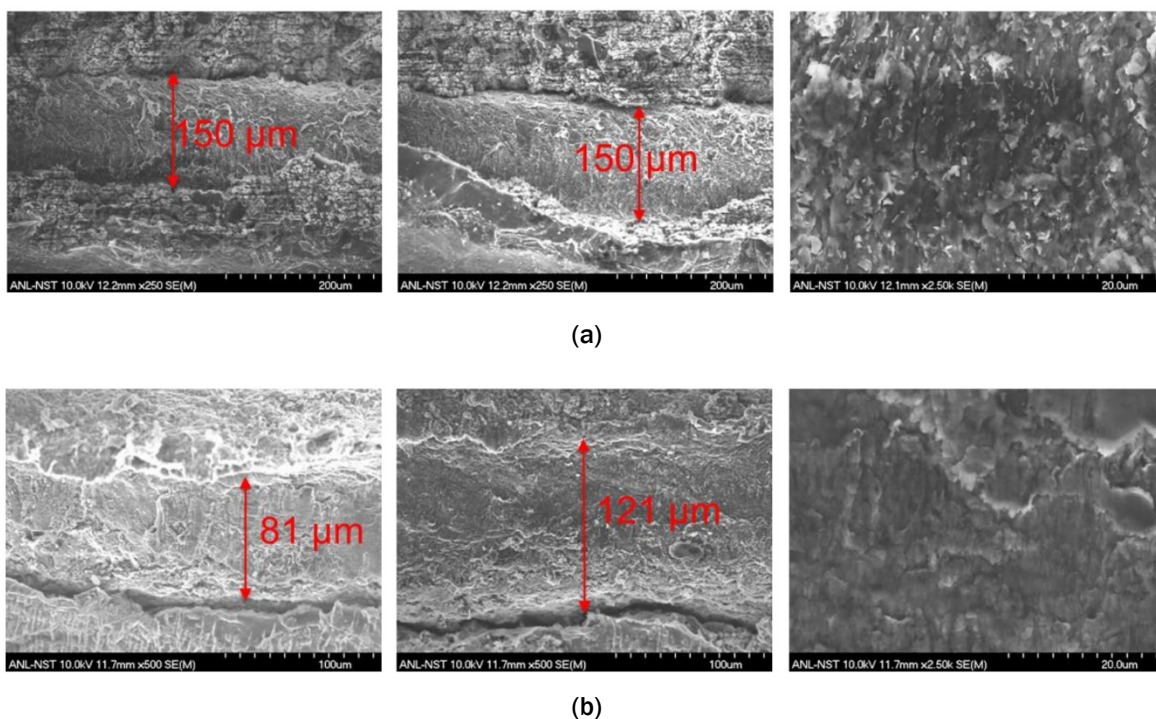


Figure 11. SEM images for (a) PEO-LiFTSI-LLZO and (b) PEO-LiTFSI. Source: ANL

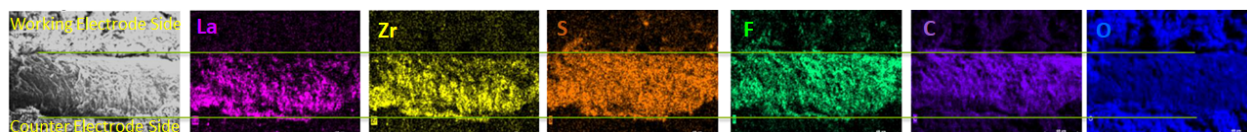


Figure 12. SEM-EDS elemental maps for a slot-die coated PEO-LiFTSI-LLZO sample after cycling. Source: ANL

Spinning scale-up for fibers containing surface electrocatalyst particles

Particle-on-fiber mesostructures were prepared by ES using a polymer solution with CuAg nanoparticles. CuAg has shown to be an effective electrocatalyst in reduction reactions involving CO_2 , CO, or oxygen. In CO_2 or CO reduction reactions, the catalyst aids in suppressing hydrogen evolution [11][12]. In oxygen reduction reactions, the catalytic activity of bimetallic CuAg could be comparable to that of platinum [13]. Polymer/particle solutions electrospun using the ANL bench-top ES apparatus resulted in well-formed nanofibers with CuAg nanoparticles embedded within the fibers as shown in Figure 13(a) (low resolution) and Figure 13(b) (high resolution) for the nanoparticles agglomerated on the fiber, and Figure 13(c) for the uniformly-dispersed nanoparticles without clusters.

In initial attempts, CuAg particles were added directly to the polymer solution and mixed, which led to particle agglomeration. To improve particle distribution, the spinning precursor solution preparation process was altered so that the particles were dispersed into the solvent separately, and subsequently incorporated into a polymer solution. This modification led to favorable results where the particles have an improved distribution throughout the fibers as shown in Figure 13(c). Further research is needed to increase the particle loading while maintaining well-formed nanofibers.

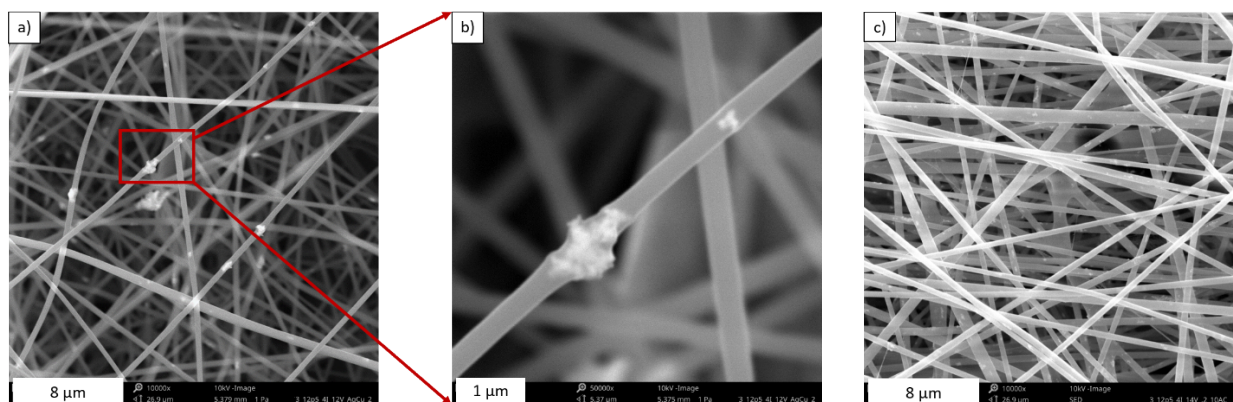


Figure 13. SEM images of CuAg nanoparticles embedded in polymer fibers where nanoparticles in (a) and (b) agglomerated and in (c) were dispersed more uniformly and showed less clusters. Source: ANL

Cationic and anionic fiber spinning scale-up for deionization membranes

A scalable ES process based on co-ES was developed to fabricate dual-fiber deionization membranes used for water treatment applications with the recipes shown in Table II. Nafion (a cationic) and Sustanion (an anionic) spinning processes were optimized for a higher production rate. Increasing the production rate required the creation of more spinning events, i.e., more microjets, which can be achieved either through a higher precursor injection rate or using more nozzles where both have been tested. To obtain well-mixed Nafion and Sustanion fibers in the membrane, the spinning nozzles were arranged on two parallel supporting bars next to each other. With this geometry, homogeneously intermixed fibers of two different ionic fibers were fabricated as shown in the SEM images of Figure 14(a) (low magnification) and Figure 14(b) (high magnification). However, this geometry has certain limitations: (1) the two fiber materials had to use the same ES working distance because their spinning nozzles are mounted on the same needle rack, which reduced the number of spinning parameter choices; and (2) the cationic and alkaline fibers were in close proximity which led to electric field interference between the two materials and an unstable spinning process that increased the experimental complexity. The latter was observed when the fiber diameters of the Sustanion fibers deposited alone were compared with those deposited simultaneously with Nafion, e.g., the fiber diameter was almost doubled for the co-spinning case (~1200 nm vs. 700 nm of single fiber).

Table II. Optimized Recipe for Fiber Deposition

Parameter	Nafion	Sustanion
Solid Concentration [wt.%]	15	15
Solvent	nPA:H ₂ O = 2:1 (wt.)	EtOH:H ₂ O = 2:1 (wt.)
Carrier Polymer	Poly(ethylene oxide)	Poly(ethylene oxide)
Ionomer : Carrier Polymer	99:1	99:1

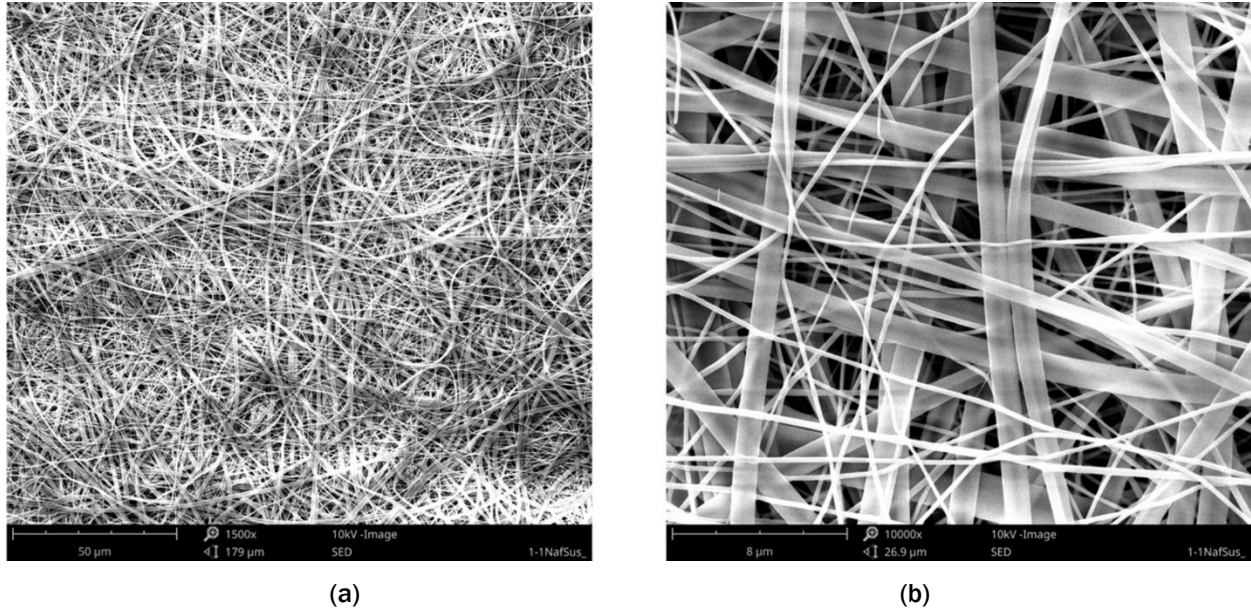


Figure 14. (a) Low and (b) high magnification SEM images of co-spun Nafion and Sustainion fibers. Source: ANL

To avoid the above limitations, an experimental setup that employs two needle racks located at the opposite sides of the drum collector was used to achieve co-ES. The older ES tool that could perform ES only on one side is shown in Figure 15(a) and the newly developed co-ES tool with multi-nozzles and needle racks mounted on the opposite sides of a drum collector is shown for comparison in Figure 15(b). The modified setup allowed for deposition of a mixed fiber mat (i.e., dissimilar polymer nanofibers simultaneously electrospun onto the collector) where each fiber can be electrospun using independently optimized conditions. This apparatus was utilized to fabricate a thick deionization membrane consisting of cation-exchange fibers (Nafion) and anion-exchange fibers (Sustainion). The electrospinning apparatus during fiber production is shown in Figure 15(b) where Nafion and Sustainion nanofiber deposition is visible on the drum.

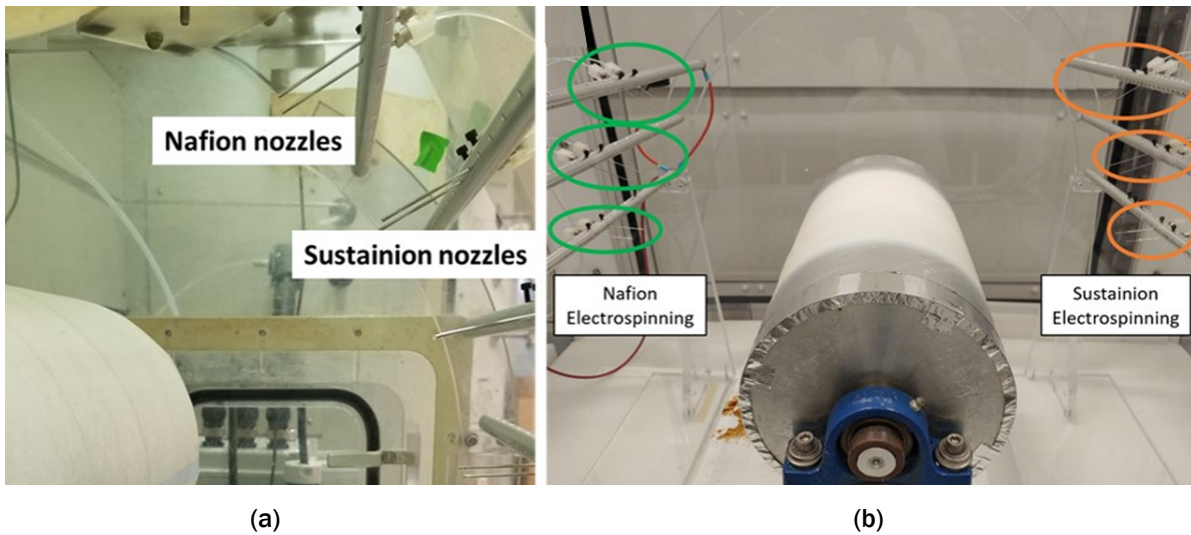


Figure 15. (a) The old ES unit that has one-sided spinning and (b) the new multi-nozzle co-ES unit with needle racks mounted on the opposite sides of a drum collector. Source: ANL

Previous deposition of the mixed-fiber mat shown as the plan-view SEM image in Figure 16(a) resulted in a mat thickness of 130 μm after 14 hours of deposition (i.e., 0.15 $\mu\text{m}/\text{min}$). Scaled-up co-ES was successfully performed with an increased number of active needles to increase the deposition rate of more than three times (i.e., 0.55 $\mu\text{m}/\text{min}$). The plan-view SEM images in Figure 16(b) showed well-formed nanofibers. The resultant fiber mat had a thickness of 200 μm . The scale-up of the co-ES process led to a slight reduction in fiber diameter from previous 444 ± 305 nm to 310 ± 74 nm.

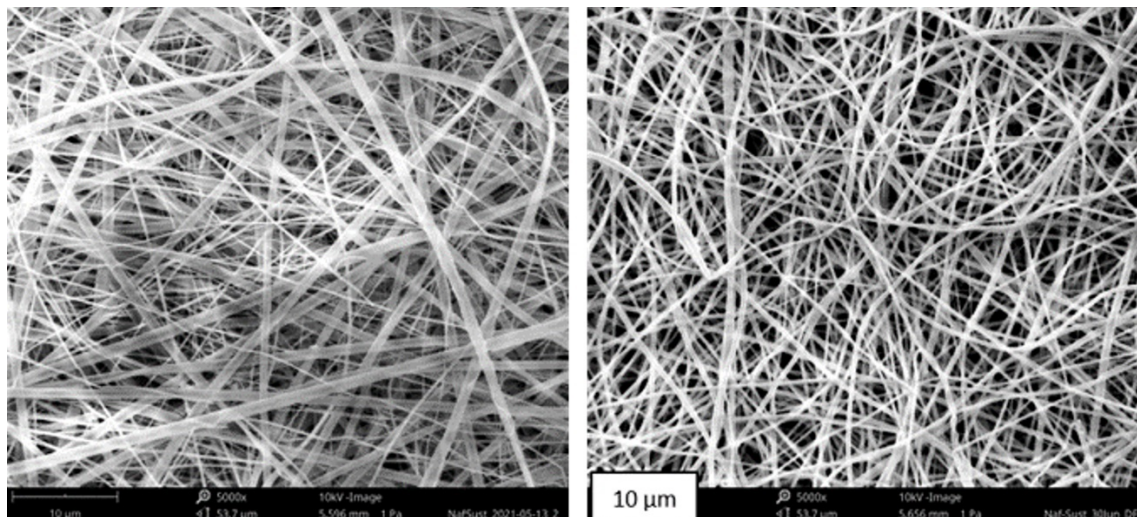


Figure 16. Plan-view SEM images of Nafion-Sustainion mixed-fiber mat using (a) the previous co-ES setup and (b) the new co-ES setup. Source: ANL

After the ES process, the ionic conductivity of the fiber mat was characterized. The fiber mat was first annealed at 120 $^{\circ}\text{C}$ for 30 minutes under vacuum to induce crystallinity of Nafion and improve the fiber mat mechanical properties. The annealed fiber mats, as well as an as-spun fiber mat, were soaked in 0.085 M NaCl water solution overnight in preparation of the conductivity measurement that was also performed in 0.085 M NaCl using an inductance, L, capacitance, C, and resistance, R meter. As shown in Table III, the fiber mats exhibited slightly higher conductivities as compared to the mats fabricated previously using a benchtop tool. The change could be due to slight variations in compositions (e.g., cationic polymer : anionic polymer weight ratio) or mat porosity. While the thermal treatment of the fiber mat did not change its conductivity, the fiber mat appeared to be stronger during the soaking process. This is a beneficial effect because the fiber mat exhibits improved physical stability when wet without compromising its conductivity.

Table III. Ionic Conductivity of Nafion/Sustainion Dual Fiber Mat in 0.085 M NaCl

Mat	Ion Conductivity [mS/cm]
As-spun	0.488
Annealed – 120 $^{\circ}\text{C}$, 30 min	0.474
As-spun previously	0.357

SOFC fiber spinning scale-up

In addition to cationic and anionic fibers, R2R ES of LSCF electrode materials for SOFC applications was demonstrated. SOFCs are electrochemical devices that convert fuels directly into electricity, which have been recognized as one solution to address the problem of high emissions and low efficiencies in conventional combustion engines. The current fuel cells operate at high temperatures, which results in high system costs and limits material selection. Therefore, low-temperature and intermediate-temperature SOFC material systems were investigated. LSCF is a ceramic cathode material proposed for use in intermediate-temperature SOFCs. Nanofiber LSCF has the advantages of high specific surface area, long conduction length, and high porosity, making them good candidates for SOFC cathodes. A scalable synthesis process of LSCF nanofibers using R2R ES technology was developed.

The LSCF precursor contained an overall solids content of 10% (w/v) with a molar ratio of 0.6:0.4:0.2:0.8 nitrate salts that utilized polyvinylpyrrolidone (PVP) as the carrier polymer. Once the salts were dissolved in a solvent system of dimethylformamide, ethanol, and deionized (DI) water, PVP was added to the solution and allowed to mix until fully dissolved.

Scale-up of the LSCF precursor on the R2R electrospinner was completed using two bars with 14 nozzles on each bar. The fibers were electrospun in an environment with 5-20% relative humidity with a flow rate of 10-12 mL/h as the working distance and voltage were varied. Figure 17(a) shows a SEM image for fibers spun at a working distance of 10 cm and voltage of 22 kV and Figure 17(b) is the SEM image for fibers spun at a working distance of 17.5 cm and 28-30 kV. Well-formed fibers were electrospun from these two conditions with a slight decrease in fiber diameter (156 ± 27 nm to 135 ± 39 nm) at an increased working distance of 15 cm to 17.5 cm and voltage of 22 kV to 28 kV. A summary of the conditions and resulting fiber diameters can be seen in Table IV. The generated electrospun fibers were then annealed at 500°C to crystallize and form perovskite LSCF.

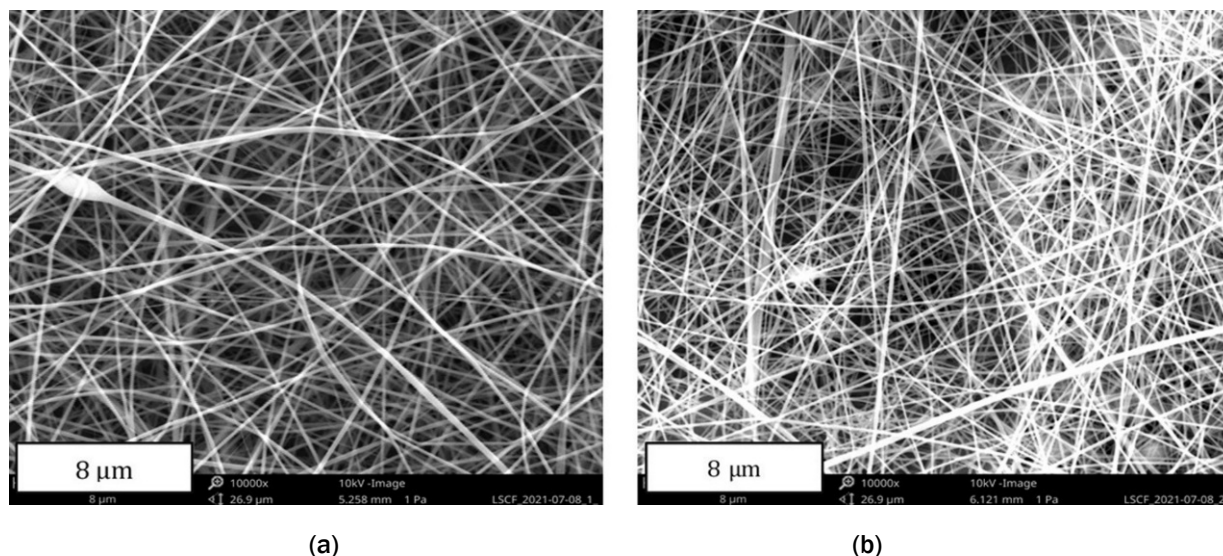


Figure 17. SEM images of LSCF:PVP nanofibers from the R2R electrospinner of (a) fibers spun from a working distance of 10 cm and voltage of 22 kV and (b) a working distance of 17.5 cm and 28-30 kV. Source: ANL

Table IV. Summary of R2R ES Conditions and Measured Fiber Diameters

Condition	Working Distance (cm)	Voltage (kV)	Current (mA)	Flow Rate (mL/h)	Fiber Diameter (nm)
1	15	22	5-6	10	156 ± 27
2	17.5	28-30	10	10	135 ± 39

Fiber ink rheological property measurements

Customized fiber inks were developed based on in-house synthesized LLZO electrospun fibers. These fibers can form percolation networks more easily than particles and thus can show improved transport properties when they are used in Li batteries. In addition, fiber networks can also effectively prevent fracture propagation within the fiber-reinforced composite materials, leading to improved mechanical strength. Therefore, it is beneficial to develop LLZO fiber inks for ceramic-polymer composite solid-state electrolyte applications. Ink formulations were prepared for a broad range of fiber loading ratios and solid concentrations, and the ink viscosity properties were investigated. All inks showed a shear thinning behavior as can be seen by the data in Figure 18 and were workable for slot-die coating. The shear thinning is more pronounced for high solid content inks (e.g., 22.3 wt.% solid). Adding fibers to the pure polymer inks did not change ink rheological behavior, which is likely due to the alignment of fibers in the ink flow direction.

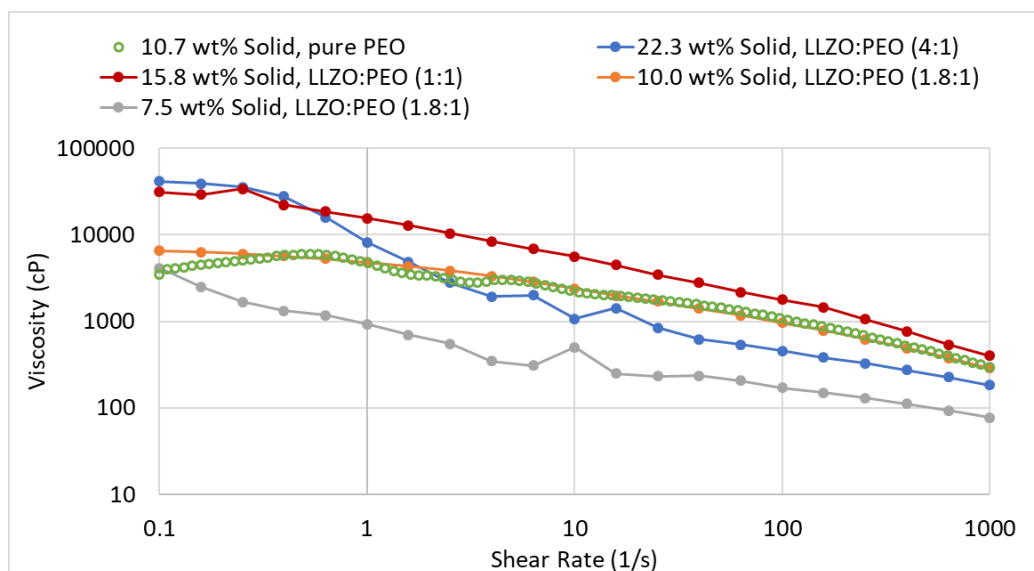


Figure 18. Viscosity versus shear rate for pure PEO polymer ink and the LLZO-PEO fiber-polymer composite inks with different solid contents and fiber loading ratios. Source: ANL

Task 7 - Printed Electronics - flexible electronics with micro- and nano- structuring

The goal of this task was to study the feasibility of printable electronics within the R2R program. Under this scope, the commonly used commercial inks were characterized to evaluate their performance in printing (e.g., aerosol jet and flexographic printing). During printing, several parameters can be adjusted to modify printing quality such as ink dilution, temperature, and ink flow rate. These parameters have large implications on the printability of the ink being used, so initial efforts were to understand ink rheological properties.

Conductive and dielectric ink study for R2R printed electronics

Rheological properties and printing conditions were studied for the conductive and dielectric inks using aerosol jet printing because aerosol jet printing can achieve relatively high printing resolution among non-conduct printing methods (e.g., minimum linewidth of 10 μm) and is also capable of incorporating a broad ink viscosity range from 1-500 cP. To print an electronic device, three types of inks are required: (1) conducting, (2) insulating, and (3) semiconducting. Aerosol jet printing has made strides in expanding the list of available inks that provide good printability and suitable electronic properties. Various properties of the ink itself including the viscosity, volatility of the solvent, surface tension, and the size and shape of the solid materials all play a role in the aerosol jet printing process. Additionally, the inks must be compatible with each other to make a working device.

Viscosity is one of the first considerations needed for selecting and preparing a suitable ink for aerosol jet printing. The number of commercial conductive inks meant for aerosol jet printing are rapidly expanding, but a large number of inks that were developed for other printing methods like inkjet, gravure, and screen printing are also readily available. The viscosity of these inks may not be directly suitable for aerosol jet printing but can be modified to be applicable. Two common methods to affect the viscosity of an existing ink is to increase ink temperature during printing or to dilute/thicken the inks. The heating of a silver flexographic ink was examined. The viscosity of this ink is in the order of 10^4 cP at room temperature which is a value significantly higher than the operating range of aerosol jet printing. As shown in Figure 19, the viscosity of flexographic ink drops from 10,515 cP to 282 cP upon heating from room temperature to 50 $^{\circ}\text{C}$, indicating heating can be an effective way to enable a high viscosity ink. For comparison purposes, Ag and Cu aerosol jet inks were also tested. These two inks have relatively low viscosity already at room temperature. Their temperature dependence of viscosity is not as significant as the flexographic ink.

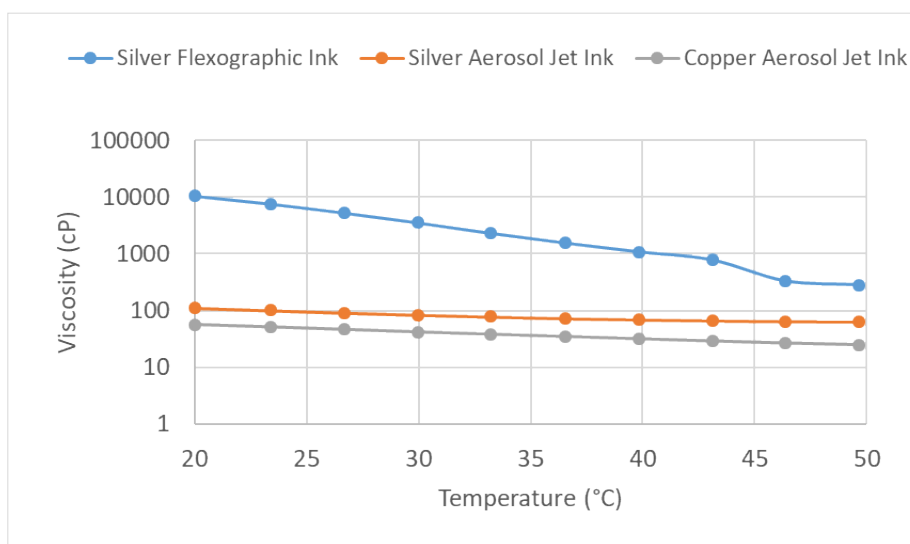


Figure 19. Viscosity as a function of temperature plots for three conductive inks. Source: ANL

Heating of the inks is a conceivable option to expand the number of inks available to use with the aerosol jet printer, but this method was proven to be ineffective for many dielectric inks. These dielectric inks can be enabled by simple dilution. A UV-curable dielectric ink with a viscosity in the printable range of aerosol jet printing was tested. However, the ink showed a clogging issue during printing. The ink was diluted to 25 wt%, 33 wt.%, and 50 wt.% using acetone and the viscosity measured as shown in Figure 20. The ink that was diluted to 33 wt.% was found to fit the viscosity range of the ultrasonic atomizer of the aerosol jet printer and was used for printing of electronic structures.

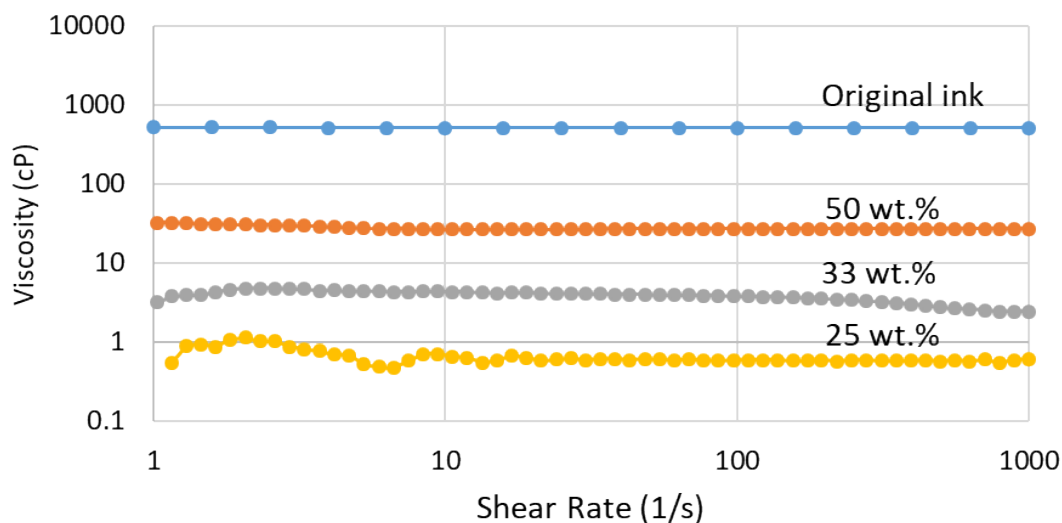


Figure 20. Shear rate plot for a neat UV-curable dielectric ink and for various dilutions. Source: ANL

Post-printing thermal treatment of the prints is necessary to remove the remaining solvent and cure the polymers. This also serves as an engineering step to improve the microstructure and the electronic property of the prints made from particulate inks. Among various curing processes (such as oven thermal heating, UV curing, and photonic annealing), photonic curing is one of the rapid annealing processes that can significantly reduce annealing time, improve energy cost, and avoid thermal diffusion and damage to the underlying printing layers or plastic substrates that cannot survive high temperatures.

Photonic curing was investigated for a silver conductive ink that was originally formulated for oven annealing at 200 °C for one hour. Different light energy densities were applied during testing, which were controlled by the applied voltage/power and pulse number. The resistance of the prints was measured after the curing process as one ink processing evaluation criteria, i.e., small resistance indicates high conductivity and good electronic property of a conductive ink. The experiments were performed on identical dog-bone structures printed with silver particulate inks. For each photonic curing process, only the power and number of pulses were changed. The pulse length and repetition rate were fixed to be 500 μ s and 1.7 Hz, respectively. Table V gives the results for this experiment. The thermally annealed sample was measured with the lowest resistance of 6.1 ohm (e.g., best conductivity). The samples cured with photonic curing showed a large range of resistance depending on the single pulse energy density and accumulative energy density of multiple pulses. High pulse energy density promoted conductivity development of the prints as indicated by the 290 V, 48 pulse case. For the cases where similar pulse energy density was applied, a higher accumulated energy density (e.g., larger number of pulses) improved sample conductivity as indicated by the 260 V pulse cases. The sample that was annealed using 192 pulses showed a much smaller resistance than the sample that was annealed with 96 pulses. For the sample that was annealed with 48 pulses, the resistance was above 50 mega-ohm. These results suggested microstructure difference between the samples that were treated at different photonic curing conditions.

Table V. Resistance of Printed Dog Bone Structures That Were Annealed at Different Conditions

Thermal Cure	Photonic Cure			
200°C for 1 Hour	260 V, 48 pulses	260 V, 96 pulses	260 V, 192 pulses	290 V, 48 pulses
-	0.23 J/cm ² per pulse	0.23 J/cm ² per pulse	0.23 J/cm ² per pulse	0.34 J/cm ² per pulse
-	11.0 J/cm ² accumulated	22.1 J/cm ² accumulated	44.0 J/cm ² accumulated	16.5 J/cm ² accumulated
6.1 Ω	> 50 MΩ	181.1 Ω	23.3 Ω	6.9 Ω

SEM characterization of the samples as shown in Figure 21 indicated that the samples that were annealed with low pulse energy density (e.g., 260 V, 48 pulses) had small silver particle sizes after annealing resulting in a poor electrical conductivity. Conversely, the samples that were treated with high pulse energy density (e.g., 290 V, 48 pulses) or accumulative energy density (e.g., 260 V, 192 pulses) had larger silver particle sizes leading to an improved conductivity. Also, the thermally annealed sample did not only experience particle growth but also showed particle coalescence which formed a connected electron transport network. Although such particle growth and coalescence were prohibited during the rapid photonic curing processes, the photonic cured samples were denser and thus also showed good conductivity (or low resistance). As a comparison, even though the high pulse density photonic curing sample and thermally annealed sample showed a similar resistance of 6-7 ohm, the photonic curing process was about 125x faster than the thermal annealing (e.g., 28 second photonic curing versus 3600 second thermal annealing).

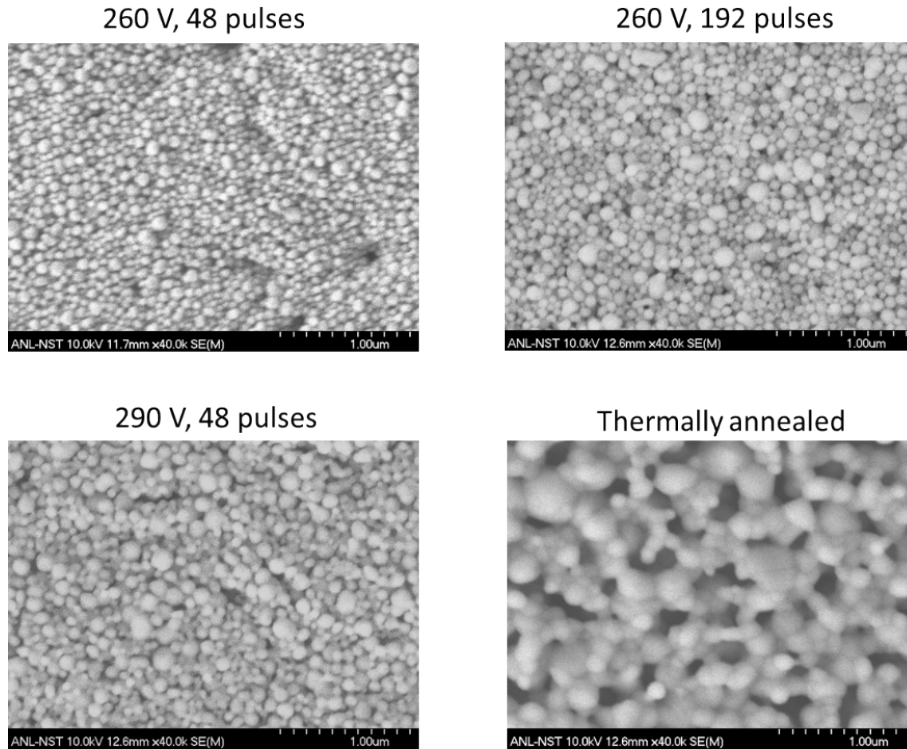


Figure 21. SEM plan-view images of the photonic curing samples processed with different power level and pulse numbers and thermally annealed sample. Source: ANL

Design of a logical device circuit

Printed logic devices were fabricated to demonstrate the feasibility of printed electronic technology in microelectronics applications. Currently, most printed electronics are limited to interconnects and passive electronic components which limits the function of the devices and keeps the technology dependent on surface mount logic components fabricated by traditional silicon wafer process. To enable fully printed, high-end electronic devices, active components such as transistors and logic gates need to be directly printed onto the substrate. An inverter, which is a NOT logic gate, is the most basic building block of all digital logic gates. By demonstrating the function of a printed inverter, all logical gates and complex functions can be achieved by printed electronic technology.

An inverter was fabricated on Kapton substrate using aerosol jet printing. For this, the inverter was designed using p-channel metal-oxide semiconductor (PMOS) logic design that operates in the negative voltage region. The logic gate consists of a resistive load and a PMOS transistor. For the resistive load, a SWNT ink was used to print the resistors. For the transistor, a top gate design architecture was employed using poly(3-hexylthiophene) (P3HT) as the semiconducting channel and Nordland Electrical Adhesive (NEA) 121 as the insulating layer. The gate electrode is also printed using SWNTs. All interconnects on the Kapton substrate were printed using silver particulate inks. Figure 22(a) shows the device layout and Figure 22(b) is a picture of the final printed logic gate.

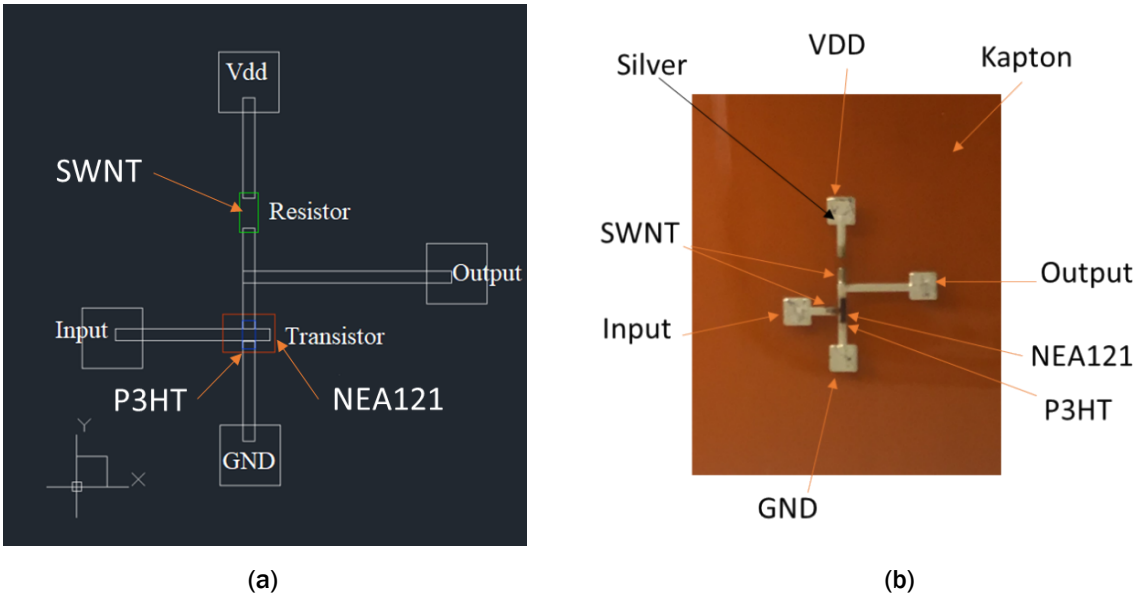
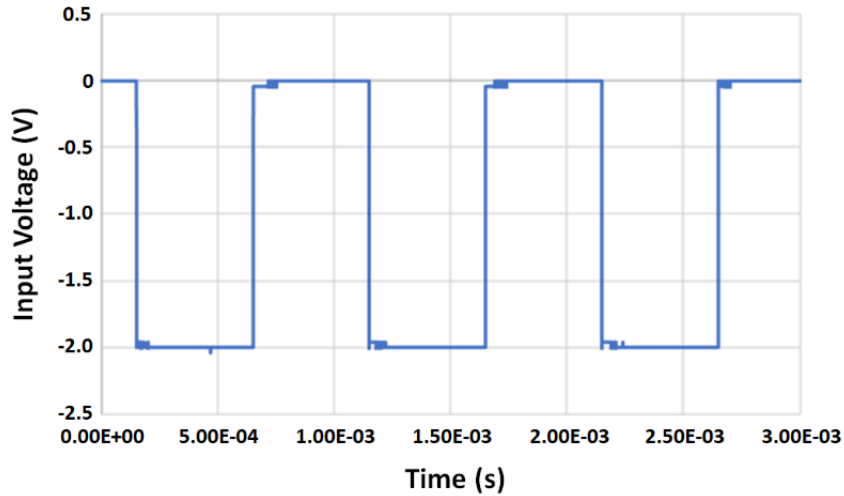
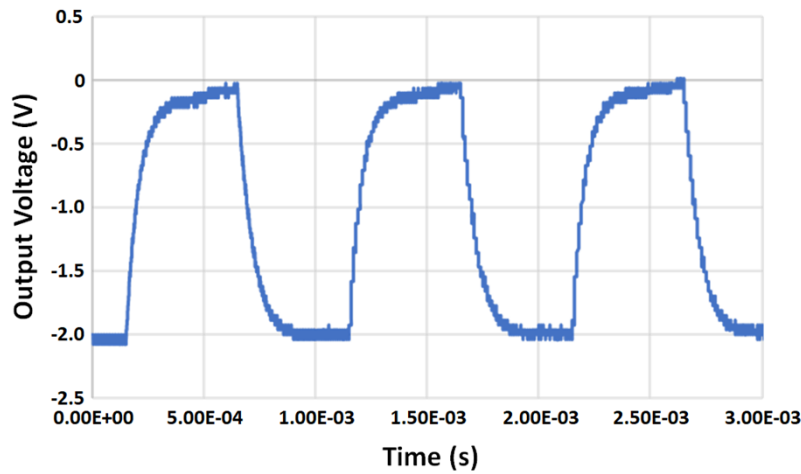


Figure 22. (a) The PMOS inverter layout design and (b) the printed device. Source: ANL

To evaluate the dynamic response of the inverter gate, a square wave switching signal between 0V and -2V was applied at the gate terminal (input electrode) repeating at a frequency of 1kHz. The logic gate was biased with a -2V DC drain voltage (VDD). Figure 23 shows the dynamic switching characteristics of the gate which exhibits a clear inverting response between the input voltage in Figure 23(a) and the output voltage in Figure 23(b). The switching time is around 252 μ s which is controlled by the resistance-capacitance time constant at the output voltage. The measured switching time is typical of polymer based transistors due to the large channel resistance. However, the gate is capable of operating at much larger frequencies.



(a)



(b)

Figure 23. The dynamic switching of the logic gates showing (a) the input and (b) output voltages. Source: ANL

Exploratory study of ML for slot-die coating process optimization

ANL performed a collaborative exploratory study of ML for slot-die coating process optimization with the researchers in the Mathematics and Computing Science Division and Data Science and Learning Division of ANL. The goal was to explore the opportunities for using reinforcement learning (RL) for slot-die coating process optimization. Within the preliminary work, the possibility to use digital twin (DT) to accelerate training of the RL agent was evaluated. An image classification model was also developed to identify defects from the optical photographs of samples. Coating defects, such as dripping, air entrainment, and break lines, can occur during the wetting and drying stages due to non-optimal process conditions. However, due to the complexity of ink rheological properties and dynamic changes during shear flow, it is nontrivial to develop theoretical models that can guide process optimization for new materials and it is time consuming to try-and-error the coating process experimentally. Thus, there is a demand to apply artificial intelligence (AI) in this domain area.

With RL, there needs to be some “States” defined as inputs and let the RL agent run a set of “Actions” to generate changes to the objects. If the change is desired, the Action will be rewarded. If the change is undesirable, the Action will be punished. Eventually, the agent will find an optimal policy that maximizes the rewards. In the case of coating, States are ink properties such as viscosity, surface tension, particle size, and shape aspect ratios, which are measured and set by the users. Actions are a combination of coating parameters, such as ink flow rate, web transfer speed, and coating gap. The agent take Actions and will be rewarded for correct actions that lead to a “defect-free” coating, until an optimum policy that maximizes the rewards by delivering high-quality coatings is achieved. RL is powerful because it will search a large Action space over many possible iterations. However, to train a RL agent requires extensive amounts of data which can be time consuming and expensive.

DT is a virtual machine that mimics the real-world experiments. By using DT, the number of physical experiments can be reduced. DT can be established by using existing experimental data or physical models. An advantage of DT is that the simulated end points do not need to be 100% accurate because RL will fine tune the results from real machines. A DT can be built through two approaches: (1) code physical models into Python script to simulate defect and non-defect inputs and determine if the inputs produce defects, and (2) use ML algorithms to explore data patterns based on existing coating data points if physical models are not available.

ANL examined the first approach by coding an empirical model of Newtonian liquid developed by Lee et al. [14]. This model, entitled the Minimum Permissible Wet Thickness model, defined relationships between the coating bid signature, stable coating window, and coating microstructure. With this model, an estimated wet thickness in the steady state can be “calculated” using ink and coating parameters. As long as the minimum wet thickness of the coated layer is smaller than the estimated steady state wet thickness, the finishing coating will have a large chance to meet the quality requirement (e.g., density of defect is less than the set value). In this exercise, an Al_2O_3 nanoparticle ink was used as the test object to validate the coding.

The parameters used in calculations and experiments are shown in Table VI. As seen from the table, over 279,888 sets of parameter combinations were calculated in a sample trial. About 20 coating experiments were performed to compare with the calculated stable and unstable process conditions. Figure 24 shows the viscosity as a function of shear rate of candidate inks. Figure 25 shows photographs of selected wet coatings prepared using 126 cP ink. Figure 26 shows the table of calculated and experimental observed stable and unstable conditions, which shows a good consistency between the two.

Table VI. Parameters for the Simulation and Coating Experiments

Parameter Inputs	Simulation	Experimental
Web transferred speed (m/s)	0.017	0.017
Flow rate (mL/min)	6-25, step size 1	10, 14, 18
Coating gap (μm)	200-500, step size 225	200-500, step size 75
Ink viscosity (cP)	30, 50, 80, 100	40, 126
Contact angle	30-60, step size 10	--
Width of coated layer (mm)	100	100

After obtaining the simulated data, real experiments were conducted to validate the model using an alumina ink Newtonian liquid. A plot of the viscosity as a function of shear rates for this fluid shows that it is

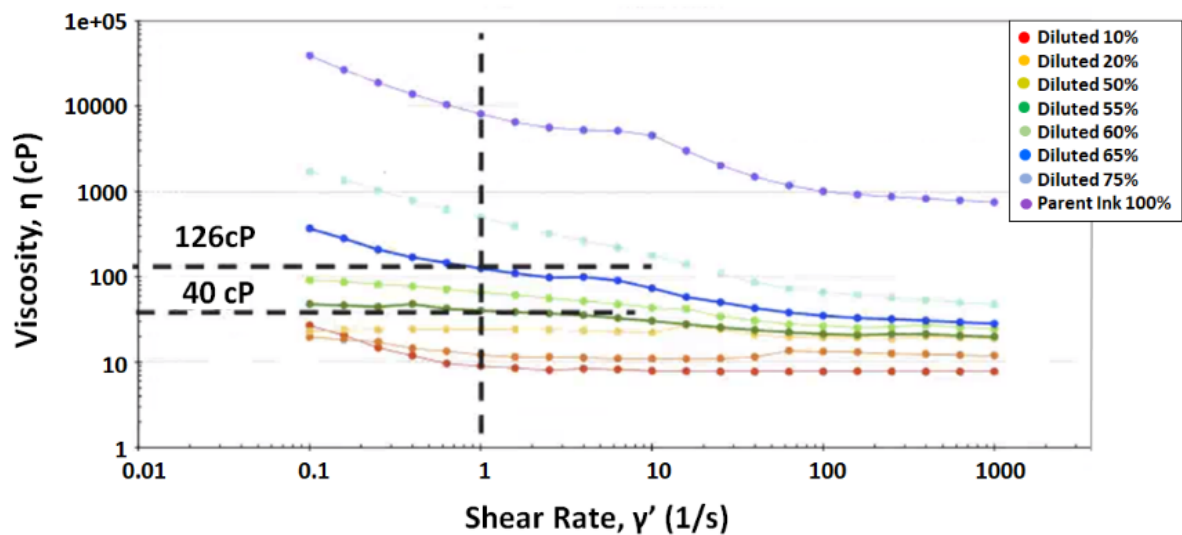


Figure 24. Viscosity measurement for alumina inks of different solute concentrations (e.g., dilution rate).
Source: ANL

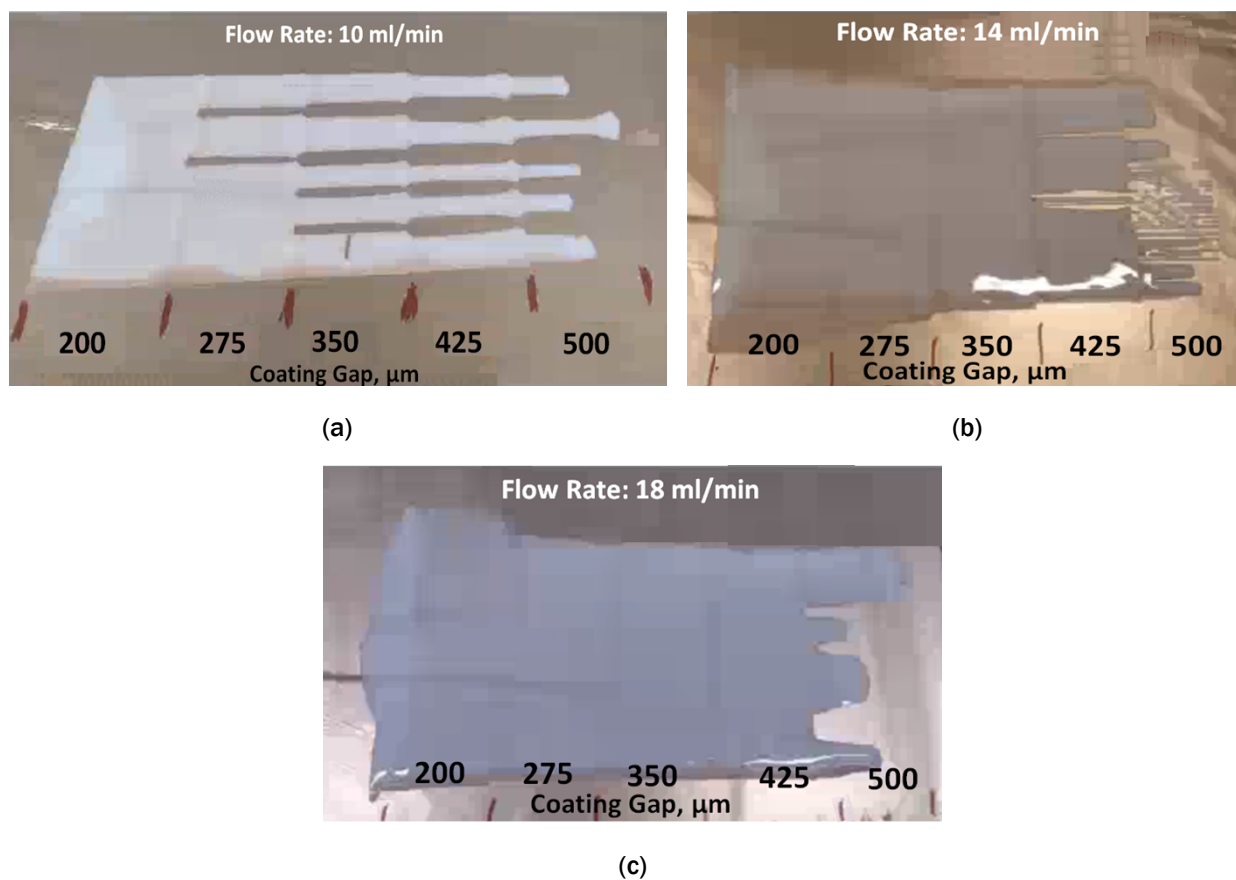


Figure 25. Photographs of alumina coatings prepared using 126 cp ink and three different flow rates: (a) 10 ml/min; (b) 14 ml/min, and (c) 18 ml/min and coating gaps between 200-500 μm. Source: ANL

							Simulation	Coating Result
	th_jw	contact_angle	flow_rate	coating_cap	ink_viscosity	Stable	DT simulated outputs	Experimental Observation
0	100	49	10.2	500	126.43	FALSE		
1	100	49	10.2	425	126.43	FALSE		
2	100	49	10.2	350	126.43	FALSE		
3	100	49	10.2	275	126.43	FALSE		
4	100	49	10.2	200	126.43	TRUE		
5	179.7352941	49	18.333	500	126.43	FALSE		
6	179.7352941	49	18.333	425	126.43	TRUE		
7	179.7352941	49	18.333	350	126.43	TRUE		
8	179.7352941	49	18.333	275	126.43	TRUE		
9	179.7352941	49	18.333	200	126.43	TRUE		
10	140	49	14.28	500	126.43	FALSE		
11	140	49	14.28	425	126.43	FALSE		
12	140	49	14.28	350	126.43	TRUE		
13	140	49	14.28	275	126.43	TRUE		
14	140	49	14.28	200	126.43	TRUE		
15	100	44	10.2	500	40.48	FALSE		
16	100	44	10.2	425	40.48	TRUE		
17	100	44	10.2	350	40.48	TRUE		
18	100	44	10.2	275	40.48	TRUE		
19	100	44	10.2	200	40.48	TRUE		
20	140	44	14.28	500	40.48	TRUE		
21	140	44	14.28	425	40.48	TRUE		
22	140	44	14.28	350	40.48	TRUE		
23	140	44	14.28	275	40.48	TRUE		
24	140	44	14.28	200	40.48	TRUE		

■ Stable Coating
 ■ Unstable Coating

Figure 26. Simulated and experimental observed stable and unstable conditions. Source: ANL

In addition to the DT study, ML algorithms were developed for defect identification based on SEM images of ES samples. The framework of the algorithm can be transferred for coating defect identification when coating data is available. Before training, the images were labeled by hand to differentiate regular images as shown in Figure 27(a) and images containing defects, e.g., bubbles as shown in Figure 27(b). A few different approaches were used to improve model accuracy, such as a neural network model, data augmentation method, and hyperparameter tuning and changing the number of hidden layers or the number of units. However, the accuracy scores were relatively low due to small training sample size, e.g., 222 images. One solution was to use transfer learning which allows a transfer of knowledge from other related tasks. A VGG19 model was chosen to extract image features because this model has been widely adopted and trained by more than 1.4 million images.

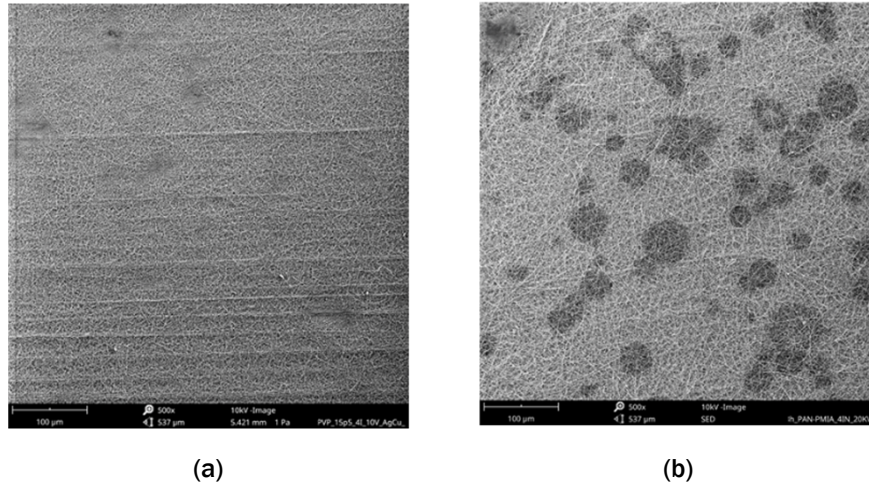


Figure 27. SEM images of (a) a regular sample and (b) a sample that has bubble defects. Source: ANL

Label images were fed into the VGG19 architecture with eight hyperparameter settings and a five-fold cross validation approach was used to address the challenge of a small sample size. The data set was divided into five sets. At each training, one set of data was used as the validation data and remaining four sets of data were

served as training data. Five iterations were made using the five validation sets. Results showed a good match between the training accuracy and validation accuracy for three models as shown in Figure 28. Only two models had overfitting, where the training accuracy is higher than validation accuracy, a common issue for insufficient training data. With this results, it can conclude that transfer learning is a feasible method for coating image classification. After training, the model can be used for predictions. The prediction process only takes a few seconds per image to predict whether defects exist in the image.

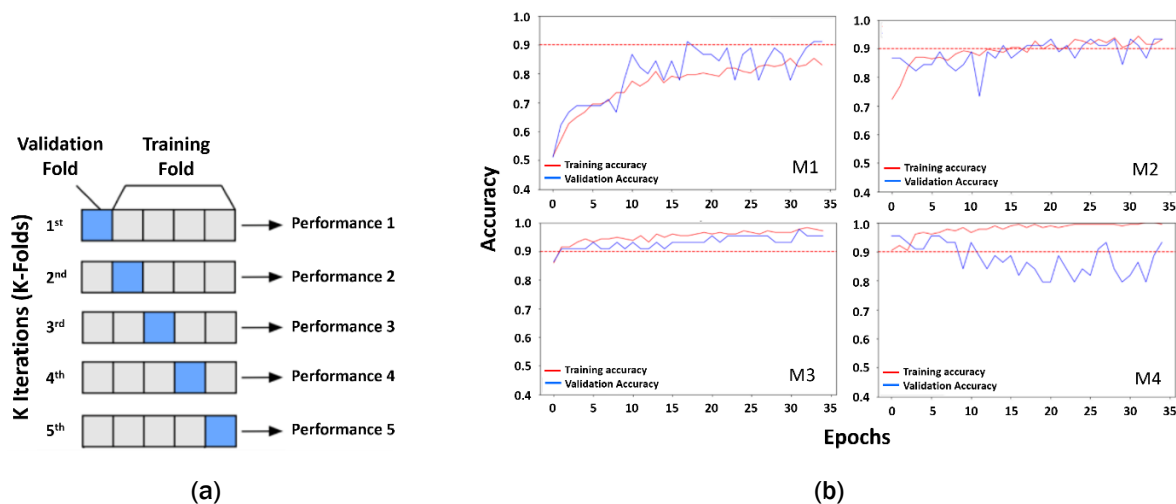


Figure 28. (a) An illustration of five-fold cross-validation approach; (b) training results of four models based on transfer learning and five-fold cross-validation. Model M1, M2, and M3 showed good consistency between the training and validation accuracy. Model M4 showed overfitting where the training accuracy is higher than validation accuracy. Source: ANL

Education, information dissemination, publications, and technology transfer

Two university graduates were hired to participate in broader ES-related R&D for R2R processing. Results of the ES research resulted in two conference publications, three patent applications, and two joint peer-reviewed papers.

Colloidal Chemistry, Surfactant Research, Slurry Processing, Deposition and Drying/Curing Methods (ORNL Lead Laboratory)

Task 1. Multilayer coatings for PEMFC and LIBs

Validation of coating window model with low solids-loading ink

Researchers at SNL (GOMA 6.0 model) and Saint Gobain (Viscicapillary analytical model) predicted the defect-free coating window for 3.5 wt.% Pt/C (3 H₂O:1 n-propanol, I/C = 96%). The models were validated at the +/-0.5 in. H₂O vacuum pressure resolution of the ORNL vacuum generator by coating the 3.5 wt.% Pt/C slurry on aluminum foil. Foil was chosen as the substrate to use for model validation to eliminate the GDL's >60 µm variation in thickness. The validation was performed by sampling a vertical (applied vacuum) and horizontal (line speed) line cut through the coating window to find the transition between a defect-free coating and a defected coating. As shown in Figure 29, the coating was defect-free at 7 and 9 ft./min. at 1 in. H₂O vacuum. However, if the line speed was decreased to 5 fpm or if the vacuum was increased to 1.5 in. H₂O, rivulets formed in the coating.

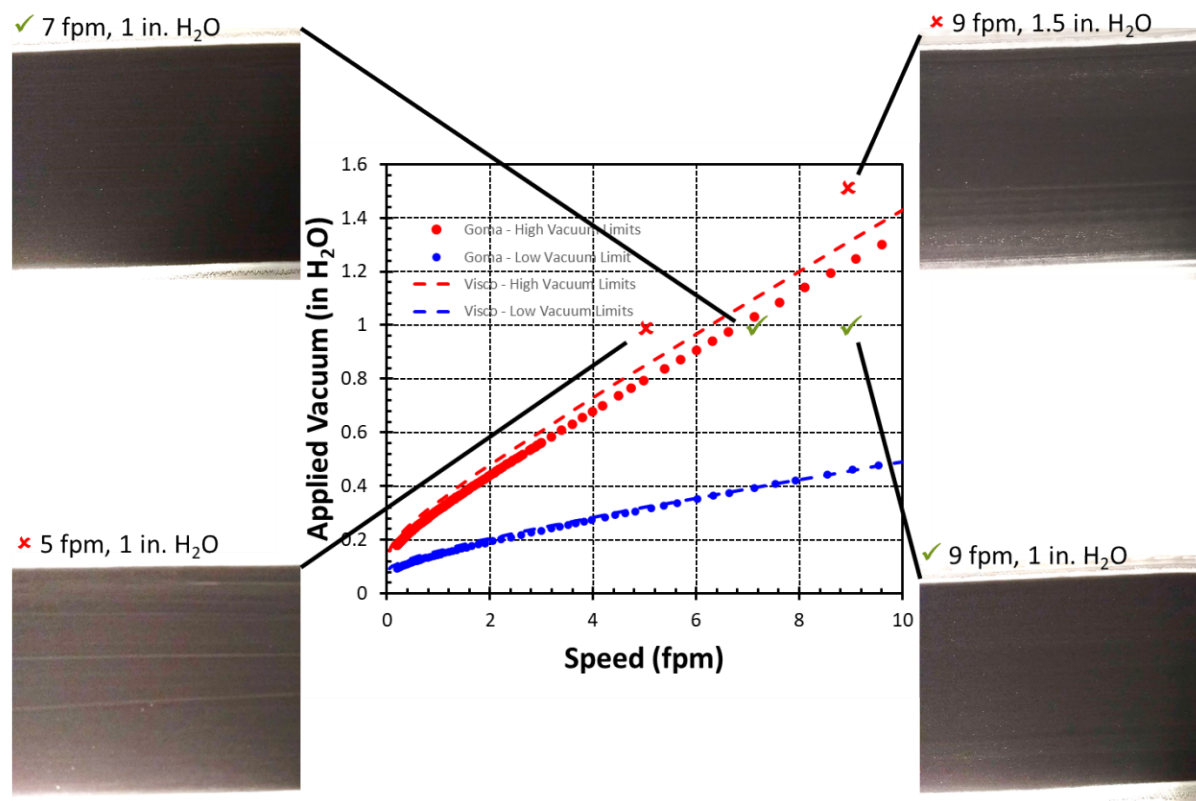


Figure 29. Results from the GOMA and Viscocapillary modeling studies for coatings applied at different vacuum and line speeds. Source: ORNL

Additionally, the models predicted that the coating window for wider coating gaps were strict subsets of narrower coating gaps. For coating the 3.5 wt.% Pt/C slurry on the non-uniform GDL substrate, the gap between the slot die lips and the substrate was set so that the gap at any given point along the non-uniform GDL fell between a known minimum and maximum gap. By targeting the line speed and vacuum pressure in the narrowest coating window for the widest gap, a defect-free coating on the GDL was applied. This strategy was used to coat a more viscous 8 wt.% Pt/C slurry on the GDL.

Accurate modeling of the coating window for high-solids inks

The coating window for 8 wt.% Pt/C ink for PEMFC cathodes was also predicted with the models, but ORNL was not able to establish a defect-free coating on the GDL substrate. To eliminate the difficulty in wetting the hydrophobic microporous layer coating on the GDL substrate and other GDL coating difficulties, ORNL coated the 8 wt.% Pt/C ink on an Al foil substrate. A stable, defect-free catalyst layer coating was established at multiple line speeds (with constant wet thickness) and vacuum pressures. The experimental coating window for the Al foil closely matched the modeled coating window produced by SNL. The knowledge of the coating window boundaries on Al foil helped ORNL find one set of coating parameters that resulted in a defect-free coating on the GDL.

SNL and their collaborators at Saint Gobain refined their Carreau-Yasuda rheology models to fit the ORL data for the two ink concentrations, 3.5 wt.% and 8 wt.% Pt/C as shown in Figure 30. The shear viscosity profile of the 8 wt.% concentrated ink is very sensitive to the measurement conditions. The Viscosity 1 profile was measured after the ink was agitated and pre-sheared at a high rate. The Viscosity 2 profile was measured after the rested ink was pre-sheared at a low rate.

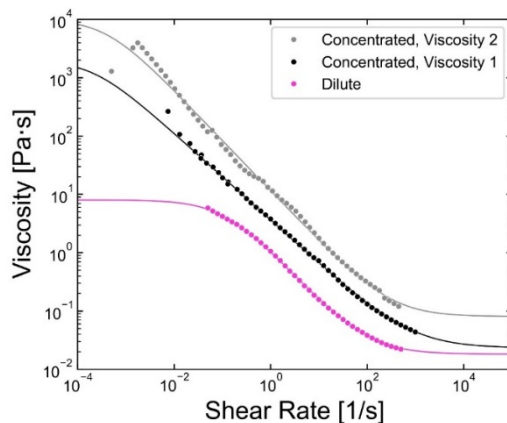


Figure 30. Comparison of the measured shear viscosity (dots) and Carreau rheology model fits (lines) for the dilute and concentrated inks. The viscosity of the concentrated ink depends on the measurement conditions (Viscosity 1, Viscosity 2). Source: ORNL

ORNL validated the defect-free vacuum/web-speed coating windows predicted from the rheology models and the GOMA finite element method or viscocapillary modeling framework. Only one experimentally defect-free point lies outside the coating windows predicted for the dilute ink shown in Figure 31(a) and concentrated ink, Viscosity 1, shown in Figure 31(b). The coating window for concentrated ink, Viscosity 2 clearly does not match the experimental results as can be seen in Figure 31(c). The high-shear conditions the ink is exposed to during coating more closely matched the mixing and shear conditions of Viscosity 1.

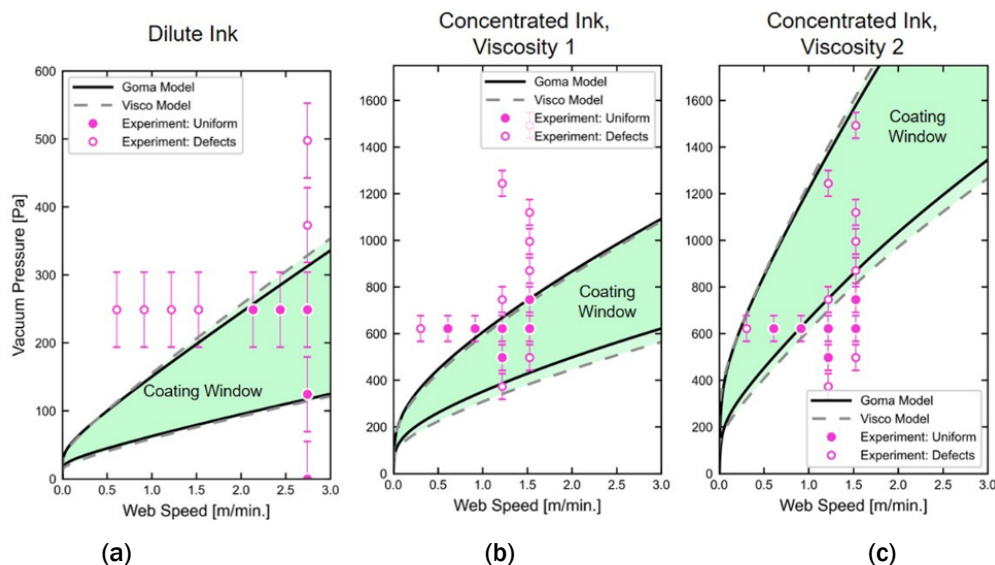


Figure 31. Predicted and experimental defect-free slot die coating windows for catalyst inks. GOMA predictions are solid lines and viscocapillary predictions are dashed lines. Closed circles are for an experimentally defect-free coating and open circles are for an experimentally defected coating. (a) Coating window for dilute ink, (b) coating window for concentrated ink, Viscosity 1, and (c) coating window for concentrated ink, Viscosity 2. Source: ORNL

Multilayer coating of PEMFCs

ORNL produced 50 feet of R2R simultaneous-bilayer slot-die-coated PEMFC decals on PTFE. The bottom layer interfacing with the Teflon is Pt/HSC-based fuel cell cathode ink while the top layer interfacing with air is Pt/Vu-based (Pt on Vulcan carbon) ink. The Pt/Vu ink was prepared with a lower water/1-propanol ratio than the Pt/HSC to give the ink a lower surface tension. Previous studies from NREL and SNL indicated that a lower surface tension is needed on the top of the simultaneous multi-wet-layer coatings to prevent layer mixing. To determine the effect of the ratio of Pt/HSC to Pt/Vu on fuel cell performance, the fraction of the Pt/HSC layer (in terms of wet thickness) was varied from 0% to 100% in increments of 25% and samples were distributed to NREL for in-situ testing.

The coatings appeared optically to be mostly defect free though the Pt/HSC wet layer usually had a few bubbles, and the Pt/Vu wet layer spread out wider than the internal slot die shim used to define the coating width. There was no understanding of why the Pt/HSC had so many bubbles as the slurry was allowed to degas under gentle magnetic stirring overnight. The Pt/Vu spreading problem was corrected when the R2R web speed was increased from 1 to 3 m/min as shown in Figure 32 indicating that the Pt/Vu ink viscosity is too low for low web speeds but appropriate for higher web speeds.

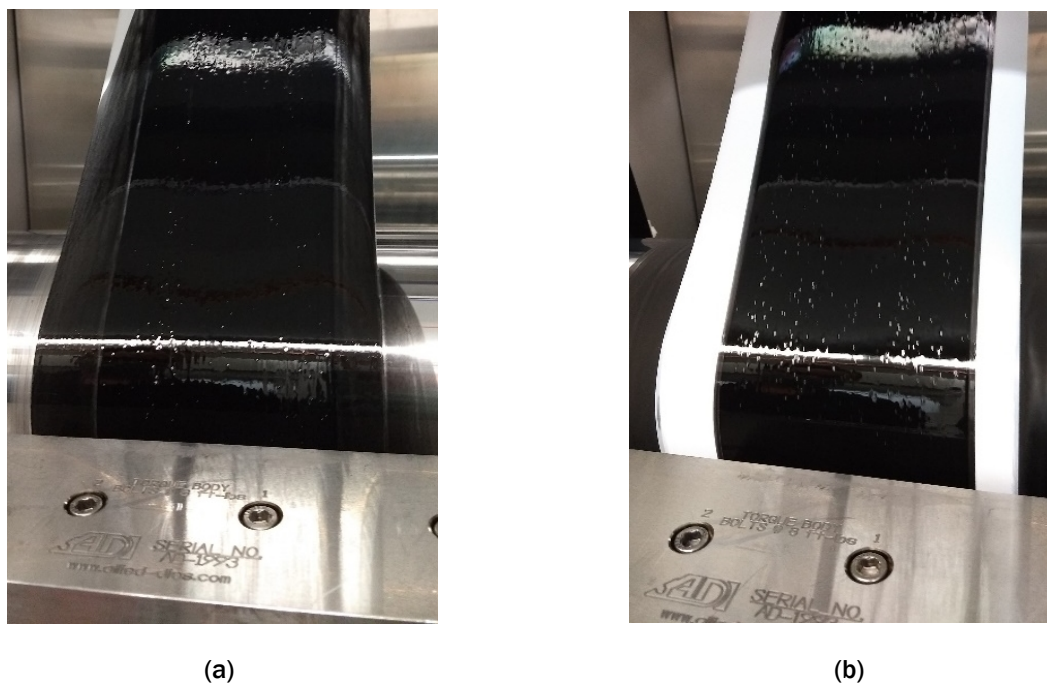


Figure 32. Simultaneous bilayer R2R slot die coating of Pt/Vu ink on top of Pt/HSC ink. (a) At web speeds of 1 m/min, the Pt/Vu layer spreads out wider than the width defined by the shim inside the slot die. The Pt/HSC layer that does not spread out is visible underneath (darker area in the middle of the coating width). (b) At web speeds of 3 m/min, both Pt/Vu and Pt/HSC layers are coated in the width defined by the slot-die shim. Source: ORNL

Previous literature studies on the simultaneous bilayer coating of Newtonian fluids have shown that inversion and layer mixing occur when the wet thickness of the bottom layer is less than one-third of the slot-die-web gap. To explore whether this transition ratio works for non-Newtonian fluids like the shear thinning fuel cell inks, ten thickness/gap ratios from 0.21 to 0.43 were explored. Cross sectional transmission electron microscopy (TEM) was used to check whether the layers mixed. Figure 33 shows images for the unmixed layers for the thickness/gap ratio of 0.37.

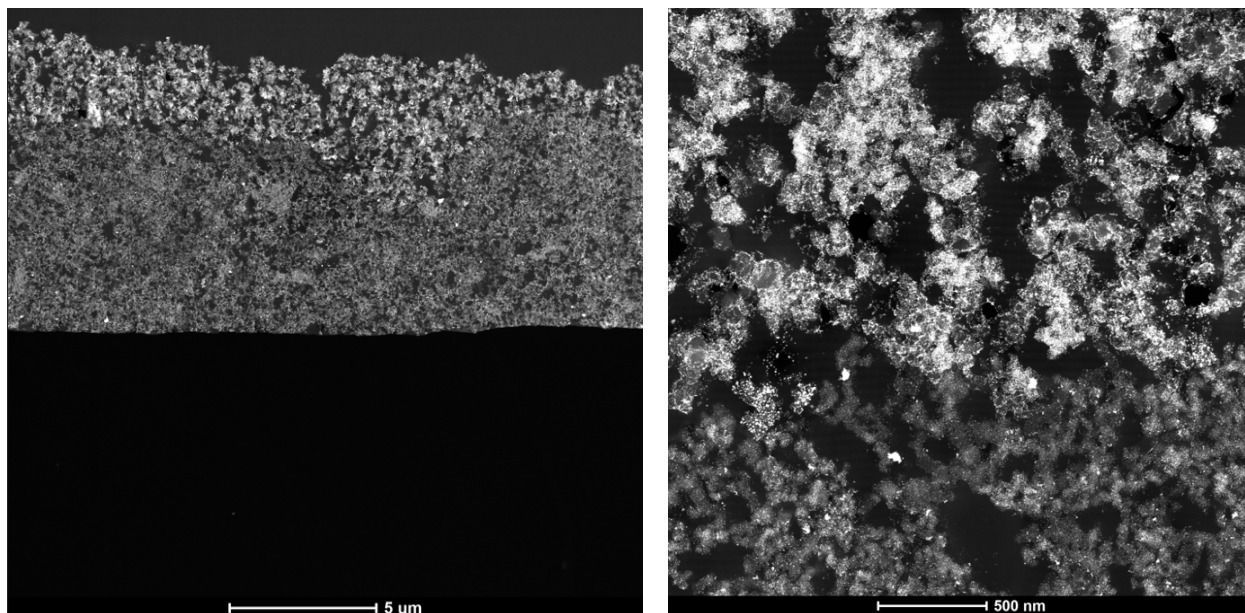


Figure 33. TEM images showing the simultaneously slot-die-deposited bilayer of Pt/Vu on top of Pt/HSC. The Pt/Vu layer has larger primary particle sizes than the Pt/HSC layer. Source: ORNL

Small angle neutron scattering measurements were performed at the HFIR at ORNL to characterize the ink dispersions that were used in the multilayer architectures. Advanced characterization techniques available at ORNL were also employed to investigate the properties of polymer/LLZO electrolyte films and the structure of the electrospun LLZO electrolytes. Operando neutron imaging radiography and tomography experiments at HFIR and neutron diffraction measurements at the SNS at ORNL were completed.

Task 2. Formulation chemistry including mixing, deposition, and drying/curing

Effect of mixing method, time, and speed on PEMFC cathode morphology

Large agglomerates of Pt/C catalyst can limit oxygen diffusion and reduce active Pt area in PEMFC cathode catalyst layers. Proper mixing of the catalyst ink before deposition is critical in breaking up these agglomerates, but excessive mixing wastes time and energy and may even damage the catalyst particles. While there has been prior work on how ultrasonication time and energy affect cathode performance and agglomerate size, there has been little work on mechanical mixing methods. In a joint effort with NREL, ORNL investigated the effects of mixing time and speed on five different mechanical mixers. At each mixing time point, shear viscosity was measured and a Mayer rod coating of the ink on a GDL was prepared. Quantitative agglomerate particle analysis was performed on a $667\ \mu\text{m} \times 500\ \mu\text{m}$ microscope image of each cathode GDE. An example set of images with detected particles indicated in black is shown in Figure 34. The number of agglomerates with an equivalent diameter—diameter of a circle having the same cross-sectional area as the particle—above $15\ \mu\text{m}$ was plotted as a function of mixing time.

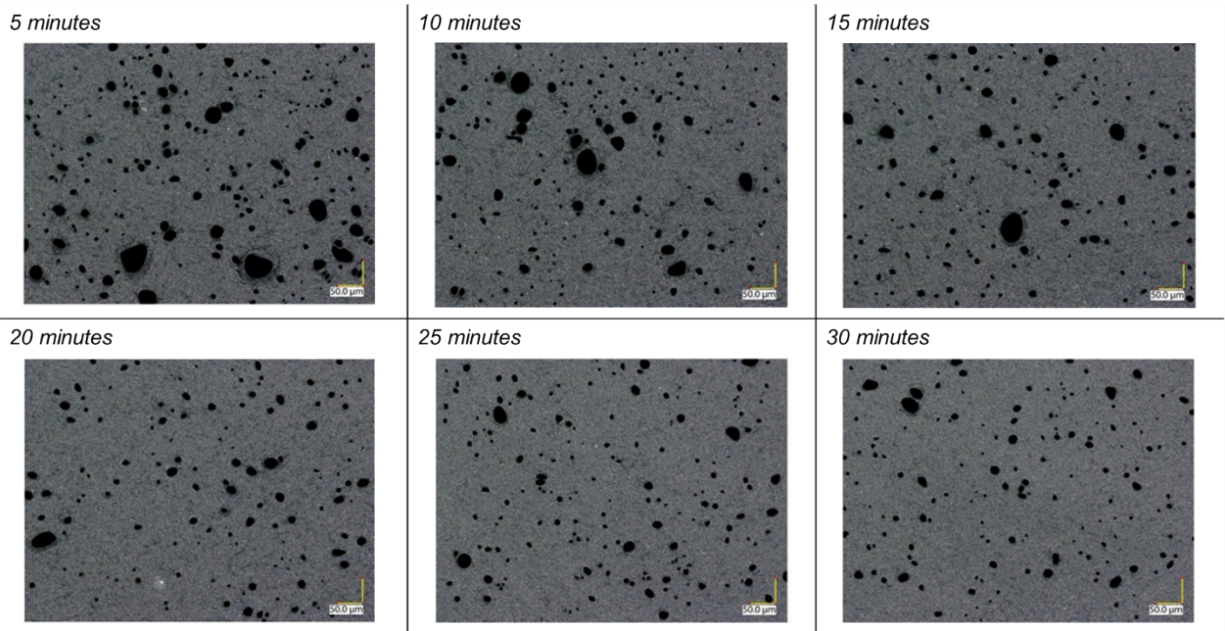


Figure 34. Agglomerate particles (black) in optical microscope images at various durations of mixing with an 18G mixer at 10,000 rpm. Source: ORNL

An IKA S25N-18G rotor-stator dispersing element was used to mix the same ink composition at four rotational speeds from 6,000 to 20,000 rpm. In a rotor-stator mixer, a rotor element rotates inside a stationary stator element with each element sharing a common axis of symmetry, which—in the case of the rotor—is the rotational axis. The Figure 35 shows the exponential decay of the number of large agglomerates over mixing time for several mixing speeds. Even after one minute of mixing, higher mixing speeds show a considerably lower number of large agglomerate particles, indicating that a significant number of agglomerates have been broken up after brief shear mixing. The number of agglomerates for each speed decreases with mixing up to ~20 min where the number of large agglomerates reaches near equilibrium. After 20 min, there is little further reduction in agglomerates. Mixing speed, therefore, is the ultimate driver of agglomerate particle size. If a reduction in particle size is desired, an increase in mixing speed is more effective than an increase in time mixed, except possibly in the case of very short mixing times.

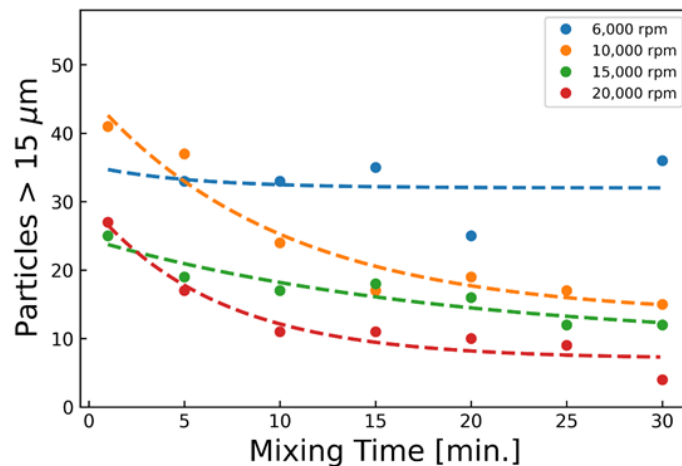




Figure 35. Number of agglomerates with equivalent diameter larger than 15 µm in the dry cathode catalyst layer made from inks mixed with an 18G mixer for various times and rotational speeds. Source: ORNL

To investigate the effect of rotor-stator geometry on mixing efficiency, the same particle analysis in dry cathode coatings over mixing time was performed with an IKA S25N-25F (25F) dispersing element. The specifications for the two rotor-stator mixing heads are shown in Table VII. Despite the smaller rotor-stator gap on the 18G mixer that might indicate higher shear forces, the slower 25F rotational mixing speeds resulted in improved agglomerate break up better than the 18G rotational speeds that were several thousand rpm higher as shown in Figure 36. The larger diameter of the rotor on the 25G mixer results in a significantly higher linear velocity of the rotor tips, even at the lower rotational velocities (7,000 rpm vs. 10,000 rpm and 16,600 rpm vs. 20,000 rpm). However, 20,000 rpm on the 18G mixing head results in fewer large agglomerates than 7,000 rpm on the 25F mixing head because the smaller rotor-stator gap increases the shear rate between the rotor and stator.

Table VII. Comparison of Rotor-Stator High Shear Mixing Elements

Characteristic	IKA S25N-18G	IKA S25N-25F
Rotor Diameter (mm)	12.7	18
Rotor-Stator Gap (mm)	0.3	0.5
Number of Rotor Teeth	2	8
Number of Stator Teeth	10	12
Rotor Image		

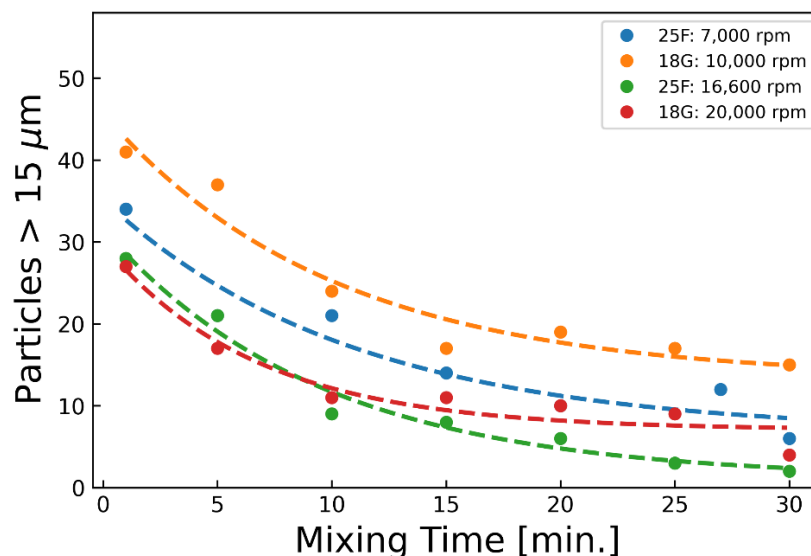


Figure 36. Number of agglomerates with equivalent diameter larger than 15 μm in the dry cathode catalyst layer made from inks mixed at various mixing times and mixing speeds with two different rotor-stator mixers, 18G and 25F. Source: ORNL

Less energy-intensive mixing methods like ball milling and planetary mixing require much longer mixing times to break up agglomerates as shown in Figure 37, but ultimately result in the lowest number of agglomerates in the dried catalyst layer. The final mixing method, IKA Ultra-Turrax Tube Drive, does not seem to result in a negative exponential trend of large agglomerate sizes like the other mixing methods and achieves a particle size distribution close to its equilibrium distribution fairly quickly as shown in Figure 38.

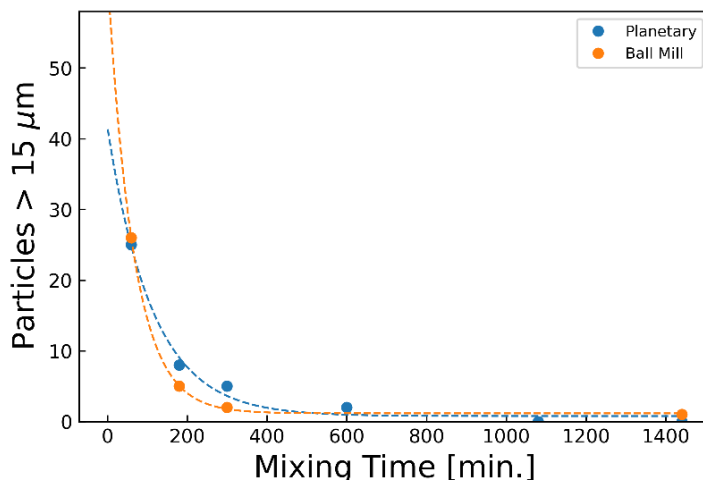


Figure 37. Number of agglomerates with equivalent diameter larger than 15 μm in the dry cathode catalyst layer made from inks mixed at various mixing times with a planetary or ball mill mixer. Source: ORNL

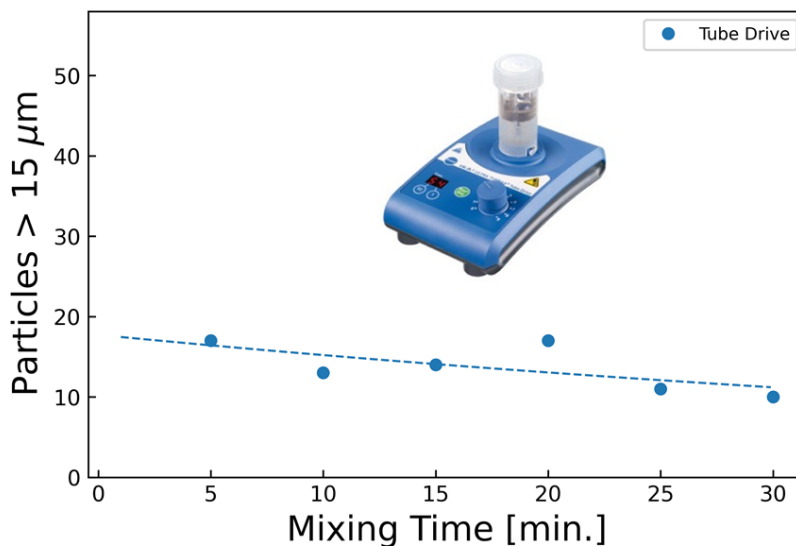


Figure 38. Number of agglomerates with equivalent diameter larger than 15 μm in the dry cathode catalyst layer made from inks mixed at various mixing times with a tube drive mixer shown as an overlay on the plot. Source: ORNL

Planetary mixing

To continue studies comparing mixing methods, optical microscopy was performed on electrodes coated at ORNL with PEMFC catalyst inks mixed using a planetary mixer as shown in Figure 39. Data was generated and evaluated by ORNL for a 500 g mixture using the planetary mixer at a planetary speed of 70 rpm, a disperser speed of 5,000 rpm, and mixing times from 60 to 1440 minutes to compare the results with smaller

batches. The planetary mixer has a spinning disperser with blades in the middle and a Teflon blade that scrapes mixture off the sides of the mixing chamber. The Teflon blade rotates on its axis as it revolves around the inside of the mixing chamber, therefore, the name of planetary mixer. Similar trends were observed between the larger and smaller quantities of mixtures.



Figure 39. Planetary mixer used in the ORNL and NREL mixing studies. Source: ORNL

The number of large agglomerates decreases exponentially with increase in mixing time until the mixing reaches a steady state as shown in Figure 40. The equivalent diameter did not decrease for mixing times greater than 600 minutes as shown in Figure 41, so further mixing was not beneficial. This information is useful for one of ORNL's industry partners for their process design. The large agglomerate's median diameters decreased from about 25 μm to 10 μm up to 600 minutes and no change between 18 hours and 24 hours where the diameters are 8 μm to 11 μm . XRF measurements showed that the concentration was about 0.1 mg Pt/cm² which is within the range for light-duty fuel cell cathodes. Shear viscosity measurements showed that the viscosity will increase after an hour of mixing until it stabilizes after 18 hours as shown in Figure 42. When the shear viscosity is plotted as s^{-1} over the mixing time, the trend for the shear viscosity is just opposite of the particle size over the mixing time. This is reasonable because the large agglomerates are being broken up which increases the available surface area of the active particles in the fluid medium resulting in a higher viscosity ink. The rotational speed of the planetary mixer was 70 rpm, so the mixing time is longer which is similar to the ball mill mixer. Figure 43 provides a summary of the data obtained for other mixing methods.

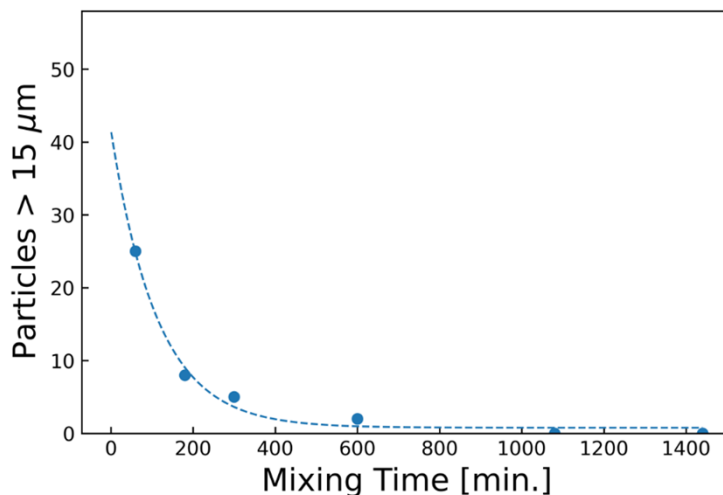


Figure 40. Exponential decrease in large agglomerates for various mixing times. Source: ORNL

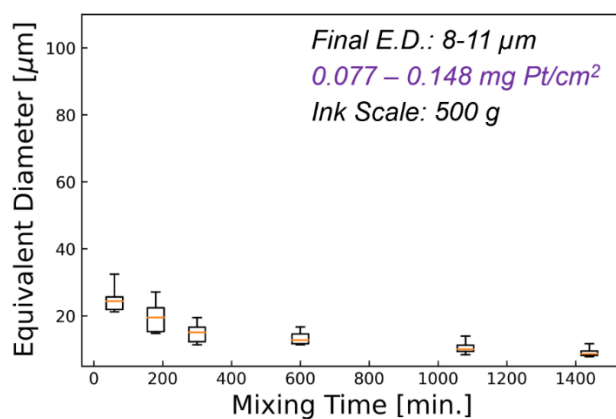


Figure 41 .Decrease in equivalent diameter for various mixing times. Source: ORNL

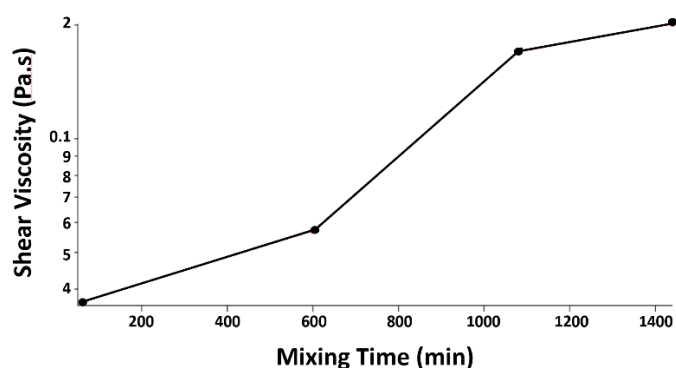


Figure 42. Shear viscosity measurements showing increasing viscosity after an hour and stabilizing after 18 hours. Source: ORNL

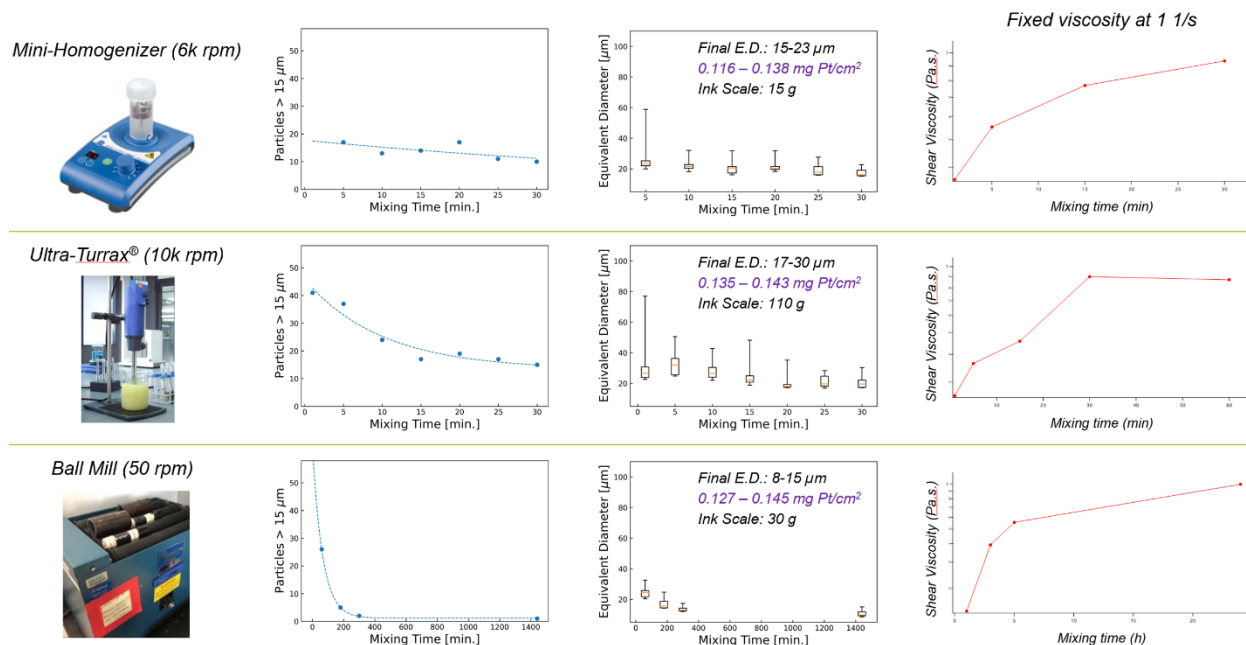


Figure 43. Summary of data obtained from three mixing methods. Source: ORNL

Drying physics studies

The distribution of the binder during the drying of the cathode was investigated using to spatially resolve sodium substituted carboxymethylcellulose (CMC) binder in ultra-thick aqueous processed cathodes. Both survey maps and line scans were used to determine the distribution of binder content and provide experimental verification of binder segregation typically observed in battery electrodes that are dried at elevated temperatures. Sodium was chosen as the element of interest because it can be detected at 15 kV acceleration voltage and is present in the electrode in sufficient amounts. Fluorine is also being investigated as the electrodes of interest contain a combination of fluorinated acrylate binders and sodium substituted carboxymethylcellulose binders.

Ultra-thick (8 mAh/cm²) aqueous-processed nickel-manganese-cobalt (NMC) 811 - CB - CMC electrodes were coated using a Frontier slot die coater in two 4 mAh/cm² passes. The electrodes were calandered to 30% porosity and samples were taken for cross-sectional analysis with a MERLIN SEM. Both elemental maps and line scans were used to determine elemental distribution. Elemental maps were preferred due to the time required for each line scan (5 minutes per scan). One elemental map could be acquired, and the data could be saved as a text file for further manipulation in plotting software. The interaction volume of the electron beam and subsequent x-ray generation was 1.8 μ m in radius and 3.2 μ m in depth.

Both line scans and elemental map data show similar trends, suggesting both scanning techniques are effective. However, the binder distribution was found to be greater near the current collector and lesser near the top of the electrode, opposite of what has been previously reported. Further investigation using additional techniques such as TEM or spatially resolved X-ray photoelectron spectroscopy (XPS) and more electrode architectures will be helpful in understanding the observed differences.

Figure 44(a) is the area of the electrode selected for EDX analysis and Figure 44(b) and Figure 44(c) are the sodium and fluorine signals acquired from this area, respectively. Figure 45 shows the five horizontal line scans performed on the same electrode area and illustrates a five point smooth of the sodium and fluorine signals normalized to one as well as the average signal from each line scan, also normalized to one, as shown in Figure 46.

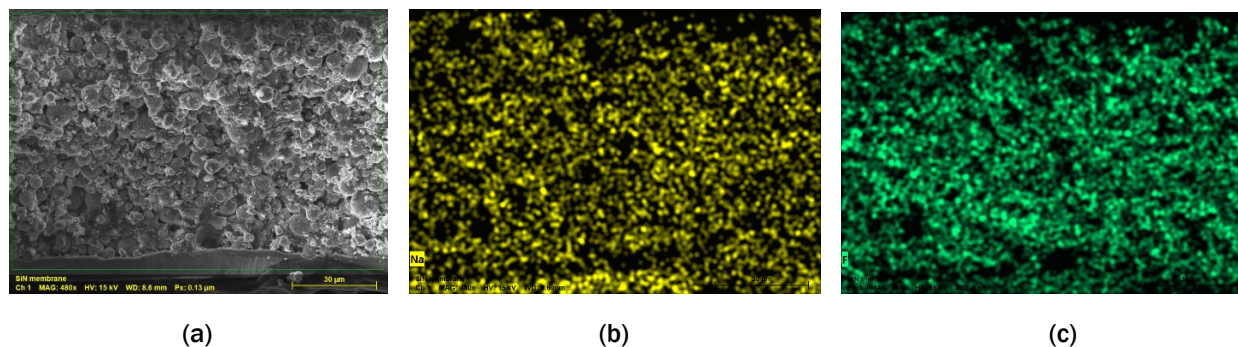


Figure 44. (a) The cross-sectional EDX area of the electrode with minimal void space and topological differences, (b) the sodium signal, and (c) the fluorine signal acquired from cross-sectional EDX map. Source: ORNL

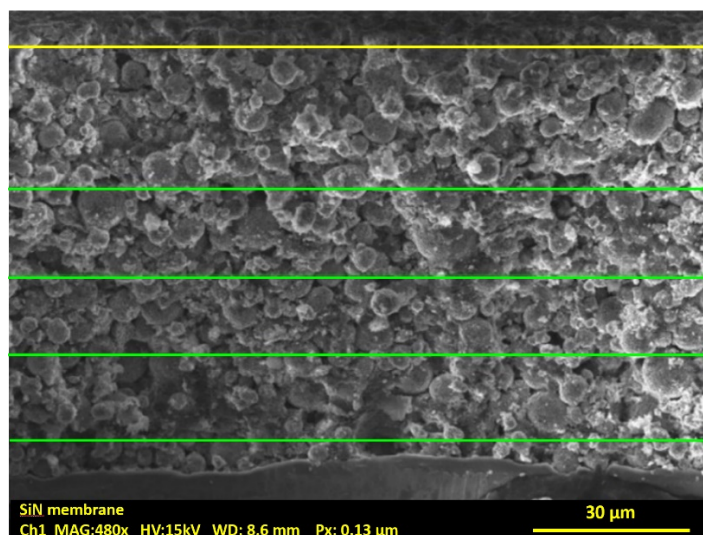


Figure 45. Horizontal line scans acquired from cross-sectional EDX maps. Source: ORNL

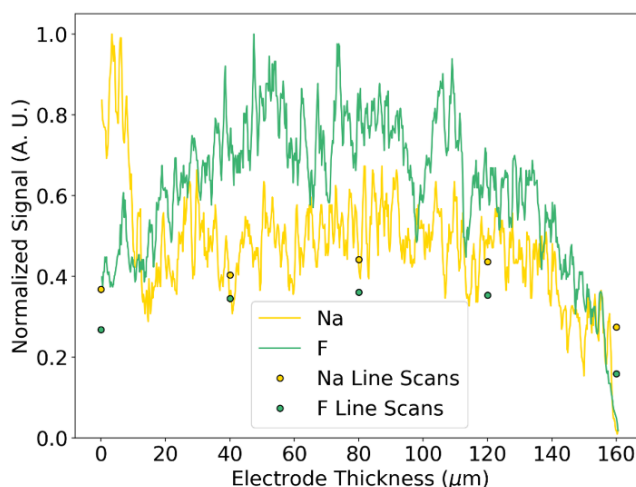


Figure 46. Five point smooth of both sodium and fluorine signal text files acquired from cross-sectional EDX analysis. Each signal has been normalized to highlight the difference in distribution rather than total content. Data from the horizontal line scans were also plotted to confirm the distribution across the total thickness of the electrode. Source: ORNL

Task 3. R2R ES recipe and platform development support

Synthesis and characterization of composite cathodes for SSBs based on the fiber electrolytes

Post-mortem analyses were performed on composite cathodes based on Al-LLZO fibers using XPS techniques. The cathodes fabricated from electrospun Al-LLZO fiber scaffolds showed the formation of a more stable cathode-electrolyte-interface (CEI) with higher C-C content and less organic compounds due to the degradation of the electrolyte. Survey XPS data and the percentages of the elements are shown in Figure 47. High resolution XPS data were also acquired and analyzed. These baseline measurements utilized a Gen 2 electrolyte and Li foil for the anode and were performed to evaluate the chemical stability of the composite cathodes with garnet electrolyte additives. Solid state composite electrolytes based on PEO/LiTFSI (3:1 weight ratio) and Al-LLZO fibers were synthesized, and representative SEM images are shown in Figure 48. The Al-LLZO fibers can be clearly seen.

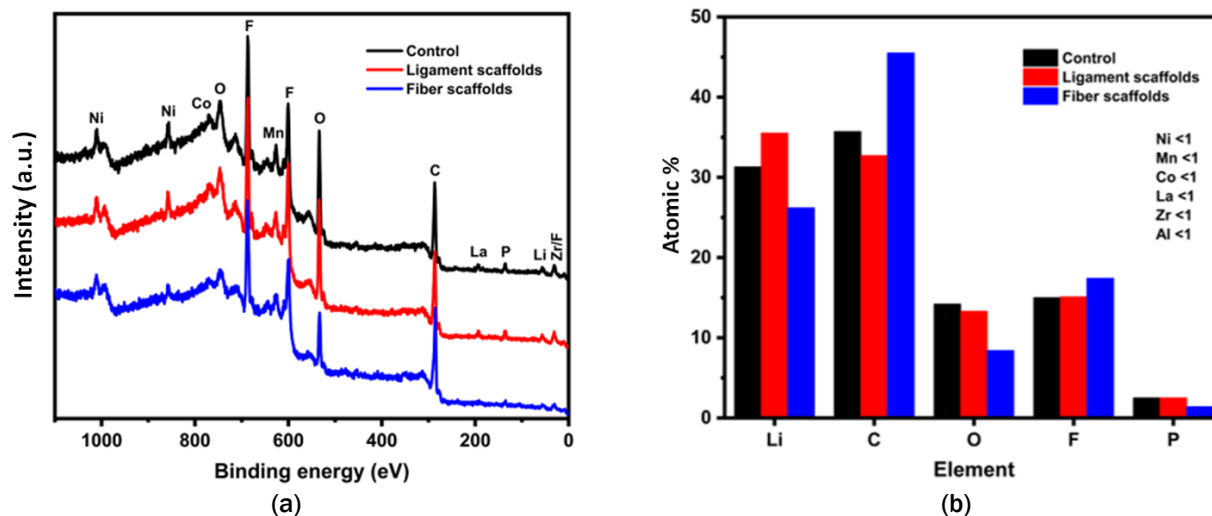


Figure 47. (a) Post-mortem XPS survey spectra of the composite cathodes with and without (control) Al-LLZO scaffold additives. (b) Element atomic percent. Source: ORNL

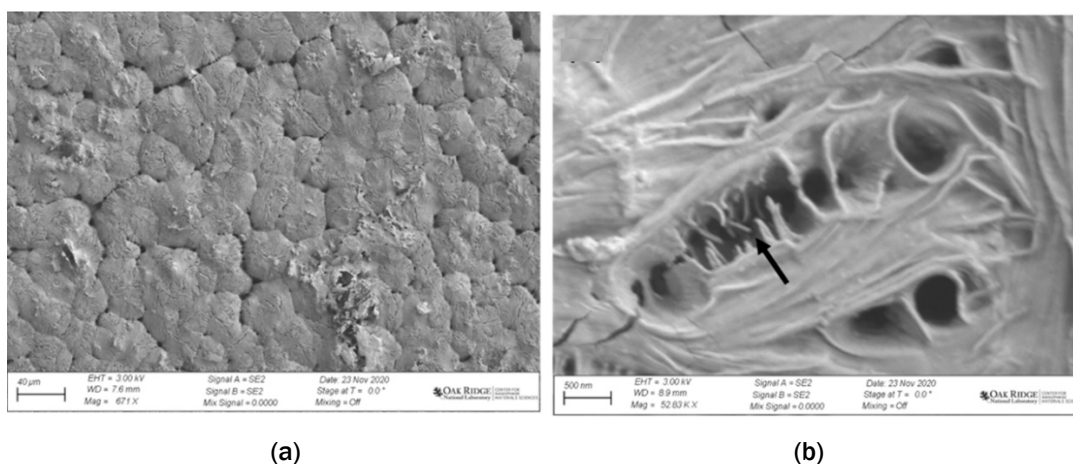


Figure 48. SEM images of solid-state electrolyte based on PEO/LiTFSI and Al-LLZO fibers. (a) The formation of spherulites and (b) Al-LLZO fibers indicated by the arrow. Source: ORNL

An additional post-cycling chemical analysis of the CEI of the composite cathodes was performed using high-resolution XPS measurements, as shown in Figure 49. The cathode filled with Al-LLZO nanofibers showed lower concentration of compounds that are associated with the degradation of the liquid electrolyte such as Li alkyl carbonate, carboxylic and ether groups. The nanostructured Al-LLZO fiber scaffolds tailored the chemical functionalities of the CEI layer (~ 5 nm thick) and resulted in significant improvements in the macroscopic electrochemical properties of the assembled coin cells.

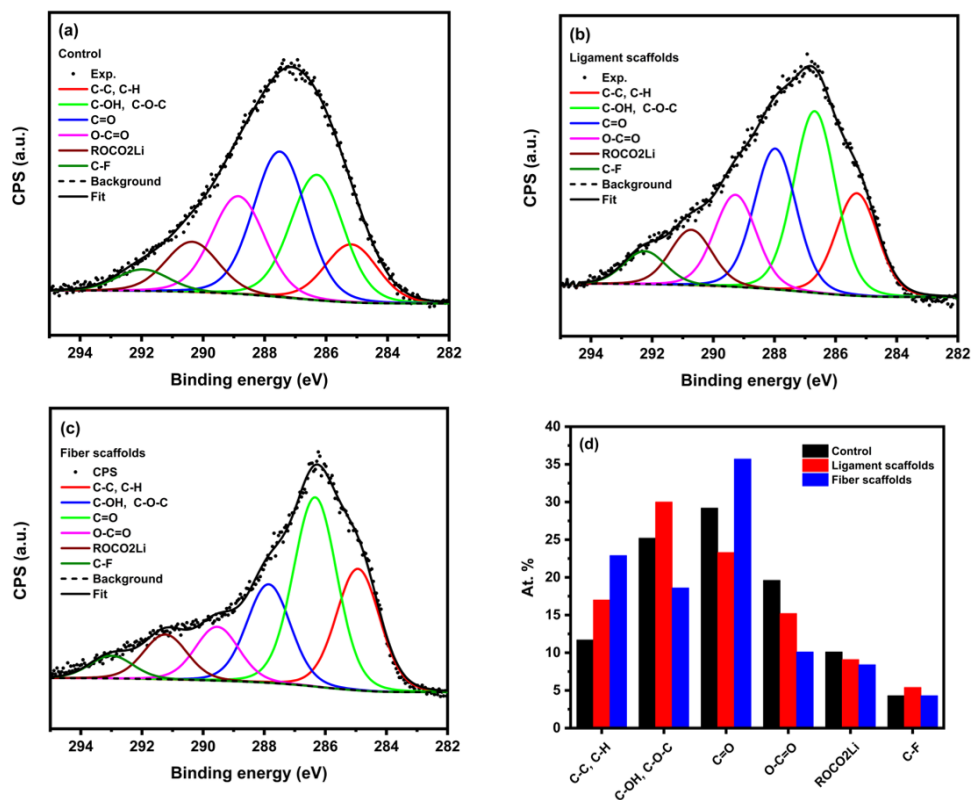


Figure 49. Post-cycling high resolution XPS spectra and peak fit analysis of the composite cathodes (a) control cathode, (b) cathode with ligament scaffold additives and (c) cathode with fiber scaffold additives. (d) summarized plot of the CEI chemical functionalities. Source: ORNL

Composite polymer electrolytes based on PEO (MW 400,000) were fabricated using the Al-LLZO ligament scaffolds. The Al-LLZO scaffolds were dispersed in PEO/LiTFSI (3:1 weight ratio) and the Al-LLZO content was 7 wt.%. Electrical measurements were performed in a broad frequency (10^7 to 10^{-2} Hz) and temperature range (55 °C to 120 °C) using dielectric relaxation spectroscopy. The Arrhenius plot for the conductivity of the PEO/LiTFSI and PEO/LiTFSI/Al-LLZO electrolytes is shown in Figure 50. The composite electrolyte is more conductive than the PEO/LiTFSI electrolyte. At 70 °C, which is the typical operating temperature of the PEO, the conductivity increased from 7.5×10^{-5} S/cm to 2.4×10^{-4} S/cm. The threefold increase was due to the ionically conductive Al-LLZO phase.

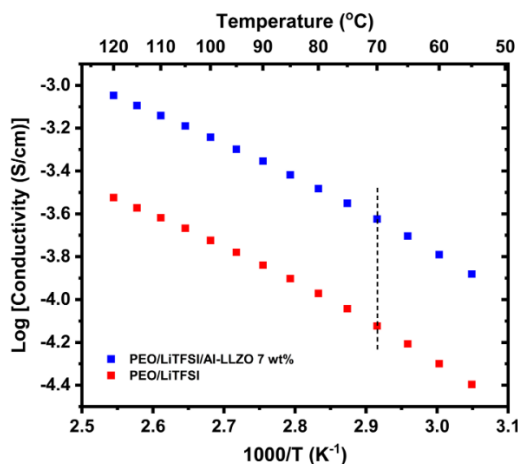


Figure 50. Arrhenius plot for the conductivity of the PEO based electrolytes. Source: ORNL

PEO electrolyte fiber scaffolds can be utilized in flexible electronics. PEO is soluble in water and PEO electrolytes can be electrospun without using hazardous organic solvents. Aqueous formulations are environmentally friendly, less expensive and can reduce manufacturing costs associated with the capture and processing of the organic solvents. For the ES of the fibers, a solution of 9 wt.% PEO in DI water was used. The solution was stirred at 80 °C to dissolve the PEO. The applied voltage was 11 kV, the needle-collector distance was 15 cm, and the feed rate was 0.3 mL/h. SEM images of the electrospun nanofibers are shown in Figure 51 at different magnifications. The fibers are uniform and their diameter ranges from 90 nm to 120 nm.

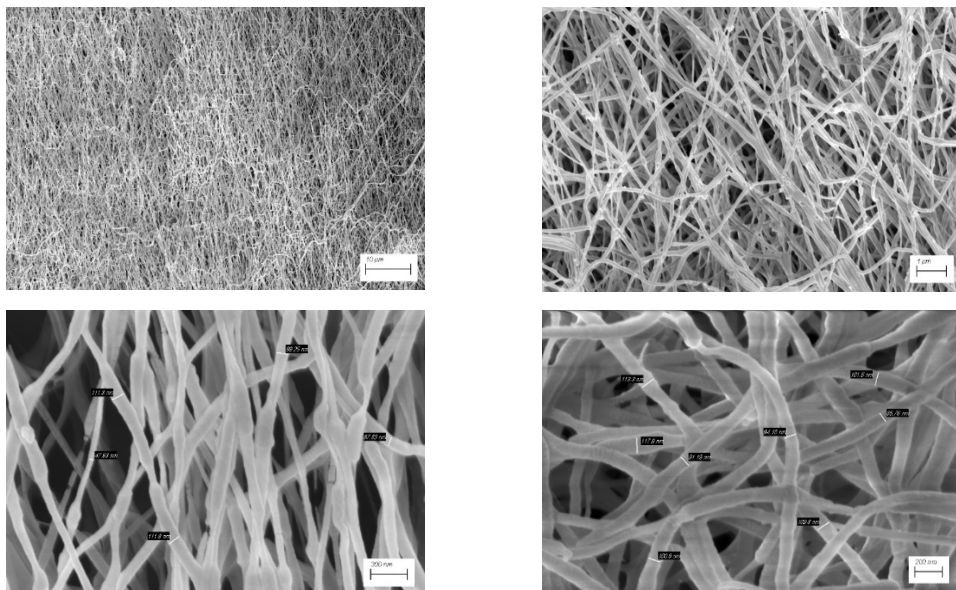


Figure 51. SEM images of the electrospun PEO fiber at different magnifications. Source: ORNL

Electrospun YSZ nanofibers were synthesized using the same processing conditions that were used previously for the synthesis of the LLZO nanofibers. Zirconium acetate and yttrium nitrate precursors were mixed in a 97:3 molar ratio and dissolved in dimethylformamide solvent and acetic acid. SEM images of the electrospun YSZ nanofibers with diameters of 150 nm to 200 nm are shown in Figure 52.

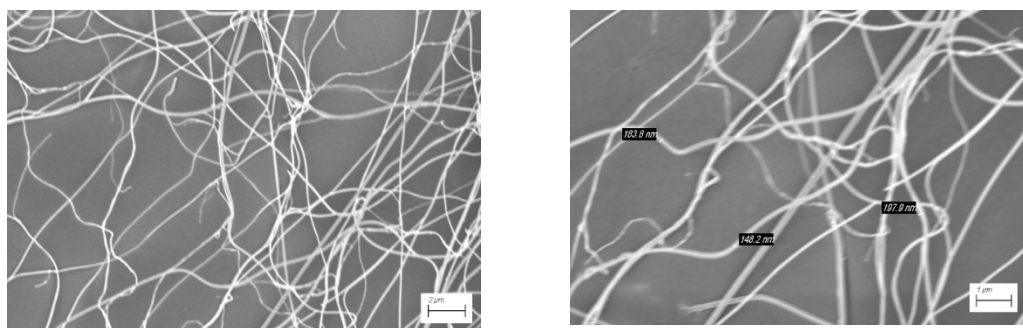


Figure 52. SEM images of the electrospun YSZ nanofibers. Source: ORNL

Education, information dissemination, publications, and technology transfer

Two university graduates were hired to participate in broader ES-related R&D for R2R processing. Results of the ES research resulted in two joint peer-reviewed papers.

Physics and Methodologies for Multilayer Coatings/Deposition; Fabrication and In-Situ Testing of Prototype Components and Devices; and Novel Non-Destructive Evaluation, Quality Control and Metrology (NREL Lead Laboratory)

Task 1. Multilayer coatings for PEMFC and LIBs (including device fabrication and testing, in-line NDE, metrology and defect detection development)

Slide die development

In continuation of FY 2020 efforts to establish a new coating technology capability for the consortium, NREL performed extensive modifications to the die mounting hardware of its R2R coating line, beyond the original design for use of slot dies, due to the larger and heavier slide die, and also because the point of application of the ink from the slide die is much higher in the coating enclosure than that for slot die. Figure 53(a) shows the mounting plates, an extended base plate needed because of the much greater weight of the slide die, and a new and higher quality micrometer mount for control of the die-to-roll gap. Also included in the redesign were components to enable smooth motion and yaw (cross-web die gap angle) control of the heavier die. Figure 53(b) shows the slide die installed on the R2R setup. The new mechanism enables flexibility for the mounting and use of either the slide die or a slot die. These equipment design and operational modifications were made with the intention of installing a vacuum system in the future to support a broader range of stable slide die coating conditions and better enable the coordinated slide die coating modeling and model validation at SNL.

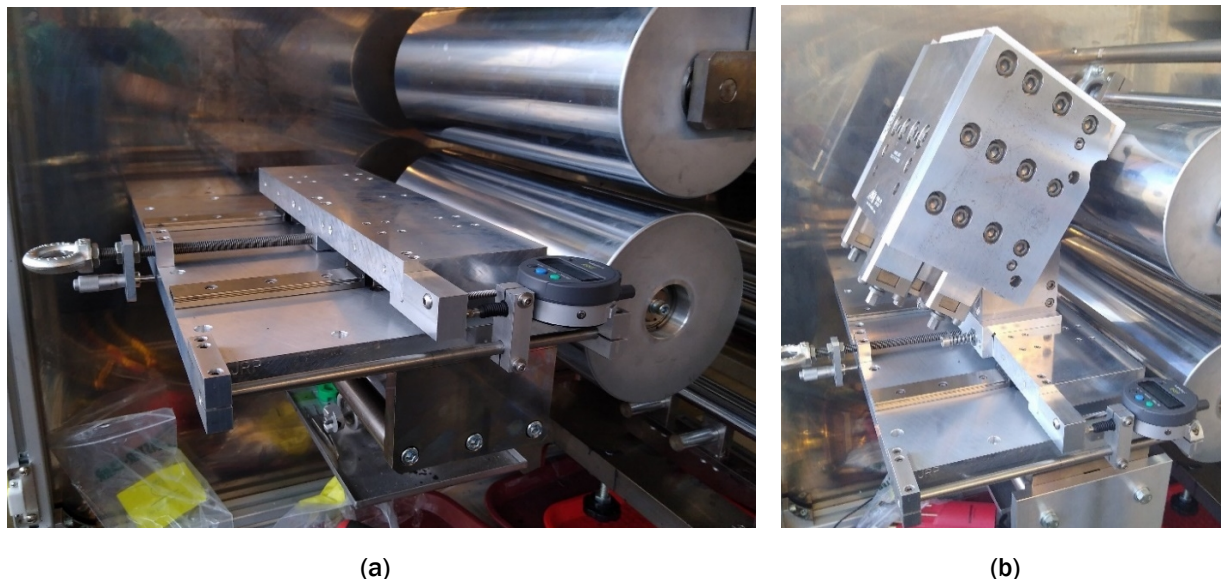
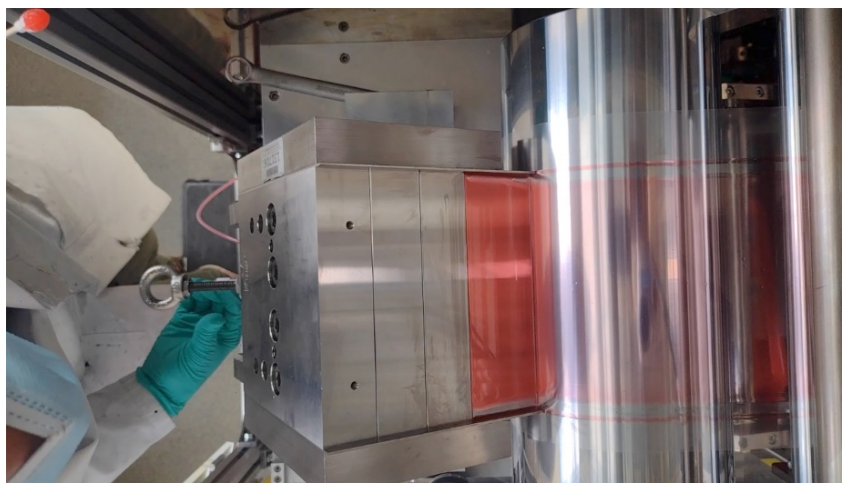


Figure 53. (a) Machined base and mounting plates with gap and yaw control, and (b) the slide die mounted on new hardware. Source: NREL

As a first step toward establishing understandings and a framework for the operation of the multilayer slide die, dyed poly(ethylene oxide) (PEO) inks in water and isopropyl alcohol (IPA) dispersion media were coated using the slide die. These inks had been formulated previously to have viscosities tunable to the PEMFC functional inks. The 2 wt.% polymer solids inks were tested first. While the slide flow appeared fine, the ink was observed to be highly elastic because of the high molecular weight polymer used (even though the viscosity was as desired) and had trouble forming a good bead at the slide lip. These inks were subsequently diluted to 1 wt.% which appeared to work well. Single layer coatings were successfully made, as shown in

Figure 54(a). Dual layer coatings were then successfully made, as shown in Figure 54(b). Die gaps from ~ 45 - $600\ \mu\text{m}$ were tried during the experiment, and all seemed to work fine. All coatings were at 1 m/min line speed.



(a)



(b)

Figure 54. (a) Single layer slide die flow using red-dyed 1 wt.% solids PEO ink and (b) two-layer slide die flow with red layer on bottom and blue layer on top. Source: NREL

The fully commissioned multilayer slide die was set up in a fume hood to do flow testing and stability imaging. Using research reported in the open literature, a set of ink property guidelines were established in collaboration with SNL for the stable multilayer slide coating. A key aspect of this commissioning testing was the verification of these guidelines. Extensive two-layer flow studies were performed using polymer dispersions with red and blue dye. Slurries of PEO at 1 and 2% solids were used as the basis of these inks because prior studies have shown that PEO dispersions can be formulated with viscosity similar to that of the (much more expensive) target Nafion ionomer solutions. A particular focus was on understanding the impact of the relative surface tension and viscosity between the top and bottom flows where the ratio of dispersion media constituents and the solids loading of the polymer, respectively, have been used to adjust these properties. Table VIII shows measured dispersion properties for the experimental bottom (dyed red) and top (dyed blue) layer inks as a function of polymer solids% and the ratio of water and n-propanol in the dispersion

medium. The expected surface tension values as a function of solvent ratio were not observed owing to more of an impact of the dye materials on surface tension than was expected given the low fraction of the dye material in the inks. However, the impact of the ink properties on flow stability were still explored.

Table VIII. Critical Dispersion Properties for Two-layer Slide Die Flow Testing

Flow Test No.	PEO (%)	Bottom (RED)				Top (BLUE)			
		Solvent Ratio (H ₂ O:IPA)	Surface Tension (mN/m)	Density (g/cm ³)	Viscosity (Pa · s) Shear Rate : 119 1/s	Solvent Ratio (H ₂ O:IPA)	Surface Tension (mN/m)	Density (g/cm ³)	Viscosity (Pa · s) Shear Rate : 119 1/s
1	1	75:25	26.6±0.39	0.979±0.002	0.03969	25:75	26.6±0.65	0.867±0.002	0.03053
2	1	75:25	26.6±0.39	0.979±0.002	0.03969	75:25	26.6±0.21	0.988±0.002	0.03951
3	1	25:75	24.5±0.37	0.865±0.006	0.03342	75:25	26.6±0.21	0.988±0.002	0.03951
4	1	90:10	27.3±0.59	0.998±0.002	0.01994	75:25	41.1±0.38	0.971±0.008	0.03405
5	1	25:75	26.8±0.48	0.879±0.003	0.02777	10:90	26.3±0.30	0.847±0.003	0.02020
6	2	75:25	30.6±0.74	0.991±0.008	0.137	25:75	24.6±0.17	0.874±0.003	0.136
7	2	75:25	30.6±0.74	0.991±0.008	0.137	75:25	24.8±0.19	0.869±0.005	0.108
8	2	25:75	23.3±0.57	0.875±0.002	0.127	75:25	24.8±0.19	0.869±0.005	0.108

Figure 55 shows representative flow stability imaging for the 1% solids PEO dispersions. It is seen, in agreement with the literature guidelines, that “top:bottom” property ratios of less than 1 generally lead to more stable flows. Property ratios much greater than one, at least in the case of these inks, clearly lead to unstable flow, with layer mixing evident. Figure 56 shows analogous data for the 2% PEO dispersions. In this case, because of the higher viscosity (which is expected, at least in the range formulated for these experiments, to enable the flows to be less sensitive to the property ratios) and also the effects of the dyes, relative ratios greater than one were not obtainable. Unsurprisingly, all of these flow conditions showed stable flows. The impact of a higher viscosity fluid in the bottom layer, which is expected to be the case for several of the target PEMFC electrode structures, was also explored. Figure 57 shows the results, where even with property ratios slightly above 1, the flows were stable. A final study was performed where the flowrate (thus, layer wet thickness) of the top layer was increased above the flowrate for the bottom layer, up to a factor of 2.5, which will be the case for membrane-electrode two-layer target structures. The flowrate adjustment was done arbitrarily, but no significant impact to flow stability was observed.

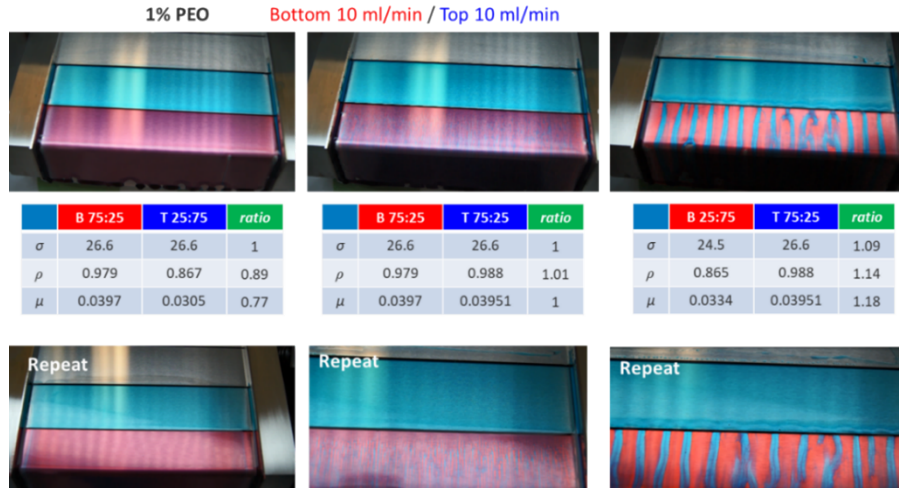


Figure 55. Flow stability imaging of two-layer slide flows of 1% PEO dispersions. Source: NREL

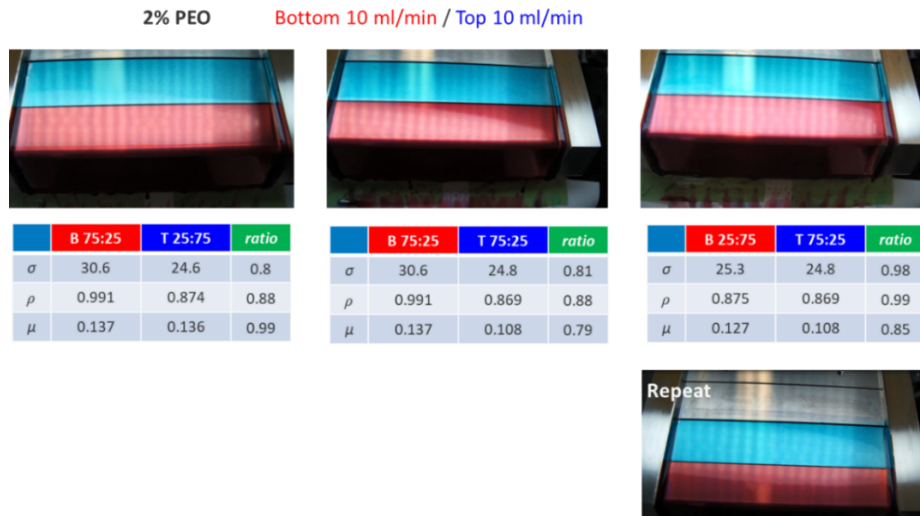


Figure 56. Flow stability imaging of two-layer slide flows of 2% PEO dispersions. Source: NREL

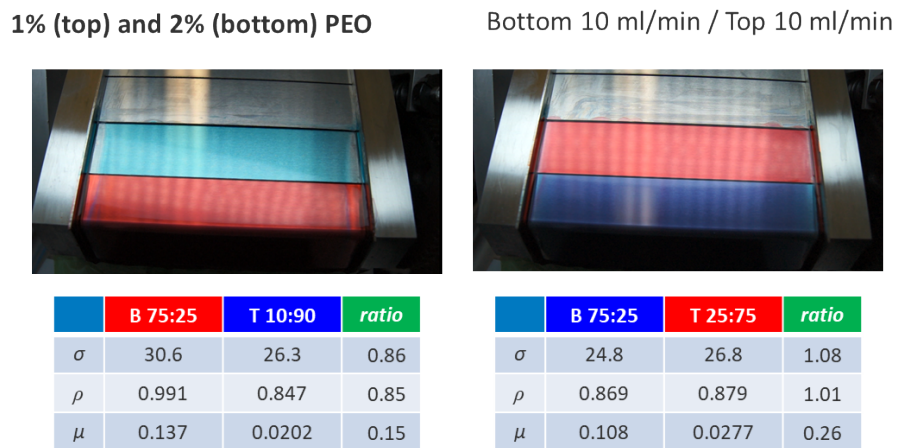


Figure 57. Flow stability imaging with higher viscosity dispersion in the bottom layer. Source: NREL

Subsequent to the preparatory dyed ink experiment, coatings were performed with two different catalyst inks for two-layer electrode coatings. The overall ink formulations were chosen based on a literature study where catalysts with different supports were used in a two-layer structure and provided improved performance under some testing conditions. This study, however, was performed using sequentially spray-coated layers of dilute inks. Thus, the ink solids loadings in this study were modified for the simultaneous coating. The bottom layer was made using a Pt/HSC supported catalyst ink and the top layer was made using a Pt/Vu supported catalyst ink. Both inks were in water/n-propanol solvent mixtures. Upon initial coating of the Pt/HSC ink that was formulated at five catalyst wt.% solids (a standard solids level for slot die coating), the single-layer slide flow was hindered by the high viscosity of the ink. It was difficult to establish a uniform and good quality flow. However, to aid the transition from slide flow to bead flow, both the line speed and ink flowrate were reduced by half. The slide flow was still poor, but a fully coated substrate was established at this condition. The coating looked very non-uniform, with streaks seen in a poor coating. Upon initiation of the top layer of the less-viscous Pt/Vu ink, the slide flow for the top layer appeared to be good, and the top layer did flow over the bottom layer. Figure 58 is an image of the dried two-layer coating showing poor quality due to high viscosity of bottom layer ink. Even with the top coating, the final quality was poor, with streaks and thickness variations. Both flows were then stopped, the slide was cleaned, and just the top layer ink was coated as a single layer. As shown in Figure 59, the less viscous Pt/Vu ink coated very well with good apparent uniformity. This ink was coated at three different flowrates over a factor of two. At the highest flowrate, weeping of the ink was observed onto the incoming uncoated substrate, whereas at the two lower flowrates, no weeping was observed. Overall, the key understanding was that a 5 wt.% Pt/HSC ink is too viscous for good slide flow (despite the fact that it works well for slot die coating), and subsequent runs will use lower solid loadings for this material.



Figure 58. Two-layer slide die electrode coating showing poor quality due to high viscosity of bottom layer ink.
Source: NREL

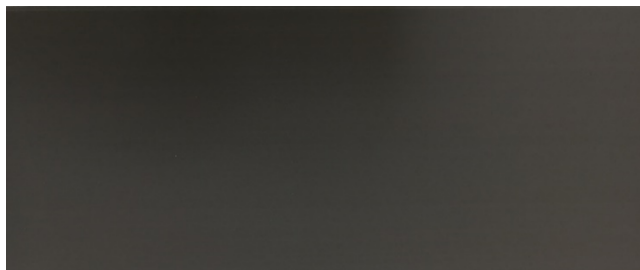


Figure 59. Single-layer slide die electrode coating using lower viscosity Pt/Vu ink showing good quality.
Source: NREL

After completing a successful two-layer slide die coating, additional formulation experiments and rheology measurements were performed to understand the poor slide flow results observed for the 5 wt.% Pt/HSC ink, which had previously coated fine in slot die studies. Figure 60 shows steady shear viscosity of a range of Pt/HSC and HSC-only (just the carbon support) inks as well as the viscosity for the intended second-layer Pt/Vu ink. With the formulation parameters of ionomer to carbon ratio and solvent mixture, results showed that (a) reducing the catalyst solids of the Pt/HSC ink can significantly reduce the viscosity, with the 3.2 wt.% Pt/HSC ink having similar high-shear-rate viscosity as the baseline 5 wt.% Pt/Vu ink, and (b) the range of rheology of all catalyst inks was spanned by the 4 wt.% and 5 wt.% HSC-only inks. The latter is useful relative to formulation of dummy inks for more detailed process-window experiments where the use of the very expensive catalyst is undesirable. The lack of major behavioral differences in rheology between these inks motivated further exploration of the complex rheological behavior of the inks. As shown in Figure 61, plotting the oscillatory shear data as a function of stress (instead of strain rate) indicates that the 5 wt.% Pt/HSC ink does yield at a significantly higher stress than the lower solids inks, in particular those at 3.2 wt.% and 4 wt.%.

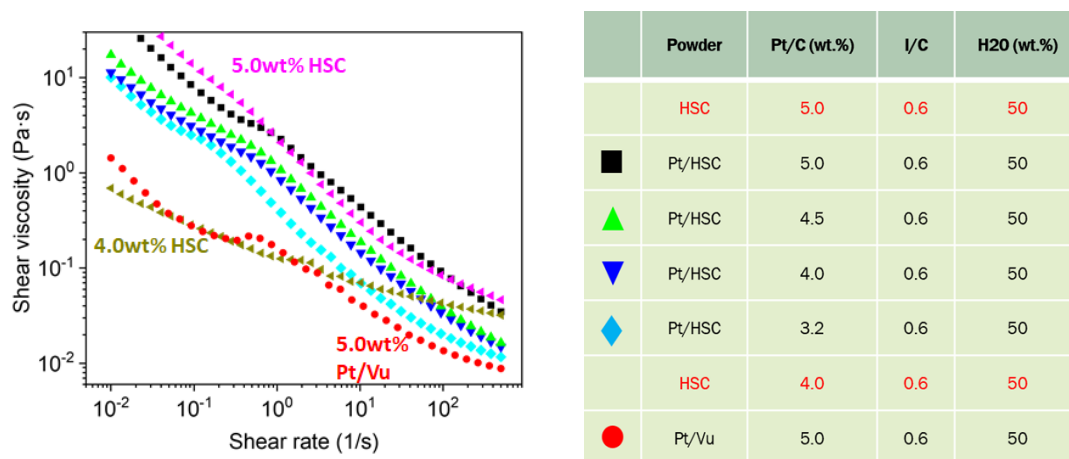


Figure 60. Rheology and formulations of Pt/HSC and HSC-only inks. Source: NREL

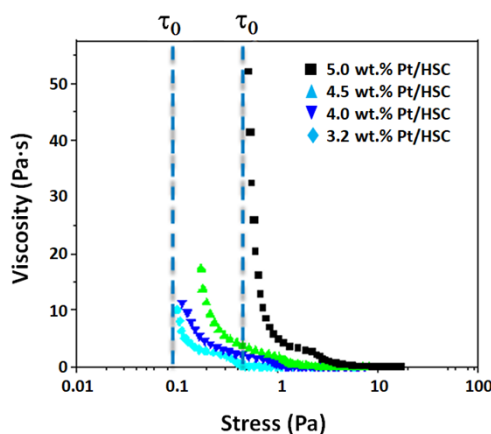
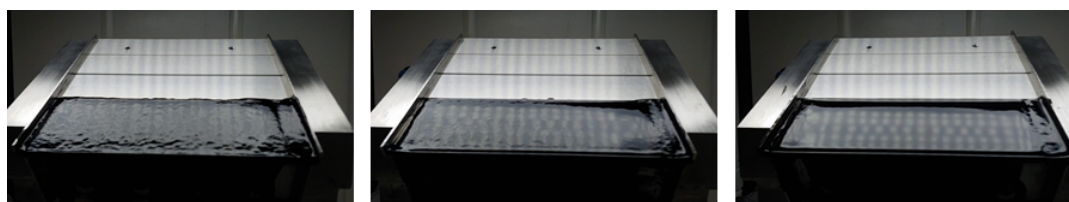


Figure 61. Yield stress assessment of the Pt/HSC inks. Source: NREL

Based on this information, single-layer slide flow experiments were performed to understand the implications of the rheological behavior. Figure 62 shows the slide flow of 3.2, 4, and 5 wt.% Pt/HSC inks at a pumping rate through the manifold of 7.5 mL/min. Again, an instability (“lumpiness”) was observed in the 5 wt.% ink. The 4 wt.% ink appeared more stable, but not fully. The 3.2 wt.% ink had a very clean/smooth stable appearance. These results appear to validate the results from the rheology measurements where the 3.2 wt.%

ink flows on the slide similar to the 5 wt.% Pt/Vu ink. Figure 63 shows slide flows for the 3.2 wt.% ink at four flowrates. The flow appears stable at all rates, though perhaps slightly less so at the lowest flowrate, i.e., where the shear rate on the slide is highest. Figure 64 shows the slide flows for the 4 wt.% ink at three flowrates. At the lowest flowrate, instability is observed, whereas at the highest flowrate, the flow appears fairly stable.

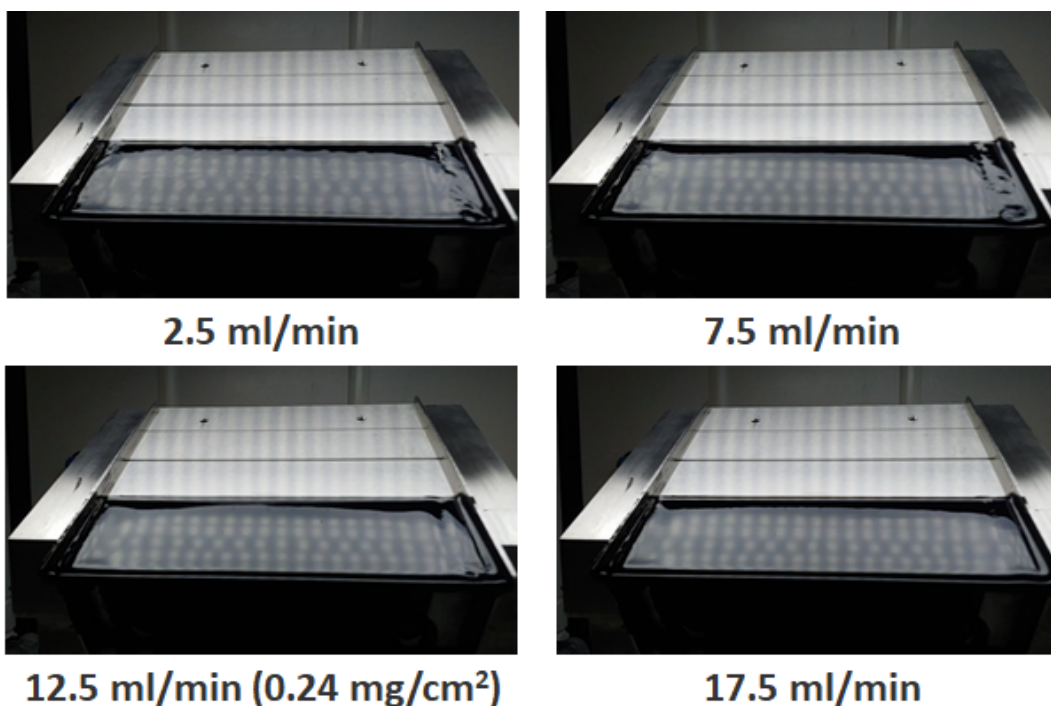


5.0wt% Pt/HSC

4.0wt% Pt/HSC

3.2wt% Pt/HSC

Figure 62. Slide flow at 7.5 mL/min as a function of catalyst solids. Source: NREL



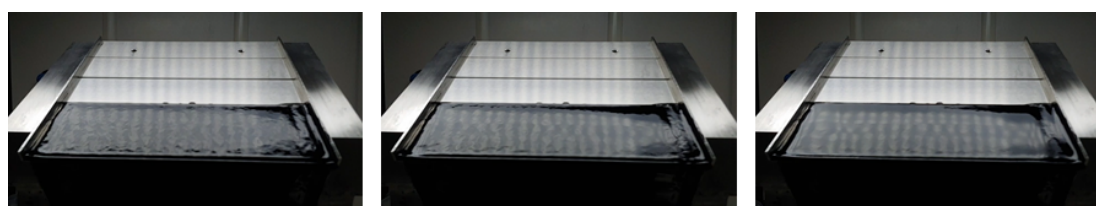
2.5 ml/min

7.5 ml/min

12.5 ml/min (0.24 mg/cm²)

17.5 ml/min

Figure 63. Slide flow for 3.2 wt.% ink at four flowrates. Source: NREL



2.5 ml/min

7.5 ml/min

12.5 ml/min

Figure 64. Slide flow for 4 wt.% ink at three flowrates. Source: NREL

In-line spectroscopic method development

The target structure for a spectroscopic in-line measurement technique is a heterogeneous, generally opaque active layer on a polymer layer, which is a structure that is highly relevant to all of the studies of coating electrochemical energy storage and generation materials. For this study, catalyst-coated membrane samples (with membranes and active layers (electrodes) relevant to fuel cells and electrolyzers) having a range of membrane and active layer thickness were used. Long-wavelength IR spectroscopy was used in this work based on previous work that generally showed increasing energy transmission at higher wavelengths. All measurements were taken incident on the active layer (when present), to simulate a two- or multilayer structure with the membrane on the 'inside' of the structure.

Figure 65 shows IR spectroscopy for three samples (two measurements each): (1) a 25 μm thick membrane, (2) the same 25 μm membrane with a thin active layer, and (3) a 125 μm membrane with an active layer of similar thickness. As an example, at 4.5 μm wavelength, the three samples can be strongly differentiated. Figure 66 shows transmission spectroscopy for membranes of three different thickness (two measurements each). Again, at 4.5 μm wavelength, the different membranes are strongly differentiable, with the difference in transmission (on a logarithmic scale) appearing to be linear with thickness (75 and 100 μm points added without measurement to show the expected trend). Figure 67 shows that the differences in the active layer thickness is also differentiable for samples with 25 μm membranes and three different active layer thicknesses (1x, 2x, 3x). Other wavelength ranges were identified that appeared to provide differentiated signals, for example as shown in Figure 68 at 17 μm wavelength, for 50- μm thick membrane samples with and without a thick active layer, and a 175- μm thick membrane sample with a similarly thick active layer.

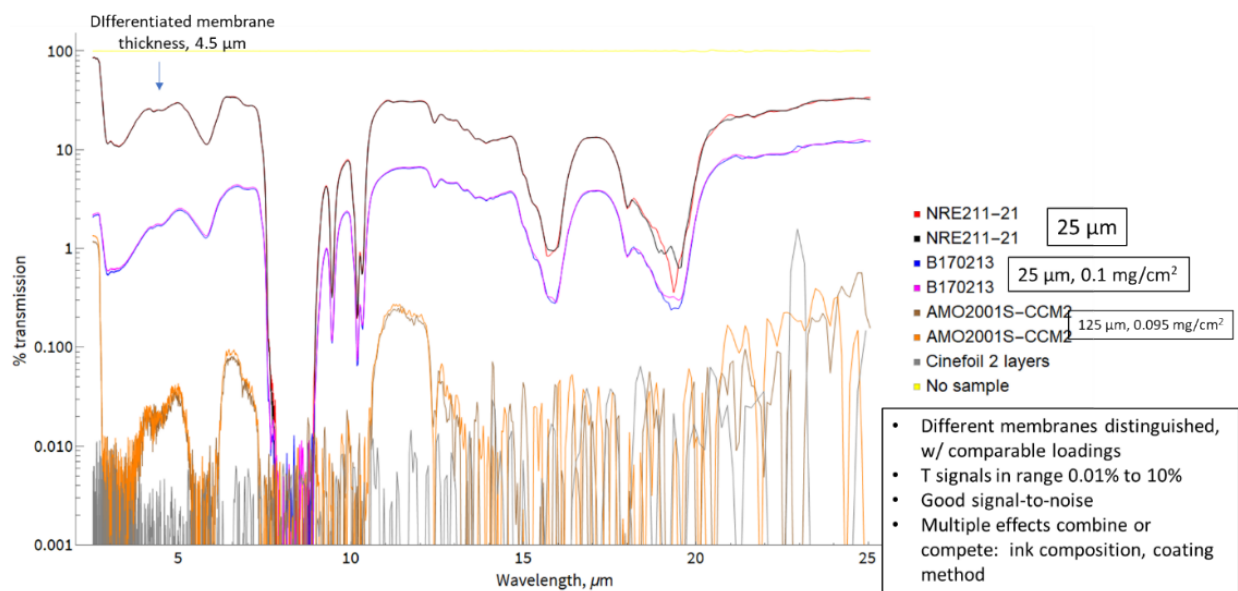


Figure 65. IR transmission spectra for 25- μm and 125- μm thick membrane samples with two having a thin active layer. Source: NREL

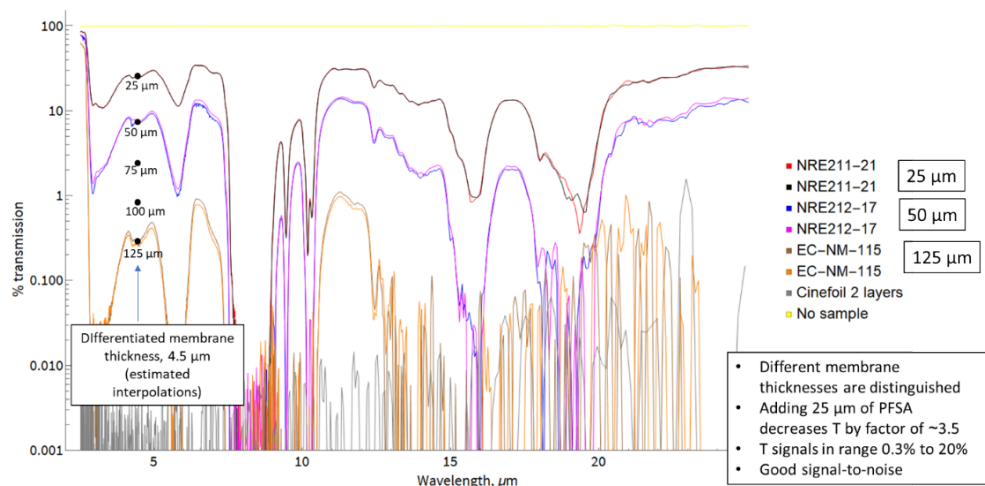


Figure 66. IR transmission spectra for uncoated membrane samples of different thickness. Source: NREL

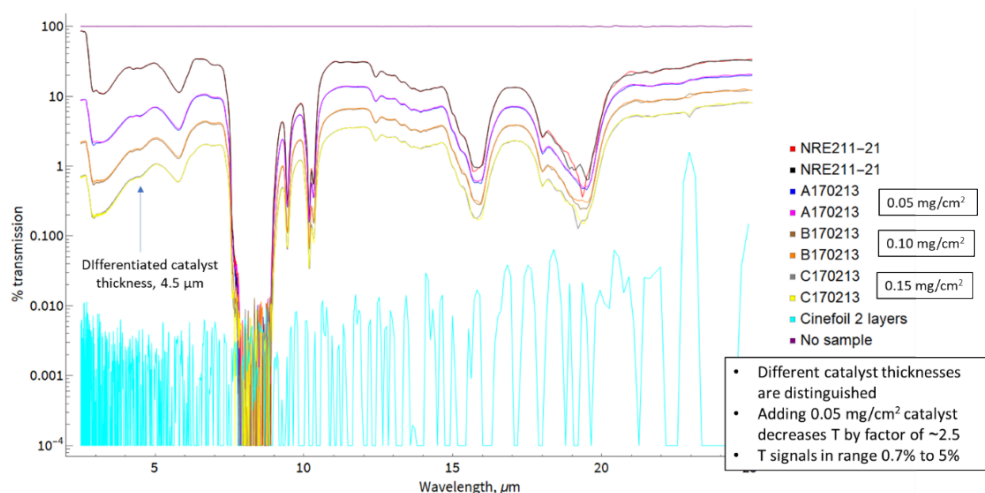


Figure 67. IR transmission spectra for 25-μm thick membrane samples with no active layer and with three different active layer thicknesses. Source: NREL

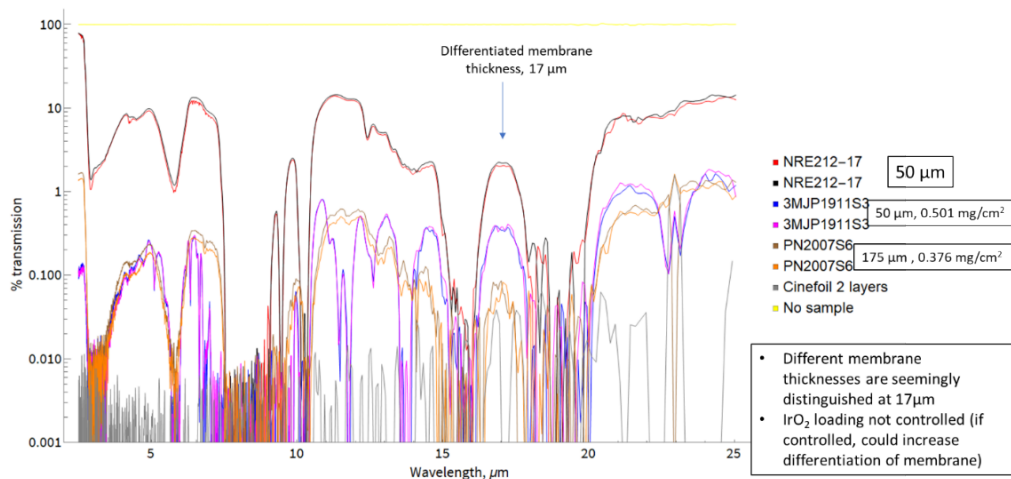


Figure 68. IR transmission spectra showing sensitivity to membrane thickness and active layer at 17 μm. Source: NREL

A processing algorithm was then pursued that could potentially simultaneously measure both membrane and electrode thicknesses utilizing data at multiple wavelengths in the spectra. As shown in Figure 69, agreement between the algorithm (“model”) and the electrode loading as measured by XRF was good except for at the highest loading. Transmission as a function of loading is expected to be exponential, so the lack of agreement at the highest loading is not surprising, and modification of the algorithm at high loading should be possible to improve agreement. Figure 70 shows good agreement of the algorithm with membrane thickness. Overall, a method was demonstrated to simultaneously measure membrane and electrode thickness in a half-CCM using benchtop methods. A record of invention was filed on this method. More work is needed to further refine the algorithm and begin to explore equipment and configurations that could enable an analogous in-line measurement.

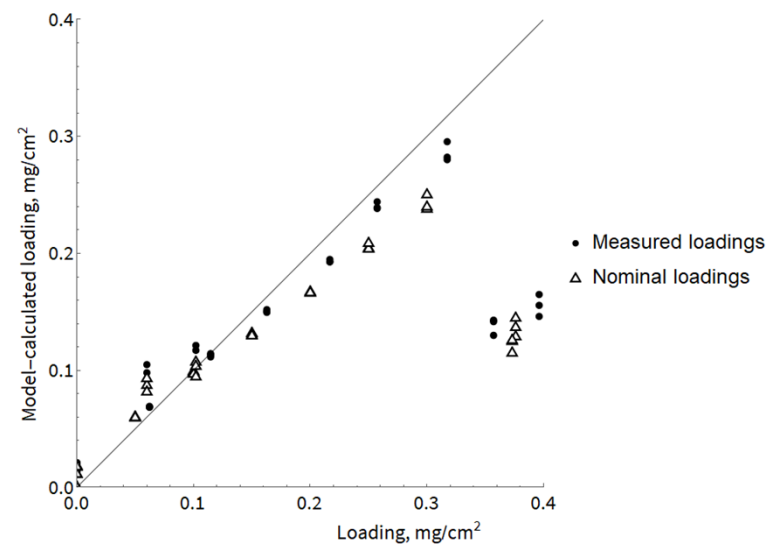


Figure 69. Agreement between algorithm and actual half-CCM electrode loadings by FTIR method. Source: NREL

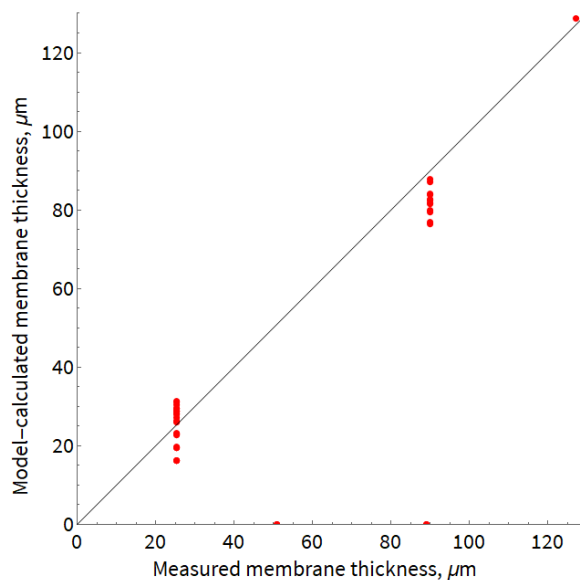


Figure 70. Agreement between algorithm and actual half-CCM membrane thickness by FTIR method. Source: NREL



Task 2. Formulation chemistry for multilayer architectures

Mixing studies

A study of mixing method and time for heterogeneous catalyst inks was conducted in collaboration with ORNL. The previous work, which was mainly focused on ball milling, was extended to high shear mixing using several Turrax (brand) mixer types and mixing heads. NREL's focus was on the standard Turrax mixing device as well as a smaller Turrax device, called a 'Tube Drive' that is designed for smaller volumes. Figure 71 provides an overview of the mixing study including both NREL and ORNL activities showing batch sizes, mixing speeds and times, and methods and devices used.

NREL			
Geometry	Batch size (g)	Mixing Speed (rpm)	Mixing Time (min)
18 G	30	10 (<i>order of add.</i>)	10 – 30 min
	80	6	1 – 30
		10	1 – 30
	110	10 (<i>order of add.</i>)	15 – 30 min
		10	25 – 300
		15	1 – 30
		20	1 – 30

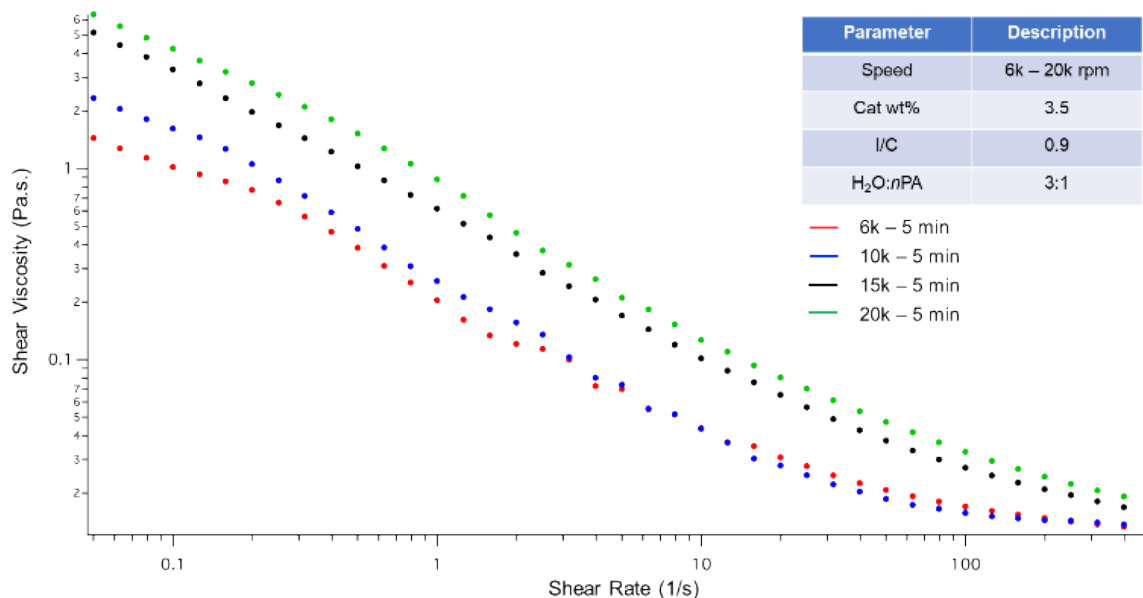
NREL			
Mixing Tool	Batch size (g)	Mixing Speed	Mixing Time
Ball Mill	30	20 units	1 h – 72 h
Tube Drive	10	6k rpm	5 – 15 min

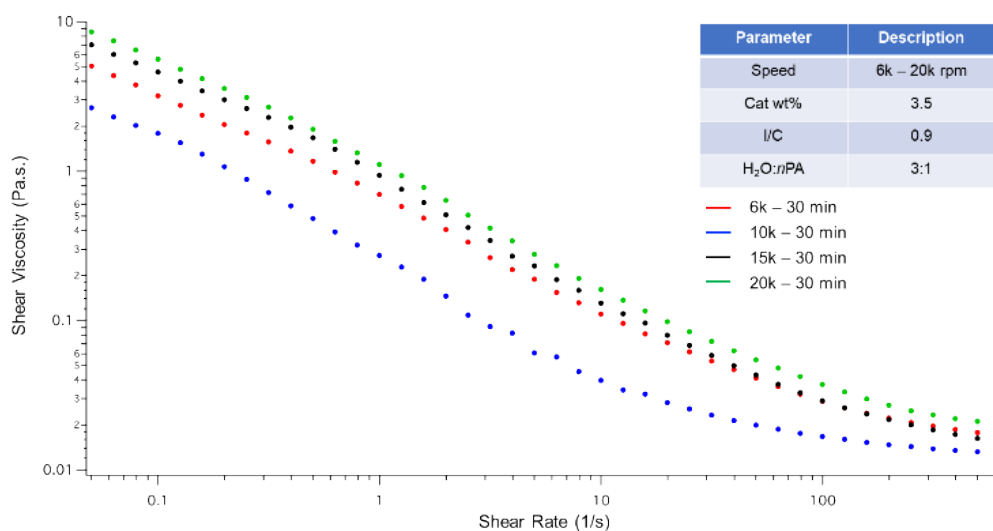
ORNL			
Geometry	Batch size (g)	Mixing Speed (rpm)	Mixing Time (min)
18 G	110	10	1 – 30
25 F		16.6	1 – 30

Figure 71. Overview of mixing study. Source: NREL

Figure 72(a-b) shows a comparison of the shear viscosity of inks mixed at various speeds for 5 and 30 minutes. The difference in viscosity with mixing time did not appear significant, but there was a significant trend with mixing speed where higher speed increased viscosity. Interpretation of this data is that there is more breakup of large agglomerates at the higher mixing speeds leading to more secondary (smaller) agglomerates (also referred to as 'flocs') that are lower density and thus have a higher volume fraction which leads to higher viscosity. However, further characterization, e.g., USAXS or a similar technique to directly measure particle size in the ink, will be required to better understand this trend. The resulting ink properties were then assessed as to the impact on coating morphology over the same range of mixing speed and time.



(a)



(b)

Figure 72. Rheology comparison of inks mixed with a Turrax 18G head over a range of mixing speeds at (a) 5 and (b) 30 minutes of mixing time. Source: NREL

As shown in Figure 73, for the example of 30 minutes mixing time, increased mixing speed appears to generally lead to coatings with less and smaller observable catalyst clusters or agglomerates, which would be expected (and which appears to be consistent with interpretation of the rheology data). Figure 74 shows comparisons of coatings made with the same ink and compares ball milling to Turrax mixing at two different mixing times. Because of the great differences in the mechanisms of these two methods, the energy input to the ink at a given mixing time could be very different. Nevertheless, for both mixing times, the ball milled coating appears to have more micro-scale roughness, but possibly a lower number of large agglomerates. Figure 75

shows the comparison between the standard Turrax device and the Turrax Tube Drive for the same mixing time and speed. The exact geometry of the Tube Drive mixing head is not known, but it is suspected that it has a smaller characteristic gap between the rotor and stator, leading to greater agglomerate breakup (at least at the speed – which is the highest speed possible for the Tube Drive – and mixing time used). This indicates the criticality in understanding critical dimensions of the mixing devices relative to the measured or expected agglomerate sizes in the inks.

Parameter	Description
Speed	6k – 20k rpm
Substrate	H23C8
Rod Size	30
Drying T	80 °C
Magnification	500x

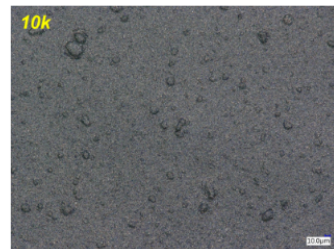
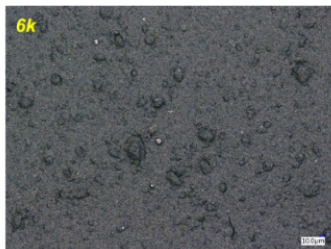
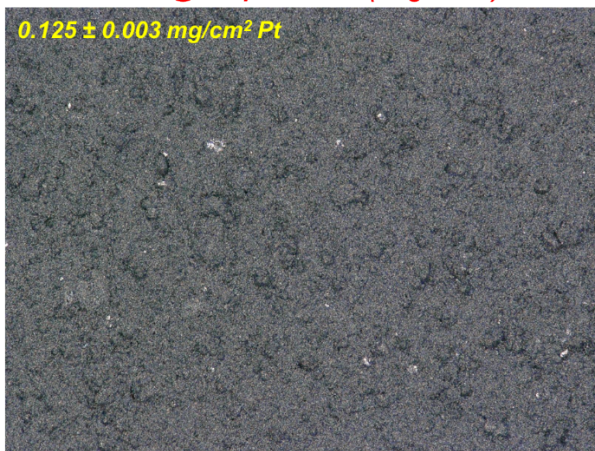


Figure 73. Optical microscopy of coated catalyst ink mixed for 30 minutes at different RPMs with Turrax mixer/18G head. Source: NREL

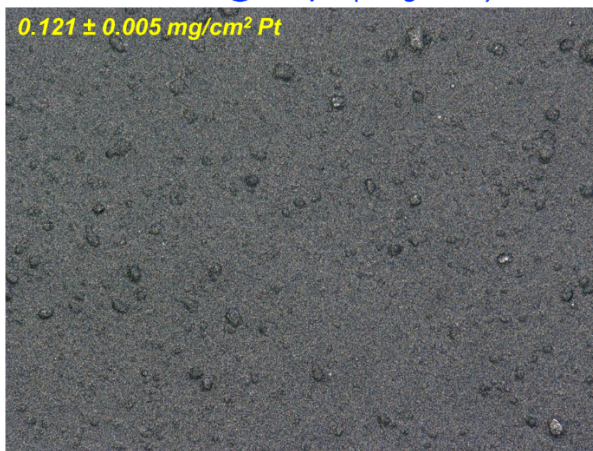
Ball Mill – 1 h @ 20 speed units (30 g batch)

0.125 ± 0.003 mg/cm² Pt



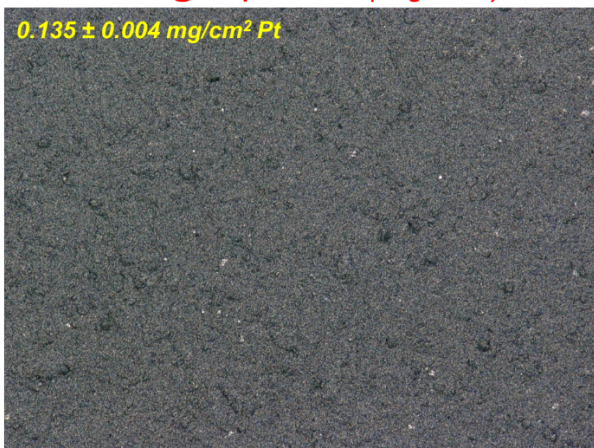
Ultra-Turrax® – 1 h @ 10k rpm (110 g batch)

0.121 ± 0.005 mg/cm² Pt



Ball Mill – 5 h @ 20 speed units (30 g batch)

$0.135 \pm 0.004 \text{ mg/cm}^2 \text{ Pt}$



Ultra-Turrax® – 5 h @ 10k rpm (110 g batch)

$0.123 \pm 0.020 \text{ mg/cm}^2 \text{ Pt}$

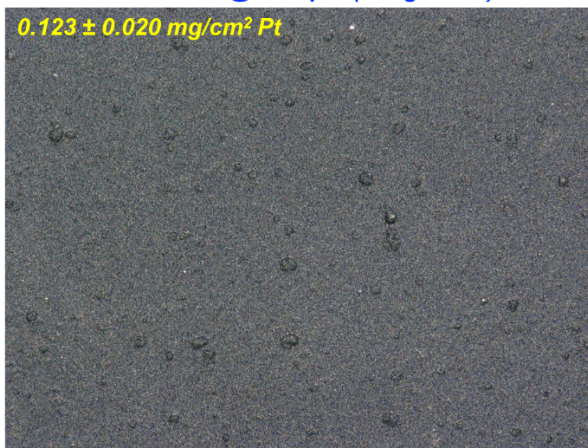
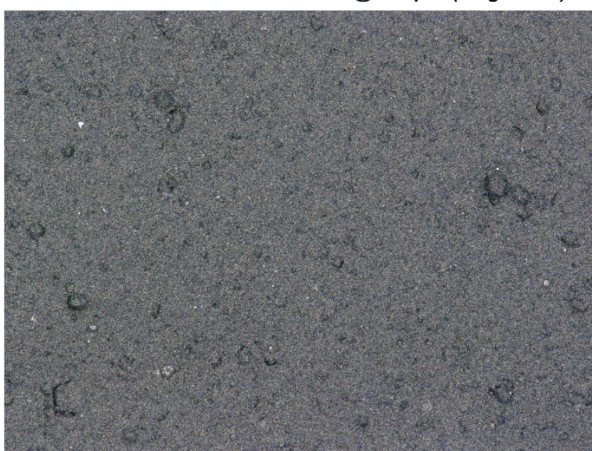


Figure 74. Comparison of ball milled and Turrax mixed coatings after 1 (top) and 5 (bottom) hours of mixing. Source: NREL

Ultra-Turrax® Tube Drive – 15 min @ 6k rpm (10 g batch)



Ultra-Turrax® – 15 min @ 6k rpm (110 g batch)

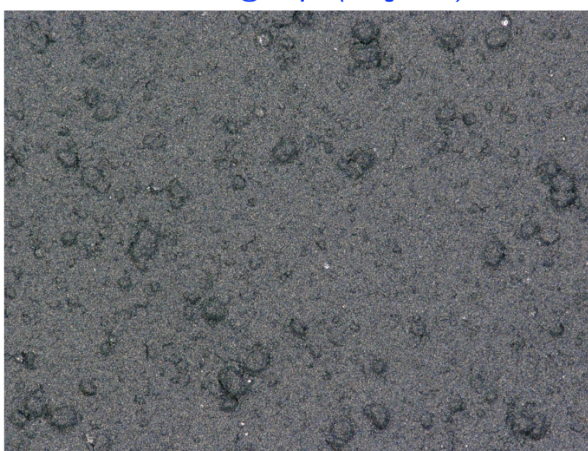


Figure 75. Comparison of Turrax Tube Drive and standard Turrax mixed coatings, both at 6k RPM, after 15 minutes of mixing. Source: NREL

During attempts to baseline the standard Turrax with the 18G head used by both NREL and ORNL, the ORNL coatings appeared to have larger agglomerates based on mixing time. This can be seen in the top and bottom rows of images in Figure 76. Upon further investigation, it was found that the two labs were using slightly different mixing orders for the ink constituents, where, after combining the catalyst particles with water, NREL added the ionomer and then the nPA, whereas ORNL added the nPA and then the ionomer. As a follow-up, NREL formulated the ink using ORNL's mixing order and made coatings, as shown in the middle row of Figure 76. The number of agglomerates appeared to slightly increase using the ORNL mixing order although the agglomerate sizes still appeared to be different. This result shows the criticality of mixing order, especially in the case of a system where the particle, polymer, and dispersion media are all highly interacting, and in fact can have different interactions as a function of their relative concentration. Figure 77 shows the rheology data for the cases of the two mixing orders at different mixing times. In general, the nPA-first mixing order led to slightly higher viscosity, which likely is consistent with the microscopy in Figure 76 with both inks having significant agglomeration, but the nPA-first ink having slightly larger agglomerates.

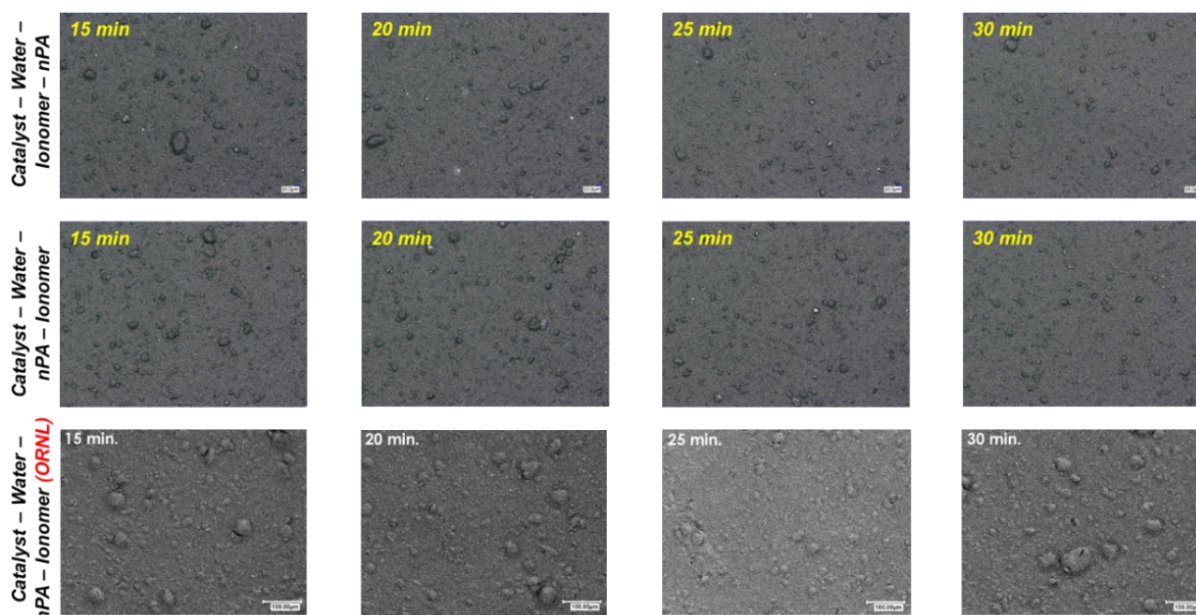


Figure 76. Order of mixing analysis with standard Turrax 18G head showing the NREL standard mixing order (top), the NREL comparative case to match ORNL mixing order (middle), and the ORNL mixing order (bottom).
Source: NREL

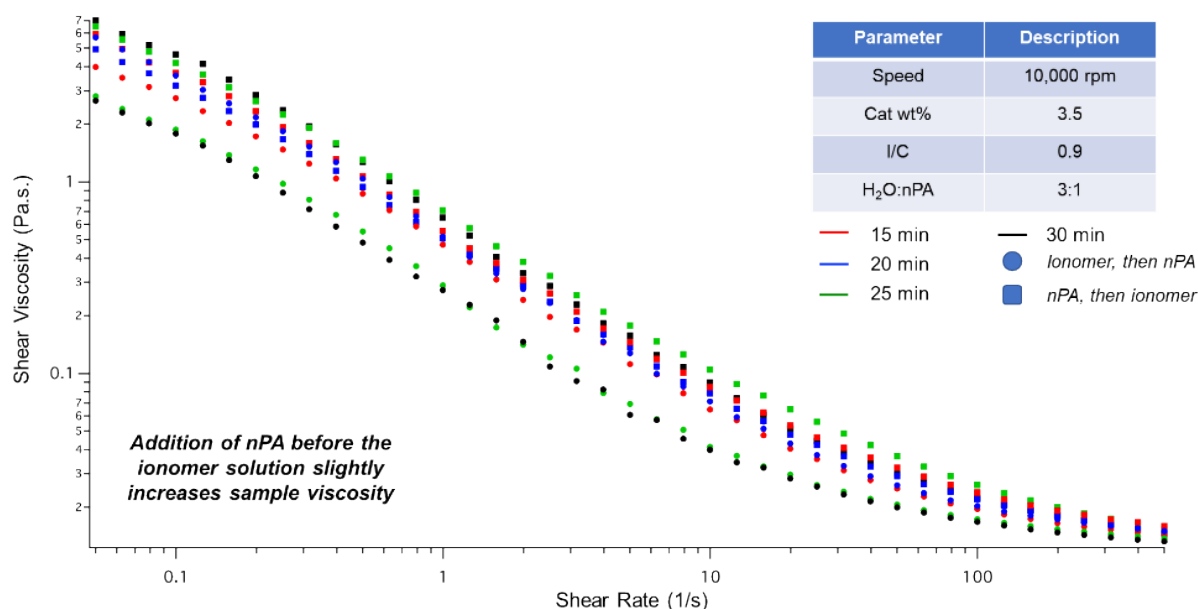


Figure 77. Rheology comparison of Turrax mixed inks, at several mixing times, using the two different mixing orders. Source: NREL

Optical microscopy images taken at NREL of the electrodes coated with these different inks were used for image analysis by ORNL to generate surface particle size distribution data. NREL supported the development of this methodology and data generation. Additionally, the resulting viscosity of inks mixed with different methods and for different durations were further explored. Figure 78 shows shear viscosity at a shear rate of 1/s for four different cases. All are qualitatively similar in that a plateau in the amount of agglomerate breakup is reached after a couple tens of minutes.

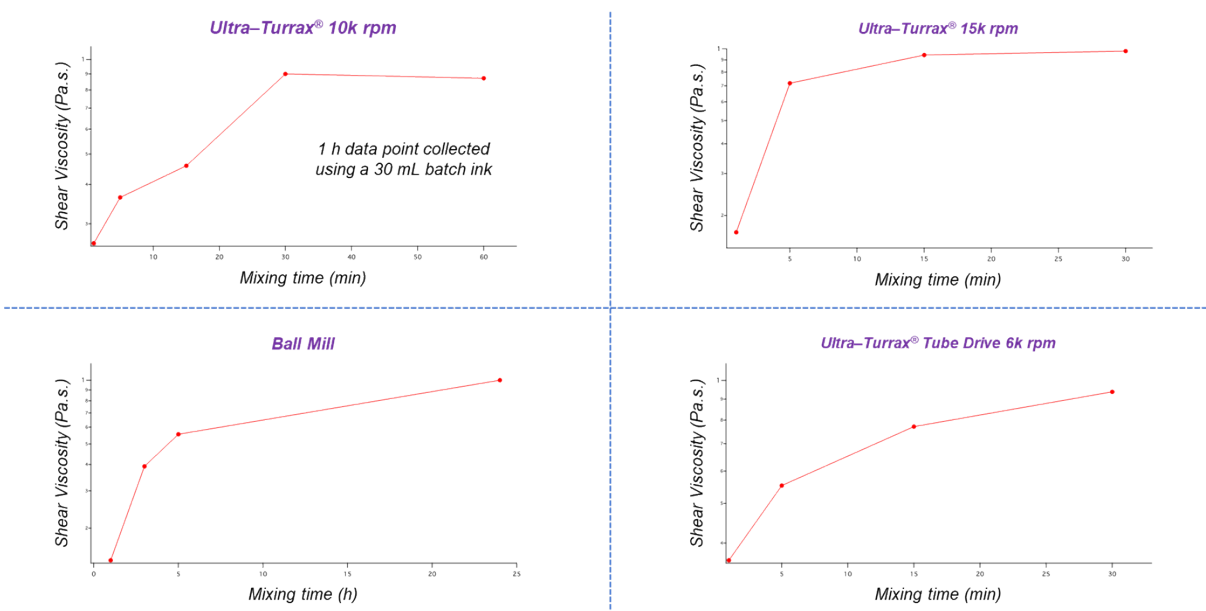


Figure 78. Shear viscosity at 1 /s for four mixing cases. Source: NREL

Task 3. Electrospinning scale-up

NREL continued the exploration of the behaviors of ES slurries with PAA as the carrier polymer, in particular with focus on two topics that had not been previously explored: (1) the impact of ES process conditions at the same PAA concentration, and (2) the impact of the ratio of water and IPA in the dispersion media. For the first topic, a previously used slurry formulation was found to form large diameter fibers, but the slurry also included a large fraction of fibers that were not completely dried and were partially liquid in the captured sample. The experimental conditions were that the slurry was composed of 3.44 wt.% PAA, a 50:50 mixture of water and IPA, a needle to drum distance of 10 cm, and 35% relative humidity in the spinning chamber. The fibers resulting from the original conditions are shown Figure 79(a). Figure 79(b) shows the case where the flowrate was reduced from 0.5 to 0.2 mL/h, leading to less of the not completely dried fibers. Figure 79(c) shows the case where the excitation voltage was decreased from 15 to 7.5 kV that led to good thin fibers with very little incompletely dried content. Much of the literature for ES implies that voltage generally has very little impact on fiber quality (it is rather seen as a binary – you either have a high enough voltage for good fiber formation or not). Clearly this was not the case here, where fibers formed in all cases, however, the voltage impacted the quality. For the second topic, the ratio of water and IPA was varied in the dispersion media. As shown in Figure 80, increasing the IPA content leads to more uniform fiber formation. Also, at the lower PAA concentration, fiber formation is more sensitive to the dispersion media ratio. However, interestingly, Figure 81 shows that it is the intermediate level of IPA that leads to the largest fiber diameters, perhaps because that slurry has slightly higher viscosity.

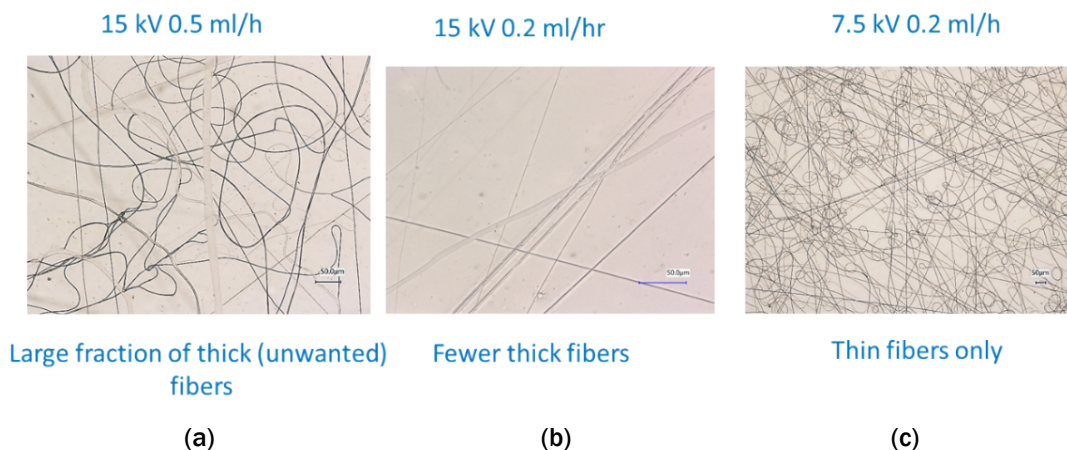


Figure 79. PAA fiber formation as a function of excitation voltage and slurry flowrate. Source: NREL

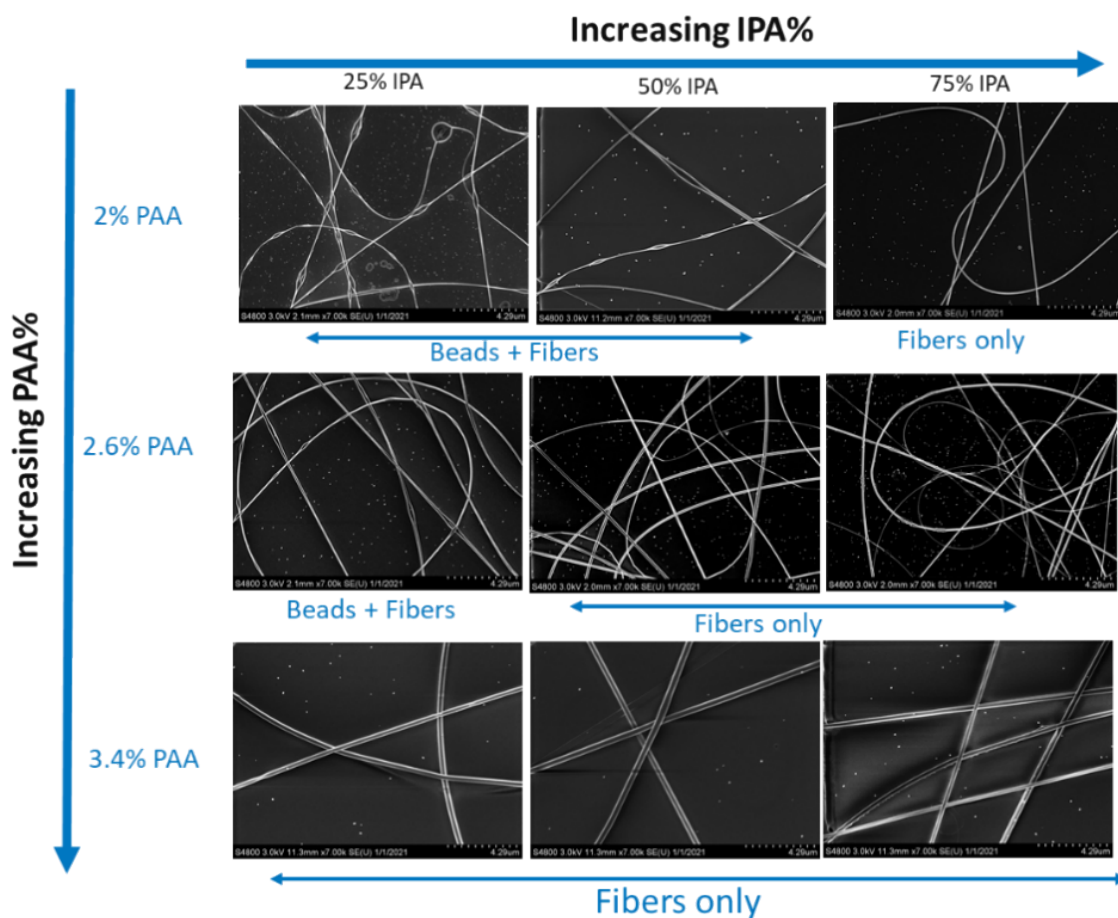
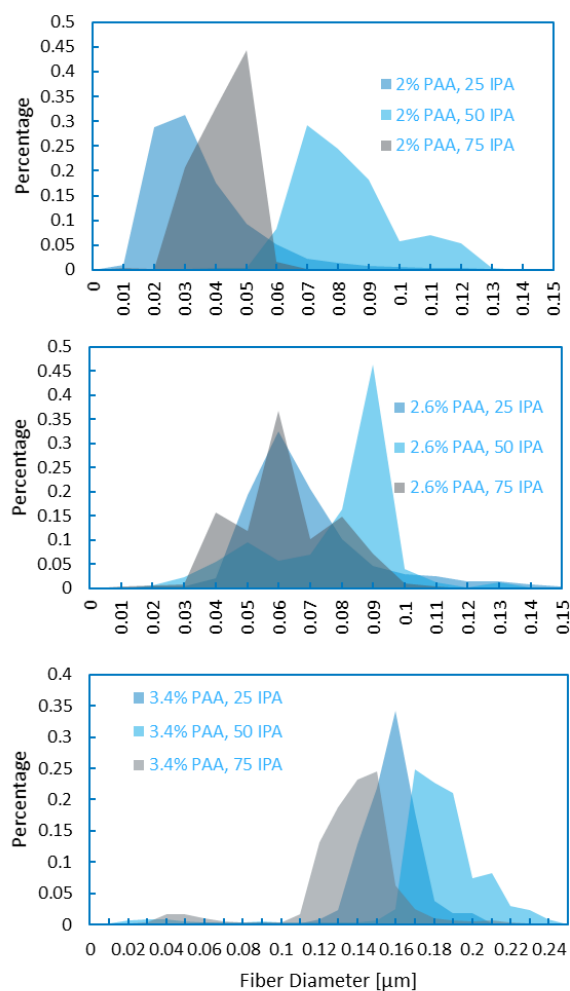
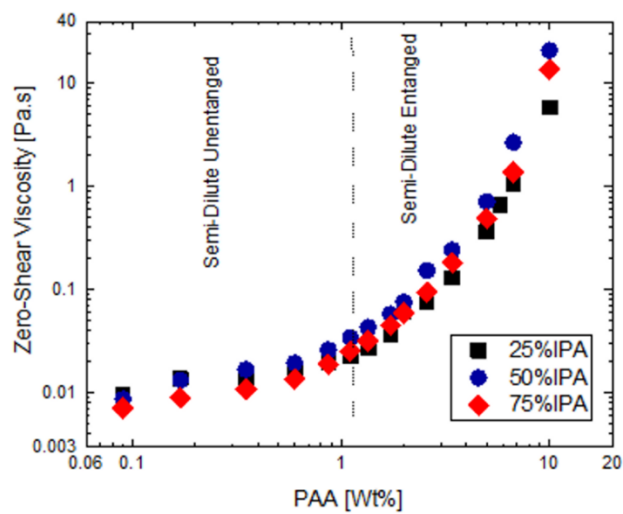


Figure 80. PAA fiber formation as a function of PAA concentration and IPA content. Source: NREL



(a)



(b)

Figure 81. (a) Fiber diameter distribution and (b) rheology as a function of PAA concentration and IPA content. Source: NREL

Additional extensional rheology results related to the PAA-carrier-polymer study were obtained from the University of Massachusetts, Amherst. Of particular interest were slurries of PAA with different mixtures of water and IPA. Steady shear rheology trends did not match the trends observed in the quality of fiber formation as a function of the water:IPA ratio. Good fiber formation was observed to occur at higher fractions of IPA, whereas the shear viscosity trend was non-monotonic. However, relaxation time data from the extensional rheology measurements, as shown in Figure 82, resulted in a monotonic increase with IPA fraction that matched to the observed fiber formation trend. The lack of agreement between shear and extensional rheology appears to indicate that the agglomeration of the PAA (indicated by shear viscosity) is not impacting spinnability; rather, it is the elongational properties of the slurry as a function of IPA fraction (indicated by extensional rheology) that is driving spinnability.

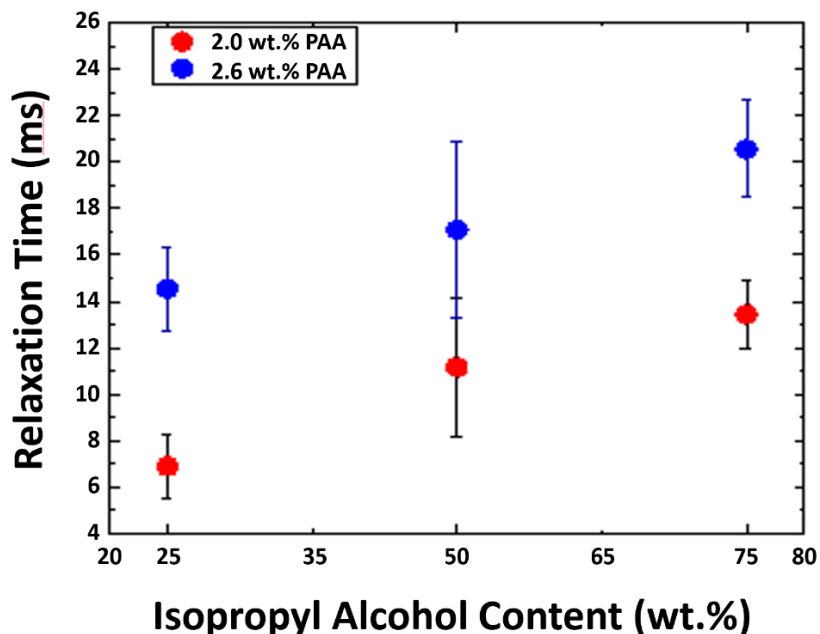


Figure 82. Filament relaxation time for PAA slurries as a function of IPA fraction. Source: NREL

Further experiments were conducted to modify rheological properties of inks to attain optimized fiber or electrode morphologies and/or ink agglomerate structures with an overall goal to develop ES slurries for fuel cell electrodes that do not need carrier polymers, thus eliminating the loss in porosity and protonic conductivity resulting from the presence of the carrier polymer in the catalyst layer. Proton-conducting ionomers from 3M and Ionomr as well as an anion-conducting ionomer from Ionomr were used initially. Upon exploration of spinnability, none of the proton-conducting ionomer-only (no carrier polymer) slurries were spinnable as shown in Table IX. However, good fiber formation was achieved from no-carrier-polymer anion-conductive-ionomer slurries, as seen in the SEM images in Figure 83. The rheological behavior of the spinnable slurry is not that different from that of the not spinnable slurries, so there are additional interactional forces within the anion slurry that are not being captured by rheology.

Table IX. Spinning Conditions and Results for Carrier-Polymer-Free Slurries

No.	Ink	Rate (mL/h)	Distance (cm)	Relative Humidity (%)	Voltage (kV)	Notes
1	5% 3M725EW in 75% IPA	0.2	8	35	15	Spray droplets
2					20	Spray droplets
3	15% Aemion in 75% Ethanol	0.2	8	35	5	Mixt of droplets & short fibers
4					10	Fibers-coils
5					15	Fibers
6				45	10	Fibers
7				55		Fibers
8				25		Fibers
9	10% Aemion in 75% Ethanol	0.2	8	35	10	Fibers
10					15	Fibers
11					20	Fibers
12	5% Aemion in 75% Ethanol	0.2	8	35	10/15	Spray droplets

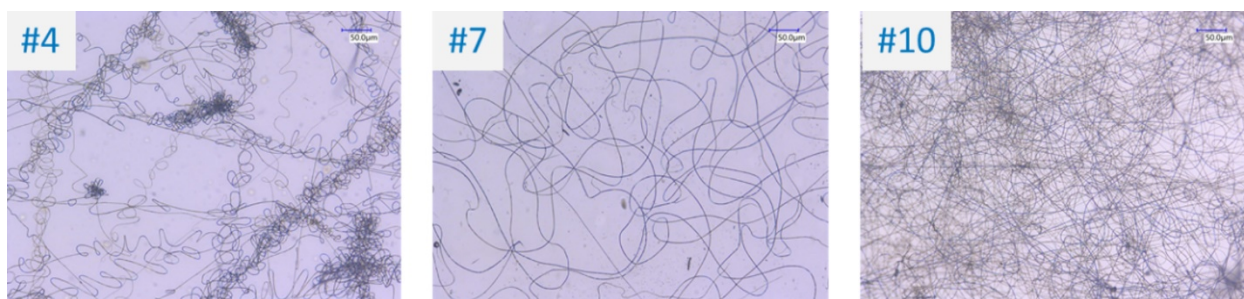


Figure 83. SEM images of anionic ionomer fiber formation under different conditions. Source: NREL

Studies were then conducted to explore fiber morphology as well as performance (e.g., conductivity) for promising carrier-polymer-free (i.e., pure ionomer) inks. Slurries containing both proton- and anion-conducting ionomers were studied. For the protonic ionomer, slurries with different dispersion medium constituents and mixtures and different solids wt.% of the ionomer were electrospun. Most of the compositions were unspinnable because of low viscosity. A few compositions were able to be jetted, but only droplets were formed, not fibers. For a single formulation, using methanol as the solvent shown in Table X, a combination of fibers and droplets were formed, as shown in Figure 84. For the anionic ionomer, more success was obtained. Good fiber formation was observed for slurries with 10 wt.% of the ionomer with a 75:25 ethanol:water dispersion media, as shown in Figure 85 (at 10 kV acceleration voltage, 0.2 mL/hr flowrate, 8 cm needle-to-drum distance, and 55% humidity in the chamber). From the SEM imaging, the fiber diameter distribution was observed to be mainly from 150 to 275 nm. Dynamic light scattering measurements of the anionic ionomer

indicate larger particle sizes for this polymer than the protonic ionomer (as well as for a standard protonic ionomer like Nafion), which likely contributes to the observed improved spinnability. Similarly, extensional rheology comparison of the 10 wt.% slurry to a 5 wt.% slurry showed increased filament lifetime for the higher solids composition. Slurries of 15 wt.% ionomer also successfully spun fibers, but the fiber formation was ribbon-like, rather than round.

Table X. Protonic Ionomer Slurry Formulations and Results

Concentration (%)	Solvent	Notes
10	IPA:DI = 1:1	Un-processable
5	IPA:DI = 1:1	Spray
2.5	IPA:DI = 1:1	Spray
10	Ethanol: DI = 1:1	Un-processable
5	Ethanol: DI = 1:1	Spray
10	Methanol	Un-processable
7.5	Methanol	Un-processable
5	Methanol	Spray + fiber

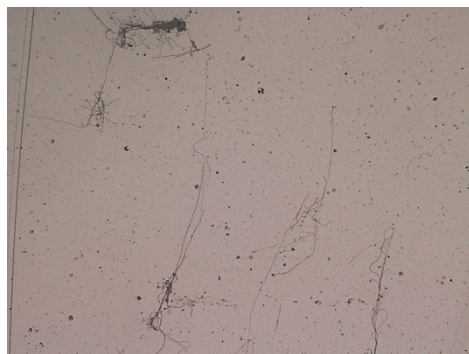
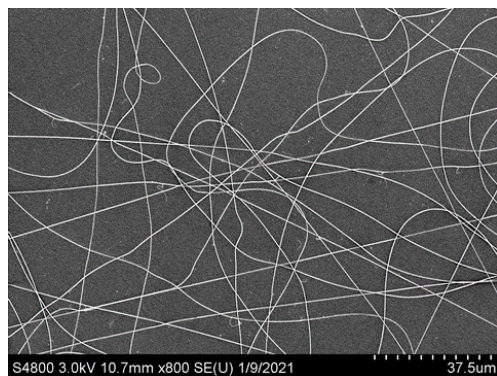
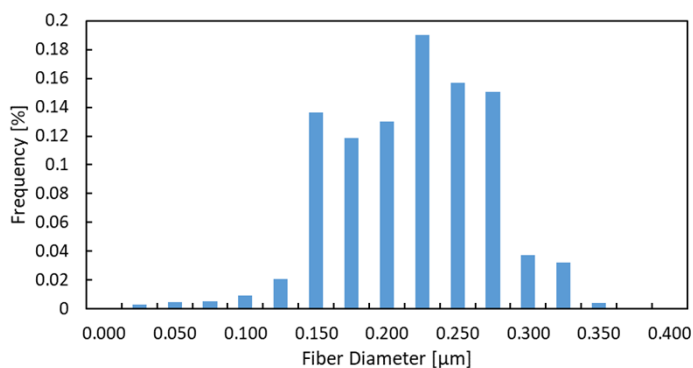


Figure 84. SEM image of a 5 wt.% composition in methanol with some fiber formation. Source: NREL



(a)



(b)

Figure 85. (a) Anionic ionomer fiber formation and (b) fiber diameter distribution (right). Source: NREL

Given the minimal success of the no-carrier-polymer effort, especially for protonic ionomers (the primary objective) and to support and leverage parallel work in HFTO-funded efforts, the effort was refocused on ionomer-polymer and carrier-polymer slurries containing an NREL-developed low molecular weight, high ionic conductivity polymer. The objective here was the same as the original study – to overcome the decrease in conductivity caused by the carrier. In this case, this would be achieved by the addition of the novel polymer to counteract the negative contribution of the carrier polymer to proton conductivity. Table XI shows the formulations including the novel polymer, Nafion ionomer, PEO as the carrier polymer, and the dispersion media. Results were initially less than ideal. The solids in these solutions have been precipitating out, and when the solutions are stable enough to run, they are generally not spinnable with only droplets being observed.

Table XI. Slurry Compositions with the NREL Novel Ionic Polymer

Component	Ratio		Ratio		Ratio	
NREL Polymer	85	9	85	9	85	9
Nafion		90		89		89
PEO		1		2		2
Water	15	50	15	50	15	65
IPA		50		50		35
Result	Made, but not spinnable		Made, but not spinnable		Made	

Task 4. Drying physics studies

A drying physics chamber was designed that would integrate with the NREL small-scale autocoater and enable application of multiple metrology methods in studying drying dynamics in directly-coated layers. The testbed will enable in situ measurement during the drying process of real inks and will provide key data for the drying model development effort at SNL. Figure 86 shows a schematic of the apparatus which will provide the ability to control heat transfer coefficient and temperature during drying.

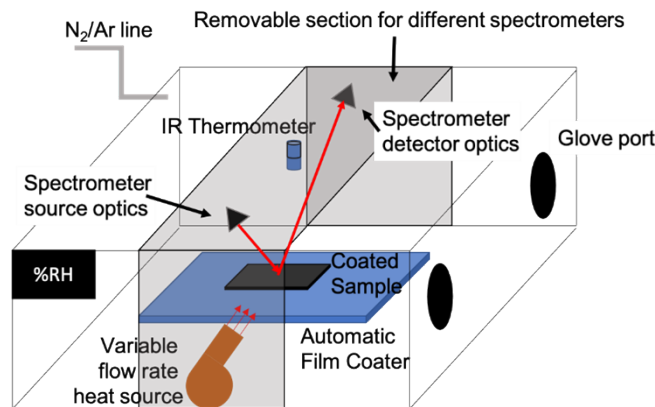


Figure 86. Schematic of drying physics chamber. Source: NREL

As a sub-assembly for the drying physics chamber, the development of a cantilever beam apparatus to measure stress in drying coatings was pursued. The apparatus has a flexible metal substrate, an automated coating head to coat the metal substrate, and laser displacement sensors above and below, one of which detects the thickness of the wet coating, and the other detects the displacement of the metal substrate under the stress of the drying coating. This apparatus will enable detailed study of drying dynamics as a function of ink formulation and constituents, for example to better understand thick-film cracking.

Education, information dissemination, publications, and technology transfer

Six university graduates participated in R&D for R2R processing. Results of the research at NREL resulted in two conference publications and six joint peer-reviewed papers.

Macroscopic Mathematical Model of the Drying of a Single Layer Generic Slurry Containing Monodispersed Colloidal Particles, Binder and Solvent (LBNL Lead Laboratory)

Task 6. Modeling

Slurry mixing experiments and drying model

Using a computer-controlled mixing setup developed in the prior FY, particle size measurements were performed on 27 distinct dispersions of Ketjenblack EC-300J CB (selected to match the formulation provided by ORNL) and Nafion diluted in mixtures of IPA and DI water. Typical results of 0.001 wt.% of CB, a level of dilution needed to ensure accurate measurements with the instrument, are shown in Figure 87. For these very dilute solutions, the CB has a typical main particle size peak around 10^{-6} m. Variation in Nafion concentration and in solvent composition in the experimental ranges considered had little effect on the main peak position. The subtle differences among the different measured distributions will require further analysis.

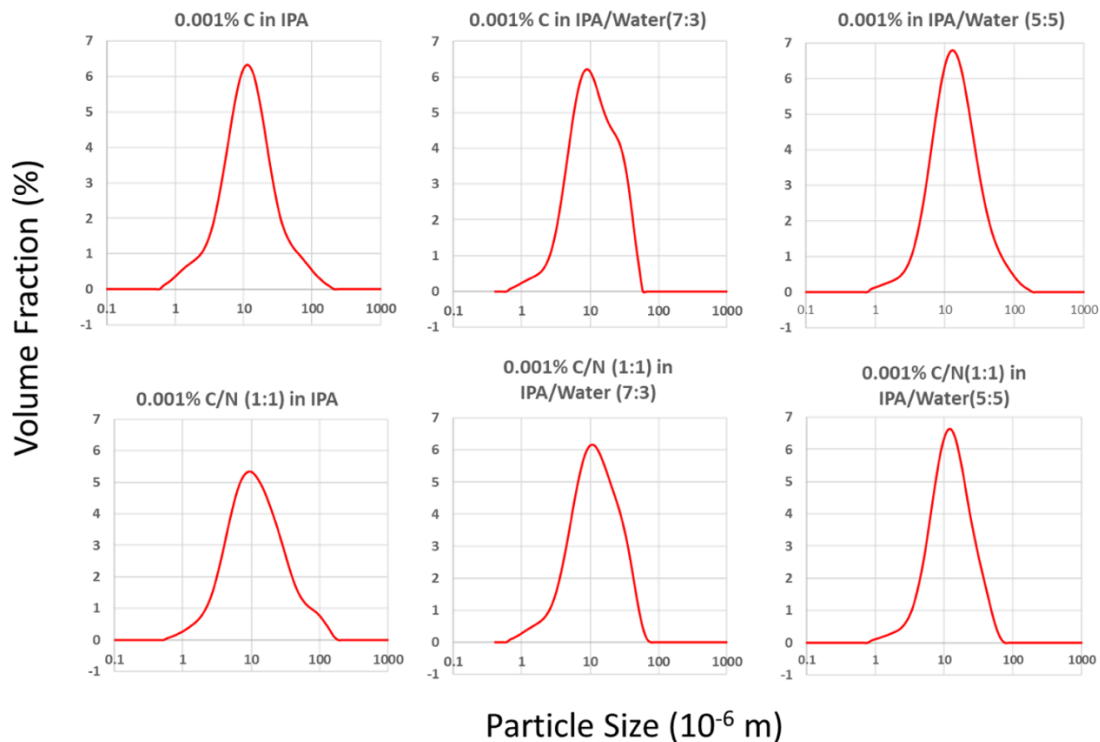


Figure 87. Steady-state particle size distributions of CB and CB/Nafion in different mixtures of IPA and DI water at a mixing speed of 2000 rpm. Source: LBNL

Mixing experiments were designed to determine particle size distributions in dispersions. Initial experiments were conducted with CB using 5 wt% Nafion in water and IPA with no mixing, as shown in Figure 88(a). When the volume fraction was plotted as a function of particle size, two peaks for particles were observed at about 0.3 μm and 1 μm for water but no peaks were observed for the IPA, likely indicating excellent dispersion of the nanoparticles. Another experiment was conducted with 5 wt% Nafion in water at two different mixing speeds of 2000 rpm and 3000 rpm. As the mixing speed increased, the particle size distribution developed a peak at 4.5 μm , as shown in Figure 88(b). The first peak is suspected to show the primary particles and the second and third peaks are suspected to be particle agglomerates. These results will be used in modeling efforts.

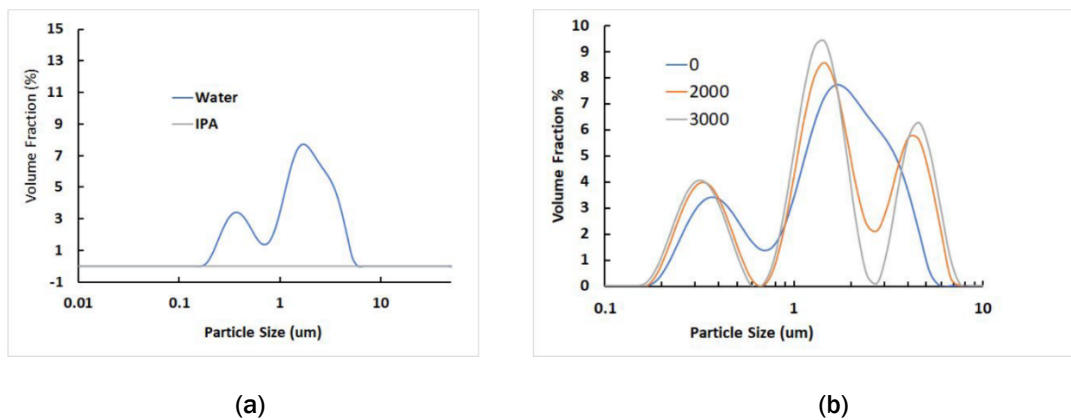


Figure 88. Initial results of mixing experiments for (a) 5 wt.% Nafion in water and in IPA without mixing and (b) 5 wt.% Nafion in water at three mixing speeds. Source: LBNL

An optical table and confocal microscope was installed for the slurry drying studies. An open flow chamber shown in Figure 89 was constructed for use as part of the larger experimental setup, shown in Figure 90, to observe the particle dynamics (particle size and morphology) in dilute dispersions under the confocal microscope. This cell has several important design features: (1) ability to install in the limited space available between the microscope head and stage, (2) built entirely from materials that are chemically compatible with the dispersions being investigated, (3) produces a stable fluid surface to aid in observation, (4) useable with continuous operation of the larger system, (5) provides a range of reduced flow rates to assist in observation, (6) limits evaporation, and (7) avoids the use of glass coverslip windows that would cause further image distortion due to changes in refractive indices and which might be vulnerable to mechanical damage. The mixer, a PSA, and flow cell were connected via tubing in a single loop, allowing particle size information from the same sample to be simultaneously measured by the PSA and microscope.

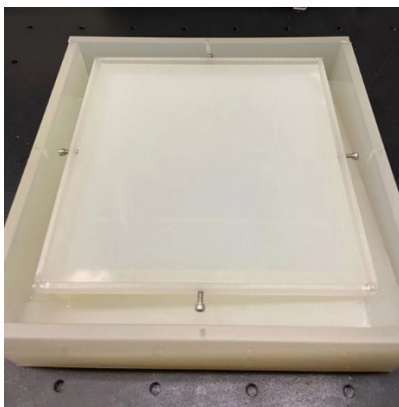


Figure 89: Open flow cell used to observe particle dynamics. Source: LBNL



Figure 90: Complete experimental setup. Source: LBNL

LBNL conducted experiments with Li-ion electrodes containing relatively large active material particles, and thick and thin electrode samples were provided by the battery fabrication group at LBNL. Laser-illuminated images at 10X magnification (the lowest level on the microscope) for thin graphite and thick Li-ion electrodes are shown in Figure 91(a). The confocal microscope allows the use of either white light or laser illumination. The thin Li ion electrode was imaged at 150X (the highest magnification), as shown in Figure 91(b). The image is monochrome because the laser only has one frequency. The color images of the thicker electrode at 150X magnification, which looks different from the thin electrode because of experimental settings on the microscope, are shown in Figure 91(c). The larger particles in the images are NMC particles and the darker and smaller particles are a mix of Li-iron-phosphate and CB. Cracks and CB aggregates are clearly visible with the laser illumination. All images are from static samples.

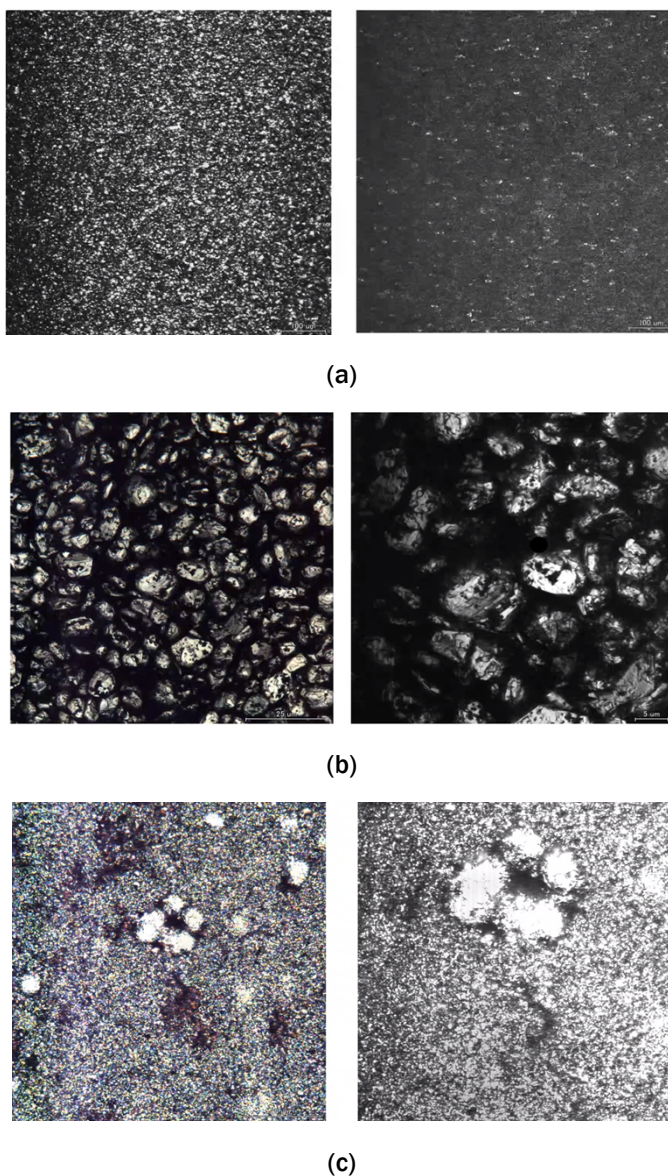


Figure 91. (a) 10X laser-illuminated thick and thin graphite and thick Li-ion electrodes, (b) 150X white light and laser-illuminated thin Li-ion electrodes, and (c) 150X white light and laser-illuminated thick Li-ion electrodes. Source: LBNL

Initial drying experiments were conducted manually by placing a drop of material containing graphite in carboxymethyl cellulose (CMC) on a microscope slide and monitoring the droplet as it dried. These materials were used because graphite particles are large, and the CMC is inert. The images shown in Figure 92 are not image slices but rather all-in-focus images obtained by scanning through a volume of material. The microscope system combines multiple images to focus everything. The sequence of the images shows the surface (of the droplet) receding and exposing the CB beneath the surface. The visual images for the brightness are shown in the top row on Figure 92 from 0 second to 120 seconds of drying time. The lower row of images shows the height of the material, as detected by movement of the focal plane through the sample.

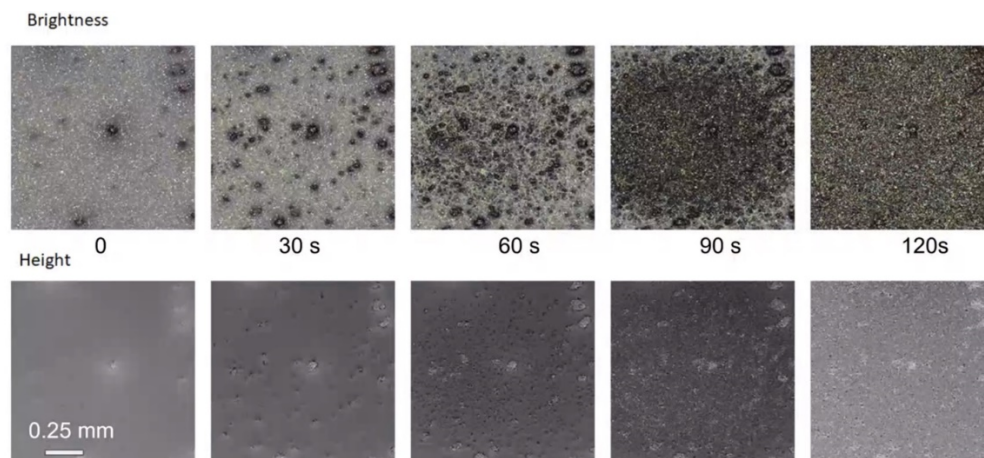


Figure 92. Drying process of graphite slurry for 25 wt.% graphite in 1 wt.% CMC in water. Source: LBNL

LBNL developed a new optical sectioning capability that takes advantage of the confocal microscope has a narrow depth-of-field, visually isolating the material closest to the focal plane. This means that a sweep can be performed through a sufficiently transmissive volume to get 3D information because the position of the focal plane is known. This is important to determine the appearance of the particle networks. This feature was not supported by the confocal microscope software from the manufacturer. LBNL's development operates at the full microscope hardware capture rate (up to 120 Hz). This unique capability supports the study of the dynamic component behavior. The microscope stage has a 200 nm motor resolution, but this is not the actual optical resolution. The microscope sweeps through in the "z" direction so that different parts of the material enter the microscope's view. This will enable observations of phenomena such as the effects of increasing mixing speed on agglomeration size and structure.

LBNL also investigated the effect of adding Nafion, which acts as a surfactant to inks. Results of the microscopic analysis show that mixing without Nafion produces many agglomerates and mixing with Nafion breaks up the agglomerates for the same mixing speeds. The images obtained with the confocal microscope need to be converted to useful information using image analysis. Low-magnification optical section images of dilute CB/ionomer/water/IPA inks were captured using the confocal microscope. Initially, strategies were tested for image analysis using the ImageJ / Fiji software package. ImageJ is convenient for manual use but fairly inflexible and usually not well-suited to processing large amounts of data. After developing a suitable approach for identifying agglomerates, the approach was transplanted into the Python programming language, making use of the scikit-image library.

As the microscope sweeps across the material, some particles become darker than others because they are closer to the focal plane. The particles that are most emphasized are selected to create a histogram which would require much data to get close to the continuous distributions that are observed with the particle size analyzer. Figure 93 shows samples of the optical section image and the processed image, and Figure 94 shows a histogram of optical size for agglomerates in the focal plane, as determined by the image analysis program.

Large numbers of images would need to be processed in order to produce histograms that approach smooth size distributions. Optimization of agglomerate detection parameters might also be needed under different conditions.

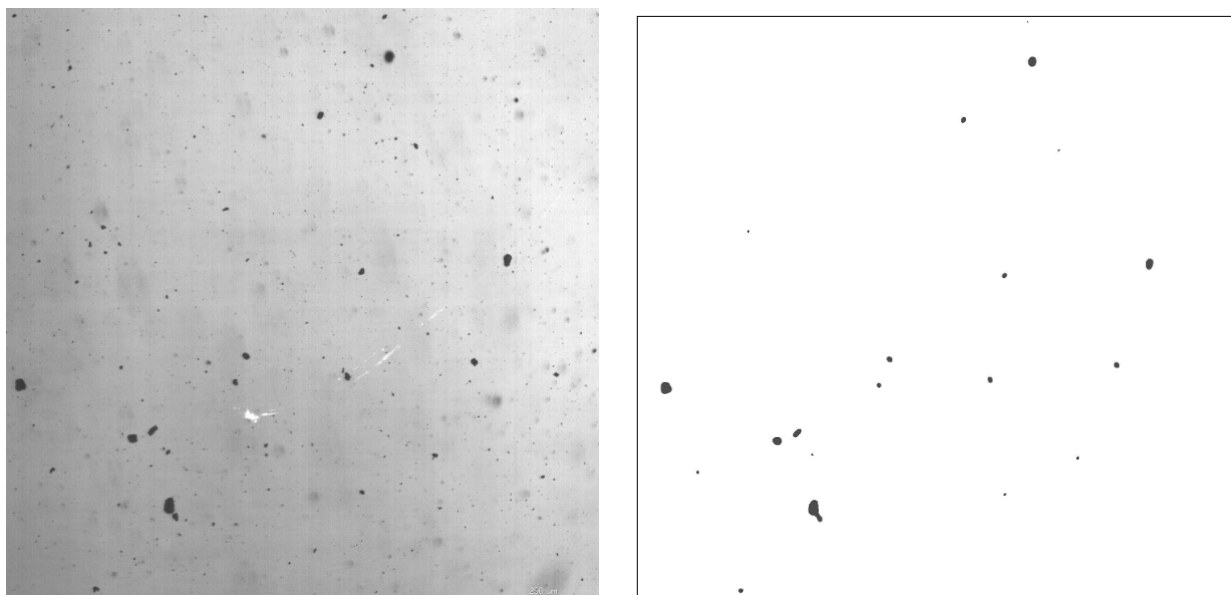


Figure 93: An optical section of an ink sample and the processed image. Source: LBNL

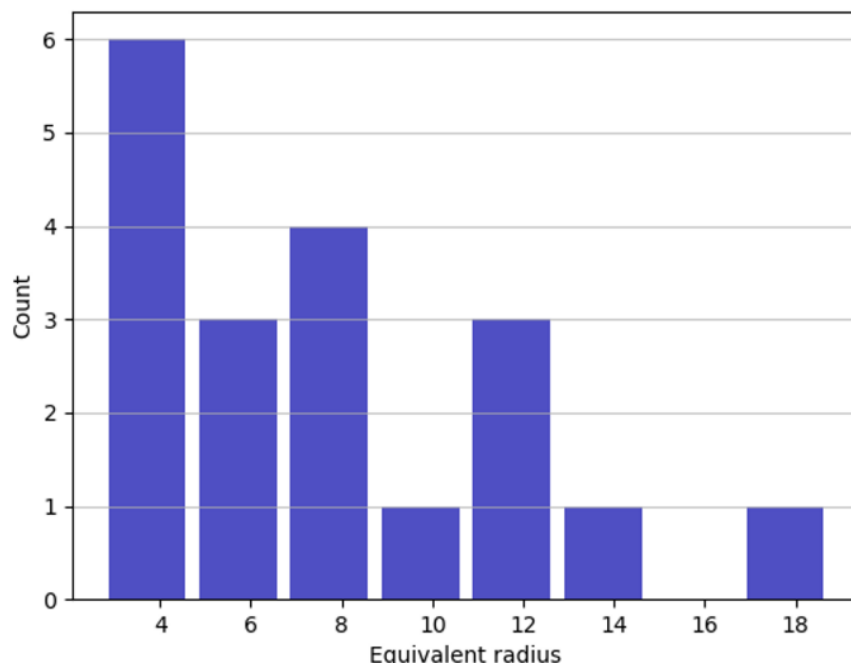


Figure 94: Histogram of particle sizes generated from an image (radii are measured in μm). Source: LBNL

A modular automated miniature coating drying observation platform was constructed and made operational. Additional funding from VTO and HFTO supported the software engineering and construction and alignment of a module that enables observation using the confocal microscopy. The full assembly is shown in Figure 95. The design of the system balances construction cost, maintainability, weight, and robustness. This miniature coating line includes a custom computer-controlled doctor blade which can vary coating height during a

coating process, and the entire doctor blade assembly lifts out of the way to prevent spills and to maximize use of space. The “active” module of the system can be detached and is designed to fit into the ALS 8.3.2 hard X-ray microtomography beamline hutch. System operation was tested by demonstrating the doctor blade coating of an NMP-based slurry followed immediately by confocal imaging.

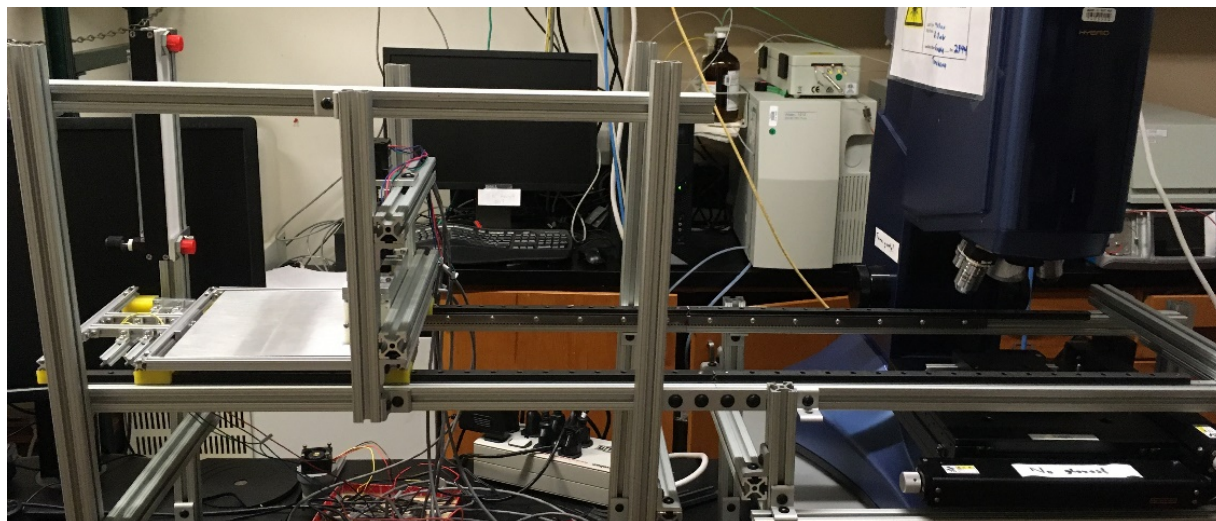


Figure 95: The modular automated coating/drying observation system for use with the confocal microscope.
Source: LBNL

Ink crack dynamics

While the drying platform was under construction, some initial drying experiments were performed using the confocal microscope to investigate crack dynamics. The aims of the study were to understand how cracks generate and develop in the ink coatings. Results from previous technical papers showed very few studies on cracking. So, the LBNL study attempted to understand cracking mechanisms and how to control crack dynamics for mixing and drying conditions. Also, the research will later attempt to understand how cracks affect the cell performance. The focus will be on crack dynamics, i.e., the generation and development of cracks and crack static properties such as shape, spacing, and density. A 4.5% high-surface CB in water and IPA was used to study cracks that occurred in the coating. The cracks appear to start at the aggregates or agglomerates, but not necessarily at the largest or smallest of these. Different crack orientations were seen at different wetting thicknesses of 100 μm , 150 μm , and 200 μm and more cracks were observed for I:C of 0.5 than for I:C of 0.2 as shown in Figure 96. A second finding was that the temperature does not significantly affect the crack pattern, i.e., crack patterns at 400 K were the same as at room temperature for the same thickness of material (200 μm). The confocal microscope was used to capture the drying process of a Li-ion battery cathode slurry. Examination of images for the wet slurry and the dried slurry show that active material (NMC particles) and the polymer can be distinguished in the wet slurry and the solid particles can be easily seen in the dried sample in Figure 97.

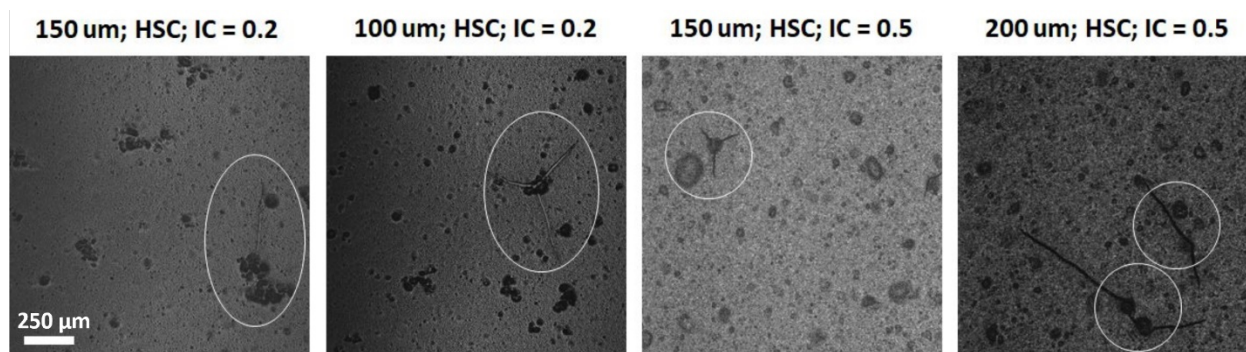


Figure 96. Crack formation starting at aggregates at different wetting thicknesses of 100 μm, 150 μm, and 200 μm, more for I:C of 0.5 than for I:C of 0.2. Source: LBNL

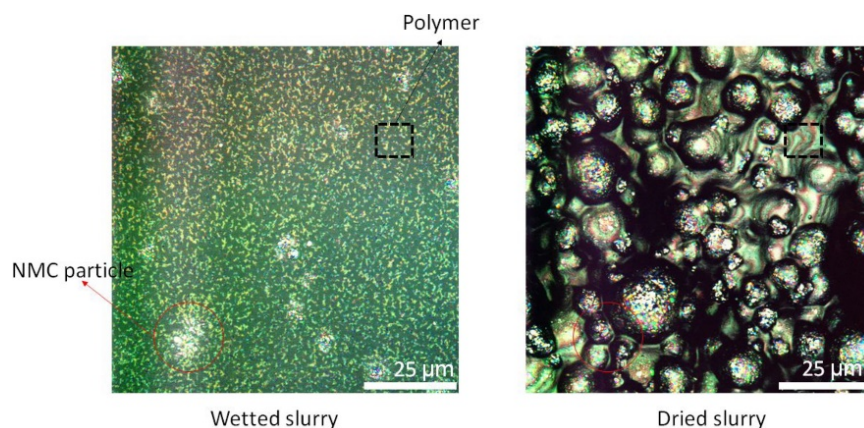
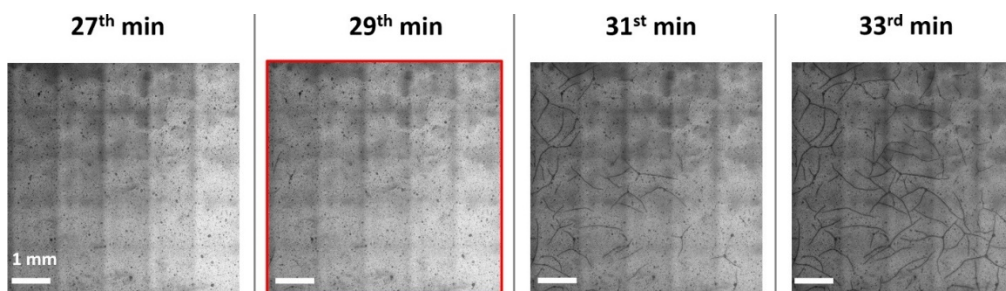
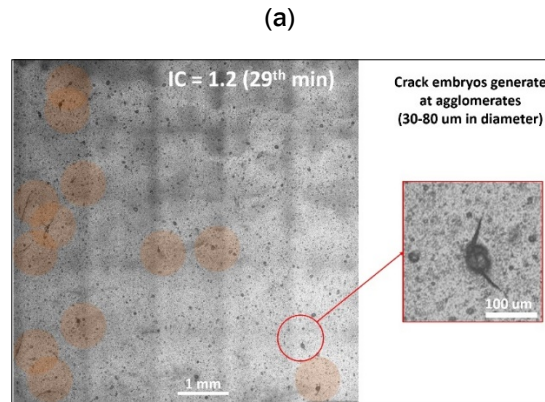


Figure 97. Confocal microscope images for the drying process of a Li-ion battery cathode wetted and dried slurries showing NMC particles. Source: LBNL

Additional experiments were conducted with an ink composed of 4.5% HSC CB, a water-to-IPA ratio of 3:1, and an I:C ranging from 0.5 to 1.2. Mechanical mixing was performed at 10,000 rpm for 15 mins. The method for fabricating the coating was to apply the coating on a gas-diffusion layer (Freudenberg H23C8) using a doctor blade at a rate of 2 cm/s and with a 200 μm gap. The coating was dried at room temperature for a total of 30-40 mins. Figure 98(a) shows photomicrographs of crack generation and development. Cracks started to develop at 29 mins into the drying process and were fully developed at 39 mins. Initial crack lengths were about 1 mm. The confocal microscope was used to get higher resolution images of the cracks and agglomerates. The cracks appear to originate at the agglomerates which are estimated to be 30 μm to 80 μm in diameter as shown in Figure 98(b). The crack generation process was observed using a higher resolution lens. Liquid can be observed around the agglomerate and a crack forms when the liquid is dissipated through drying. The surface of the coating at the agglomerate is very rough as shown in Figure 99.





(b)

Figure 98. Crack generation and development at I:C or 1.2. Source: LBNL

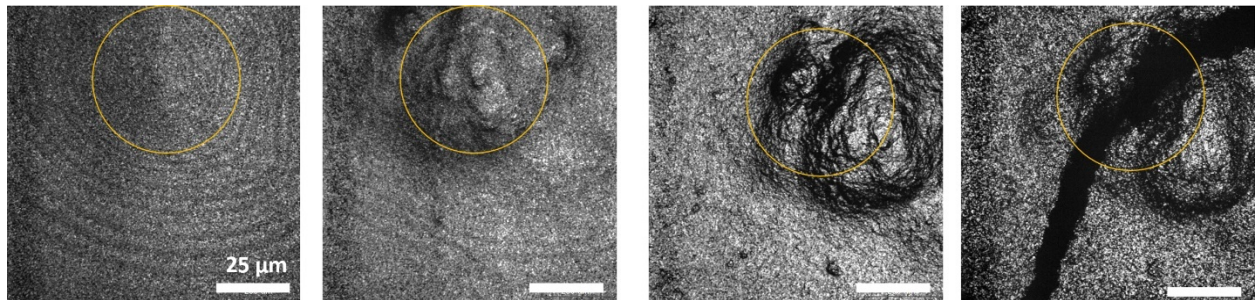


Figure 99. Close view of crack generation process. Source: LBNL

All cracks appeared at the same elapsed time (29 minutes) into the drying process regardless of the I:C ratio, however, the crack patterns were different. At an I:C ratio of 0.5, there was a high density and low spacing of cracks that were networked. At an I:C ratio of 0.8, there was a high density and low spacing of cracks that were not networked. At an I:C ratio of 1.0, there was a low density and large spacing of the cracks and they were not networked. At the I:C ratio of 1.8, there was a low density and large spacing of cracks that were networked. Figure 100 shows the crack patterns obtained at the different I:C ratios.

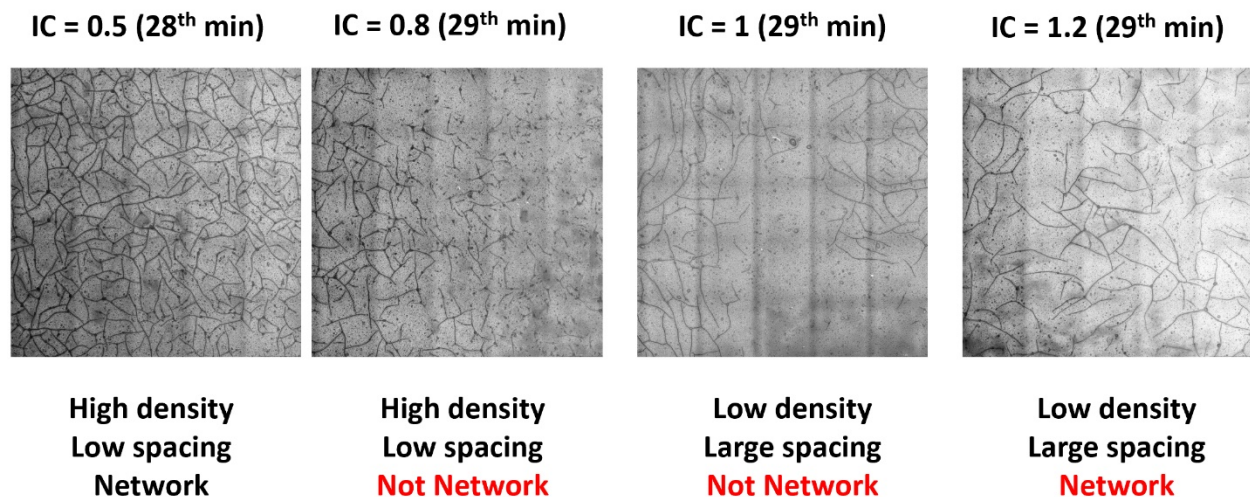


Figure 100. Crack patterns at different I:C ratios. Source: LBNL

Education, information dissemination, publications, and technology transfer

Three university graduates were hired to participate in macroscopic modeling R&D for R2R processing. Results of the modeling research resulted in two joint peer-reviewed papers.

Validated Continuum-Scale Models to Accelerate Design and Scale-up of Simultaneous Die Coating Process Technology (SNL Lead Laboratory)

Task 6. Model development and validation for multilayer R2R applications

Deposition model

SNL and UNM continued to advance the deposition models of single- and two-layer slot-die coating flows, using coating trials at ORNL for validation. Qualitative validation of the single-layer slot-die coating model was achieved against coating trial observations with less concentrated inks. Details on coating substrates were assumed and some unforeseen difficulty in identifying the actual process parameter uncertainty of the experiments surfaced. Specifically, the GDL substrates of the experiments exhibited significant thickness variation, and there were significant uncertainties in the vacuum pressure and pump rates. Once these were resolved, validation against measured coating “windows” was achieved. In addition to the slot-die coating studies, a special slide-only model was completed to help NREL redesign the lip geometry. A first was achieved for a fully-converged steady state-model of three-layer slide coating flow with the actual ink rheology of a PEMFC construction, as illustrated in Figure 101. The bottom layer (blue) is Pt/Vu with a wet thickness of 64 μm , the middle layer is Nafion (green) with a wet thickness of 250 μm , and the top layer is Pt/HSC (red) with a wet thickness of 125 μm . Other operating conditions used to generate this solution were the web speed, U_w , was 7.5 cm/s, the slide-web gap was 500 μm , and the vacuum pressure, P_{vac} , was 452 dyne/cm².

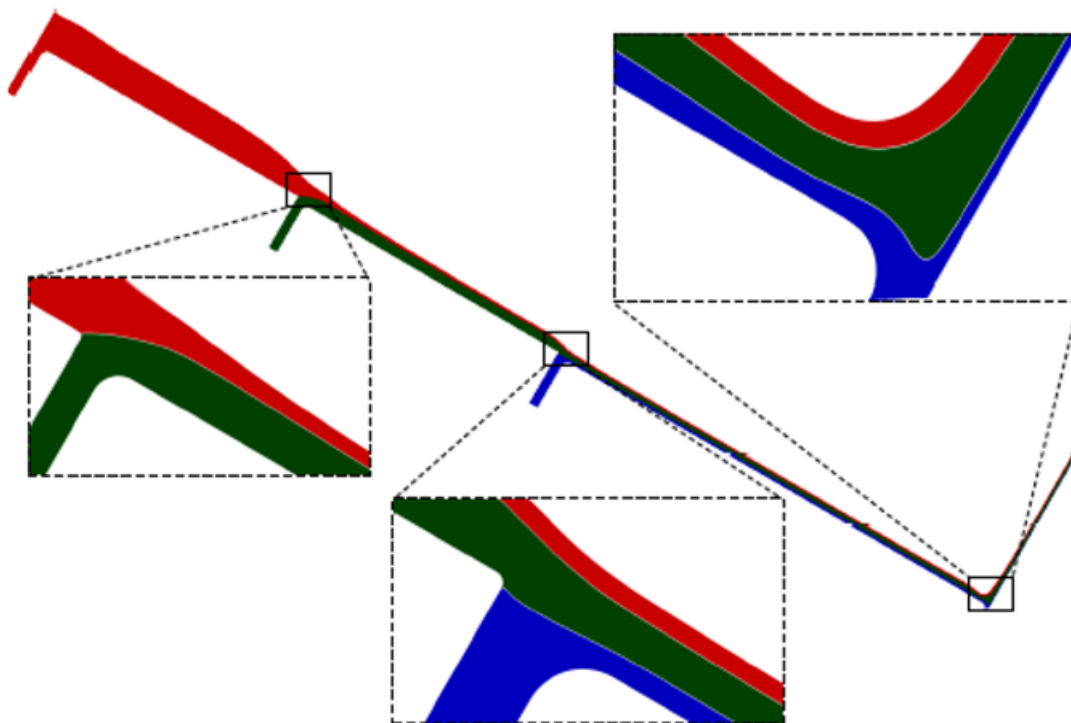


Figure 101. Computed free surface and interfacial shapes of three-layer slide coating flow. Source: SNL

The model deploys pseudo-solid mesh deformation to track free surface positions during coating deposition, a technique that was pioneered at SNL and a critical part of the R&D 100 award winning Goma 6.0 software. The computational meshes deployed in a finite element simulation deform to conform to the free surfaces. In general, the physical shape of the coating bead is not known, and so the domain of the flow is solved simultaneously with the movement of the mesh. The model will be used to predict the operability limits of the coating window to determine the set of operating conditions for a good quality coating without any defects. For a slide die coating flow, similar to slot-die coating, vacuum pressure is needed under the upstream coating meniscus to stabilize the bead. If the vacuum is too low, the rivulets will form at the low vacuum limit. If the vacuum is too high, weeping and leakage can occur at the high vacuum limit. A flow physics experiment was devised that used a mirror inside a transfer glass wall so the coating bead could be observed from the front. From a top view with too little vacuum, the bottom meniscus was observed to travel upward and penetrating the coating bead. If the vacuum is too high, the bottom meniscus will travel downward producing weeping and leakage which defines the high vacuum limit. Using these types of basic experimental observations and knowledge of capillary hydrodynamics, the model can be guided to solve for the low and high vacuum limits needed to place the upstream contact line at either edge of the die face.

For PEMFCs, two ink compositions were considered using platinum on layers of Vu-Nafion-HSC and on Vu-Nafion-Vu. Figure 102 has a plot of the applied vacuum from 0 to 0.17 kPa as a function of web speed from 2.5 to 12 m/min showing the maximum and minimum conditions for both compositions. Figure 102 also has a plot of the viscosity as a function of the shear rate for 7.5 wt% Pt-Vu and 7.5 wt% Pt-HSC inks compared to the Newtonian rheology of Nafion. For very low web speeds, successful coating depositions can be performed without any vacuum for the Vu-Nafion-Vu composition because the viscosity is very low, and the shear rate is on the order of 1000 s^{-1} . Initial results for the simulations of the three-layer slide coating flow are shown in Figure 104 for Vu-Nafion-HSC and Vu-Nafion-Vu coatings.

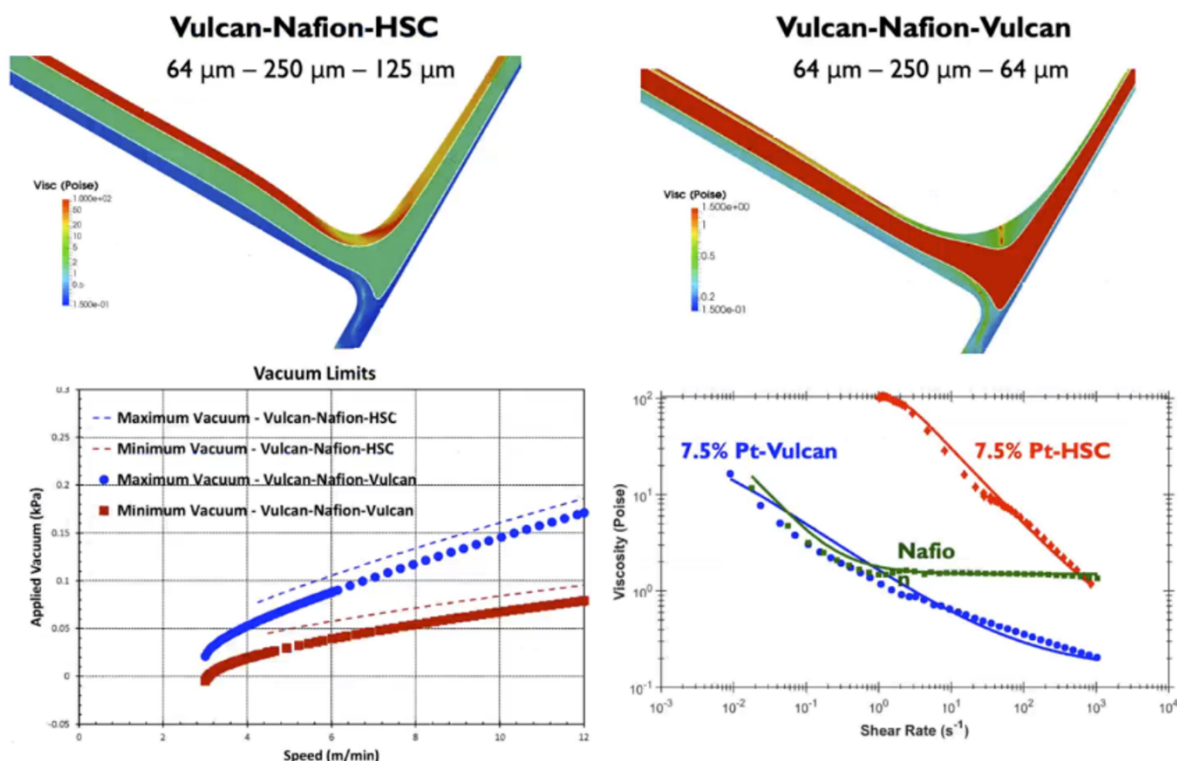


Figure 102. Initial results for the three-layer slide die flow. Source: SNL

SNL and UNM continued to advance the deposition models of single- and two-layer slot-die coating flow with inks at various concentrations of catalyst and carbon support. Using the 3.5 wt. % and 8 wt.% catalyst ink, coating process window predictions in terms of operating vacuum and web speed, as shown in Figure 103, were used by ORNL to refine their experimental procedures of achieving a smooth coating without streaks, thereby saving valuable material and time. Coating trials were performed with metal foil substrates rather than the highly nonuniform GDL web. Discrepancies in measured ink rheology (viscosity vs. shear rate) between ORNL and SNL rheometers underpinned the inaccuracy of the predicted windows. Using the measured rheology with SNL's recently calibrated rheometer, the models did indeed predict an accurate and useful coating operability window.

SNL focused on the single-layer and multi-layer slide coating trials (slide flow only) at NREL with various ink layer configurations. While the single-, two- and three-layer models with standard fuel cell ink combinations were demonstrated previously, the emergence of an interesting instability on the slide coating (developing a lumpy pattern) redirected efforts at SNL to aid in helping find the stable region for slide flow only. These calculations of coating windows are a first for multilayer slide coating, and so little data exist other than those from NREL.

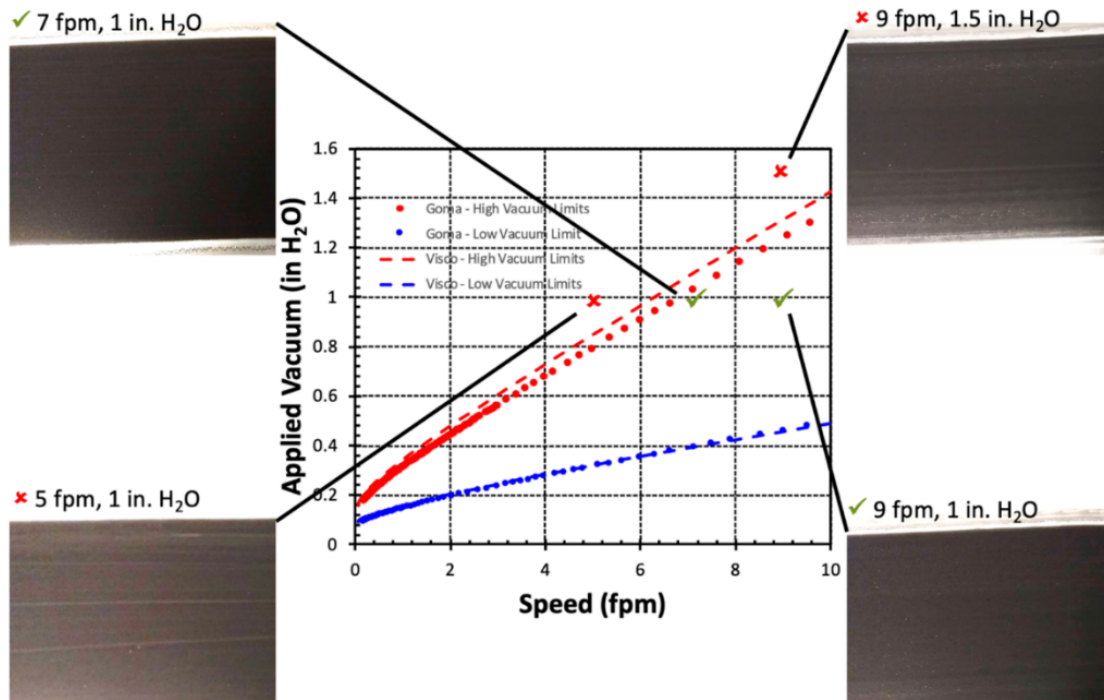


Figure 103. Experimental validation of process window predictions for 3.5 wt.% Pt/HSC with a wet thickness of 60 μm and a die gap of 150 μm . Source: SNL

Using an 8 wt% catalyst ink, which has shown evidence of complex fluid behavior and possibly a yield stress, coating engineers at ORNL confirmed that the coating operability windows do indeed coincide with experimental practice of achieving a smooth coating without streaks. The coating trials were performed with metal foil substrates rather than the highly nonuniform GDL web. It was determined that the ORNL rheology characterization, which are key inputs to the model, and a report of a viscosity level at all shear rates were roughly 10-30% above those that SNL measured. This could explain any remaining slight discrepancies. Figure 104 provides a comparison of predicted operability windows for applied vacuum pressures and web speeds, and how they capture coating observations.

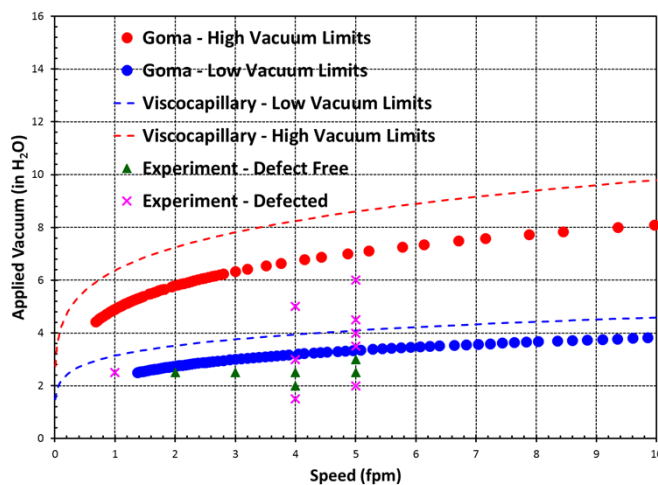


Figure 104: Comparison of predicted operability windows in applied vacuum pressure and web speed. Source: SNL

Continuum drying model development

For the continuum drying model development, a successful demonstration of a single-layer solvent-polymer drying model was regressed using machine-learning regression software (DAKOTA, <https://dakota.sandia.gov>) with experimental data in the literature to determine some diffusivity parameters. Initial simulations of colloidal particles in solvent, with and without settling, was demonstrated to extend the model to include conductive particle and active ceramic. An experimental setup at SNL was completed to obtain drying weight time histories for model validation and tuning. Considerable work this year was aimed at analyzing the drying conditions of the experiments so that the model initial and boundary conditions could be determined.

The solvent-polymer model was extended to include a particle phase. The model ran successfully and showed the expected results with “fast” drying, indicating a particle skinning effect. Experiments were initiated for the drying validation setup with a moisture balance. The test fixture design shown in Figure 105(a) was to better control the start-up of the drying coat-weight measurements. The arrangement of the Rheolaser (to monitor particle thermal motion during drying) and radiative heating elements is shown in Figure 105(b).

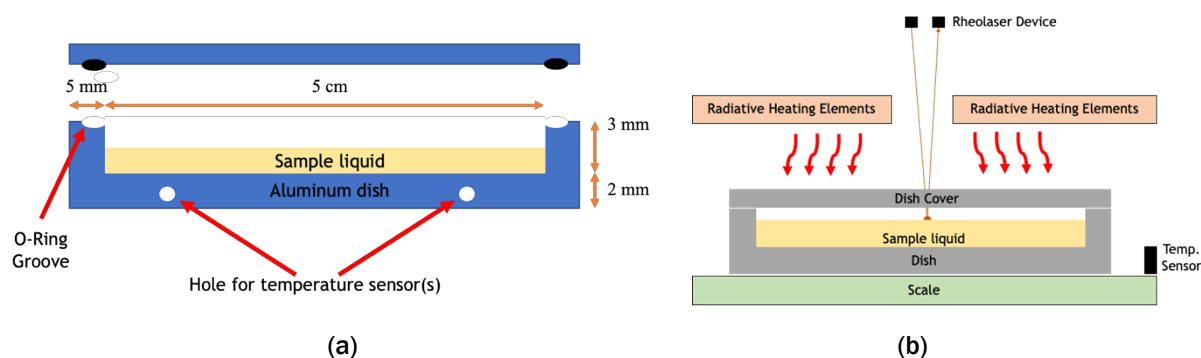


Figure 105. (a) Sample chamber design with a lid to control initial drying transient, and (b) the configuration for the rheolaser and radiative heating elements. Source: SNL

A Sartorius Model MA35 Moisture Analysis Balance was modified with a heater in the upper lid and the optical grid removed so it could be placed underneath the two monitoring heads of a Rheolaser COATING Optical Film Formation Analyzer for to observe light scattering at the surface of a film. Figure 106 provides photographs of these instruments. The moisture analyzer was evaluated for its thermal ramp up which takes about two minutes from a cold start to 60 degrees. The manufacturer was contacted to get the thermal output in terms of optical values to provide the thermal information for the drying modeling. The goal is to integrate the mass loss measured by the moisture analysis balance with the optical changes measured by the Rheolaser analyzer. This will allow optical speckle scattering from the surface and follow the drying process. This Rheolaser analyzer has been used previously to study the formation of dispersed system to an ordered system to a consolidated system.



Figure 106. Sartorius M35 moisture balance and Formulation rheolaser COATING Optical Film Formation Analyzer. Source: Sartorius and Formulation

Next, silica particles were incorporated with binders as cited in previous studies and used in the model to evaluate the impact of the ratio of particles to solvent and the effect on skinning and stresses in a system. SiO_2 spheres were processed with a diameter of 120 nm. Surfaces were modified using 3-methacroyloxypropyltrimethoxysilane. This provided a charged system in a toluene environment, so there should be some electrostatic repulsion producing good dispersion. Figure 107 shows the particle fluidity during sample drying, indicating high correlation to particle motion during the constant rate (early time) period. The MA35 Moisture Analysis Balance with a radiative top will be modeled for the effect of heat transfer from the resistive element.

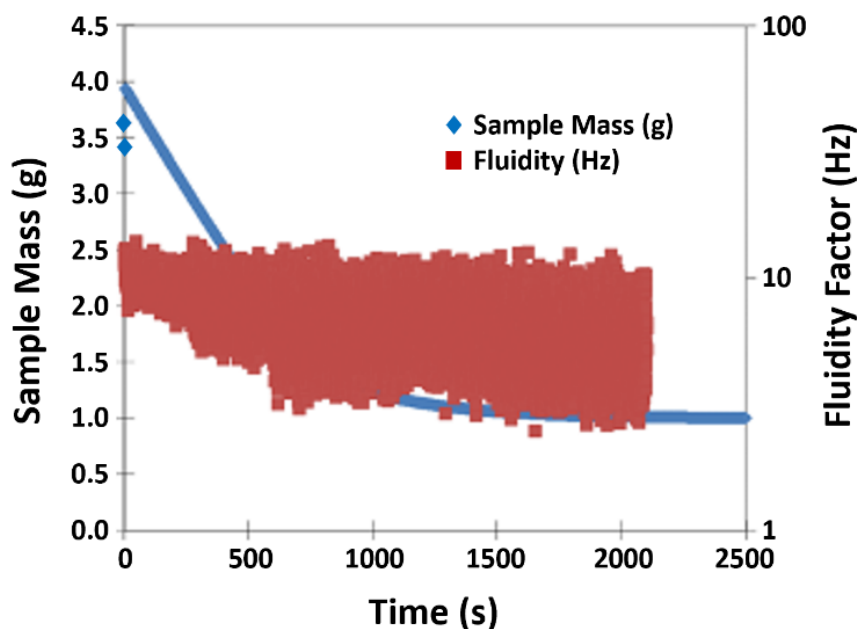


Figure 107. Rheolaser measurements showing the particle fluidity during drying for a toluene+ SiO_2 +poly(vinyl acetate) sample. Source: SNL

Figure 108 shows a set of parameters for a toluene-polyvinyl acetate system that was fit using DAKOTA with varying compositions, set temperatures, and durations of experiments that were used to generate the data for fitting the model. For the first eight parameters, optimization was carried out by minimizing the error between individual predictions and experiments, while the final set of parameters was obtained by minimizing the error over all the experiments that were listed in the previous eight tests. There was some difference between the parameters fit to all the experiments simultaneously and those fit to individual experiments. The pre-exponential term, D_0 , obtained from fitting all the experiments simultaneously falls within the range of the individually-fit terms for D_0 . Of the remaining three parameters, some vary greatly from their individually set values which is likely due to the non-linear nature of the multi-parameter optimization that DAKOTA is executing. Regardless of whether the parameters are individually fit or fit to a collection of experiments, there is a reasonable agreement between the predicted residual solvent and the measured residual solvent as seen in Figure 109. The blue curve is the measured residual solvent, the solid red line is the prediction obtained using parameters in set 7 of Figure 108, and the dashed red line is the prediction obtained using parameters in set 9. A reasonable agreement can be seen between the measured and predicted residual solvents.

#	Test	Duration (s)	$\frac{K_{12}}{\gamma} \left(\frac{\text{cm}^3}{\text{gm} \cdot \text{K}} \right)$	$K_{22} - T_{g2} \text{ (K)}$	ξ	$D_0 \left(\frac{\text{cm}^2}{\text{s}} \right)$	% rms error
1	1, 10%, 60°C	2000	4.840E-04	-261.68	0.200	7.300E-04	5.84
2	2, 10%, 60°C	2000	5.958E-04	-315.27	0.095	1.108E-03	9.16
3	3, 30%, 60°C	1500	4.974E-04	-241.08	0.314	5.561E-04	1.79
4	4, 30%, 60°C	1500	5.028E-04	-232.36	0.312	5.620E-04	2.31
5	5, 30%, 80°C	1400	4.842E-04	-251.87	0.305	5.619E-04	4.55
6	3, 30%, 60°C	4000	4.845E-04	-261.94	0.289	5.839E-04	3.52
7	4, 30%, 60°C	4000	4.880E-04	-254.53	0.302	5.697E-04	6.39
8	5, 30%, 80°C	3800	4.611E-04	-310.05	0.175	7.306E-04	2.93
9	All		9.839E-05	-123.61	0.101	6.928E-04	12.87

Figure 108. Parameters for a toluene-polyvinyl acetate system. Source: SNL

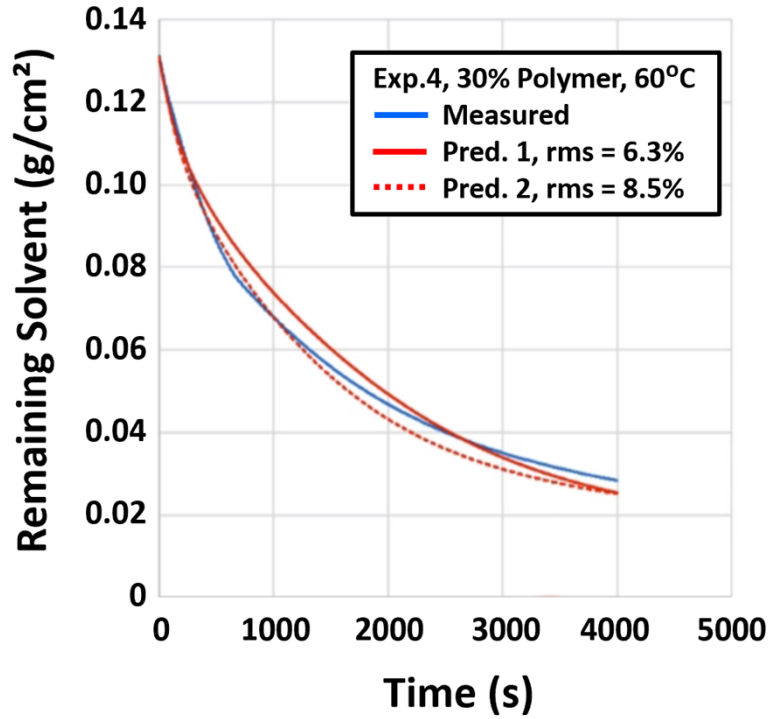


Figure 109. Results for the predicted residual solvent and the measured residual solvent. Source: SNL

GOMA was the physics engine and DAKOTA was used for the ML aspects. DAKOTA is a collection of mathematical tools used to optimize parameter studies. The model development requires connecting the elements of the user simulation code (GOMA) and DAKOTA through a feedback loop that learns from each iteration. SNL simulations using GOMA agree perfectly with previously published data. The model can also predict the solvent mass fraction for the polymer-solvent layer over the drying time using inputs for the solvent free volume parameter, the free volume transfer parameter, the solvent-polymer jumping unit ratio, the binary diffusivity, and the convection coefficient. The sensitivity of the transient solvent mass fraction for the inside and outside of the polymer-solvent layer can also be predicted as shown in Figure 110.

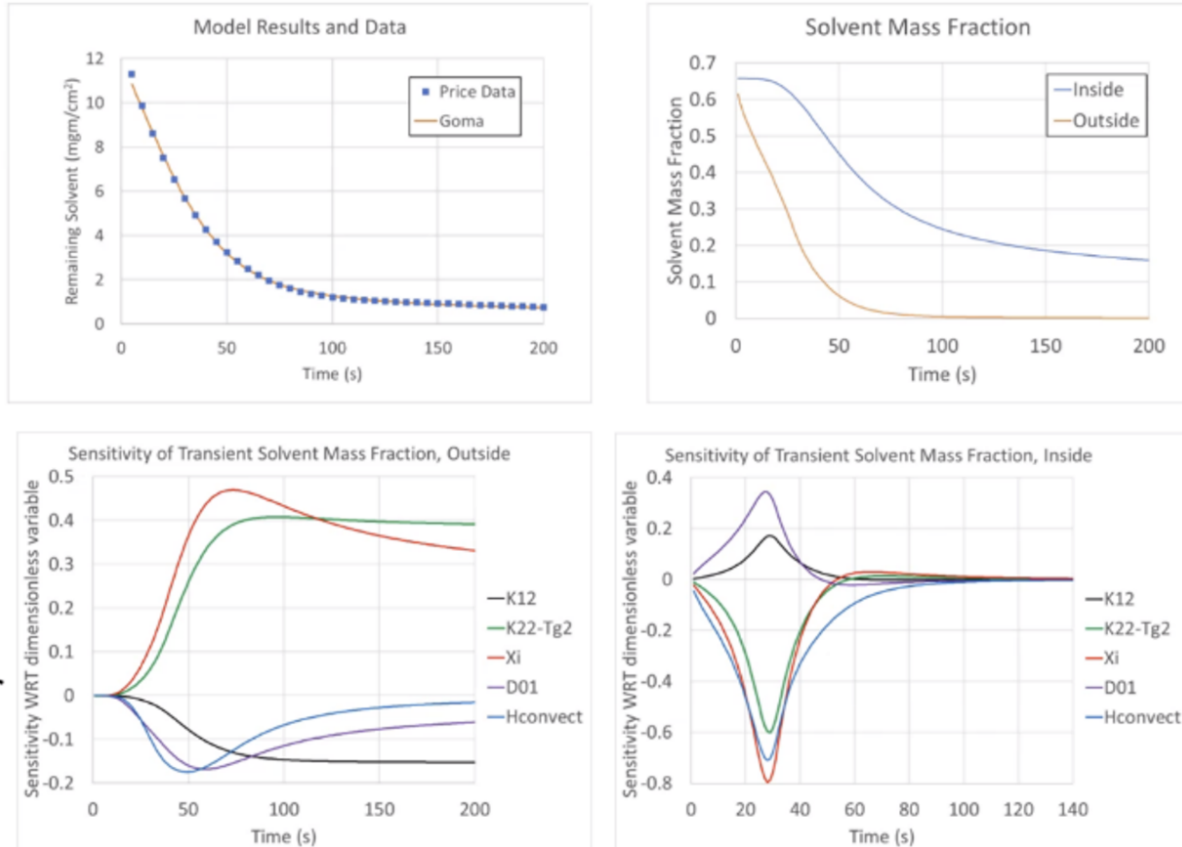


Figure 110. Model results and sensitivity of the transient solvent mass fraction for the inside and outside of the polymer-solvent layer. Source: SNL

Tensioned web model

Slot-die coating is an ideal method for precisely coating a single layer or two layers. The thickness is controlled solely by the flow rate and the coating speed through a pre-metered method. The coating quality depends on the liquid properties and the operating conditions which are components of the coating window which is the region defined by key processing input parameters in which the coating is uniform. Usually, some level of vacuum is applied to the upstream meniscus to prevent breakdown of the coating bead. The vacuum level has to set within limits. Vacuum that is too high will produce weeping or leaking of the liquid coating with loss of pre-metering. Vacuum that is too low will result in rivulets when the upstream meniscus invades the coating bead. Another important limit is the limit for low flow. The thickness of the coating is controlled by the slot-die gap, and for thinner coatings even with vacuum, the gap must be smaller which can produce problems. Even vibrating motors for the rollers can cause gap variations. Surface imperfections in the roll and in the slot die are also concerns.

One solution is to replace the backing roll with a tensioned web – over – slot-die – coating where there is no backing web. The web is wrapped around the die lip and tension is applied as shown in Figure 111. The die gap is governed by the elasto-hydrodynamic interaction which means there is a relationship between the web elastic force and the liquid hydrodynamic force. By placing tension on the web, the die gap can be controlled. The upstream meniscus position is controlled by adjusting the applied tension and the wrap angles. In this manner, there is no reliance on vacuum for controlling the meniscus to prevent weeping or bead breakdown. Vacuum can be applied, but the coating can be controlled by web position and applied tension. The precision requirement now shifts from the backing roll and motor to web handling.

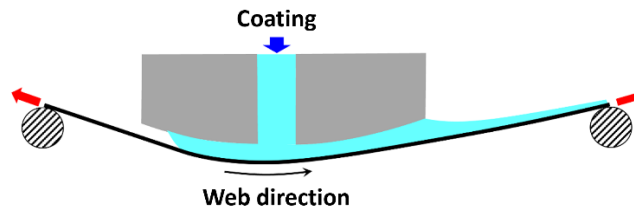
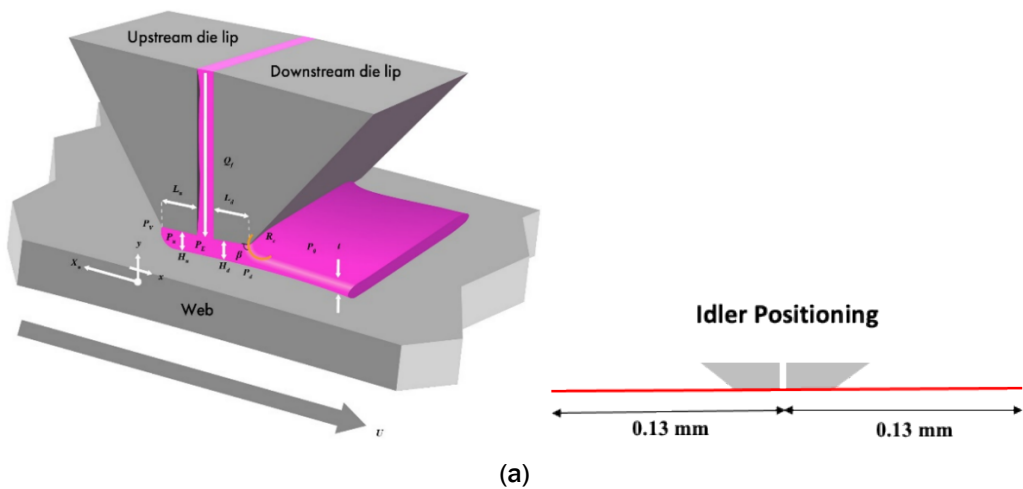


Figure 111. Schematic of the tensioned web over the slot-die coating. Source: SNL

Efforts were to refine tensioned web (sans backing roll) models for a surface-treatment ink for precision coatings. The basic coating configuration is shown in Figure 112(a), with idler positions noted, and the flow field is shown in Figure 112(b). The large aspect ratios and very small coating gaps enable a thin-film coating.



Flow Features

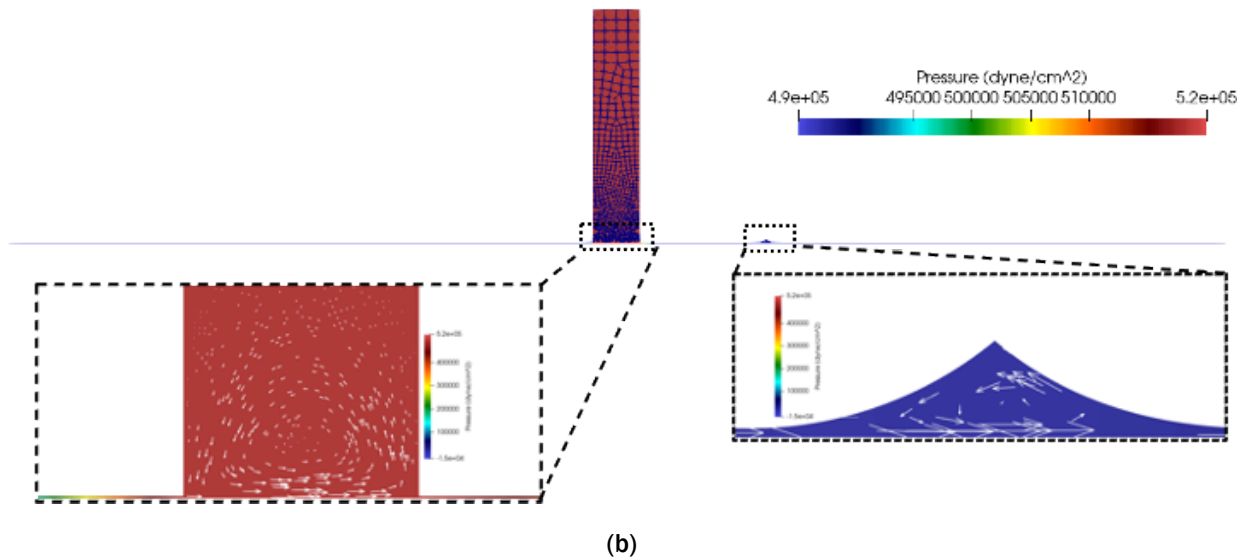


Figure 112. (a) Basic coating configuration and (b) finite element model of tensioned web slot coating of a surface treatment ink. Source: SNL

The modeling approach, as shown in Figure 113, used GOMA. In the liquid region, there is a Navier-Stokes system for conservation of momentum, and, in the web region, a thin-shell observation is used including an equation of elasticity because of the thinness of the web coating. The term, k , is the temperature of the web and the term, T , is a function of the modulus and thickness of the web. Both equations are solved simultaneously so that they are fully coupled to get a steady-state solution. For the case study, the fluid and web properties and operating conditions were established based on National Science Foundation Engineering Research Center (NACENT) requirements to achieve a 500-nm web thickness. One of the steady-state solutions from solving the equations is shown in Figure 114. There was one potential problem. When the film thickness of the coating is greater than the width of the fixed slot gap, or the ratio of the wet thickness to the slot gap is less than 0.2, there can be vortices, and this was observed in the SNL/UNM models. If the coating has a suspension of particles, the vortices will be problematic because there will be a dead zone where the particles can flocculate and produce non-uniformity across the web causing defects, such as bubbles. If a 500-nm wet thickness with a 10- μm gap is targeted, then the ratio is 0.05.

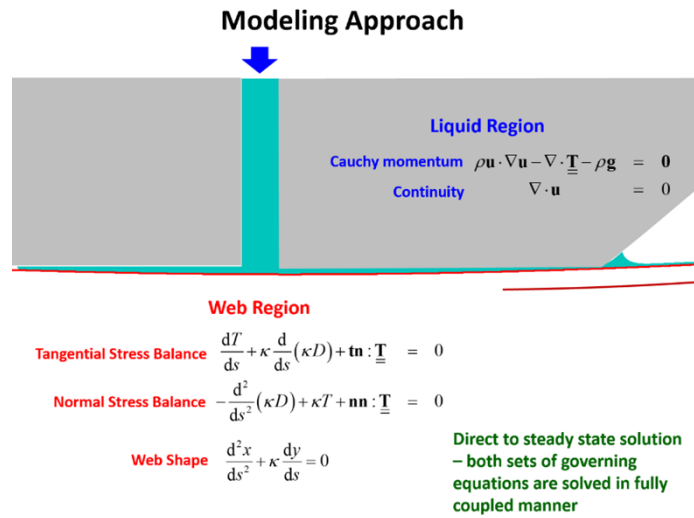


Figure 113. The modeling approach for tensioned web slot-die coating. Source: SNL

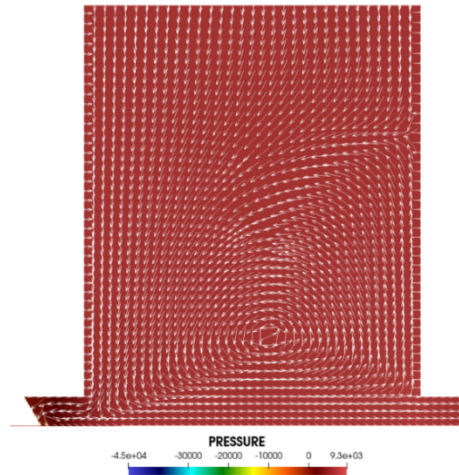


Figure 114. Computational steady-state solution from equations for tensioned web slot-die coating. Source: SNL

For the coating window used for the fixed gap slot-die coating, the web speed was increased while adjusting the wrap to give a stable meniscus. This is the low wrap limit as shown in Figure 115. The high wrap limit is

more complicated. At a high wrap, the liquid contact line retracts back to the feed slot although the weeping limit not reached, after reaching critical maximum wrap. From this, it was concluded that the liquid does not exert enough hydrodynamic force to keep the die web gap fully lubricated and air will be entrained.

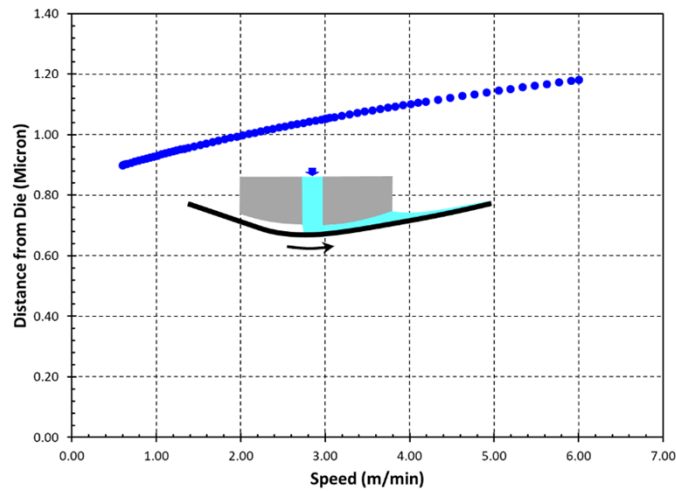


Figure 115. Coating window used for the fixed gap slot-die coating. Source: UNM

UNM experimented using a curved die lip instead of a straight die lip as shown in Figure 116. A solution was obtained where the whole gap was lubricated, but the die geometry created a couple of other problems. First, usually for the fixed gap slot-die coating, there is a tendency to have weeping instability. Second, there can be a diverging gap geometry downstream producing a ribbing instability. Also, a steady-state solution could not be obtained at a speed higher than a critical value where the gap require lubrication. The weeping limit that is achieved in lower die lip radii results in a higher wrap. Diverging gap geometry in downstream may lead to a ribbing instability. Wrap limits are more complicated than vacuum limits for a fixed gap slot-die coating.

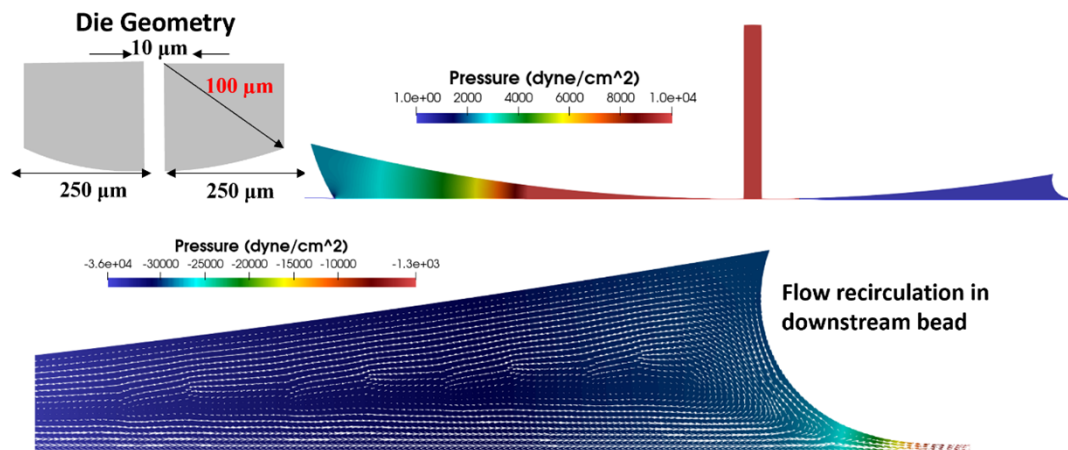


Figure 116. Simulation for a curved-lip slot-die configuration. Source: UNM

Education, information dissemination, publications, and technology transfer

One university graduate was hired to participate in broader modeling related R&D for R2R processing. Results of the modeling and experimental research at SNL resulted in one conference publication and one joint peer-reviewed paper.

Collaboration/Coordination/Outreach/CRADA Projects

Core program

The Collaboration laboratories collaborated and with each other virtually on a weekly basis. Team meetings involving the laboratory leads and principal investigators occurred bi-weekly and included the DOE Technical Managers at one meeting every month. Outreach continued through the principal investigators and researchers presenting at conferences, symposia, peer reviews and during direct contact with industry and the commercial sector. Specific research was reported in technical journals and through patent applications (see Key Publications section).

CRADA project

USC Title 15, Chapter 63, Section 3710c, paragraph 7(A) allows for non-disclosure of trade secrets or commercial or financial information that is privileged or confidential, which is obtained in the conduct of research or as a result of activities from a non-Federal party participating in a CRADA. The government agency may provide appropriate protections against the dissemination of such information for a period of up to 5 years after development of information. As such, some technical information on the CRADA projects will not be included in this report. The following information for each CRADA project was approved or provided by the CRADA partner.

Nel Hydrogen collaboration

The CRADA project team consisted of NREL for gravure coating process development and QC techniques, ORNL for slot-die coating process development, Argonne for X-ray scattering characterization, and Nel Hydrogen for in situ electrochemical testing and pilot-scale coating (with a contracted toll coater). The objective was to research R2R manufacturing of advanced (low loading, direct coated onto membrane) electrolysis electrodes for low-cost hydrogen production. Specifically, this project is targeted on manufacturing the anodic part of a MEA using a direct-coated CCM approach. The project workflow for the laboratories covered three research tasks: (1) preparation of anodic inks, (2) development of the coating technology, and investigation of QCs techniques. Nel Hydrogen performed in situ electrochemical testing in addition to guiding the kinds of materials being produced.

Nel Hydrogen has traditionally used batch-manufacturing processes so the materials they make have high manufacturing costs. Their target for cost is significantly different than the DOE target of less than \$1/kg for hydrogen production. Moving from small-scale manufacturing to large-scale manufacturing has significant benefits for reducing the costs of hydrogen production. Overall, for PEM electrolyzers, going to a manufacturing economy of scale will significantly drop the cost. The processes and technologies being developed will enable Nel Hydrogen to shift to low-cost large-scale manufacturing. For much of electrolyzer production, the catalyst layers are deposited onto a sacrificial decal and then laminated to a membrane. However, the decal substrate and lamination process add to the production costs. If the catalyst layer could be directly coated to the membrane it would simplify manufacturing by eliminating materials waste and a process step. However, the process of directly coating the catalyst layer on the membrane is challenging because the membrane tends to swell in the solvents used to cast the catalyst layer. If a process can be developed to manage or mitigate the swelling, then the number of process steps and costs can be reduced by eliminating the decal liner used to produce catalyst coated membranes.

Cost models developed by Strategic Analysis, Inc. for fuel cell production illustrate that the decal transfer process is a significant portion of catalyst layer production costs. Their analysis determined that the decal transfer process is 63% of the total catalyst layer production cost, which is significant. [15] One challenge to

developing a direct-coating process is that the membrane is hygroscopic and will adsorb the solvents used to cast the catalyst layers. Efforts were to determine how the catalyst inks can be designed to minimize the swelling of the membrane. Experiments were conducted to examine different mixtures of solvents and how the solvents affect the elongation of the membrane under tension. Using droplets of 1-propanol and water on the membrane, the change in the contact angle and the size of the droplet were determined as shown in Figure 117. For 100% water, the adsorption is slow for up to 200 seconds. For 90% and 75% water, the adsorption rate remains slow. For a 50% water mixture, the adsorption rate is faster, so mixtures with water content of 75% and higher were investigated.

Water/1-propanol mixtures on Nafion 212

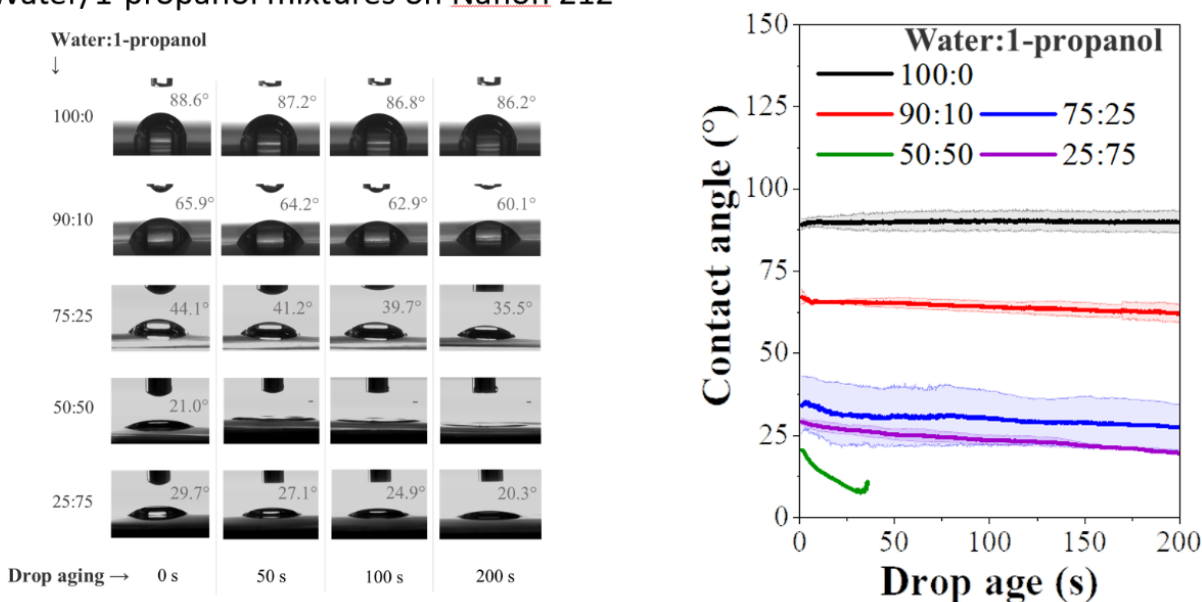


Figure 117. Change in the contact angle and droplets for varying concentrations of water and 1-propanol.
Source: NREL

IrO₂ inks

Studies were carried out on IrO₂ catalyst inks to understand ionomer-catalyst interactions and develop formulations to improve ink stability (i.e., reduce particle sedimentation). Zeta potential measurements of catalyst inks using the down-selected (by Nel Hydrogen) IrO₂ catalyst material showed a decrease in the zeta potential of the particles with the addition of Nafion ionomer to the particle dispersion, indicating adsorption of ionomer to the IrO₂ particle surface, as shown in Figure 118(a). This also corresponded with a decrease in the hydrodynamic particle diameter measured by dynamic light scattering as shown in Figure 118(b). These two measurements show that ionomer adsorption is leading to electrostatic and/or steric stabilization of IrO₂ particles and a reduction of agglomeration. However, these measurements were conducted at very dilute concentrations, which are not relevant for R2R coating. Rheological measurements conducted on baseline inks with concentrations appropriate for R2R coating were inconclusive in determining if these stabilizing effects were present at high concentrations.

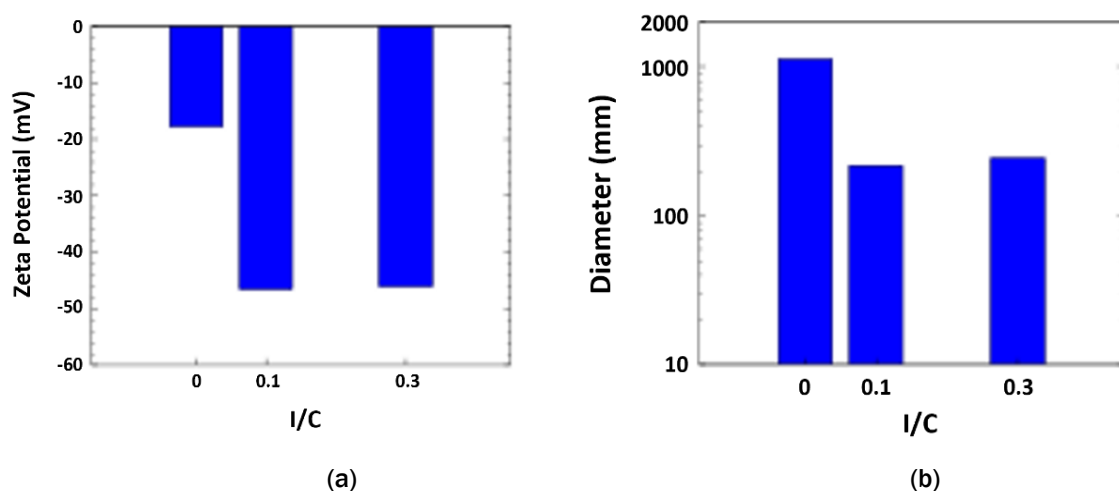


Figure 118. (a) Zeta potential measurements of dispersions of IrO₂ particles without ionomer (0 I/C) and with ionomer (0.1 I/C and 0.3 I/C). (b) Z-average hydrodynamic diameter of the same dispersions. Source: NREL

Additional studies were conducted to determine if the addition of polymer additives (not Nafion) could modify the ink rheology and improve stability. Rheological measurements showed that high molecular weight polymer additives like PEO and PAA resulted in modest increases in steady-shear viscosity but did not significantly alter rheological behavior. Bench-top studies of particle sedimentation by visual inspection of ink opacity did not indicate the polymer additives resulted in any changes in sedimentation. The addition of a non-ionic associative polymer showed more significant increases in viscosity than PEO or PAA. The viscosity was found to increase because this polymer was sensitive to the ratio of water/1-propanol ratio in the ink.

Drying studies were conducted by video recording the drying of catalyst ink droplets under an optical microscope. The primary observation of these recordings was that the down-selected IrO₂ catalyst appeared to have larger particle size distribution and more large particles than NREL's commonly used, commercially-available catalysts.

Catalyst layer coating

Anode catalyst layers using IrO₂ catalysts were prepared from two different suppliers. Gravure coating was used to make the catalyst coated membranes using the two different catalyst materials with the same ink formulation and same process. The two catalysts had different loadings of 0.45-0.5 mg/cm² (Catalyst 1) and 0.375 mg/cm² (Catalyst 2). Figure 119(a) shows the membrane as it comes from the gravure coating station with wrinkling that was caused by swelling of the membrane as it adsorbs the solvent. Figure 119(b) shows the membrane after drying as a smoother, normal membrane. The ink using Catalyst 2 resulted in a lower loading. The Catalyst 2 material is known to have a higher surface area than the Catalyst 1 material, so the difference in the coated catalyst layer loading could be due to the higher surface area of Catalyst 2 increasing the viscosity of the catalyst ink leading to lower fluid transfer from the gravure cylinder. Rheological properties of the catalyst inks were measured using steady shear rheometry and the results shown in Figure 120. Comparing the rheology of the two inks, Catalyst 2 produced a more viscous ink likely due to its higher surface area, which confirms the hypothesis that the higher viscosity of the Catalyst 2 ink is leading to lower fluid transfer from the gravure cylinder to the membrane substrate. Regardless, some very good coatings were obtained.

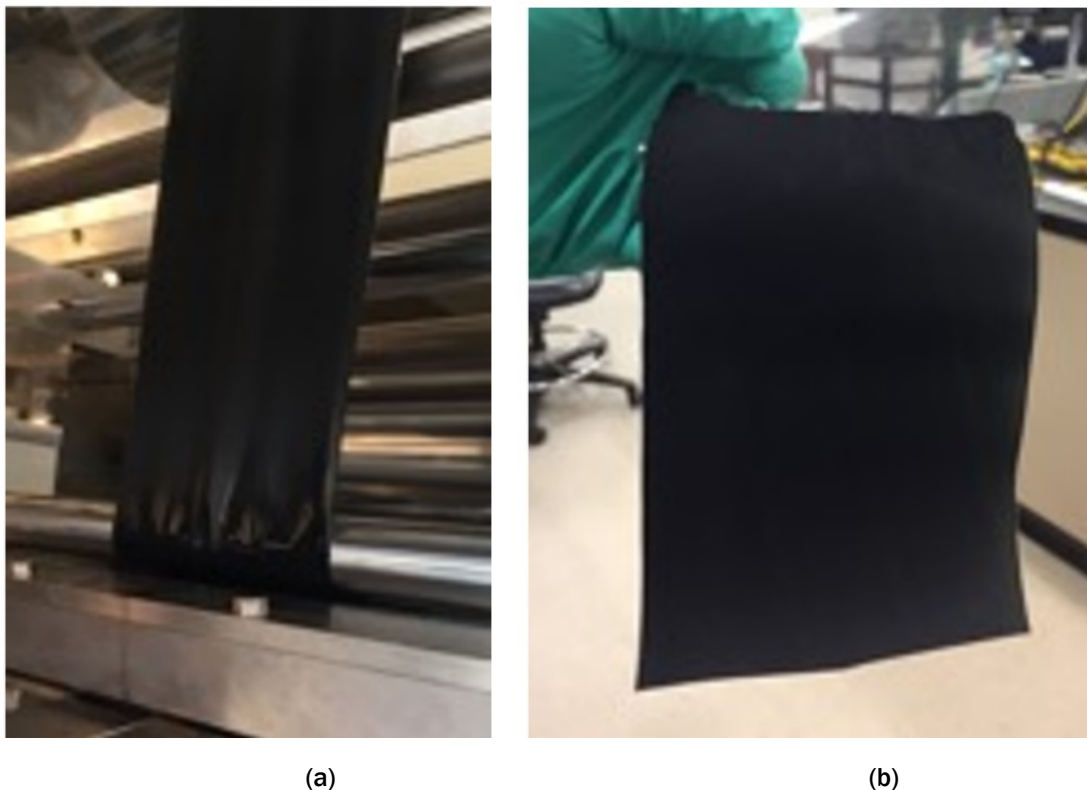


Figure 119. (a) Membrane from the gravure coating station with wrinkling caused by swelling and (b) the smooth, normal membrane after drying. Source: NREL

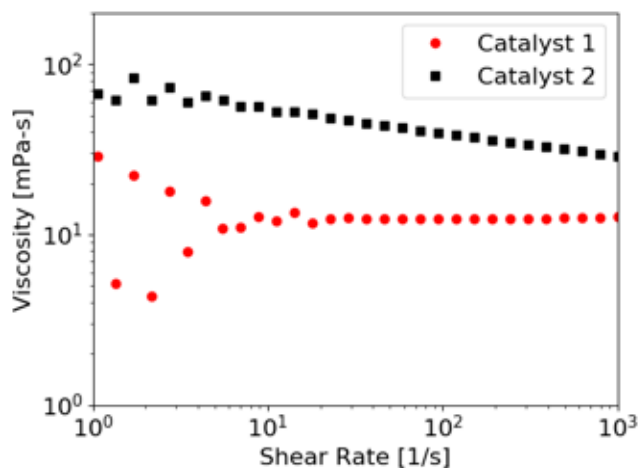


Figure 120. Steady-shear rheology of two IrO₂ catalyst inks. Source: NREL

NREL and ORNL provided anode CCMs prepared using small-scale R2R processes and samples of the catalyst coated membranes were sent to Nel Hydrogen to conduct in situ testing. The results of the stack testing are shown in Figure 121. All cells showed stable performance, even after unplanned interruptions to the operation at 122 hrs. and 357 hrs. Nel Hydrogen has been performing scale up using the NREL formulations and sending their products to Kodak Eastman Business Park to conduct pilot-scale coating trials which are expensive because of the amount of catalyst needed for pilot scale studies.

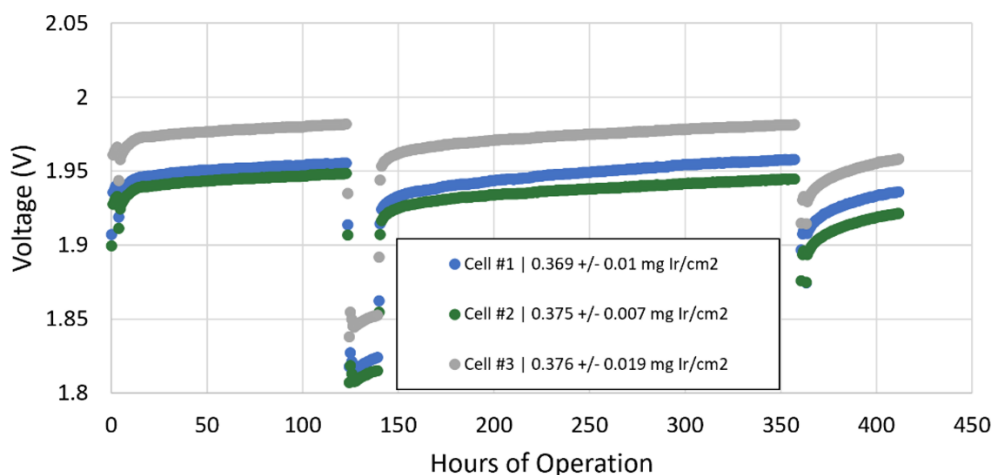


Figure 121. Electrolyzer testing of a three-cell stack at 1.8 A/cm² for anodes prepared by NREL and assembled into full MEAs and tested at Nel Hydrogen. Source Nel Hydrogen

At the direction of Nel Hydrogen, NREL determined what would be required to modify their existing R2R coating equipment to allow for gravure printing. Printing electrode patches will improve materials utilization because the catalyst will be printed in only the active area of the electrolyzer cell. Previously, gravure coating has been used to coat the membrane as a single, large stripe, as shown in the top of Figure 122. The current coating process results in a wide strip of electrode material with the catalyst coated outside the cell active area (red circle shown in the upper right), leading to much of the coated catalyst material not being utilized for electrochemical reactions. This coating process was useful for proving out the direct coating processes but is less desirable for manufacturing due to the low material utilization of the expensive IrO₂ catalyst. Printing electrode patches that match the cell active area, as shown in the bottom of Figure 122, will result in 100% of the coated catalyst material being utilized for electrochemical reaction. Limiting the catalyst to the active area will also improve sealing of the cells for operation at high differential pressure. The printed cell active area will be 28 cm². However, due to difficulties finding a company that would be able to supply the patterned cylinders and the long lead times to produce them it was decided that it was not feasible to pursue this further.

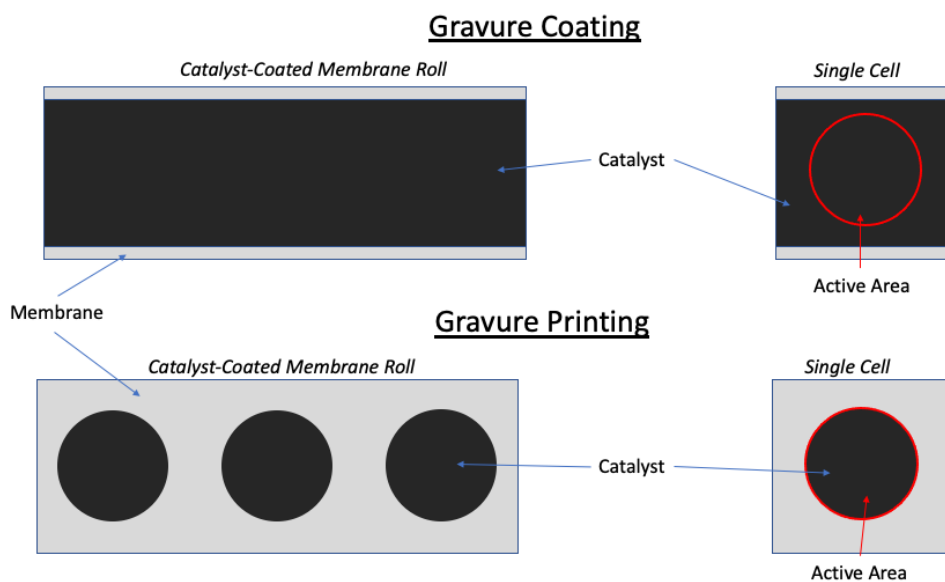


Figure 122. Comparison of gravure coating and gravure printing. Source: NREL

QC technique

Optical transmission imaging of half CCMs was evaluated to assess catalyst layer loading uniformity. IrO₂ catalyst layers on a membrane that were created at NEL Hydrogen and NREL were imaged using a desktop scanner to measure light transmission. The same catalyst layers were also measured using XRF spectroscopy. The average loading of the whole catalyst layer area was compared to the average transmission of the same area. These results, presented in Figure 123, show that there is a strong correlation between XRF-measured loading and the optical transmission.

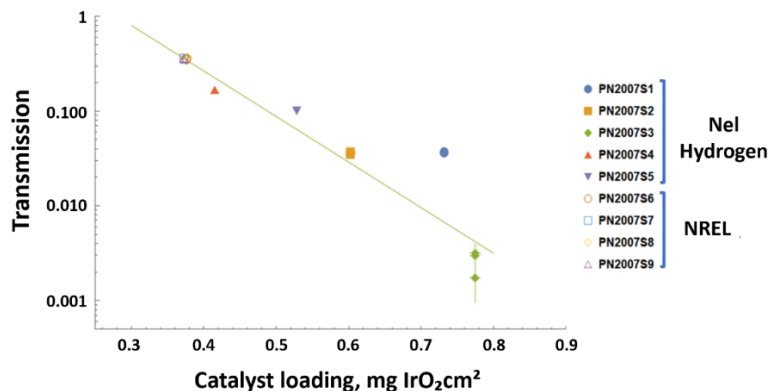


Figure 123. Correlation of XRF-measured catalyst loading and optical transmission for Nel Hydrogen and NREL CCMs. Source: NREL

The next step was to create high resolution images providing a loading map of the catalyst layers. There were 80 local XRF loading measurements obtained along two lines within the sample, as shown in Figure 124(a). XRF measurement spots were then aligned spatially with the corresponding transmission images to obtain the transmission-to-loading correlation parameters, as shown in Figure 124(b). Finally, the high-resolution loading maps of the two anodes were obtained, as shown in Figure 124(c). Good correlation exists between Ir loading and transmission values. This method has a potential to become a valuable loading characterization technique for in-line monitoring of fabrication processes of PEM water electrolyzer anodes.

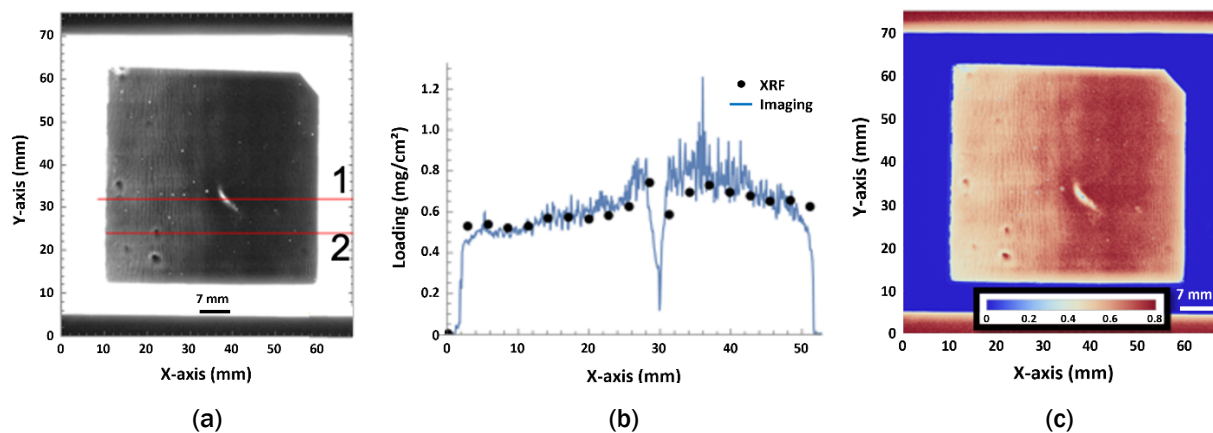


Figure 124. (a) Optical transmission image of half CCM. (b) Comparison of transmission and XRF-measured loading along line 1 in (a). (c) High resolution spatial map of loading based on transmission-to-loading correlation generated from line scans. Source: NREL

NREL continued QC studies on the Pt-based catalyst coated membranes by developing optical transmission measurement techniques to determine the loading on the coated catalyst layers. The optical transmission images are shown in Figure 125(a). The estimated loadings on the graph shown in Figure 126(b) are based on these images. The data in Figure 125(b) correlate the transmission results from NREL and Nel Hydrogen catalyst coated membranes. The data are for the average transmission of a single electrode area versus the average loading in the same area and is not a point measurement but a single sample scale correlation. There is still a good correlation between the optical transmission and the measured loading obtained by XRF. If a line scan is performed across the optical image, the XRF measured loading track well with the optically measured loading including apparent defects as shown in Figure 125(c).

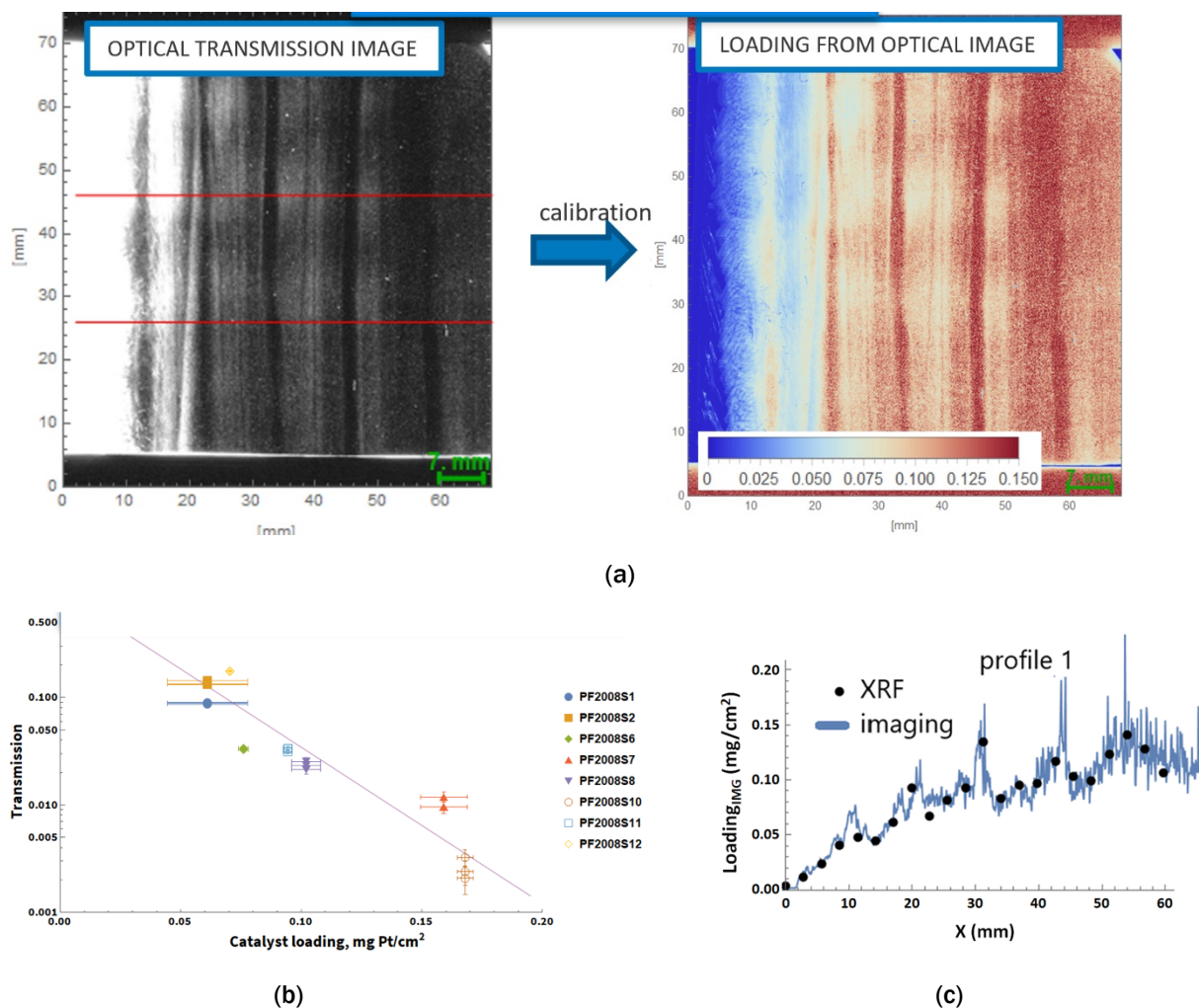


Figure 125. (a) Comparison of the optical transmission image with the loading from the optical image after calibration, (b) transmission results from NREL and Nel Hydrogen CCMs, and (c) XRF measured loading compared to the optically measured loading including apparent defects. Source: NREL and Nel Hydrogen

Additionally, four anode decals produced by Nel Hydrogen on a R2R pilot-coating line at Kodak Eastman Business Park were scanned. The samples were with IrO₂ catalyst on PTFE substrates coated with different wet-film thickness. These scanning measurements were conducted as an initial evaluation of correlation between a high-resolution optical signal and catalyst areal loading. The anode materials were free of known defects and were scanned in transmission-mode only, as shown in Figure 126. Features of high-transmission points, variations on the scale of ~ 1 cm, vertical (coating machine direction) lines, and varying uniformity were observed. The observations in transmittance were consistent with XRF-measured loading values with

lower transmittance corresponding to higher Ir loading. While this method proved useful in detecting loading variations in lower loaded catalyst layers (50% and 75% of the baseline wet film thickness), which are in the range of DOE loading targets for electrolysis anodes, a more sensitive camera and/or brighter light source is likely needed to successfully image the higher loadings that still may be required for near-term Nel Hydrogen products (83% and 100% of the baseline wet film thickness).

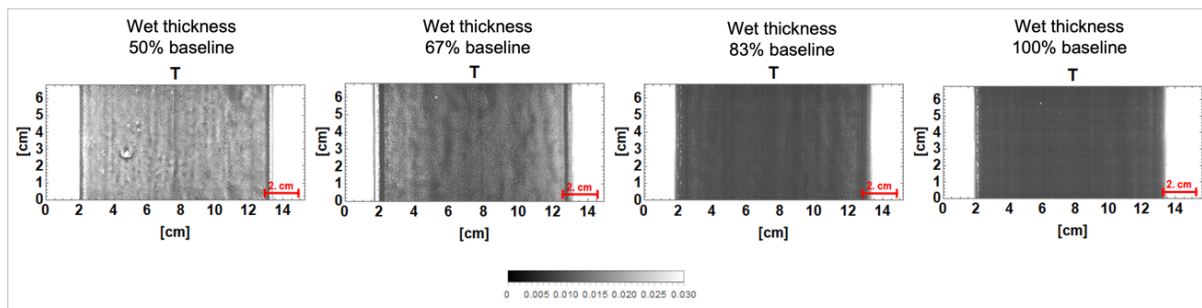


Figure 126. Transmission-mode optical scanning images of anode decal materials, with increasing catalyst coating wet thickness. In the cross-web direction, the second and third samples show a trend of decreased signal in the central region of the coating, likely corresponding to the slight increase in loading in the same region seen in XRF measurements. Source: NREL

Workforce Development/Educational Outreach

The Collaboration laboratories integrated students and postdocs into all aspects of the program and ensured proper education and dissemination of information from the program thereby promoting a workforce with skill sets that support research, development and modeling for manufacturing technologies and processes. The R2R AMM DOE Laboratory Collaboration expanded its workforce development and educational outreach efforts in Phase 2 for the laboratories and universities listed in Table XII.

Table XII. Educational Development at the R2R Collaboration Laboratories in Phase 2

Collaboration Lab	Post Doc/Student/Intern	University
LBNL	Fuduo Ma, Post Doc	Colorado School of Mines
	Olga Kononova, Post Doc	University of Massachusetts Lowell
	Eongyu Yi, Post Doc	University of Michigan
	Zhi Huang, Post Doc	Purdue University
	Buyi Zhang, Graduate Student	University of California Berkeley
	Bei Fan, Post Doc	University of California San Diego
ANL	Pallab Barai, Post Doc	Texas A&M University
	Firat Cetinbas, Post Doc	University of Delaware
	Lauren Valentino, Post Doc	University of Illinois at Urbana-Champaign
	Varada Palakkal, Graduate Intern	Louisiana State University
	Patrick Yang, Associate	Stony Brook University
	Devon Powers, Post Doc	Vanderbilt University
	Ashley Simmons, Consultant	Kettering University
	Mark Koziel, Consultant	University of Illinois at Chicago
	Kathleen Dewan, Undergrad Student	Northwestern University
	Kyle Jiang, Undergrad Student	Georgia Institute of Technology
	Jaehyung Park, Post Doc	University of Connecticut

	Jacob Wat, Undergrad Student Hazel Galvan, Undergrad Student Li Cao, Research Associate Mones Omari, Research Associate	Northwestern University Gettysburg College University of Chicago University of Wisconsin – Milwaukee
ORNL	Marissa Wood, Post Doc Ritu Sahore, Post Doc Anand Parejiya, PhD Student TJ Christensen, Tech Intern Erin Creel, Post Doc Alexander Kukay, PhD Student Xiang Lyu, Post Doc Manufa Assoc.	University of Washington Cornell University University of Tennessee Bredeben Center N/A University of California Berkeley University of Tennessee Ohio University
NREL	Sunil Khandavalli, Post Doc Brian Green, Undergraduate Derek, Jacobson, Graduate Intern Janghoon Park, Post Doc Carlos Baez-Cotto Sanghun Lee	University of Massachusetts Amherst University of Denver Colorado School of Mines University of Massachusetts Amherst University of Minnesota–Twin Cities. KAIST (Daejeon, Korea)
SNL	Chris Wall, Graduate Student Ben Wall, Graduate Student Lena Hoover, Graduate Student Sebastian Valencia, Graduate Student Robert Malakhov, Graduate Student Andrew Cochrane, Post Doc Chance Parrish, Post Doc	New Mexico Tech (Albuquerque, NM) New Mexico Tech (Socorro, NM) University of New Mexico Georgia Institute of Technology University of New Mexico University of New Mexico University of New Mexico
Total	41	34 Different Universities/Colleges

Results of the research was published (see Key Publications below) and, where applicable, intellectual property was filed in collaboration with all contributing laboratories. The collaboration continued to reach out to industry to ensure technology transfer and established an Industry Engagement Panel to support this effort.

Challenges/Contingencies

In Phase 2, the R2R AMM DOE Laboratory Collaboration built upon successes from the previous Phase 1 R2R Consortium efforts in battery and fuel cell materials R&D and expanded to include ES, multilayer coating, ion-exchange membrane materials, air filtration media, continuum coating flow modeling, and printed electronics inks. The biggest programmatic challenge was to meet established and approved milestones after schedules were impacted by the COVID-19 pandemic. Task schedules and milestone dates were adjusted contingent on access for approved personnel to laboratory facilities. Typical challenges occur when additional time is needed to get test equipment operational (downtime) or to receive new equipment and materials from vendors as well as negotiating contractual agreements which creates delays. This challenge was exacerbated by the closure of all laboratory facilities including procurement offices and machine shops that prevented parts and equipment from being ordered or fabricated in a timely manner.

Risks and Risk Handling

Early stage research usually has higher risks for the outcome of successful technologies compared to advanced development because of the nature of the basic science and phenomenology being investigated. Other risks

occur when funding or materials/equipment are not readily available to begin experimentation, but FY 2020 and FY 2021 had an additional risk – COVID-19 – that was not anticipated nor effectively mitigated without a timeframe for the laboratories to return to a normal full-time operation. Once restrictions started to relax, a staged reopening of the laboratories was initiated. Initially, some minimum amount of research was conducted in limited blocks of time and on a special case basis and with limitations on the number of people occupying each laboratory at a given time to ensure distancing. This significantly impacted the research tasks and milestone schedules, which required reprogramming in FY 2021, with the expectation that all the National Laboratories would return to full operations, and lost time could be made up by focusing on the major tasks and accelerating efforts on those tasks.

Project Ratings

Project performance assessments are determined through quantitative and qualitative methods in accordance with DOE Program and Project Management for the Acquisition of Capital Assets. [16] Programs are assessed by the following definitions: green – project is expected to meet its current performance baseline; yellow – project is potentially at risk of not meeting an element of the current performance baseline; red – project is highly at risk of requiring a change to the performance baseline by the Acquisition Executive or is not being executed within the acquisition strategy and Project Execution Plan.

Based on reprogramming of ongoing tasks in FY 2020 to FY 2021, the five R2R Collaboration laboratories met their performance targets and milestones on time and within their schedules and costs and were assessed green.

Conclusions

FY 2021 was the third and final year of a three-year Phase 2 project for early stage R&D on R2R advanced technologies in a national multi-laboratory collaboration. Efforts delivered advances in the fundamental understanding of R2R processing on moving webs, carriers, or other substrates and developed tools, metrology approaches, processes, and new materials to improve yields, overall quality, processing rates and reduce cost. Technologies developed and scientific breakthroughs achieved will enable industrial scalability and a better understanding of the fundamental chemistry and materials properties applicable to R2R manufacturing that were demonstrated on selected key technology applications with cross-cutting impacts.

ANL developed new synthesis pathways for making LLZO nanofiber-polymer composite solid-state Li battery electrolytes using R2R ES and slot-die coating technologies. The nanocomposite solid electrolyte membranes had improved mechanical and chemical stability over the conventional polymer electrolytes, which enabled high current density cycling up to 8 mA/cm² at 1 mAh/cm² for several hundred hours with a small polarization voltage. A 10x higher production rate of the LLZO nanofibers was achieved by improving R2R ES processing conditions, which demonstrated scale-up potential for the nanofiber-based solid electrolytes. A methodology to integrate nanoparticulate catalysts into nanofibers to form catalyst-on-fiber membranes was developed based on R2R ES. This will enable a more efficient electrocatalysis process for a number of electrochemical applications, such as water splitting, biological treatment of wastewater, and CO₂ conversion with the benefits reaction and/or conversion efficiency enhancement and catalysts operation life improvement. The production rate of dual-fiber deionization membranes was increased for more than 3x by simultaneously optimizing ES conditions for cationic and anionic fiber deposition during a continuous co-ES process. An ink material exploration study was performed for printed electronics, an emerging electronic device fabrication method that has niche applications in flexible and wearable devices. ANL also demonstrated the feasibility of applying a printed electronic technology to active microelectronic device fabrication by developing a fully printed PMOS inverter. Inverters are the most basic building blocks within all digital logic gates used in active components of electronic devices. The work performed showed promise for making logic devices via additive manufacturing,

which is more compatible to R2R manufacturing and is less costly than traditional silicon wafer manufacturing processes.

ORNL conducted coating trials that validated the SNL 2D GOMA model by coating a 3.5 wt.% Pt/C slurry on Al foil using the predicted defect-free coating window. Characterization of composite cathodes based on Al-LLZO fibers was completed and superior cycling performance at high rates of the Al-LLZO based cathodes was obtained. Solid state composite electrolytes based on PEO/LiTFSI and Al-LLZO fibers were synthesized. The effects of mixing time and speed was investigated for five different mechanical mixers with results that higher mixing speeds showed a considerably lower number of large agglomerate particles, indicating that a significant number of agglomerates have been broken up after brief shear mixing. A stable, defect-free catalyst layer coating with constant wet thickness was established at multiple line speeds and vacuum pressures on Al foil. The experimental coating window on the foil closely matched the modeled coating window produced by SNL. Nanostructured Al-LLZO fiber scaffolds were employed to tailor the chemical functionalities of a cathode-electrolyte-interface layer resulting in significant improvements in the macroscopic electrochemical properties of assembled coin cells. Composite polymer electrolytes based on PEO were fabricated using the Al-LLZO ligament scaffolds resulting in a threefold increase in electrical conductivity attributed to the ionically conductive Al-LLZO cubic phase. Electrospun YSZ nanofibers were synthesized using the same processing conditions that were used for the synthesis of the LLZO nanofibers to demonstrate flexible ES. Electron beam radiation of 180 kGy was demonstrated for curing a two-layer coating at a line speed of four feet per minute that used aqueous dispersions of acrylated polyurethane and carboxymethyl cellulose as binders.

NREL developed and demonstrated a novel IR-spectroscopy-based quality-inspection method to simultaneously measure membrane and electrode thickness in a CCM which resulted in filing a record of invention. A stable slide flow and good coating quality of simultaneous two-layer slide die coatings was demonstrated for a wide range of ink properties and coating conditions using analog particle-polymer inks with similar rheological behavior as PEMFC catalyst inks. This successfully established a basis for lower-cost, lower-energy-consuming processing of multilayer structures across a range of applications. NREL also provided constituent- and ink-level property measurement data for 62 different PEMFC and electrolyzer catalyst inks to LBNL in support of novel heterogeneous non-Newtonian ink model development.

LBNL implemented equations from the literature to describe drying a coating with a moving surface, and a progression of particle volume fraction profiles in a simulated coating undergoing drying were generated. An optical table and confocal microscope was installed and constructed an open flow cell for use with the automated mixing setup to observe particles in dilute aqueous dispersions under the confocal microscope. A novel optical sectioning capability was developed for the confocal microscope, which is more known as a microscope for surface analysis. Optical section images were collected, and an image analysis program was developed to obtain histograms of optical size for agglomerates. A modular automated miniature coating observation platform was constructed to observe drying coating samples with the confocal microscope and ALS 8.3.2. hard X-ray microtomography beamline. This miniature coating line includes a custom computer-controlled doctor blade which can vary coating height during a coating process. LBNL demonstrated the system using a doctor blade coating of an NMP-based slurry that is used in battery applications, followed immediately by confocal imaging.

SNL completed a special slide-only model to aid redesign of a slide die lip geometry. A fully-converged steady-state model of three-layer slide coating flow with the actual ink rheology of a PEMFC construction was achieved for the first time. Calculations of coating windows are a first for multilayer slide die coating, and very little data exist currently exists. A single-layer solvent-polymer drying model was successfully demonstrated that was regressed with ML software using experimental data in the literature. An experimental setup was completed to obtain drying weight time histories, complementary to the setup at LBNL, for model validation and tuning. Deposition models of single- and two-layer slot-die coating flow were updated and the single-layer slot-die coating model was validated against coating trial observations at ORNL. This improved the process

window for inks at various concentrations of catalyst and carbon support. The coating process window predictions for operating vacuum were used by ORNL to achieve a smooth coating without streaks on subsequent trials. SNL ran the polymer/solvent/particle drying model successfully with expected results for “fast” drying, which indicates a particle skinning effect. A test fixture to better control for start-up of the drying coat-weight measurements was designed to aid in model validation. Tensioned web (without a backing roll) models were refined and models for a surface-treatment ink used in precision coatings were developed. A test fixture was designed that can be used to measure heat and mass transfer coefficients for the drying model. The utility of rheolaser detection of particle motion during drying was also demonstrated.

For the Nel Hydrogen CRADA, NREL measured the steady-shear rheology of the catalyst inks with IrO₂ from different suppliers and one catalyst material resulted in higher viscosity and lower fluid transfer from the gravure cylinder to the membrane substrate, which was attributed to higher catalyst surface area. Catalyst ink formulations from these measurements and R2R-coating trials in FY20 were used as the basis for the pilot-scale R2R coating runs of products from Nel Hydrogen at Kodak Eastman Business Park. Optical QC inspection techniques were evaluated for measuring IrO₂ loading and defect detection using IrO₂ catalyst layers coated on membranes created at Nel Hydrogen, at NREL, and pilot R2R runs at Kodak. The average loading of the whole catalyst layer area, which was measured with XRF, showed a strong correlation to optical transmission. Good correlation was also observed between the local IrO₂ loading and local transmission values. Visually apparent defects in the coating were detected in the transmission imaging. This method has a potential to become a valuable loading characterization technique for in-line monitoring of fabrication processes of PEM water electrode anodes.

The projects in Phase 2 directly support the AMO’s Multi-Year Program Plan challenges for the use of multilayer coating technologies applicable to flexible and integrated electronics, separation membranes, PVs, and selective barrier materials addressing the AMO identified targets of technologies with a 10x production capacity increase and in-line instrumentation tools to evaluate the performance and functionality.

Key Publications

The following key publications/presentations are for FY 2021. Other publications for Phase 2 can be found in references [7] and [8].

Creel, E.B., Tjiptowidjojo, K., Lee, J.A., Livingston, K.M., Schunk, P.R., Bell, N.S., Serov, A., Wood III, D.L., 2021, “Slot-die-coating operability windows for polymer electrolyte membrane fuel cell cathode catalyst layers”, *Journal of Colloid and Interface Science*, <https://doi.org/10.1016/j.jcis.2021.11.047>

Creel, E., Baez-Cotto, C., Young, J., Mauger, S.A., Ulsh, M., Wood III, D.L., Serov, A., 2021, “Effects of Processing Time, Mixing Speed, and Mixer on Agglomerates in Fuel Cell Cathode Inks”, Presentation at the 240th Electrochemical Society Conference, October 10-14, 2021 (Virtual Meeting)

Cushing, A., Zheng, T., Higa, K., and Liu, G., 2021, “Viscosity Analysis of Battery Electrode Slurry”, *Polymers*, 13(22), 4033, <https://doi.org/10.3390/polym13224033>

Higa, K., Battaglia, V.S., and Srinivasan, V., 2021, “PyGDH: Python Grid Discretization Helper”, *Journal of Open Source Software*, 6(59), 2744, <https://doi.org/10.21105/joss.02744>

Jacobsen D.M., Rupnowski P., Porter J., Ulsh M., “Spectroscopic investigation of catalyst inks and thin films toward the development of ionomer quality control.” Accepted for publication in *Applied Spectroscopy*.

Khandavalli S., Sharma-Nene N., Kabir S., Sur S., Rothstein J.P., Neyerlin K.C., Mauger S.A., Ulsh M. “Towards Optimizing Electrospun Nanofiber Fuel Cell Catalyst Layers: Particle-polymer Interactions and Spinnability.” *ACS Applied Polymer Materials*, 3, 2021.

Mauger S.A., Wang M., Cetinbas F., Dzara M.J., Park J., Van Cleve T., Hu L., Litster S., Ahluwalia R., Pylypenko S., Myers D.J., Neyerlin K.C., Ulsh M. “Influence of ink formulation and drying conditions on ionomer distribution in high-performance roll-to-roll coated gas-diffusion electrodes.” Oral presentation at the Fall ESC Meeting (virtual); October 2020.

Mauger S.A., Wang M., Cetinbas F., Dzara M., Park J-H., Myers D., Ahluwalia R., Pylypenko S., Hu L., Litster S., Neyerlin K.C., Ulsh M. “Development of High-performance Roll-to-roll-coated Gas-diffusion Electrodes.” *J Power Sources*, 506, 2021.

Nikitin, V. De Andrade, A. Slyamov, B.J. Gould, Y. Zhang, et al., 2021, “Distributed optimization for nanorigid nano-tomography”, *IEEE Trans. Computational Imaging*, 7, 272

Park J., Kang Z., Bender G., Ulsh M., Mauger S.A. “Direct roll-to-roll coating of catalyst-coated membranes for low-cost PEM water electrolyzers.” Oral presentation at the Fall ESC Meeting (virtual); October 2020.

Park J., Kang Z., Bender G., Ulsh M., Mauger S.A. “Roll-to-roll Production of Catalyst Coated Membranes for Low-temperature Electrolyzers.” *J Power Sources*, 479, 2020.

Park J., Ulsh M., Mauger S.A. “Solvent Absorption Rate of Perfluorosulphonic Acid Membranes Towards Understanding Direct Coating Processes.” *International Journal of Hydrogen Energy*, 46, 2021.

Polizos, G., Sharma, J., Jafta, C.J., Muralidharan, N., Veith, G.M., Keumc, J.K., Kukay, A., Sahore, R., Wood, D.L. III. 2021. “Nanostructured ligament and fiber Al-doped $\text{Li}_7\text{La}_3\text{Zr}_2\text{O}_{12}$ scaffolds to mediate cathode-electrolyte interface chemistry.” *Journal of Power Sources*, Vol. 513, 30 November 2021,

Tjptowidjojo, K., Park, J., Mauger, S.A., Ulsh, M., Schunk, P.R., 2021, “Process model for multilayer slide coating of polymer electrolyte membrane fuel cells.” *Journal of Coatings Technology and Research*, July 8, 2021, <https://doi.org/10.1007/s11998-021-00508-7>

Wang, P. L., A. Roschli, M.P. Paranthaman, M. Theodore, C.L.Cramer, C. Zangmeister, Y. Zhang, J.J. Urban, L. Love, 2021, “Recent developments in filtration media and respirator technology in response to COVID-19”, *MRS Bulletin*, vol. 46, 1-10

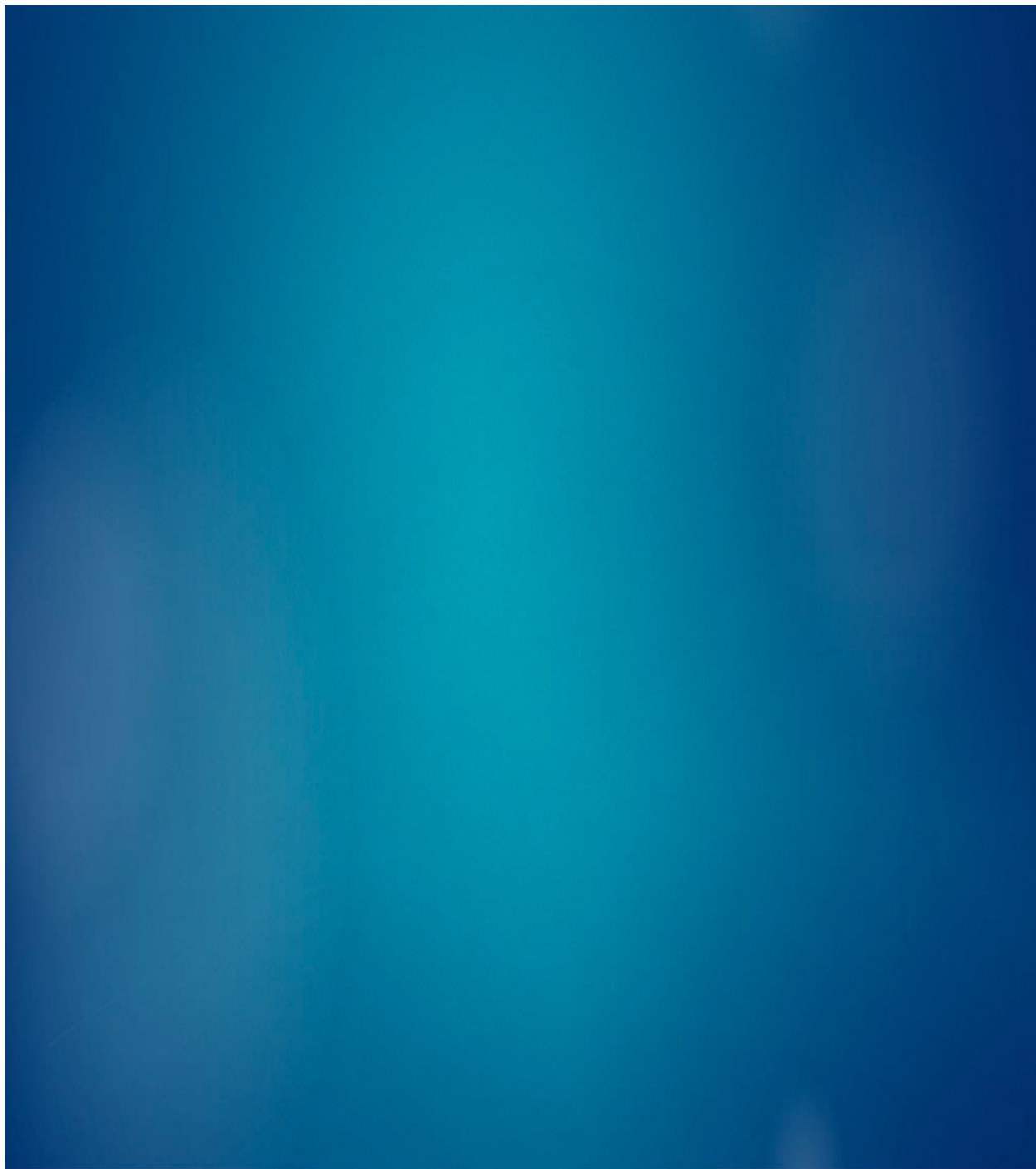
Zhang, Y., S. Tepavcevic, D. Powers, M. Koziel, M. Counihan, 2021, “ $\text{Li}_7\text{La}_3\text{Zr}_2\text{O}_{12}$ nanofiber-based composite electrolyte for solid-state lithium battery applications”, Beyond Lithium-Ion XIII Conference, Invited talk, USA

Zhang, Y., 2021, “Scalable synthesis of nanofibers for energy storage and filtration applications”, 2021 TMS Annual Meeting & Exhibition, Invited talk

References

1. Advanced Manufacturing Office (AMO) Multi-Year Program Plan for Fiscal Years 2017 Through 2021 (DRAFT). December 2016. <https://www.energy.gov/eere/amo/downloads/advanced-manufacturing-office-amo-multi-year-program-plan-fiscal-years-2017>
2. DOE Vehicle Technologies Office website. <https://www.energy.gov/eere/vehicles/batteries-charging-and-electric-vehicles>
3. DOE Energy Storage Grand Challenge Roadmap, December 2020, page 33. <https://www.energy.gov/sites/default/files/2020/12/f81/Energy%20Storage%20Grand%20Challenge%20Roadmap.pdf>
4. Energy Storage Research, University of Louisville Conn Center for Renewable Energy Research. <https://www.conncenter.org/energy-storage-research>

5. Satyapal, S., 2020, "U.S. Department of Energy Hydrogen and Fuel Cell Technologies Office and Global Perspectives)". Presentation at the Innovation for Cool Earth Forum (ICEF) 7th Annual Meeting (virtual), https://www.energy.gov/sites/prod/files/2020/10/f79/hfto-satyapal-ICEF-sept28_0.pdf
6. Macknick, J.; Newmark, R.; Heath, G.; Hallett, K.C., 2011, "A Review of Operational Water Consumption and Withdrawal Factors for Electricity Generating Technologies" 2011, Technical Report NREL/TP-6A20-50900. <https://www.nrel.gov/docs/fy11osti/50900.pdf>
7. Daniel, C., Wood III, D., Krumdick, G., Ulsh, M., Battaglia, V., Crowson, F., 2020, "Roll-to-Roll Advanced Materials Manufacturing DOE Laboratory Collaboration – FY 2019 Final Report", ORNL/SPR-2020/1443, Oak Ridge National Laboratory, Oak Ridge TN. <https://doi.org/10.2172/1606639>
8. Daniel, C., Polsky, Y., Wood III, D., Krumdick, G., Ulsh, M., Battaglia, V., Crowson, F., 2021, "Roll-to-Roll Advanced Materials Manufacturing DOE Laboratory Collaboration – FY 2020 Final Report", ORNL/SPR-2021/1892, Oak Ridge National Laboratory, Oak Ridge TN. <https://doi.org/10.2172/1814323>
9. Kun Fu, et al., 2016, "Flexible, solid-state, ion-conducting membrane with 3D garnet nanofiber networks for lithium batteries", *Proceedings of the National Academy of Sciences* 113(26), 7094-7099.
10. Zhou Li, et al., 2018, "Ionic conduction in composite polymer electrolytes: case of PEO: Ga-LLZO composites", *ACS Applied Materials & Interfaces*, 11(1), 784-791.
11. Nazir, R., Kumar, A., Saad, M.A.S., Ali. S., 2020, "Development of CuAg/Cu₂O nanoparticles on carbon nitride surface for methanol oxidation and selective conversion of carbon dioxide into formate", *Journal of Colloid and Interface Science*, 578, 726-737.
12. Wang, L., Higgins, D.C., Ji, Y., Morales-Guio, C.G., Chan, K., Hahn, C., Jaramillo, T.F., 2020, "Selective reduction of CO to acetaldehyde with CuAg electrocatalysts", *Proceedings of the National Academy of Sciences*, 117:23, 12572-12575.
13. Thanh, T.D., Chuong, N.D., Hien, H.V., Kim, N.H., Lee, J.H., 2018, "CuAg@Ag core-shell nanostructure encapsulated by N-doped graphene as a high-performance catalyst for oxygen reduction reaction", *ACS Applied Materials & Interfaces*, 10:5, 4672-4681.
14. Lee, J., Kim, S., Lee, C., 2019, "Large area electrolyte coating through surface and interface engineering in roll-to-roll slot-die coating process". *Journal of Industrial and Engineering Chemistry*, 76, 443-449. Doi:10.1016/j.jiec.2019.04.011
15. Colella, W.G., James, B.D., Moton, J.M., Saur, G., Ramsden, T., 2014, "Techno-economic Analysis of PEM Electrolysis for Hydrogen Production". Strategic Analysis, Inc presentation at Electrolytic Hydrogen Production Workshop, Golden, CO, 27 February 2014.
16. DOE Program and Project Management for the Acquisition of Capital Assets, DOE 413.3B updated April 12, 2018.



ORNL/SPR-2022/2412 March 2022

For more information, contact: R2RAMM.ornl.gov

